
Tome 34

Août 1996

Numéro 3

La mer

う み

Proceedings of the Eighth JECSS & PAMS Workshop,

26—28 September 1995, Matsuyama, Japan

1996年8月

日 仏 海 洋 学 会

La Société franco-japonaise
d'océanographie
Tokyo, Japon

SOCIÉTÉ FRANCO-JAPONAISE D'Océanographie

Comité de Rédaction

(de l'exercice des années de 1996 et 1997)

Directeur et rédacteur: Y. YAMAGUCHI

Comité de lecture: S. AOKI, M. HANZAWA, M. HORIKOSHI, M. MATSUYAMA, M. MAEDA, M. OCHIAI, T. YANAGI, S. WATANABE

Rédacteurs étrangers: H.J. CECCALDI (France), E.D. GOLDBERG (Etats-Unis), T. ICHIYE (Etats-Unis), T.R. PARSONS (Canada)

Services de rédaction et d'édition: M. OCHIAI, H. SATOH

Note pour la présentation des manuscrits

La mer, organe de la Société franco-japonaise d'océanographie, publie des articles et notes originaux, des articles de synthèse, des analyses d'ouvrages et des informations intéressant les membres de la société. Les sujets traités doivent avoir un rapport direct avec l'océanographie générale, ainsi qu'avec les sciences halieutiques.

Les manuscrits doivent être présentés avec un double, et dactylographiés, en *double interligne*, et au recto exclusivement, sur du papier blanc de format A4 (21×29,7 cm). Les tableaux et les légendes des figures seront regroupés respectivement sur des feuilles séparées à la fin du manuscrit.

Le manuscrit devra être présenté sous la forme suivante:

1° Il sera écrit en japonais, français ou anglais. Dans le cadre des articles originaux, il comprendra toujours le résumé en anglais ou français de *200 mots* environs. Pour les textes en langues européennes, il faudra joindre en plus le résumé en japonais de *500 lettres* environs. Si le manuscrit est envoyé par un non-japonophone, le comité sera responsable de la rédaction de ce résumé.

2° La présentation des articles devra être la même que dans les numéros récents; le nom de l'auteur précédé du prénom *en entier*, en minuscules; les symboles et abréviations standards autorisés par le comité; les citations bibliographiques seront faites selon le mode de publication: article dans une revue, partie d'un livre, livre entier, etc.

3° Les figures ou dessins originaux devront être parfaitement nettes en vue de la réduction nécessaire. La réduction sera faite dans le format 14,5×20,0 cm.

La première épreuve seule sera envoyée à l'auteur pour la correction.

Les membres de la Société peuvent publier 7 pages imprimées sans frais d'impression dans la mesure à leur manuscrit qui ne demande pas de frais d'impression excessifs (pour des photos couleurs, par exemple). Dans les autres cas, y compris la présentation d'un non-membre, tous les frais seront à la charge de l'auteur.

Cinquante tirés-à-part peuvent être fournis par article aux auteurs à titre gratuit. On peut en fournir aussi un plus grand nombre sur demande, par 50 exemplaires.

Les manuscrits devront être adressés directement au directeur de publication de la Société: Y. YAMAGUCHI, Université des Pêches de Tokyo, Konan 4-5-7, Minato-ku, Tokyo, 108 Japon; ou bien au rédacteur étranger le plus proche: H. J. CECCALDI, EPHE, Station marine d'Endoume, rue Batterie-des-Lions, 13007 Marseille, France; E. D. GOLDBERG, Scripps Institution of Oceanography, La Jolla, California 92093, Etats-Unis; T. ICHIYE, Department of Oceanography, Texas A & M University, College Station, Texas 77843, Etats-Unis; ou T. R. PARSONS, Department of Oceanography, University of British Columbia, Vancouver, B. C. V6T 1W5, Canada.

Preface

Tetsuo YANAGI

This proceedings contains selected papers at the Eighth JECSS (Japan and East China Seas Studies) & PAMS (Pacific-Asian Marginal Seas) Workshop held in Matsuyama, Japan on 26-28 September 1995. The Workshop was convened by Prof. T. YANAGI at Ehime University and was sponsored by Ehime University and voluntary companies. Efforts of the local organizing committee, which were consisted of the members of Laboratory of Coastal Oceanography, Department of Civil and Ocean Engineering, Ehime University, in successfully organizing both the scientific and social programmes were greatly appreciated by all participants.

Seventyfour papers were presented at this Workshop and they reflected the growing interests in physical, chemical and geological oceanography of the Pacific-Asian Marginal Seas including Japan Sea and the East China Sea. Participants at the Eighth Workshop submitted twentyfour papers to this Proceedings and fourteen papers were finally accepted after reviewing. I am very thankful to twentysix reviewers, whose comments and criticisms were so helpful to improve most of papers in this volume. I also appreciate for Prof. Kuh KIM, the Chairman of JECSS & PAMS, for his help in editing this volume.

I express my thanks to Prof. Y. ARUGA, the president of Société franco-japonaise d'océanographie, and Prof. Y. YAMAGUCHI, the Editor-in-Chief of La mer, for their help to publish this volume in La mer.

(Guest Editor, Ehime University)

Embedding an oceanic mixed layer model into an ocean general circulation model of the East Sea (Japan Sea)

Yign NOH*, Chan-Joo JANG*, Cheol-Ho KIM** and Jong-Hwan YOON**

Abstract: The oceanic mixed layer model (OMLM) is coupled with the ocean general circulation model (OGCM) of the East Sea, where the Mellor-Yamada Model is used for the OMLM. The coupled model is used to investigate the impact and the possible improvement achieved by the OMLM with the particular interest in the realization of the SST. The OMLM is found to prevent continuous warming of deep water and to improve convective mixing during the cooling season. On the other hand, the insufficient mixing near the surface, prescribed in the Mellor-Yamada Model, causes the overestimation of the SST during the warming season. It is shown that the problem can be resolved by correcting the surface boundary condition of turbulence. It is also shown that the circulation is not significantly affected by the embedding of the OMLM in the East Sea.

1. Introduction

Recently, substantial efforts are being given to the prediction of the climate system of the earth, in which the ocean plays an important role. Among the many facts of the ocean's role in the climate system, the influence of the sea surface temperature (SST) is most essential. Hence is required the more accurate oceanic mixed layer model (OMLM), as it is indispensable to determine the sea surface temperature (SST) (see, for example; CANE, 1993). Furthermore, the reliable prediction of the oceanic mixed layer is also important for the various applications including fisheries and underwater telecommunication as well.

A large number of one dimensional models have been developed to simulate the oceanic mixed layer, dealing with only the vertical transport of heat (see, for example; KRAUS, 1988). However, the presence of significant horizontal transport of heat often severely restricts the applicability of one-dimensional models; thus necessitates the three-dimensional mixed layer model including the circula-

tion. The effects are especially important in the equatorial ocean, where intensive studies on such a model have been carried out for the proper prediction of the SST in association with El Niño and Southern Oscillation (ENSO) phenomenon (SCHOPF and CANE, 1983; CHEN *et al.*, 1994; CHANG, 1994).

Heat budget analysis suggests that the horizontal transport of heat owing to the advection cannot be neglected either in the East Sea (KATO and ASAI, 1983). This is also evident from the fact that the satellite images of the SST shows the strong correlation with the circulation patterns such as the propagation of the Tsushima Current flowing in through the Korea Strait (Tsushima Strait) and the location of a front (OSTROVSKII, 1995). It is thus apparent that the three dimensional model is required for the prediction of the mixed layer in the East Sea, too.

On the other hand, the necessity for the proper parameterization of the upper ocean process increases in order to improve the ocean general circulation model (OGCM). The conventional OGCM's, in which constant values of vertical eddy viscosity and eddy diffusivity are used, show many undesirable aspects such as the continuous warming of the deep sea and the inappropriate variations of the SST

* Department of Astronomy & Atmospheric Sciences, Yonsei University, Seoul, Korea

** Research Institute for Applied Mechanics, Kyushu University, Kasuga, Japan

(WASHINGTON *et al.*, 1980; SEUNG and YOON, 1995). Moreover, the circulation pattern also appears to be often significantly affected by the inclusion of the OMLM (CHASSIGNET and GENT, 1991; STERL and KATTENBERG, 1994).

There have been several studies in which the embedding of the OMLM into the OGCM is taken into consideration. They applied the OMLM either of bulk model type in which the energy budget of a whole mixed layer is dealt with (ADAMEC *et al.*, 1981; ALDERSON, 1990; SCHOPF and CANE, 1983; HENDERSON-SELLORS, 1986; MCGREARY *et al.*, 1993; STERL and KATTENBERG, 1994; OBERHUBER, 1993), or of turbulence model type in which the turbulent flux terms are parameterized (ROSATI and MIYAKODA, 1988; NAGAI *et al.*, 1992). In general the embedding of the OMLM's of bulk model type has an advantage of smaller computational demand, but has difficulties in adjusting to fixed grids and in describing many phenomena including the formation of a seasonal thermocline. The subject of the simulation was either the global ocean (ADAMEC *et al.*, 1981, ALDERSON, 1990; HENDERSON-SELLORS, 1986; OBERHUBER, 1993; ROSATI and MIYAKODA, 1988) or the regional ocean (SCHOPF and Cane, 1983; MCGREARY *et al.*, 1993; STERL and KATTENBERG, 1994, NAGAI *et al.*, 1992).

From the perspective of investigating the embedding of the OMLM into the OGCM the East Sea also offers an ideal opportunity, since it is endowed with many typical characteristics of the large oceans in spite of the small size. For example, it is a relatively deep ocean as deep as 3700 m, and there appear most of the phenomena characterizing the global ocean such as the western boundary current, the thermohaline circulation and the topographic effects. There have been several cases of investigating the OGCM of the East Sea (SEUNG and YOON, 1995; HOLLOWAY *et al.*, 1995; SEUNG and KIM, 1989; KIM and YOON, 1994; YOON, 1982; SEKINE, 1991). However, they all used constant vertical eddy viscosity and eddy diffusivity, and the effects of embedding a mixed layer are still unknown in the East Sea.

Therefore, in this paper the circulation

model of the East Sea, into which the OMLM is embedded, is attempted for the purpose of predicting the SST and the three dimensional structure of the mixed layer, while ascertaining the effects of the embedded OMLM on the simulation of the circulation in the East Sea.

The results are examined based on the comparison with the observation data, particularly with the SST data. Based on this analysis the problems in embedding the OMLM into the OGCM is elucidated, and the suggestions are made for the improvement.

2. Model

The OGCM used in this simulation was the GFDL MOM (PACANOWSKI *et al.*, 1993) which is originated from the Bryan and Cox Model (COX, 1984), and it was modified for the East Sea in a similar way to KIM and YOON (1994). Figure 1 shows the domain of the model with topography as well as the areas of detailed study which will be discussed in section 3. The total volume transport through the southern inlets (see Fig. 1) was given by an average 2 Sv with the seasonal variation of ± 0.4 Sv; the maximum in August and the minimum in February. The influx was assumed to flow out through the Soya and Tsugaru Straits with the ratio of volume transport 6 : 4. The baroclinic components of the incoming velocity through the southern inlets were determined from the geostrophic flows based on the T, S data obtained from Korea Fisheries Research and Development Agency (1986). As for the boundary conditions of temperature and salinity the observed data were applied in the southern inlets and the open boundary conditions were applied in the Soya and Tsugaru Straits, respectively.

The sizes of horizontal grids were 1/6 degree in both longitude and latitude. The coefficients of horizontal eddy viscosity and eddy diffusivity were taken as 3×10^6 cm²/s and 1.5×10^6 cm²/s, respectively. To assess the impact of the OMLM on the OGCM the case without the OMLM were also carried out. In that case the coefficients of vertical eddy viscosity and eddy diffusivity were set to be 1.0 cm²/s. Vertically 24 layers were used with particular emphasis on the upper ocean process, ranging from 7.5 m

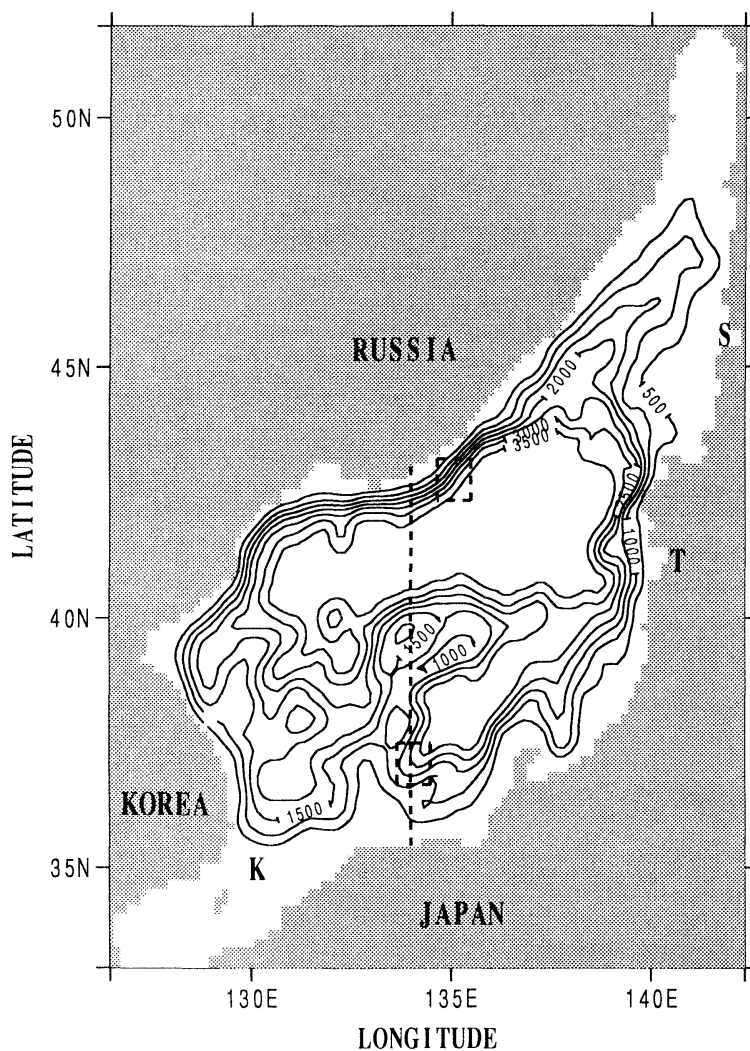


Fig. 1. Model domain with topography. Contour intervals are of every 500 m. The dotted line is the cross section in which the vertical temperature profiles are made in Fig. 10, 11 and 12. Two squares represent the regions where the seasonal variations of the SST were calculated to be shown in Fig. 8. Here K represents the location of the Korean Strait, T the Tsugaru Strait and S the Soya Strait, respectively.

at the surface to 900 m at the bottom.

For the boundary conditions at the sea surface, monthly mean values of wind stress by NA *et al.* (1992) and heat flux by HIROSE *et al.* (1996) were used. The data of heat flux Q were not wholly prescribed values, but are given partially in terms of the temperatures of the sea surface T_s and the air above T_a , i.e.,

$$Q = Q_1 + Q_2(T_a - T_s) \quad (1)$$

with the prescribed values of Q_1 and Q_2 which

vary with position and months. The restoring boundary condition was used for salinity using the observed sea surface salinity data.

The Mellor-Yamada Model of the level 2 and 1/2 was applied as the embedded OMLM (MELLOR and YAMADA, 1982). The Mellor-Yamada Model has been known to have the tendency to insufficient mixing near the sea surface which causes too shallow mixed layers and thus the overestimation of SST (MARTIN, 1985; ROSATI and MIYAKODA, 1988; NOH, 1996).

The Mellor-Yamada Model of level 2 and 1/2 includes the equation for the turbulent kinetic energy (TKE) E as well as the equation for velocity, temperature and salinity. That is

$$\frac{dE}{dt} = F + P_s + P_b - \varepsilon \quad (2)$$

where F is the flux of TKE, P_s and P_b are shear and buoyancy production and ε is dissipation. The surface boundary condition for E was determined by MELLOR and YAMADA (1982) from the assumption that all other terms are negligible except shear production and dissipation near the surface so that

$$P_s - \varepsilon = 0 \quad (3)$$

which applies to the case of the turbulent boundary layer near the solid wall such as the atmospheric boundary layer. This gives

$$E = Au^*{}^2 \quad (4)$$

with $A = 3.25$, where u^* is the friction velocity due to the wind stress. However, in the case of the ocean, in which the surface boundary is not rigid, both the observations (SHAY and GREGG, 1984; GARRETT, 1989) and the results from the recent large eddy simulation (SKYLLINGSTAD and DENBO, 1995) show that the TKE near the surface boundary is much larger in the ocean than in the atmosphere by one order of magnitude. This strongly suggests that (3) cannot be satisfied near the ocean surface. It was also shown by NOH (1995) that a seasonal thermocline cannot be formed during the warming season if the flux of TKE (F) is neglected in (2); thus the SST is overestimated. Based on these facts the surface boundary condition of TKE is assigned using the value ten times larger than that calculated from (3) in the present simulation, i.e., $A = 32.5$.

Moreover, the length scale of turbulence l is prescribed as

$$l = \kappa(z + z_0) / (1 + \kappa z / l_0) \quad (5)$$

for a given depth z , where z_0 is the surface roughness length scale, κ is von Karman constant and l_0 is the Blackadar length scale (MELLOR and YAMADA 1982). It was assumed that $z_0 = 0$ by MELLOR and MAMADA (1982) also in the same way as in the atmospheric boundary layer, neglecting the fact that the

free surface of the ocean allows large eddies near the surface. This causes strong temperature and velocity gradients in the mixed layer contradicting the observation of the oceanic mixed layer having uniform temperature and velocity profiles, as mentioned by CANE (1994). To rectify this problem a larger value of the length scale was suggested as $z_0 = 3.5$ m by NOH (1996), and the same value was used in this model.

Since the upper ocean processes are of main concern in this paper, much shorter time scale is required compared to that required for the circulation in the deeper ocean. We carried out the model run for 15 years, which was found to be sufficient to reach the equilibrium in the upper ocean (STERL and KATTENBERG, 1994). Actually major patterns and values with regards to the temperature and the circulation from the simulation did not vary noticeably after 5-6 years as far as the upper ocean is concerned. We present the results based on the comparison among three different simulations; the OGCM without the embedded OMLM (MO), the OGCM with the embedded OMLM whose surface boundary condition for turbulence is modified (MA) and the OGCM with the embedded OMLM which is the original Mellor-Yamada Model (MB).

3. Results

Figures 2 and 3 show the surface currents from the simulation without the embedded mixed layer (MO) and with the embedded mixed layer (MA) during the warming season of May-June (MJ) and during the cooling season of November-December (ND). Figs. 4 and 5 are the corresponding transport stream functions. Here MJ and ND represent the calculation results at the ends of May and November, respectively. The result from both cases of MO and MA reproduce well the general pattern of the circulation such as the split of the Tsushima Current (TC) to the East Korean Warm Current (EKWC) along the Korean Peninsula and the Nearshore Branch along the Japanese Island (NB), the separation of the EKWC and the eddies along the front following the separation. The seasonal variations in the EKWC, the NB and the North Korean Cold

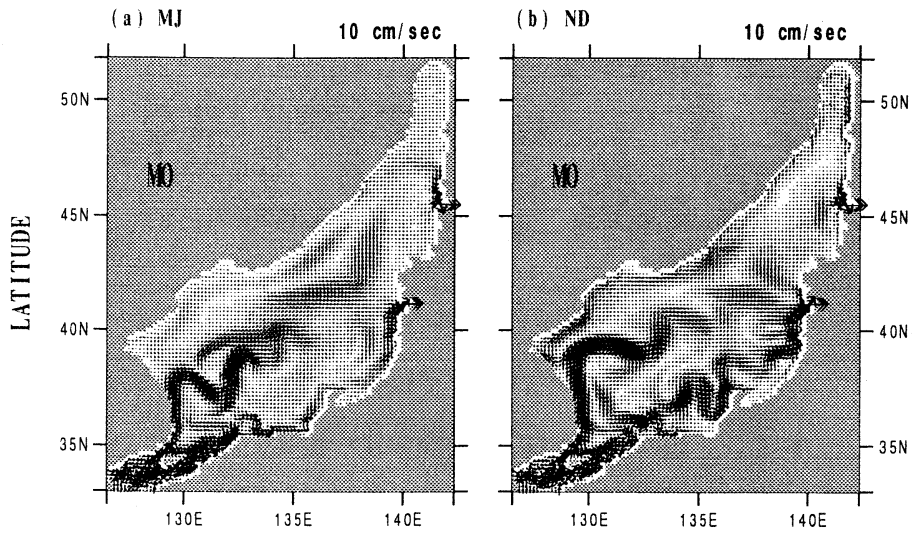


Fig. 2. Surface current velocity fields calculated from MO; (a) MJ, (b) ND.

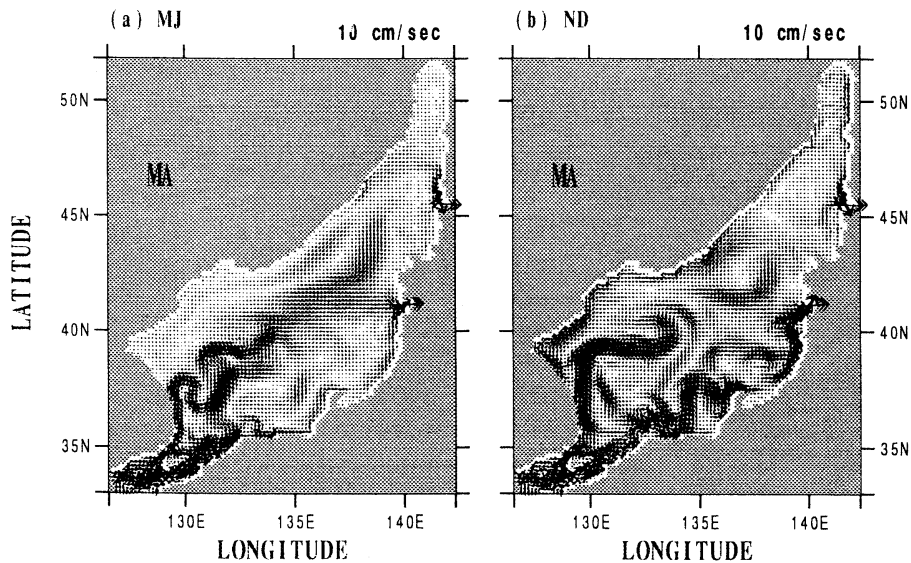


Fig. 3. Surface current velocity fields calculated from MA; (a) MJ, (b) ND

Current (NKCC) are also in good agreements with the previous results (KIM and YOON, 1994; SEUNG and YOON, 1995). Moreover, the overshooting of the EKWC, which has caused a trouble in many previous models (SEUNG and KIM, 1993; KIM and YOON, 1994; HOLLOWAY *et al.*, 1995), does not occur in both MO and MA. Major difference of the present simulation is that heat flux is used as the surface boundary condition instead of SST. It possibly implies that heat flux boundary condition may

produce more realistic temperature profiles below the sea surface, if referred from the fact that the overshooting disappears in the robust diagnostic model in which the observation temperature profiles below the sea surface are maintained (SEUNG and YOON, 1995). More investigation is required, however, for better understanding of the situation.

Meanwhile, the effects of embedding the OMLM into the OGCM are not significant in the circulation. This supports the argument by

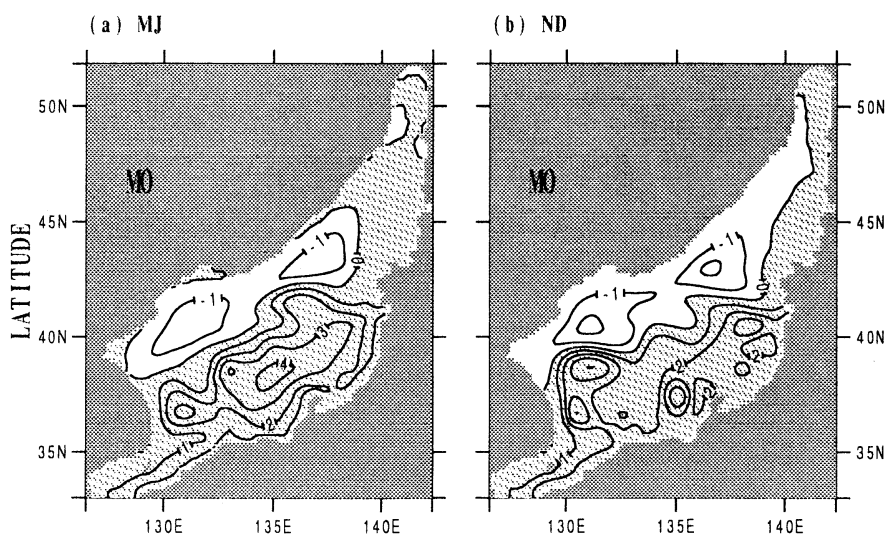


Fig. 4. Transport stream function calculated from MO; (a) MJ, (b) ND.

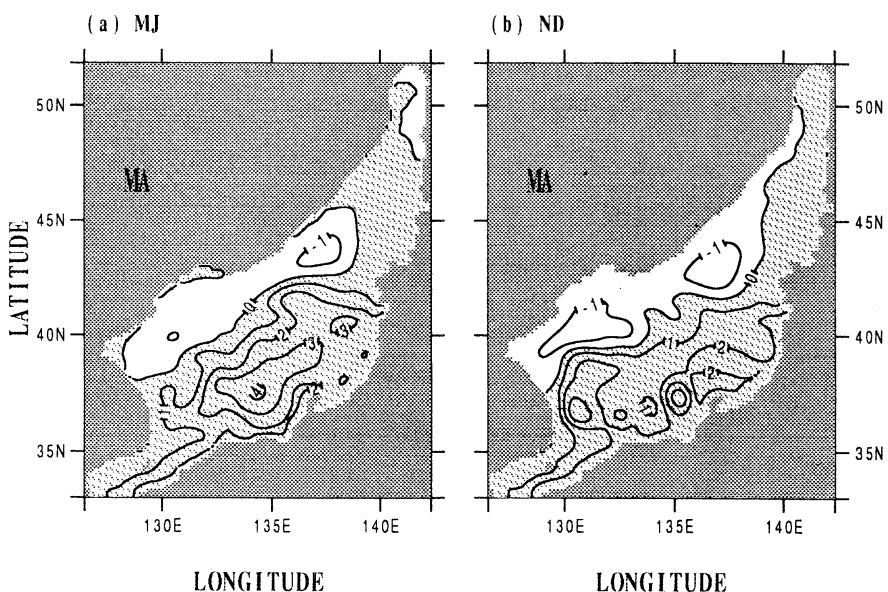


Fig. 5. Transport stream function calculated from MA; (a) MJ, (b) ND.

HOLLOWAY *et al.* (1995) that the circulation in the East Sea is basically determined by the influx through the Korea Strait, the topography and the wind stress. One minor difference between two simulations is observed near the separation point off the Korean Peninsula where more intensive meandering of the current is observed in MJ in the case of MA, resembling the eddy pattern observed by LIE *et al.* (1995). The result from the OGCM from MB,

which is not shown here, also shows very similar circulation pattern as that from MA.

On the other hand, the SST distribution shows significant differences among the simulations MO, MA and MB. Fig. 6 shows the SST distribution in MJ and ND obtained from the observation, and Fig. 7, 8 and 9 show the corresponding results from the simulations of MO, MA and MB. The observation data are from Japan Oceanographic Data Center (JODC). The

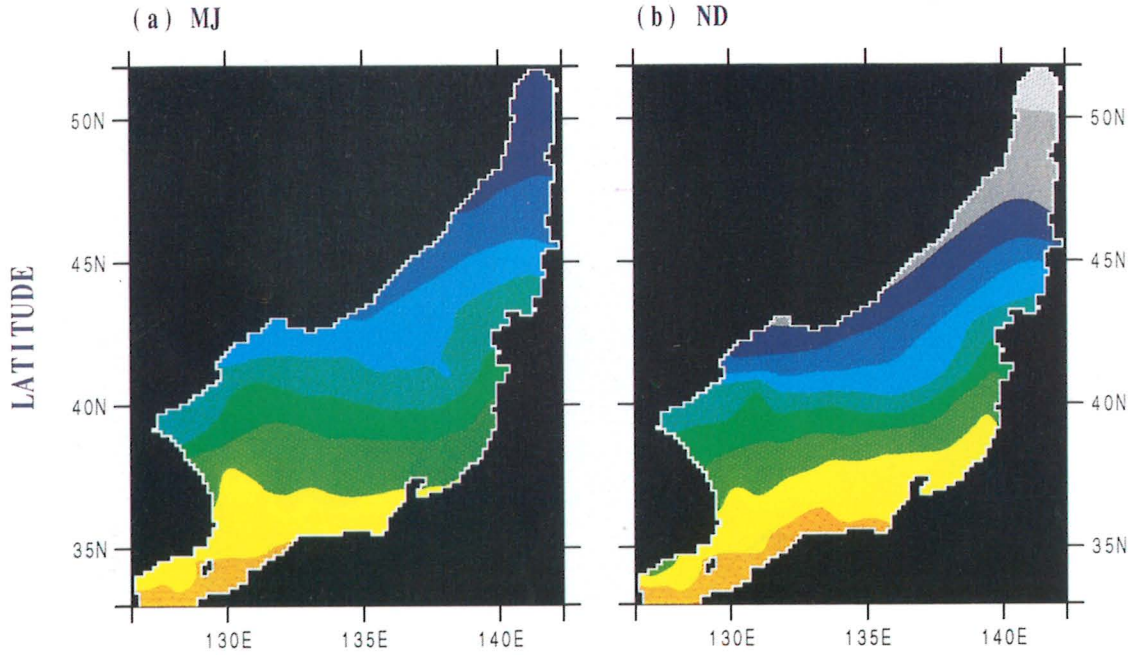


Fig. 6. The distribution of SST from the observation data : (a) MJ, (b) ND.

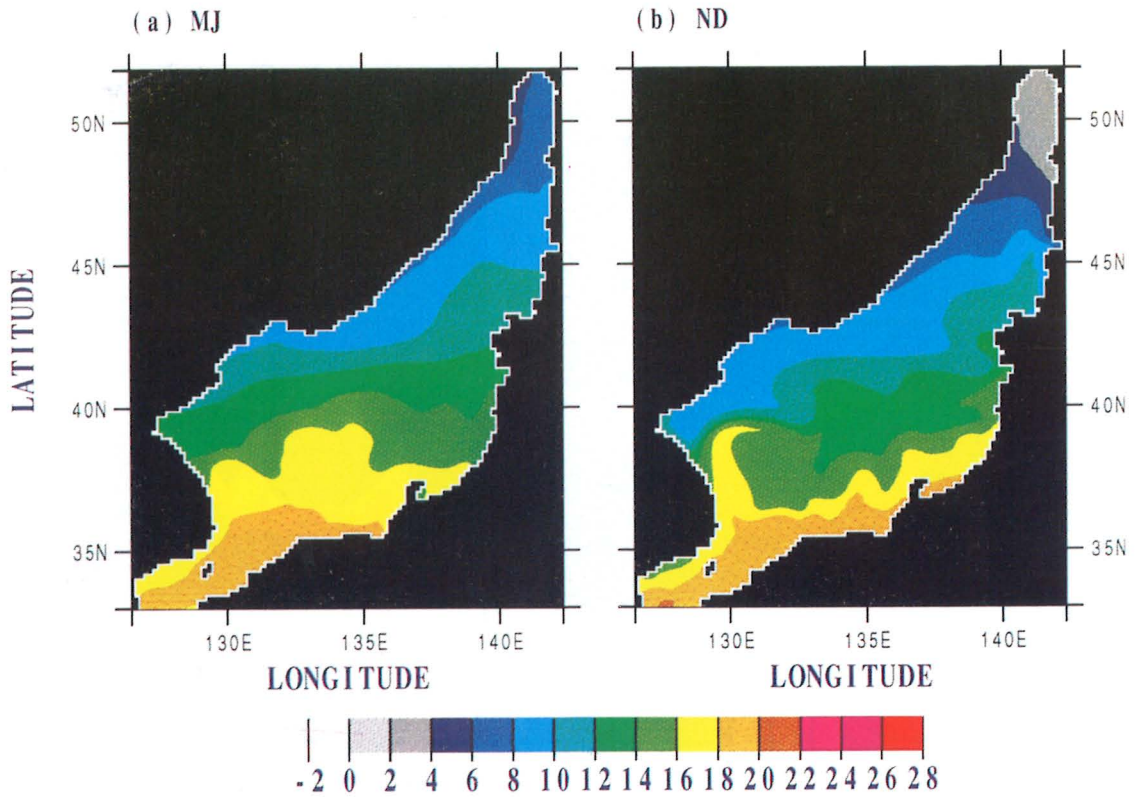


Fig. 7. The distribution of SST simulated from MO ; (a) MJ, (b) ND.

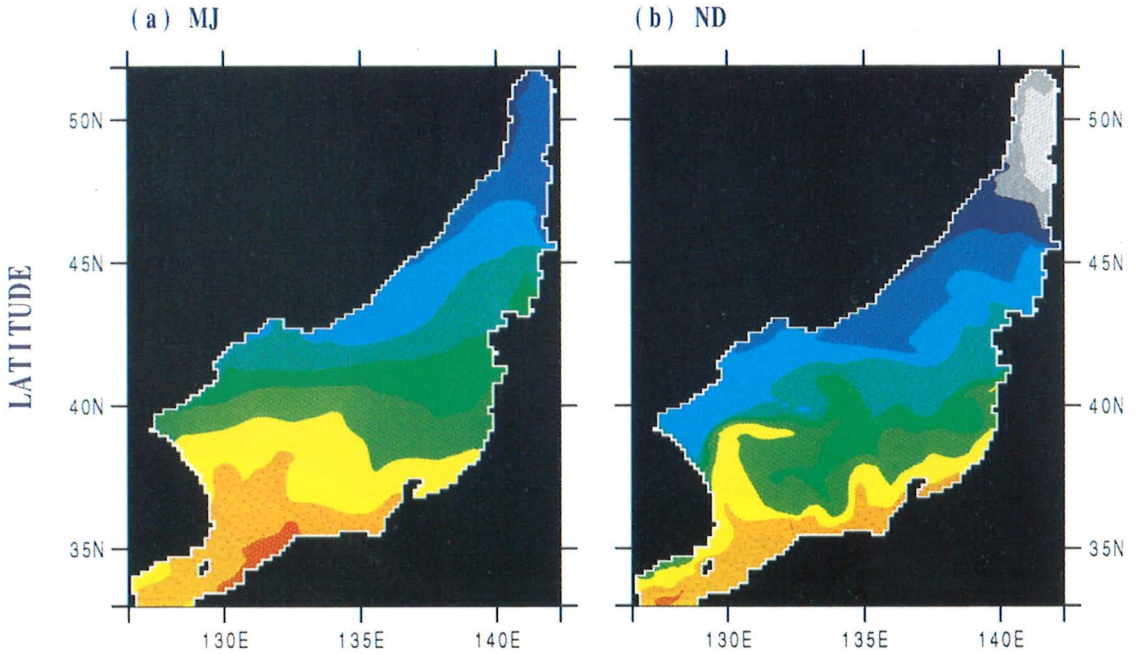


Fig. 8. The distribution of SST simulated MA ; (a) MJ, (b) ND.

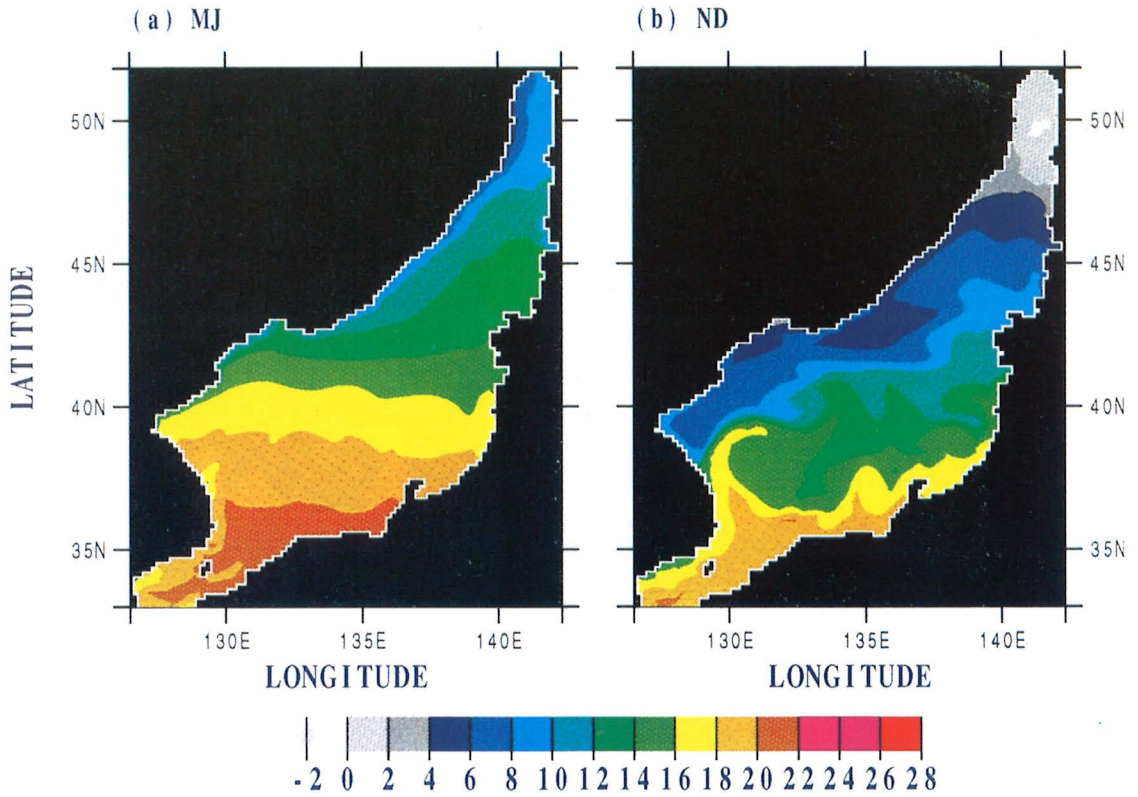


Fig. 9. The distribution of SST simulated from MB ; (a) MJ, (b) ND.

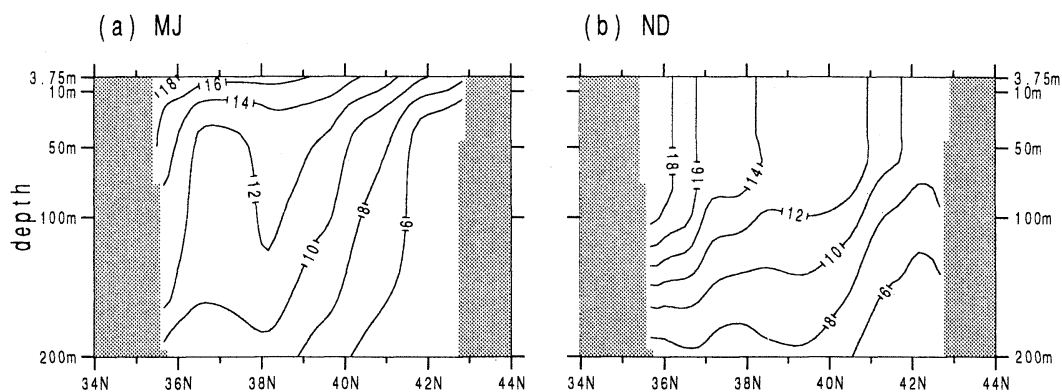


Fig. 10. Vertical temperature distribution along the north-south cross section along the longitude 134 E from MO; (a) MJ, (b) ND.

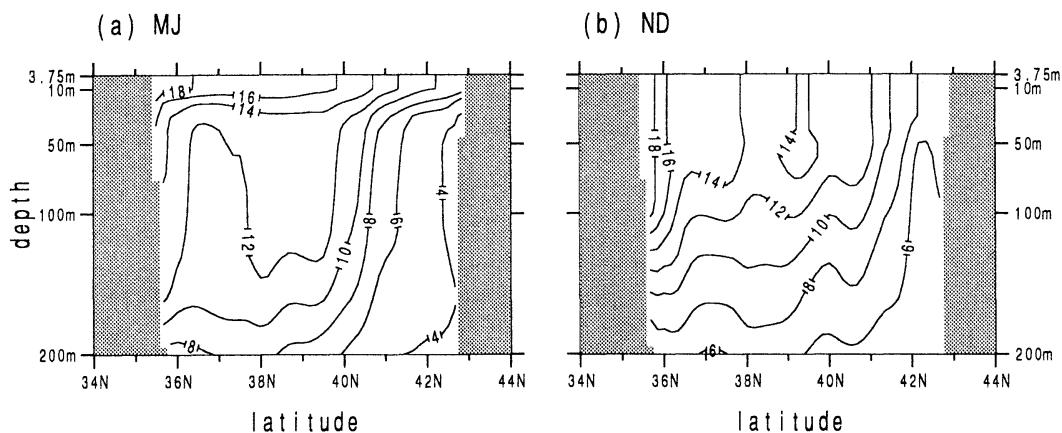


Fig. 11. Vertical temperature distribution along the north-south cross section along the longitude 134 E from MA; (a) MJ, (b) ND.

most distinguished feature is that during the warming season (MJ) the simulated SST's are generally warmer than the observation data. Particularly, when the original Mellor-Yamada model is used (MB), it causes quite serious overestimation of SST. Meanwhile, the SST in the northern region is not sufficiently cooled during the cooling season (ND), particularly in the case of MO.

Also shown are the vertical distributions of temperature in the north-south cross section at 134E (see Fig. 1) for the cases of MO, MA and MB (Figs. 10, 11 and 12). During the warming season (MJ) the mixed layer is not observed in the cases of MO and MB, while reasonable mixed layers with uniform vertical temperature profiles are reproduced up to about 10–20 m in the case of MA in accordance with the

observation (see, for example; KIM, 1994). What is also evident in the case of MO is the strong downward spread of the warm temperature of the upper ocean and the weak convection during the cooling season.

To assess the models in simulating the SST further, the seasonal variations of the SST in the region I and II from the observation and the simulations are made in Fig. 13, representing the most characteristic warm and cold regions, respectively.

The seasonal variation of SST from MO in Fig. 13 shows the cooler temperature during late summer in both regions and the warmer temperature during winter in the northern region (II) in comparison with the observation data and the other simulations MA and MB. The latter appears to be caused by insufficient

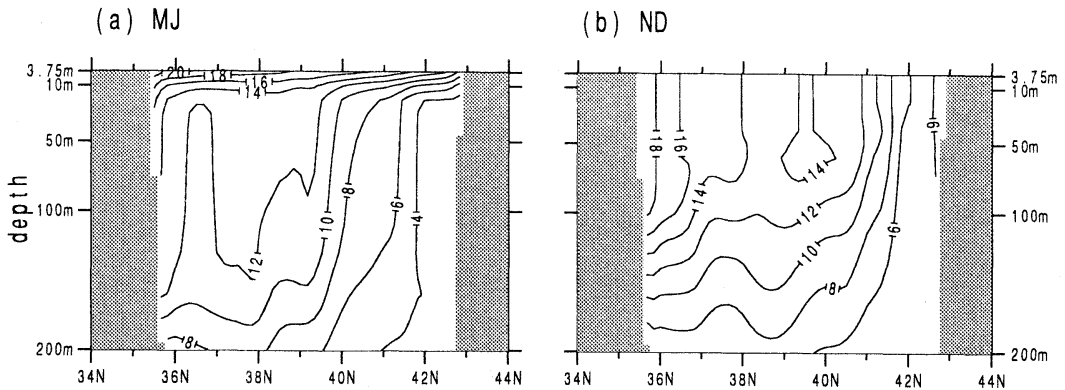


Fig. 12. Vertical temperature distribution along the north-south cross section along the longitude 134 E from MB; (a) MJ, (b) ND.

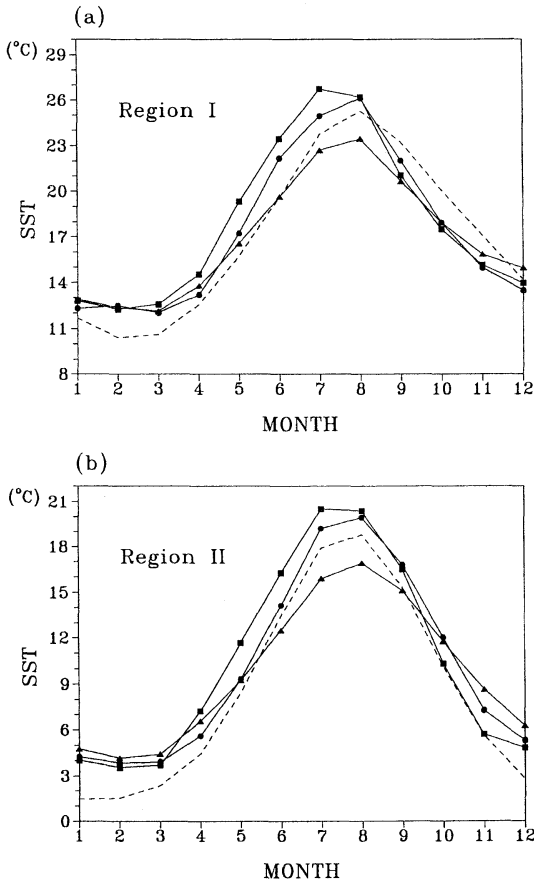


Fig. 13. Seasonal variations of the SST. Here... is from the observation data, \blacktriangle from MO, \bullet from MA and \blacksquare from MB; (a) Region I, (b) Region II.

mixing, because only non penetrative convection occurs in this case, whereas the entrainment owing to convective turbulence contributes to the additional deepening of the mixed layer in the presence of OMLM. And the former is caused by the absence of a seasonal thermocline across which the downward vertical heat transfer is prohibited.

In the case of MB, the problem of the overestimation of the SST during the warming season by 2–3 °C is a quite serious defect, and it gets even worse with increasing vertical resolution contrary to the expectation. The insufficient mixing under the stabilizing heat flux cannot form a seasonal thermocline in this case as shown by NOH (1995), but leads to the sharp temperature gradients near the surface by prohibiting the downward heat transfer beyond the first layer (Fig. 12). Therefore the received heat is accumulated mostly in the first layer, and thus even higher SST appears with decreasing the thickness of the first layer.

The SST from MA is much improved compared to the case of MB, but it is still slightly warmer than the observation data in MJ. At this point it is not clear, however, whether the remaining overestimation of SST is due to the imperfect mixed layer model or due to the other effects neglected in the simulation such as the penetration of solar radiation and the high frequency wind stress fluctuation.

The discrepancy of the SST's with the observation data during September to November in the southern region (I), which appears in all

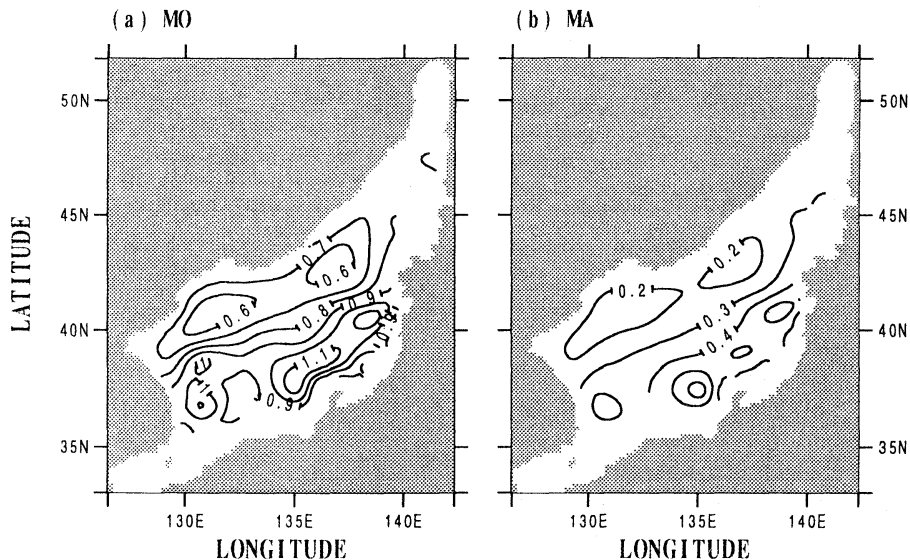


Fig. 14. Horizontal distribution of the annual mean temperature at the depth of 500 m; (a) MO, (b) MA.

three simulations, appears to occur because the southward current following the anti-cyclonic eddy off the Korean Peninsula carries the cold water from north rather than due to the mixed layer dynamics. It is also observed that the SST in the northern region (II) is still too warm during winter, although it is improved by the inclusion of the OMLM. This suggests that the parameterization of the convection process must be improved further.

Another important aspect to be noticed in association with the embedding of the OMLM is that it can prevent the excessive downward heat transfer below the mixed layer. In the OGCM without the embedded OMLM the temperature in the deep sea continues to warm up because of the large constant eddy diffusivity maintained below the mixed layer (SEUNG and KIM, 1993). The situation is much improved by the inclusion of the OMLM. For example, the typical temperature at the depth of 500 m is observed to be about 0.2–0.4 °C (KIM, 1994; MAIZURU Marine Observatory, 1985). The temperature at the same depth is overestimated as 0.6–1.1 °C in the case of MO, while those from MA is correctly 0.2–0.4 °C (Fig. 14).

Finally, it is also noticed that the simulation results of the SST are similar to the instantaneous satellite of the SST at the corresponding

time (OSTROVSKII, 1995), rather than the JODC field observation data which was obtained by averaging the data throughout several years, thus filtering out the fluctuation. This suggests that the widely used method of utilizing the observed SST data as the surface boundary condition (SEUNG and YOON, 1995; SEUNG and KIM, 1993; KIM and YOON, 1994; HOLLOWAY *et al.*, 1995) may not be appropriate for high resolution models, in which the meso-scale eddies are resolved, as in this case.

4. Conclusion and Discussion

It has been shown that the embedding of the oceanic mixed layer model into the OGCM for the simulation of the East Sea can produce more realistic SST's and vertical temperature profiles and can prevent excessive downward propagation of heat, while its effect on the circulation is minimal.

It has been also found that the overestimation of the SST during the warming season, which is a common problem in the Mellor-Yamada Model, can be improved by increasing the turbulent kinetic energy and the length scale of turbulence near the sea surface. However, the more accurate surface boundary condition for the turbulence in the mixed layer has to be made in the future study, based on the

microscale observations and the better understanding of the dynamics. Furthermore, it must be clarified how important are the impacts of the penetration of solar radiation and the high frequency wind stress fluctuation in the determination of the SST. Meanwhile, the too warm SST in the northern region in winter strongly suggests that the parameterization of convection process must be improved.

Finally, although the computational burden is already quite high in this simulation, the vertical resolution in the upper ocean is rather rough ($\Delta z=7.5\text{m}$ at the first layer) to describe various mixed layer phenomena in detail. When the major concern is the upper ocean process as in this case, it is desirable to devise the way of simplifying the deep ocean process without affecting the upper ocean process.

Acknowledgments

This work was supported by Korea Science and Engineering Foundation, the Ministry of Environment (G7 project) and Navy of Korea.

References

- ADAMEC, D., R. L. ELSEBERRY, B. W. GARWOOD and R. L. HANEY (1981): An embedded mixed layer-ocean circulation model. *Dyn. Atmos. & Oceans*, **6**, 69-96.
- ALDERSON, S. G. (1990): On embedding a mixed layer into an ocean circulation model, *Dyn. Atmos. & Oceans*, **15**, 59-86.
- CANE, M. A. (1993): Near-surface mixing and the ocean's role in climate, *Large Eddy Simulation of Complex Engineering and Geophysical Flows* (B. GALPERIN and S. A. ORSZAG, eds.), Cambridge Univ., 489-512.
- CHEN, D., A. J. BUSALACCHI and L. M. ROTHSTEIN (1994): The roles of vertical mixing, solar radiation and wind stress in a model simulation of the sea surface temperature seasonal cycle in the tropical Pacific Ocean. *J. Geophys. Res.*, **99**, 20, 345-20, 359.
- CHANG, P. (1994): A study of the seasonal cycle of sea surface temperature in the tropical Pacific Ocean using reduced gravity model. *J. Geophys. Res.*, **99**, 7, 725-7, 741.
- CHASSIGNET, E. P. and P. R. GENT (1991): The influence of boundary conditions on the midlatitude jet separation in ocean numerical models. *J. Phys. Oceanogr.*, **21**, 221-235.
- COX, M. D. (1984): A primitive equation, 3-dimensional model of the ocean. GFDL Ocean Group Technical Report No.1, GEDL/NOAA, Princeton University.
- Fisheries Research and Development Agency (1986): Mean Oceanographic Charts of the Adjacent Seas of Korea, Pusan, Korea, 186 pp.
- GARGETT, A.E. (1989): Ocean turbulence. *Ann. Rev. Fluid Mech.*, **21**, 419-451.
- HENDERSON-SELLORS, B. (1988): Embedding stratification models in ocean general circulation climate models. *Small-scale Turbulence and Mixing in the Ocean* (J. C. J. Nihoul, and B. M. Jamart eds.) Elsevier, 95-08 pp.
- HIROSE, N., C. H. KIM and J. H. YOON (1996): Heat Budget in the Japan Sea, *J. Oceanography* (in press).
- HOLLOWAY, G., T. SOU and M. EBY (1995): Dynamics of circulation of the Japan Sea, *J. Marine Res.*, **53**, 539-569.
- LIE, H. J., S. K. BYUN, I. BANG and C. H. CHO (1995): Physical structures of eddies in the southwestern East Sea. *J. Korean Soc. Oceanogr.*, **30**, 170-183.
- KATO, K. and T. ASAI (1983): Seasonal variations of heat budgets in both the atmosphere and the sea in the Japan Sea area. *J. Meteor. Soc. Japan*, **61**, 222-238.
- KIM, C. H. and J. H. YOON (1994): The circulation of the Japan Sea seen from the numerical model. *Kaiyo Monthly*, **26**, 763-772 (in Japanese).
- KIM, K. (1994): The circulation of the East Sea and CREAMS. *Kaiyo Monthly*, **26**, 773-778 (in Japanese).
- KRAUS, E. B. (1988): Merits and defects of different approaches to mixed layer modeling. *Small-Scale Turbulence and Mixing in the Ocean*, (Nihoul, J. C. J. and B. M. Jamart eds.), Elsevier, 37-50.
- Maizuru Marine Observatory (1985): Climatology of hydrographic and chemical properties of the Japan Sea. pp. 51.
- MARTIN, P. J. (1985): Simulation of the mixed layer at OWS November and Papa with several models. *J. Geophys. Res.*, **90**, 903-916.
- MCGREARY, J. P., P. K. KUNDU and R. L. MOLINARI (1993): A numerical investigation of dynamics, thermodynamics and mixed-layer process in the Indian Ocean. *Prog. Oceanog.*, **31**, 181-244.
- MELLOR, G. L. and T. YAMADA (1982): Development of a turbulence closure model for geophysical fluid problems. *Rev. Geophys. & Space Phys.*, **20**, 851-875.
- NA, J. Y., J. W. SEO and S. K. HAN (1992): Monthly mean sea surface winds over the adjacent seas of the Korean Peninsula. *J. Oceanol. Soc. Korea*, **27**, 1-10.
- NAGAI, T., M. TOKIOKA, M. ENDOH and K. KITAMURA

- (1992): El-Nino/southern oscillation simulated in a MRI atmosphere-ocean coupled general circulation model. *J. Climate*, **5**, 1202-1233.
- NOH, Y. (1996): The dynamics for the formation of a diurnal thermocline in the oceanic mixed layer. *J. Phys. Oceanogr.* (in press).
- OBERHUBER, J. M. (1993): Simulation of the Atlantic circulation with a coupled sea ice-mixed layer-isopycnal general circulation model, I. Model description. *J. Phys. Oceanogr.*, **23**, 808-829.
- OSTROVSKII, A. G. (1995): Signature of stirring and mixing in the Japan Sea surface temperature patterns in autumn 1993 and spring 1994. *Geophys. Res. Lett.*, **22**, 2,357-2,360.
- PACANOWSKI, R. K. DIXON and A. ROSATI (1993): The GFDL Modular Ocean Model User's guide Version 1.1, GFDL Ocean Group, Tech. Report No. 2, GFDL/NOAA, Princeton University.
- ROSATI, A. and K. MIYAKODA (1988): A general circulation model for the upper ocean simulation. *J. Phys. Oceanogr.*, **18**, 1601-1626.
- SCHOPH, P. S. and M. A. CANE (1983): On equatorial dynamics, mixed layer physics and sea surface temperature. *J. Phys. Oceanogr.*, **13**, 917-935.
- SEKINE, Y. (1991): A numerical experiment on the seasonal variation of the oceanic circulation in the Japan Sea. *Oceanography of Asian Marginal Seas* (Takano, t. ed.), Elsevier, 113-128.
- SEUNG, Y. H. and K. KIM (1993): A numerical modeling of the East Sea circulation. *J. Oceanol. Soc. Korea*, **28**, 292-304.
- SEUNG, Y. H. and J. H. YOON (1995): Robust diagnostic modeling of the Japan Sea Circulation. *J. Oceanogr.*, **51**, 421-440.
- SHAY, T. J. and M. C. GREGG (1984): Turbulence in an oceanic convective mixed layer. *Nature*, **310**, 282-285.
- SKYLLINGSTAD, E. D. and D. W. DENBO (1995): An ocean large-eddy simulation of Langmuir circulation in the surface mixed layer. *J. Geophys. Res.*, **100**, 8501-8522.
- STERL, A. and A. KATTENBERG (1994): Embedding a mixed layer model into an ocean general circulation model of the Atlantic: The importance of surface mixing for heat flux and temperature. *J. Geophys. Res.*, **99**, 14, 139-14, 157.
- WASHINGTON, M. W., A. J. SEMTNER, G. A. MEEHL, D. J. KNIGHT and T. A. MAYOR (1980): A general circulation experiment with a coupled atmosphere, ocean and ice model. *J. Phys. Oceanogr.*, **10**, 1,887-1,908.
- YOON, J. H. (1982a): Numerical experiment on the circulation in the Japan Sea. Part I: Formation of the East Korea Warm Current. *J. Oceanogr. Soc. Japan*, **38**, 43-51.
- YOON, J. H. (1982b): Numerical experiment on the circulation in the Japan Sea. Part II: Influence of seasonal variations in atmospheric conditions on the Tsushima Current. *J. Oceanogr. Soc. Japan*, **38**, 81-94.
- YOON, J. H. (1982c): Numerical experiment on the circulation in the Japan Sea. Part III: Formation of the nearshore branch of the Tsushima Current. *J. Oceanogr. Soc. Japan*, **38**, 43-51.

Received January 5, 1996

Accepted March 25, 1996

A hindcast experiment in the East Sea (Sea of Japan)

Inkweon BANG*, Jei-Kook CHOI*, Lakshmi KANTHA*,

Charles HORTON**, Melody CLIFFORD**,

Moon-Sik SUK***, Kyung-II CHANG***, Soo Yong NAM*** and Heung-Jae LIE***

Abstract: We describe here a hindcast experiment in the East Sea (Sea of Japan) for 1993, using a data-assimilative circulation model assimilating altimetric data. Climatological simulations and a synoptic run for 1993 are also described. The model reproduces many of the known circulation features in the East Sea. Altimetric data assimilation reproduces the anticyclonic eddy along the Polar Front displayed both by the tracks of the two drifter buoys deployed in the June of 1993 and TOPEX altimetric data.

1. Introduction

While there have been some numerical modeling studies (YOON, 1991 for example) in the Sea of Japan (East Sea), no nowcast/forecast attempt has been made so far. In this study, a near real-time nowcast/forecast system (CHOI *et al.*, 1996) developed for the Gulf of Mexico (GOM henceforth) is adapted for the East Sea (ES henceforth) and a hindcast of the circulation for 1993 is attempted. Both the GOM and ES systems rely on the assimilation of altimetric data for nowcasts.

Although the ES and the GOM share many common features there are also many differences. The ES and the GOM are both deep semi-enclosed seas (mini-basins), and their circulations are strongly influenced by the inflow through their openings in the south. In the GOM, the inflow through the Yucatan Straits is deep because of the large sill depth (~1000m), while in the ES, the Korea (Tsushima) Strait has a shallow sill, only 200m deep at its deepest point. The Loop Current and eddies shed from

it dominate the GOM circulation in the upper 1000 m. In the ES, the inflow through the Korea Strait carries 2-3 Sv into the ES, considerably smaller than the transport of 26-30 Sv by the Loop Current in the GOM, but nevertheless is responsible for most of the variability in the upper 300 m in the southern half of the ES. The variability in waters deeper than 300 m is principally due to deep convection and dense water formation in the northern parts during winter. No similar process exists in GOM waters below the Yucatan Strait sill depth.

The principal dynamical process in the GOM is that associated with the Loop Current. The Loop Current intrudes into the Gulf and eventually sheds eddies, which then propagate westward and dissipate in the western Gulf. In the ES, the Tsushima Current splits into two main branches after leaving the Korea Strait. The west branch, also called the East Korean Warm Current (EKWC henceforth), flows northward along the Korean coast and the east branch flows eastward along the Japanese coast. The EKWC separates from the coast at about 37-38°N and flows to the east. The east branch meanders and forms alternating warm and cold eddies along its path.

The ES and GOM differ considerably in their T-S characteristics (Fig. 1). In the GOM, the T-S structure is simple and its seasonal

*Department of Aerospace Engineering Sciences, University of Colorado Boulder, CO 80309-0431

**Naval Oceanographic Office, Stennis Space Center, MS 39529

***Korea Ocean Research and Development Institute P.O. Box 29, Ansan, Seoul 425-600, Korea

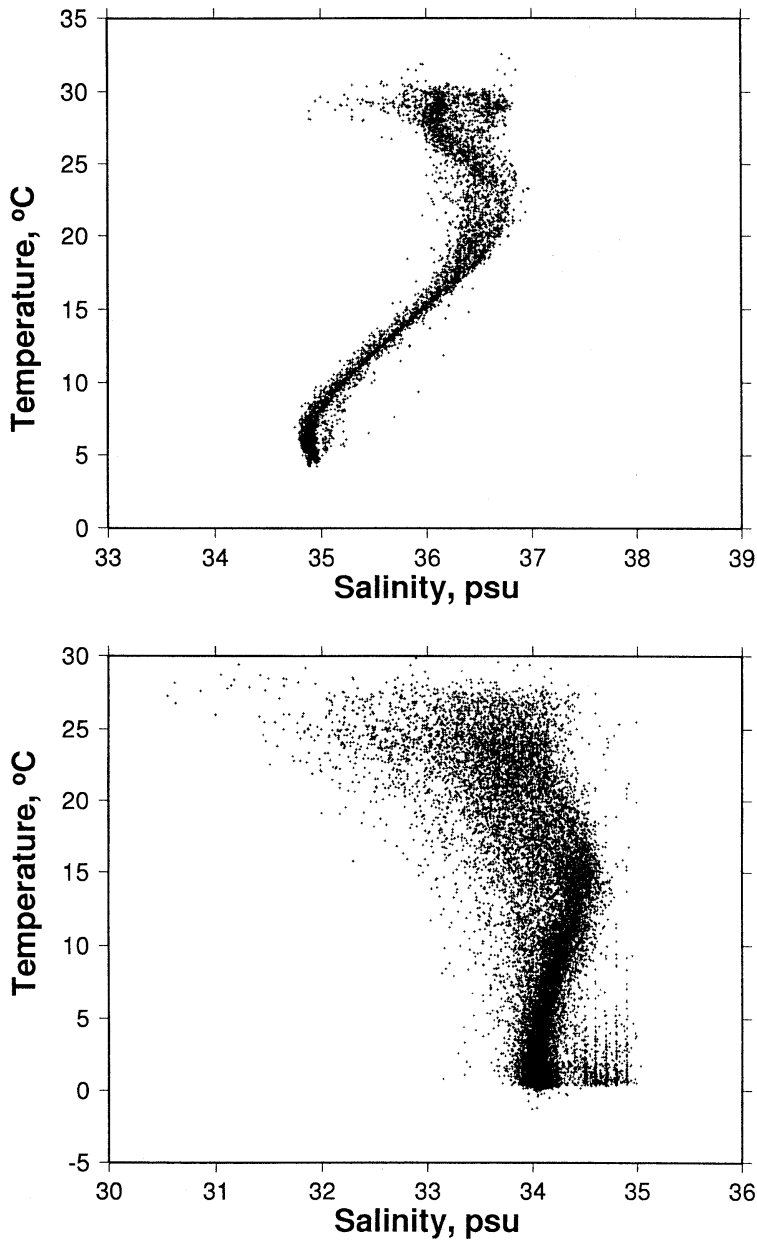


Fig. 1. T-S diagrams for the Gulf of Mexico (top) and the East (Japan) Sea (bottom) for the month of August.

variation is small. In the ES, the Polar Front running from west to east in the center of the ES separates the warm waters in the south from the colder waters in the north. The warm water in the south is due to the warm, saline Tsushima Current and shows a salinity maximum in the upper 100 m, while the cold water

in the north lacks this feature. Below 400–500 m, the ES is filled with nearly homogeneous waters called the Japan (East) Sea Proper Water (ESPW). A layer of salinity minimum and dissolved oxygen maximum called Japan (East) Sea Intermediate Water (ESIW) (KIM and CHUNG, 1984) is found in the warm water

region between the Tsushima Current water and the ESPW (MORIYASU, 1972; KIM *et al.*, 1991; SENJYU and SUDO, 1993). Both the ESPW and ESIW are thought to be formed by deep convection and dense water formation processes off the Siberian coast in the north during winter.

The anticyclonic eddies in GOM elevate the sea level 50–80 cm above the surrounding, and are therefore easier to detect in altimetric data and assimilate into the model than the anticyclonic eddies in the ES (SHIN *et al.*, 1995), which rarely exceed 10 cm. Also the large spatial and temporal variability due to the meanders of the Polar Front in the ES, and the presence of numerous mesoscale features ranging in size from a few km to several tens of km, makes the nowcast/forecast task significantly more difficult than that in the GOM.

2. Methodology

The core of the nowcast/forecast system is a three-dimensional circulation model assimilating observational data using a simple optimal interpolation (OI) method. The model is a version of the sigma-coordinate model developed at Princeton (KANTHA and PIACSEK, 1993, 1996; see also BLUMBERG and MELLOR, 1987; MELLOR, 1992), and incorporates an improved turbulence closure scheme of KANTHA and CLAYSON (1994) for a better depiction of mixing processes in the upper. It incorporates a data-assimilation module (HORTON *et al.*, 1996) designed to assimilate observational data such as multi-channel sea surface temperatures (MCSST), expendable bathy-thermographs (XBT), conductivity-temperature-depth (CTD) measurements and pseudo-BTs (bathy-thermographs) from altimetry in a continuous four-dimensional assimilation mode for nowcasting purposes. In this nowcast/forecast experiment, we have assimilated only the altimetric data, as CHOI *et al.* (1996) did for the Gulf of Mexico, whereas HORTON *et al.* (1996) used MCSSTs, and XBT/CTD surveys in their application of a similar model to the Mediterranean Sea.

The model grid size is 1/5 degree in both longitude and latitude and it has 21 vertical sigma levels. The horizontal resolution is on the

ragged edge of resolving large eddies, but not the whole spectrum of eddies observed in the ES. The model has three openings, Korea Strait to the south, and Tsugaru and Soya Straits to the east. Tatarskii Straits in the north connects ES to the Sea of Okhotsk but is narrow and shallow, and hence relatively unimportant to basin-wide circulation. Seasonal average values of currents (Fig. 2) from current meter measurements of INOUE *et al.* (1985, as presented in SEKINE, 1988) are used for the inflow through the Korea Strait. The total transport through the Korea Strait of a maximum of about 3.5 Sv in August and minimum of 1.6 Sv in February is prescribed (More recent ADCP observation by ISOBE *et al.* (1994) indicate a value as high as 5.6 Sv during September.). About 60% of the inflow was assigned to the Western Channel and 40% to Eastern Channel of the Korea/Tsushima Strait. This partitioning of the inflow is somewhat arbitrary, although reasonable on the average, since it surely has variability on a variety of time scales. Outflow occurs principally through the Tsugaru Straits, according to observations, although the frontal structure displayed in AVHRR suggest that the flow through the Soya Straits is not always negligible. Therefore, 80% of the outflow is assigned to the Tsugaru Strait and 20% to the Soya Strait in this study.

Temperature and salinity are prescribed as monthly average values (Fig. 2) for the inflow (SEKINE, 1988) and are advected out at outflow ports. During spring/summer, warm relatively fresh waters from the Yellow Sea (due to large river discharges there) flow into the ES and a strong stratification develops, whereas in winter, the flow is more saline and almost vertically homogeneous.

The model was initialized with annual mean temperature and salinity fields from LEVITUS (1981). The heat and salt flux boundary conditions at the surface are provided by simple Newtonian damping to the updated monthly mean temperature and salinity of LEVITUS (updated in 1994), with a 30-day damping time scale.

Several simulations were carried out using different wind forcing. First, the model was run

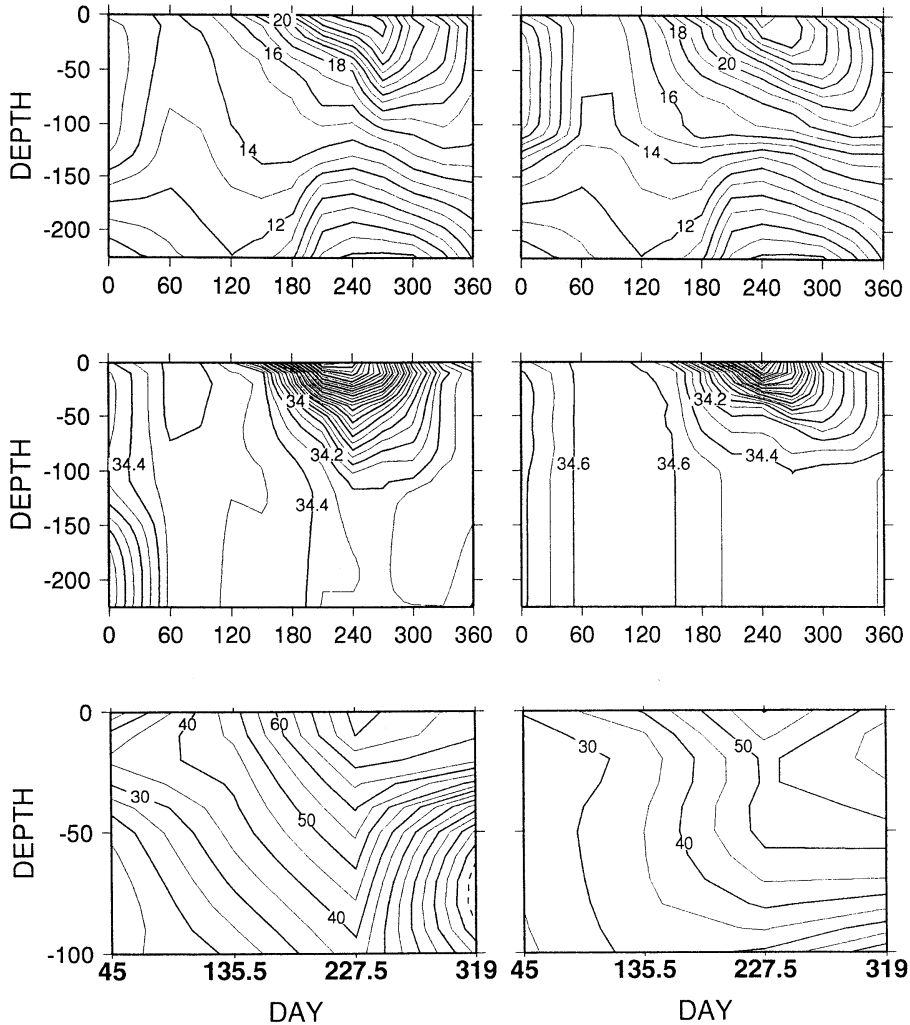


Fig. 2. Time variations of inflow temperature (top), salinity (middle) and velocity (bottom) at the western (left) and eastern (right) Channels of the Korea Strait, based on observations in Sekine (1988).

in a climatological mode forced by monthly mean HELLERMAN and ROSENSTEIN (1983) wind stress climatology. A synoptic simulation was then made for 1993 using six-hourly winds from Fleet Numerical Meteorology and Oceanography Center (FNMOC) starting from the end of the climatological run. Finally, an assimilation run was made assimilating observations from the Ocean Topography Experiment (TOPEX) altimeter for 1993 into the model, but with the same FNMOC wind as the synoptic run. Comparison of the synoptic run

and assimilation run enables us to identify the impact of assimilation. Since the assimilation technique is explained in detail in CHOI *et al* (1996), it will be discussed only briefly here.

Historical hydrographic data was passed through rigorous quality control and then subjected to Empirical Orthogonal Function (EOF) analysis to find the six most significant vertical modes of variability for each month. The dynamic height anomaly is then derived for each EOF mode, also from hydrographic data, to yield a relationship between sea

surface height (SSH) anomaly and the anomaly of the vertical temperature structure (Fig. 3). This enables SSH anomalies from altimetry to be converted to pseudo-BTs for assimilation into the dynamical model. The hydrographic data used in this study comes from the various archives : National Oceanographic Data Center, U. S. (NODC), Japan Oceanographic Data Center (JODC), Korean Oceanographic Data Center (KODC), and U. S. Navy Master Oceanographic Observation Data Set (MOODS).

Standard ionospheric, wet and dry topspheric, Electro Magnetic (EM) bias, tidal and inverse barometric corrections on the TOPEX Geophysical Data Records (GDR) were used. In addition, a standard tilt and bias technique was used to correct for orbit errors, although for TOPEX, this procedure may not be necessary. Along-track values were averaged over 1993 and subtracted out to derive SSH anomalies from the 1993, which were then assimilated into the model track-by-track in a continuous assimilation mode, after conversion into a pseudo-BT anomalies as described above.

The temperature anomaly is assimilated into the model using the following formula :

$$T_{asm} = T_{mod} + \alpha \times [(T_{ref} + T_{anom}) - T_{mod}]$$

where α is weighting factor for observation ranging from 0 to 1. T_{ref} is taken from monthly temperature of the run without assimilation. T_{anom} is temperature anomaly derived from SSH anomaly, T_{mod} is model-computed temperature, and T_{asm} is the temperature which will be used in the next timestep instead of T_{mod} . If this factor is 1, it results in direct insertion and the model temperature (T_{mod}) is merely replaced by ($T_{ref} + T_{anom}$).

Assimilation was performed only at grid points with a water column depth of 400m or more, and data assimilation is track-by-track and continuous in time (four-dimensional assimilation). New satellite tracks are inserted at 6-hour intervals to update the sea level anomaly field. Assimilation is performed only at the first 4 timesteps (1.5 hours) of the 6-hour period. How strongly the temperature anomalies are assimilated into the model is determined by weighting factor and how long the assimilation process takes place is determined by the data

insertion period. In this study, we held the insertion period fixed and varied only the weighting factors.

3. Results

3.1 Climatological Simulation

The model was run in a climatological mode for 1350 days. Fig. 4 shows that the sea level reaches an equilibrium state in the third year, and the same pattern of seasonal cycle with almost the same strength is repeated in the fourth year indicating that the barotropic spin-up process is nearly complete. To look at the baroclinic response in the upper few hundred meters where most of the seasonal fluctuation takes place, we computed the mean kinetic energy in the upper 400m (Fig. 3). The result shows that the mean kinetic energy does not increase as rapidly from the 3rd to 4th year as it has from 1st to 2nd to 3rd year. From this we may assume that the upper 400m has also reached a near-equilibrium state.

The climatological simulation reproduces the characteristic circulation features of the East Sea reasonably well (Fig. 5). The ES circulation consists of two well-developed gyres; a cyclonic gyre in the northern half and an anticyclonic in the southern half. These two gyres are separated by a Polar Front running west to east at about 40° N. In the southern anticyclonic gyre, a western boundary current, known as the East Korea Warm Current (EKWC) develops along the Korean Coast. The main source of the EKWC is the Tsushima Current through the Korea Strait. Another current (called Japan Warm Current, JWC, here) also branches off from the Tsushima Current and flows along the Japanese Coast all the way to Tsugaru Strait, the main outflow port of the ES. This branch shows strong seasonal fluctuation as a direct response to the seasonal variation in the inflow through the Korea Strait. It almost disappears during the winter-spring seasons but undergoes meandering motions during summer-fall and develops alternating small cyclonic-anticyclonic eddy structure along its path, a characteristic clearly discernible in IR images. Part of the JWC continues northward to the Soya Straits and is responsible for the thermal fronts often observed in the

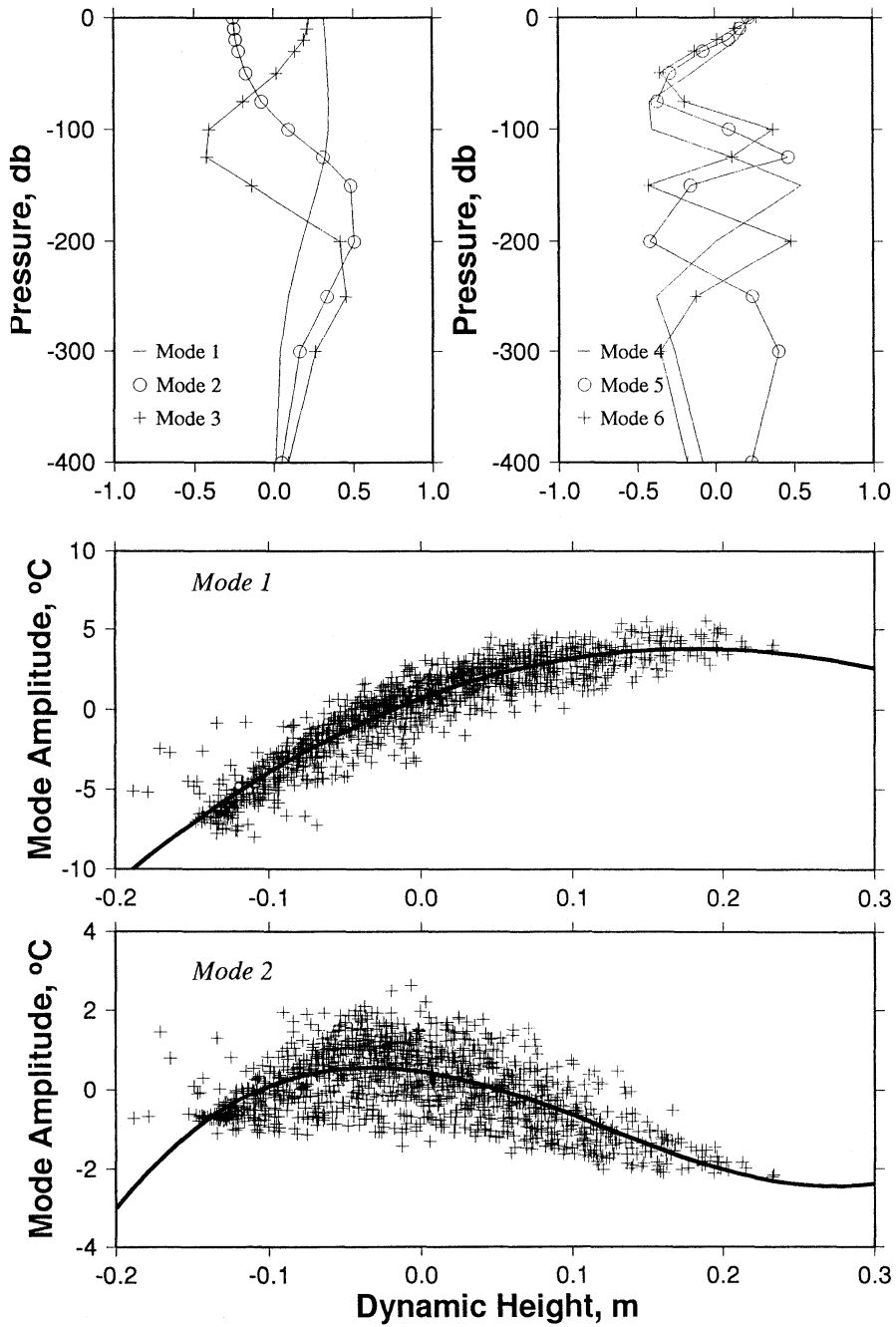


Fig. 3. Vertical profiles of the first six EOF modes of temperature variability (top) and the variation of mode amplitude with dynamic height for the first two eigen modes (middle and bottom) for the month of August.

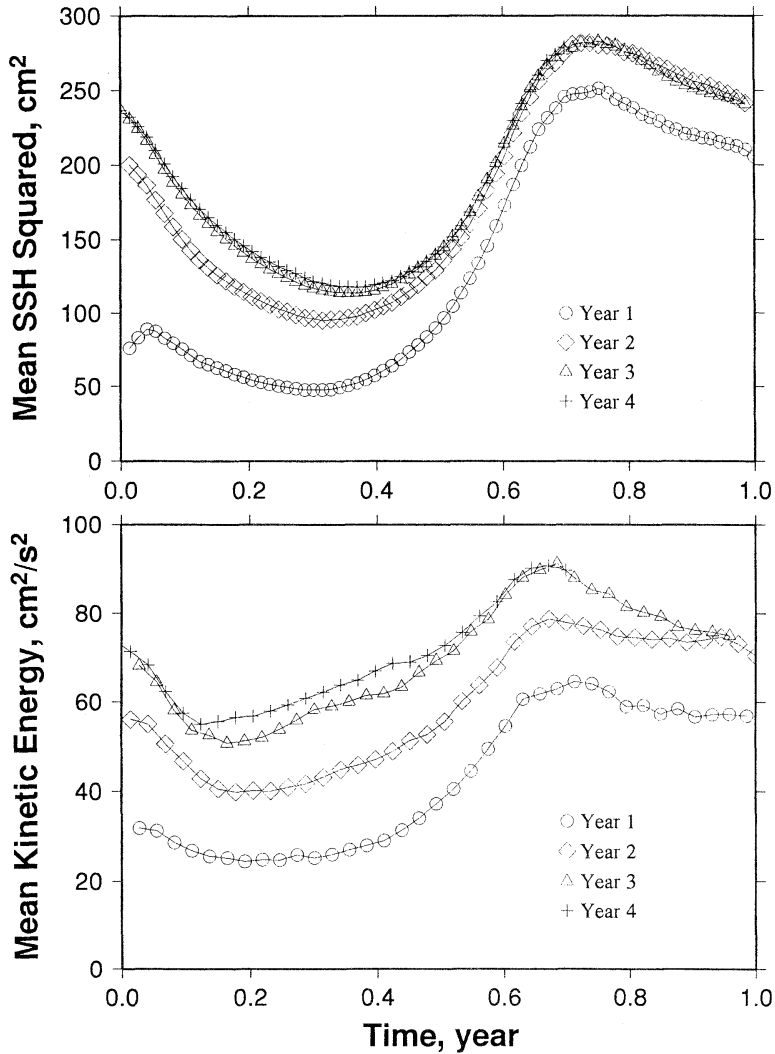


Fig. 4. Time variation of mean sea level squared (upper) and of mean kinetic energy of the upper 400 m (lower) for the climatological run.

vicinity and north of the Tsugaru Straits.

The northern gyre does not display a strong current such as the EKWC but it shows a southward-flowing current along the Russian Coast which can be identified as the Liman Current. However, the North Korean Cold Current (NKCC), which is usually observed south of the Liman Current along the Korean Coast, is not seen in these simulations, possibly because of the excessive northward intrusion of the EKWC.

One interesting and conspicuous feature in the southern anticyclonic gyre is the existence

of an anticyclonic eddy near Korean Coast with its center at 131°E , 37°N . On the other hand, there are no significant mesoscale features in the central and eastern parts of the southern gyre. The model anticyclonic eddy persists almost throughout the year except the fall, and it may be identified as the Ullung Warm Eddy (hereafter UWE) observed by many researchers (ISODA and SAITOH, 1993; KIM, 1993; SHIN *et al.*, 1995).

The time-longitude plot of sea level along 37°N can be used to find out the seasonal change of the EKWC and the UWE (Fig. 6).

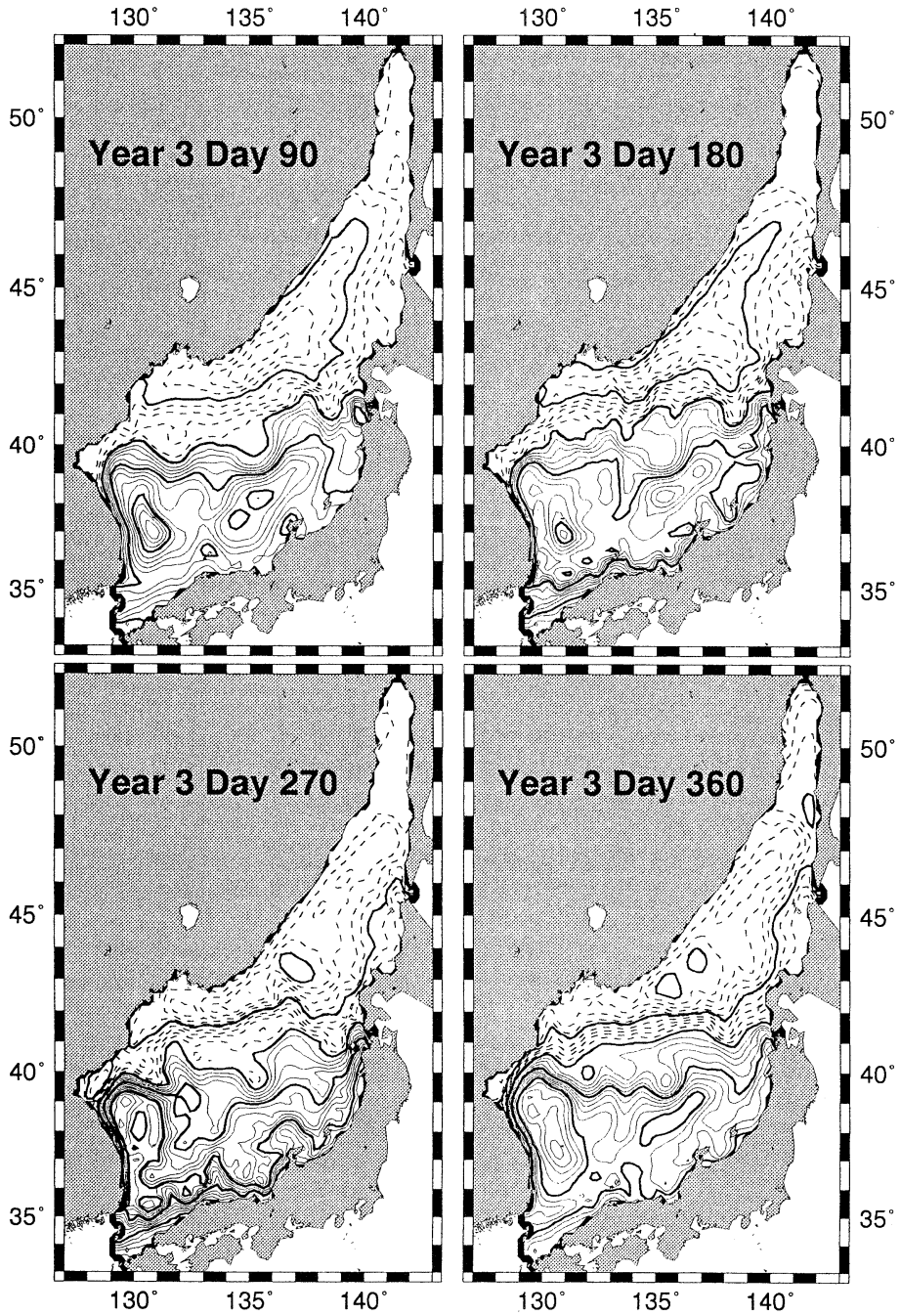


Fig. 5. Seasonal variation of sea level distribution in the climatological run. Contour interval is 2cm and the negative contours are dashed; thick lines indicate contours at 10cm intervals.

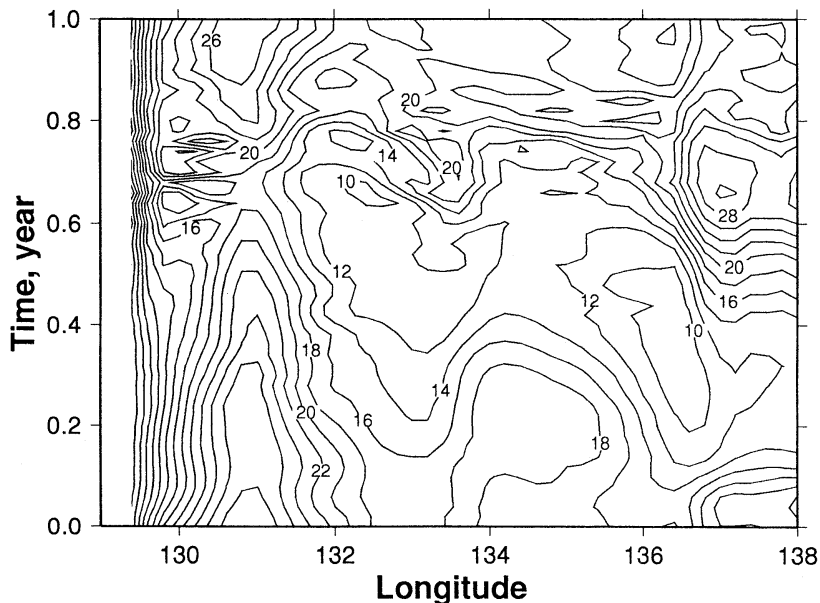


Fig. 6. Time-longitude plot of sea level (in cm) along 37°N in the climatological run.

During the first half of the year, the sea level increases gradually from Korean coast to the east and reaches its maximum at the center of the UWE. During the second half, however, the sea level increases rapidly to the east within about 50 km only from the coast. The UWE disappears during day 230-270 and small scale features appear near the EKWC. The disappearance of the UWE coincides with the time of the compression of the isolines near the coast. However, vertical section plot of v-component along 37°N (Fig. 7) shows that the EKWC stays near the coast west of 130°E all year long as a narrow current. The UWE centered about 131°E shows a northward flow in the west and a southward flow in the east. This flow pattern persists all year long except for the appearance of southward flow between EKWC and the northward flow in the west of UWE center almost the same period of the absence of UWE in the sea level signal (Fig. 6). The isotherms at depths deeper than 200m are depressed around 131°E (Fig. 8), leading to a high in the SSH at the center of the eddy. However, beginning at day 150, the isotherms in the upper 200m bulge upwards while those in deeper layers remain depressed. Therefore, the upper 200 m and the deeper layers more or less cancel each other

leading to the leveling off of the sea level and "disappearance" of the UWE in the SSH fields. This pattern persists through day 270 and the isotherms in the upper 200m again becomes level at day 300.

It is interesting to note that the bulging of the isotherms beginning from day 150 leads to the formation of the relatively homogeneous water with temperature of 6-8°C over a depth of 50 to 300m. In August, beginning at day 210, a southward current develops in the upper 100 m just offshore of the EKWC, and the UWE becomes weak and eventually disappears in the sea level signal. Day 150 corresponds to the time when the temperature in the Korea Strait becomes high at the surface, and the salinity becomes low. Day 210 is just before the transport through the Korea Strait reaches its annual maximum and the surface temperature and salinity reaches their maximum and minimum, respectively. The EKWC is also strong that the core velocity exceeds 70cm/s during day 210-270. Therefore, the inflow condition should be directly responsible for the seasonal change in the EKWC and UWE although the precise mechanism is not clear.

The model EKWC separates from the Korean Coast at a latitude of 38-39°N, at more

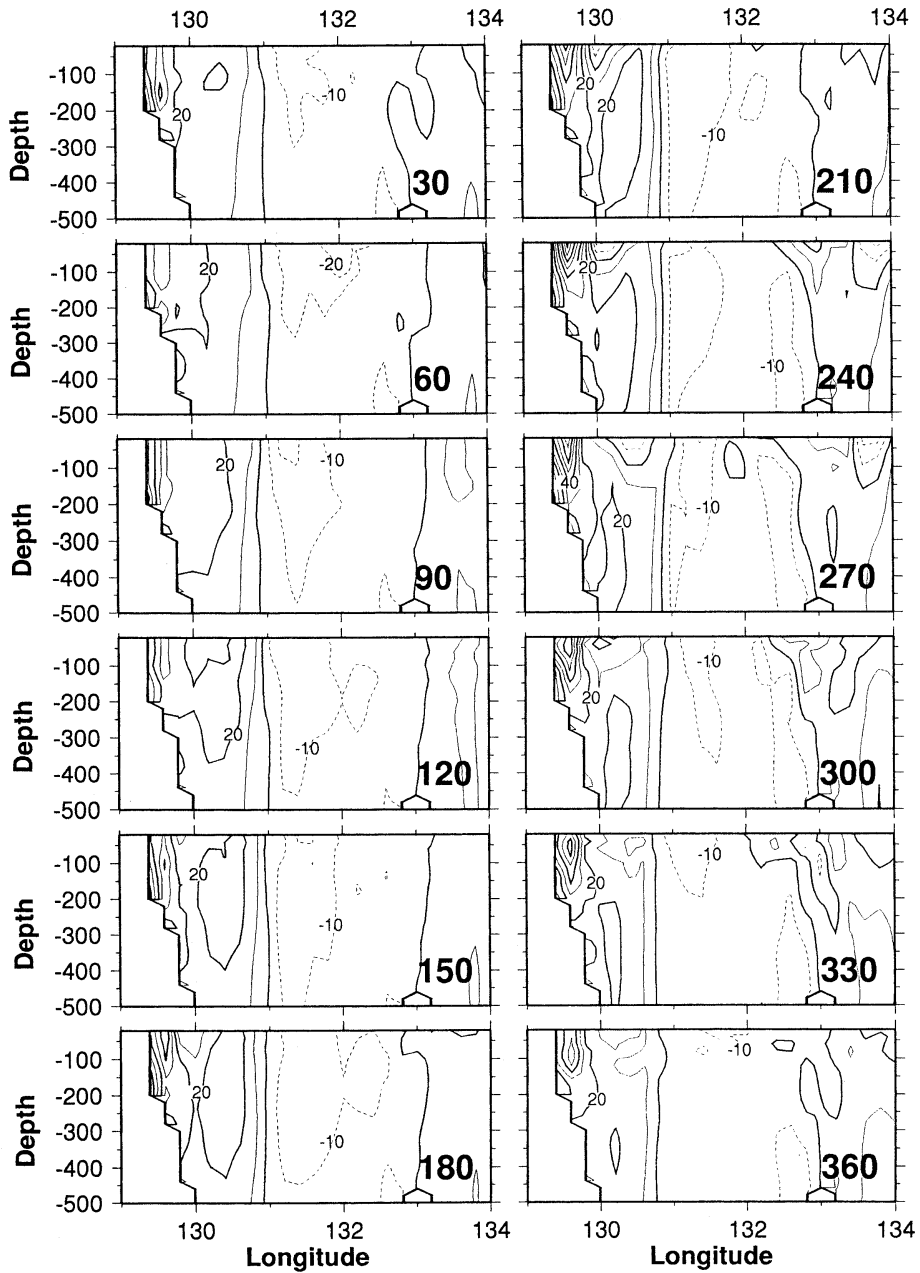


Fig. 7. Vertical sections of v-component along 37°N in climatological run plotted at 30 day intervals. Contour interval is 10cm/s and negative contours are dashed.

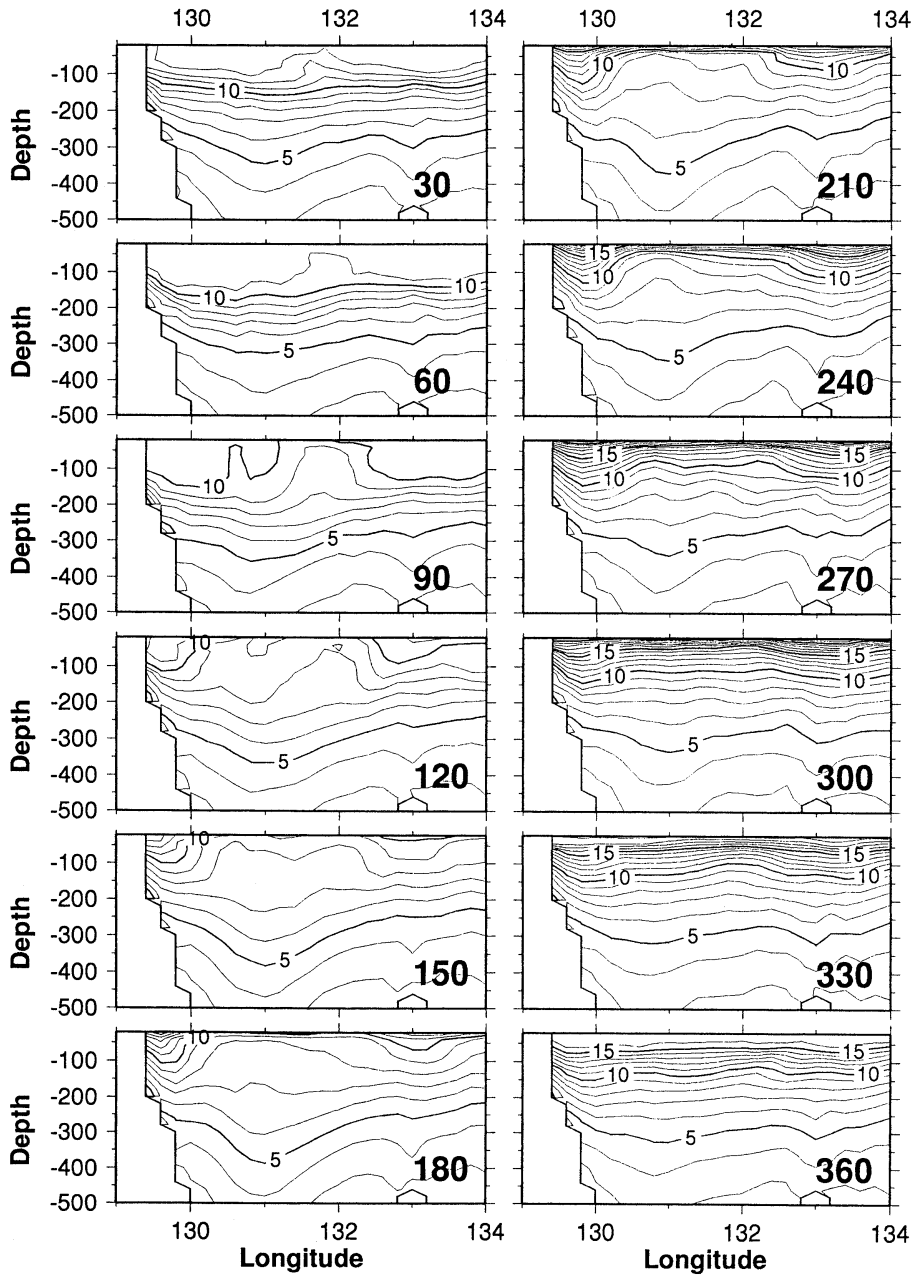


Fig. 8. Vertical sections of temperature along 37°N in climatological run plotted at 30 day intervals. Contour interval is 1°C.

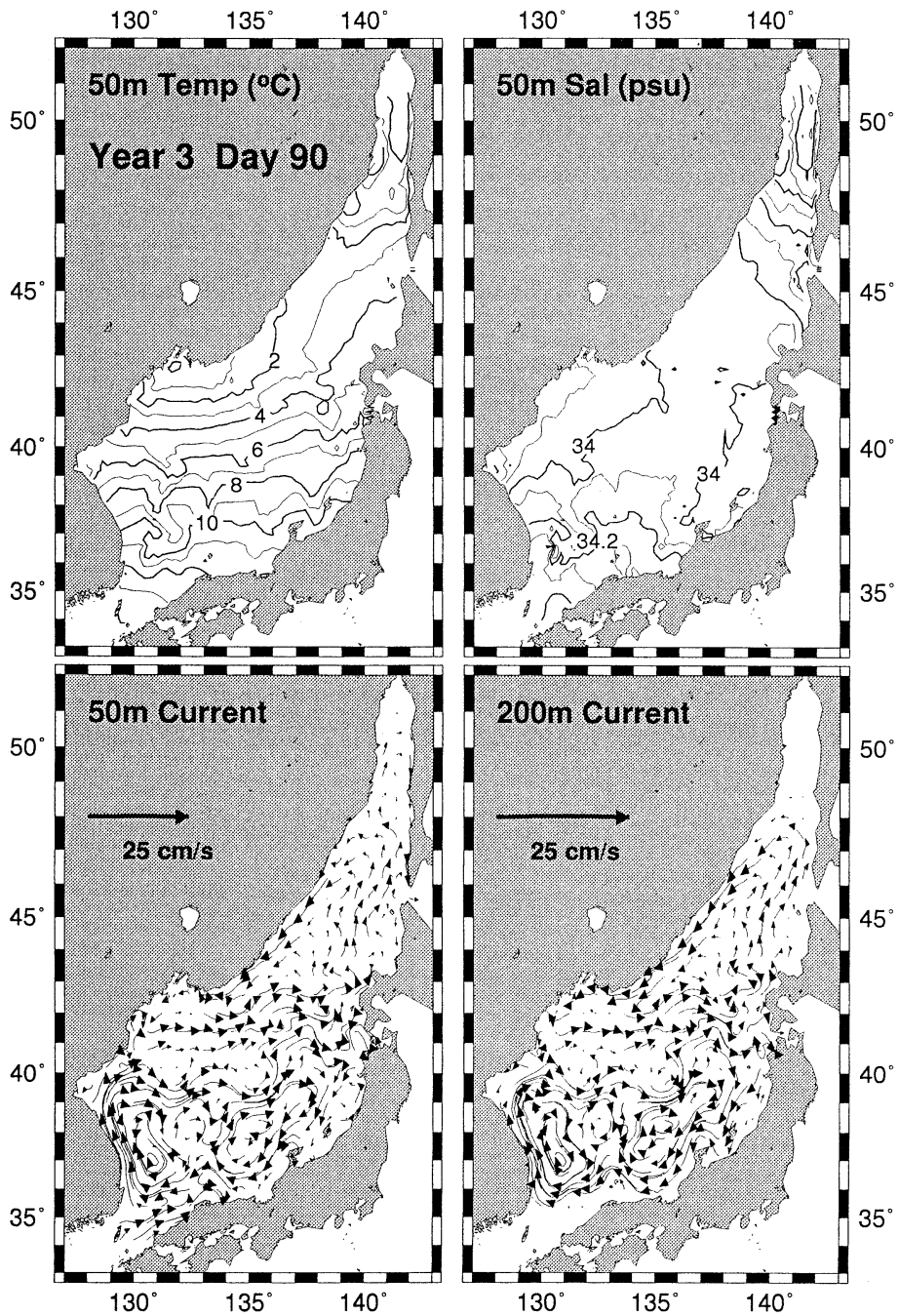


Fig. 9. Temperature and salinity at 50m, and streak plots at 50m and 200m for a winter day in the climatological run. The EKWC intrudes too far to the north and the NKCC is nearly absent.

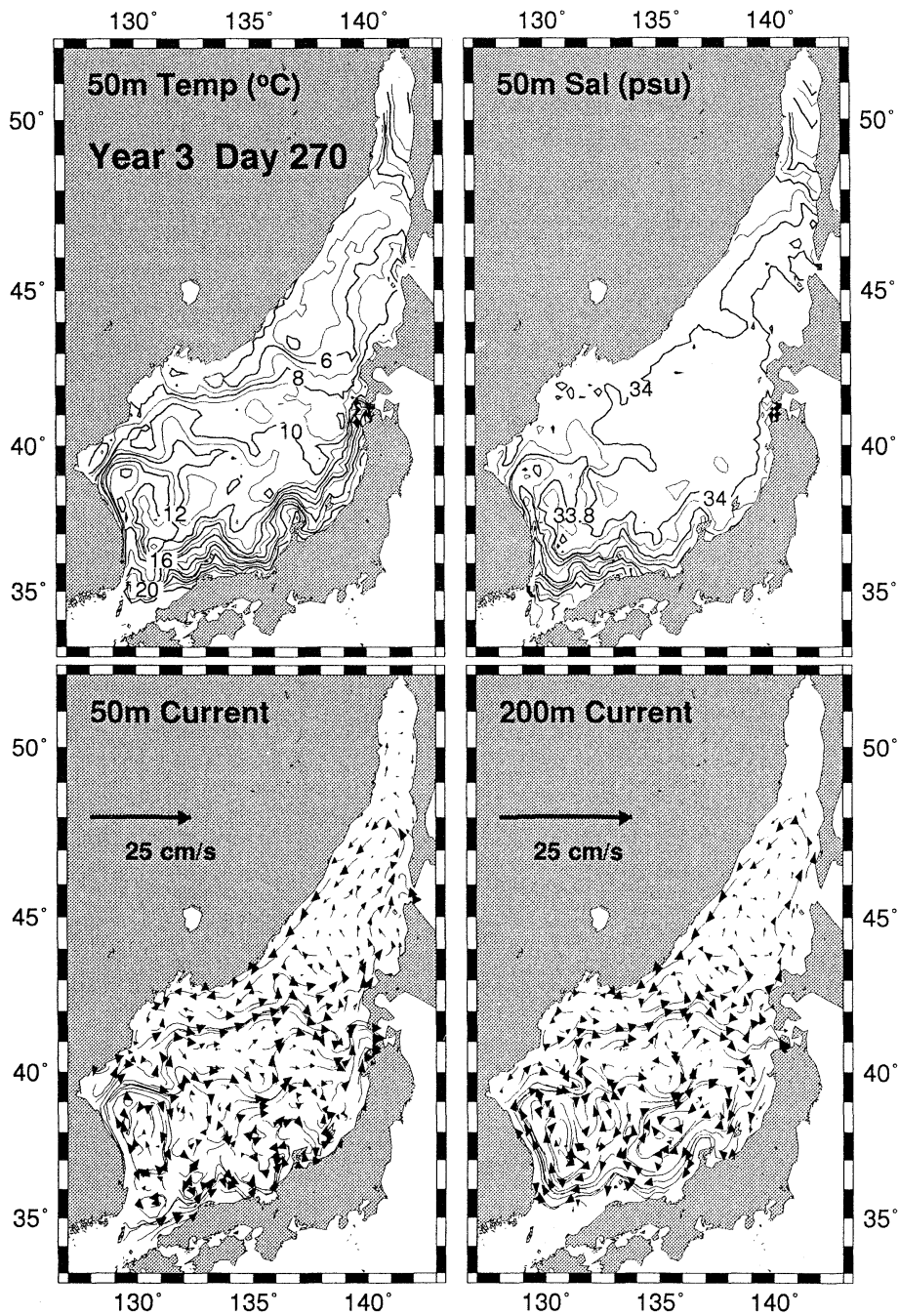


Fig. 10. Temperature and salinity at 50m, and streak plots at 50m and 200m for a summer day in the climatological run. Note the presence of warm, less saline water along the Japanese coast.

northerly latitude than indicated by observations. One possible cause is the weak wind forcing inherent in climatological forcing, as suggested by the synoptic runs described next. The EKWC continues to the east along the Polar Front.

Another interesting thing to note is the appearance of a counter-undercurrent at depths of 100–200 m underneath the eastward flowing current along the Japanese coast, which has also been observed in other model simulation (KIM and YOON, 1994; YOON, 1991; SEUNG and KIM, 1993).

Figure 9 and 10 show temperature, salinity, and current at 50m and current at 200m depth for winter and summer conditions. During the first 3-4 months of the year temperature and salinity at 50m resembles the distribution at the surface indicating strong influence from the surface either by advection (sinking) or by diffusion or both. After this period the pattern of temperature and salinity becomes complicated and resembles more closely a circulation pattern. This suggests that the distribution of temperature and salinity is controlled by horizontal advection. It is interesting to note that the flow that branches off from the separated EKWC to the south and around the center of the UWE is also seen in the temperature and salinity distributions at day 90 as an intrusion of cold and less saline waters.

The circulation at 200m depth is not much different from the 50m circulation pattern. Like in the upper layer, there is a northward-flowing boundary current along the Korean coast, it separates from the coast and flow to the east. One major difference is the presence of a consistent and strong westward flow along the southern perimeter. This flow joins to the northward flow along the Korean coast thus closing the anticyclonic circulation.

3.2 Synoptic Simulation for 1993

The major difference in this synoptic simulation compared to the climatological one described above is that the EKWC separation is more realistic, at 37–38°N rather than 38–39°N (Fig. 11). This suggests that the separation point depends strongly on the strength of wind forcing applied over the basin. One immediate

consequence of the change of the separation latitude is that the shape of UWE is now more nearly circular than in the climatological case.

Figure 12 shows the currents at various depths on day 90. Strong branching of the inflow into the EKWC and JWC can be seen at 50 m depth. The EKWC turns eastward at a latitude of 39°N and branches into two strong streams, one proceeding towards Tsugaru and the other towards Soya Straits. The Liman Current (LC) and the North Korean Cold Current (NKCC) can be clearly seen at 200m depth. These multiple current systems are responsible for the various thermal fronts seen running east-west in thermal imagery. The surprisingly strong barotropic nature of currents in the East Sea can be seen in plots of currents at various depths. Recent observations by TAKEMATSU *et al.* (1994) suggest the existence of strong nearly barotropic currents at depths as large as 3000m in the Japan basin.

The time-longitude plot of sea level along 37°N is similar to the one with climatological wind except the development of high-frequency components (Fig. 13). Quite naturally, this is because the winds used in this simulation contain more high-frequency variability both in time and space than the monthly averaged climatological winds.

In the temperature section along 37°N (not shown), the bulging of isotherms in the upper 200m that leads to the temperature homogenization in the climatological case is weaker. However, the velocity of EKWC shows similar behavior as in the climatological case that the magnitude of the core velocity is over 70cm/s during days 210–270 and a southward flow develops during the same period (not shown).

The strengthening of the EKWC and the appearance of a southward flow just offshore of EKWC and the UWE are closely related. It is possible that the strengthening of the EKWC leads to the development of an anticyclonic recirculation cell just south of the separation point. When the EKWC becomes weak after the peak inflow from the Korea Strait, the anticyclonic vorticity in the recirculation cell might diffuse to a wider area leading to the re-appearance of UWE in the south.

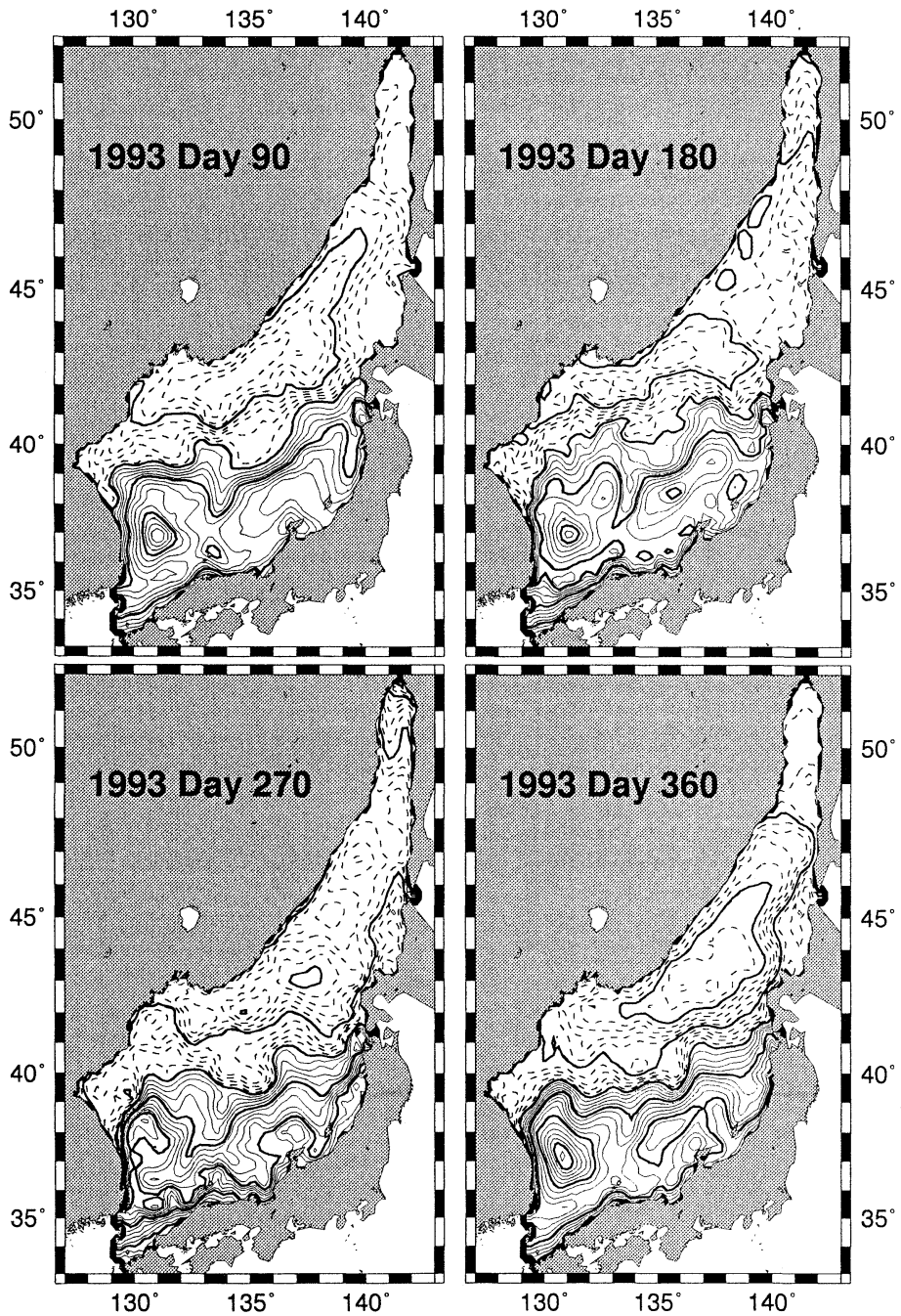


Fig. 11. Seasonal variation of sea level distribution of the synoptic run. Contour interval is 2cm and the negative contours are dashed ; thick lines indicate contours at 10cm intervals.

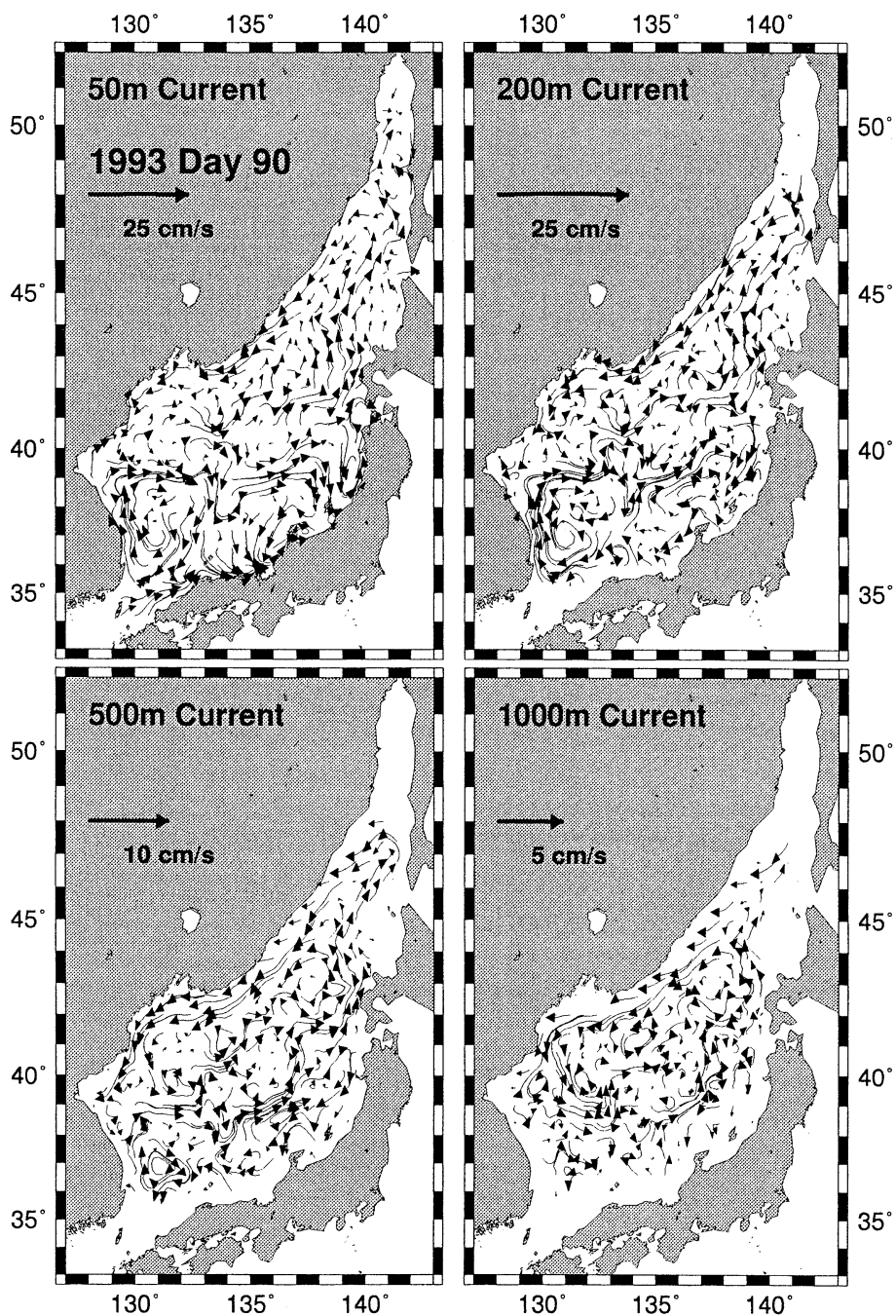


Fig. 12. Streak plots of currents at 50m, 200m, 500m and 1000m depths. Note the difference in scales. Note also the strong barotropic nature of currents, and the strong recirculation at depths below the sill depth at Korea Strait.

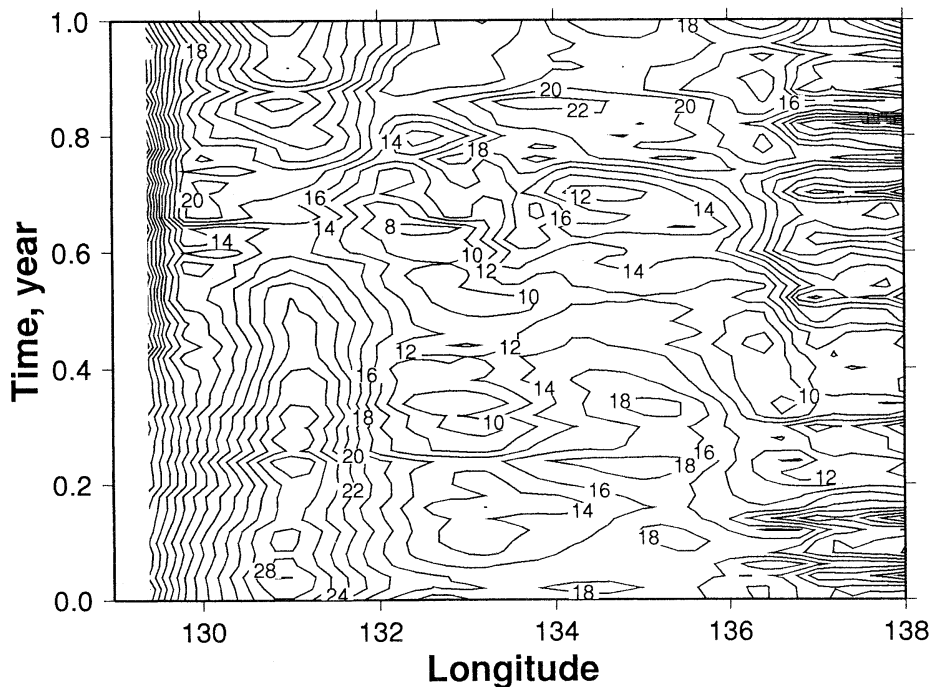


Fig. 13. Time-longitude plot of sea level (in cm) along 37°N of the synoptic run.

3.3 Hindcast

Appropriate weighting of observations and model results are an essential part of any assimilation scheme. While sophisticated schemes such as Kalman filters are ideally suited for this purpose, and take advantage of the known observational and computed model error statistics, they are prohibitively expensive and impractical for a nowcast/forecast system such as this. The simple OI scheme used with a proper choice of the weighting factor can take advantage of both dynamics and observations. Three different weighting factors (10, 20, 30%) were therefore tried.

We chose the drifter buoy tracks of LIE *et al.* (1995) as an independent set of observations to compare and verify our model results. Comparison of the TOPEX altimetry data with drifter tracks shows a remarkable agreement between the two. In particular, an anticyclonic eddy in which the two drifters were trapped for a while is also clearly seen in TOPEX altimetry (Fig. 14). This eddy is a robust feature in the altimetry data and therefore we focused on an accurate representation of this

eddy in the nowcast.

Figure 15 shows results at day 180 with different weighting factors. With 10%, the anticyclonic eddy shows up, but the size and location are not exactly the same as in TOPEX data. With 20%, there is not much difference from 10% but the eddy manifests itself more clearly. Increasing the weighting factor to 30%, however, does not help, since the eddy is now joined to the another anticyclonic circulation from the south losing its identity as an isolated eddy. Also, the sea level field becomes more plagued by high-frequency components.

As a check on the assimilation method, the sea level from the 0% assimilation run was subtracted from results of assimilation runs (Fig. 16). The resulting plot shows that the anticyclonic eddy detected by TOPEX is clearly seen. But the strength of the eddy is weaker than the TOPEX-detected signal which has about 8 cm rise above from the surroundings. Nonetheless, it is clear that the method works.

Of the three assimilation experiments, one with 20% weighting appears to best generate

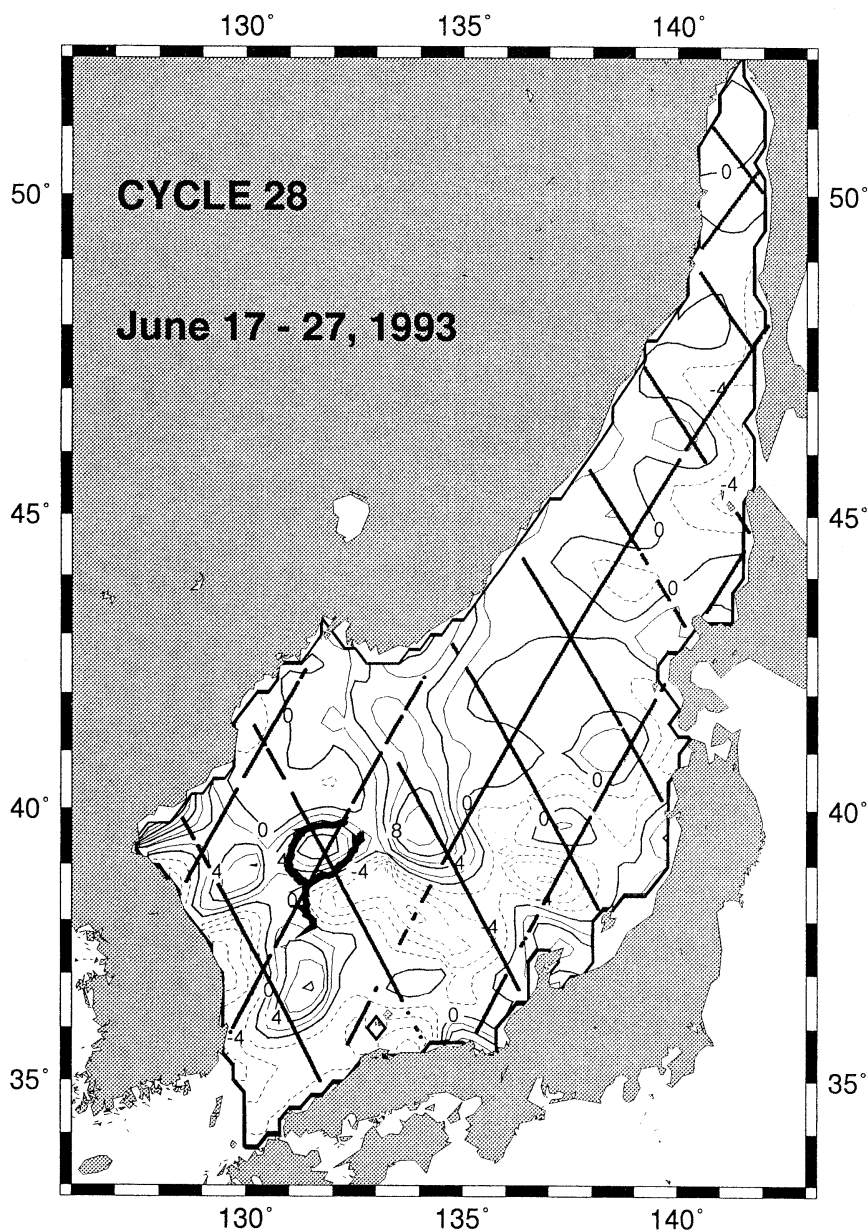


Fig. 14. Optimally interpolated sea level anomaly of TOPEX Cycle 28 (June 17–27, 1993) and two WOCE drifter buoy tracks during the same period. Contour interval is 2 cm and negative values are dashed. Heavy lines indicate satellite tracks.

anticyclonic eddy. To see if different winds affect the result we also ran a hindcast with winds derived from synoptic charts of Japan Meteorological Agency by NA *et al.* (1992). The weighting factor is 20% and the run is started from the climatological run as before. Figure.

17 shows comparison with FNMOC wind case. While this result shows stronger anticyclonic eddy than with FNMOC wind, the differences between the two are small.

ASSIMILATION RUN OF EAST SEA: DAY 180

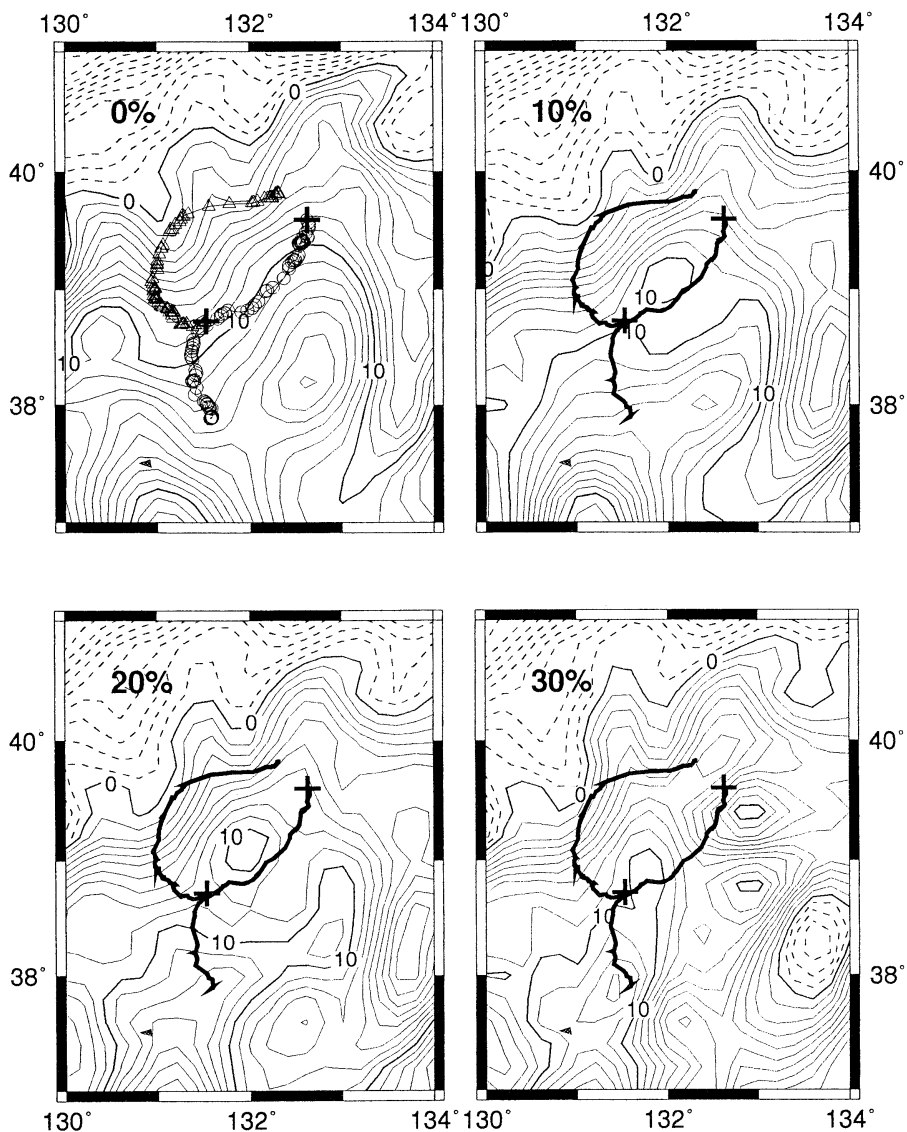


Fig. 15. Sea level distributions at day 180 from assimilation runs with various weighting factors. Contour interval is 1 cm and negative values are dashed. Plusses indicate the beginning of the drifter tracks.

4. Discussion and conclusions

The climatological simulation and the synoptic run appear to successfully reproduce many of the well-known circulation features in the ES. They also show an anticyclonic eddy, the UWE, south of Ulleung Island over the deep

Ulleung basin almost all year round in the sea level signal. From these model simulations, there appears to be a close connection between the inflow from the Korea Strait, the EKWC and the UWE. The topography of the Ulleung basin also determines the location, and the

ASSIMILATION RUN OF EAST SEA: DAY 180

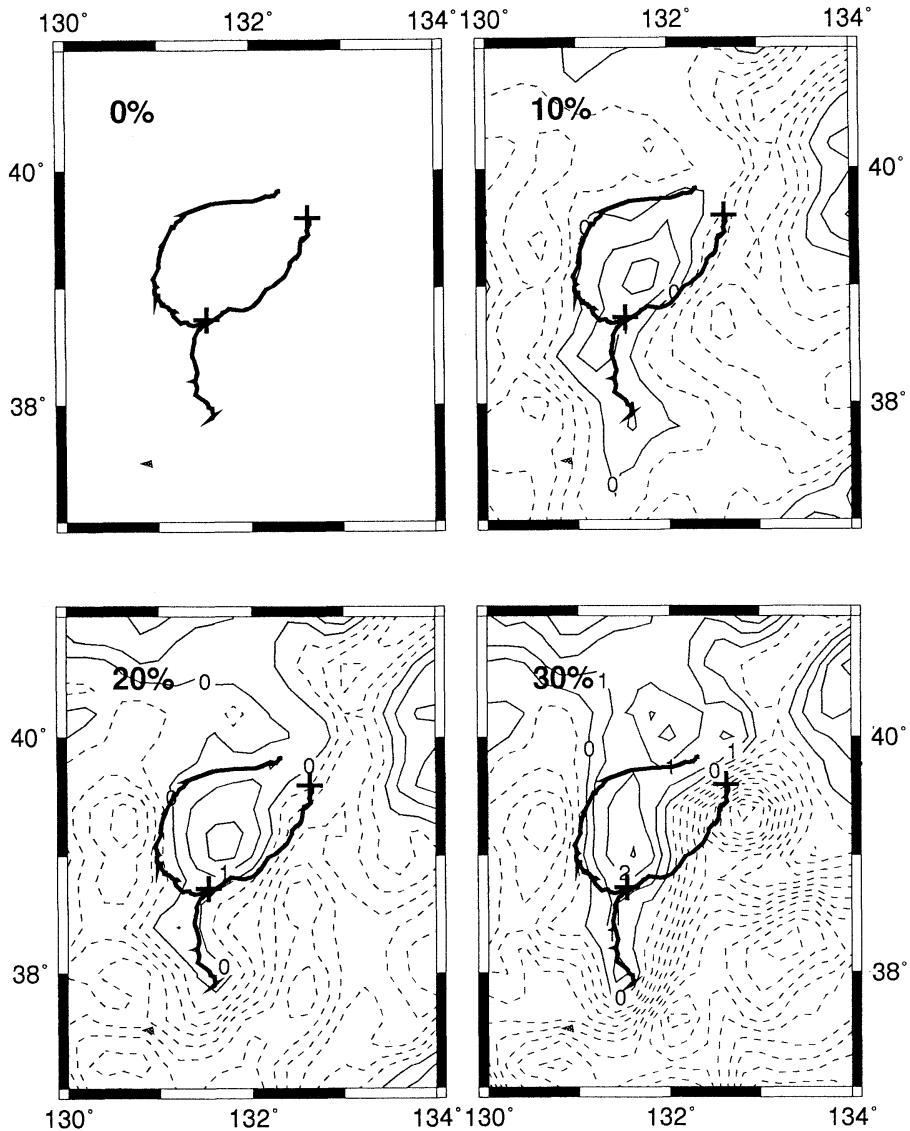


Fig. 16. Difference in sea level between runs with various weighting factors and without indicate the beginning of the drifter tracks.

formation and decay of the UWE.

A faithful simulation of the circulation in any basin depends on many factors. Of these, an accurate prescription of model forcing is of utmost importance. In the ES circulation, wind stress, surface heat/salt fluxes, inflow through

the Korea Straits are all important. In this study, only the wind data is synoptic, but the other two forcing came from a climatological source (surface heat/salt fluxes) and a short term observation (inflow condition). Using observed sea surface temperature fields or

ASSIMILATION RUN OF EAST SEA: DAY 180

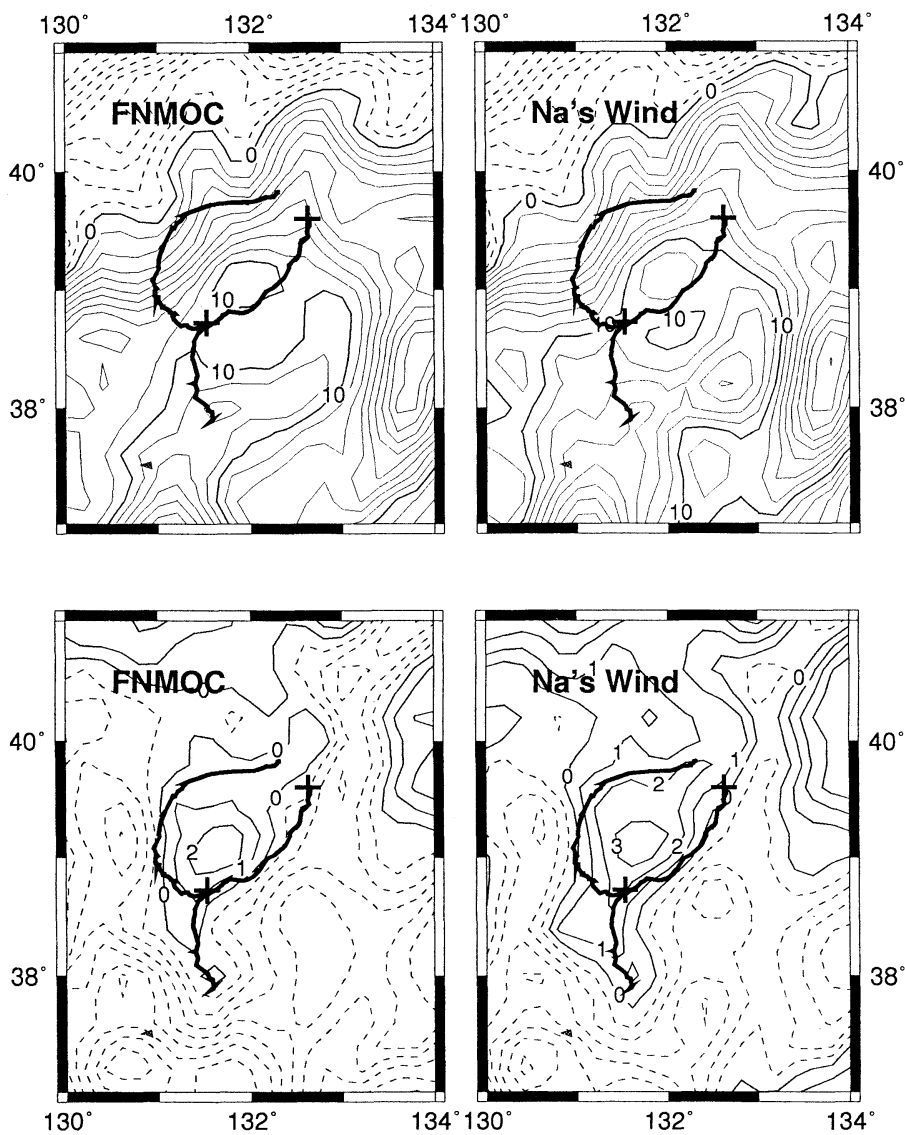


Fig. 17. Comparison of results with Na's and FNMOC winds. The upper panel shows sea level distribution and the lower panel is the difference from 0% weighting. Contour interval is 1 cm and negative values are dashed. Plusses the beginning of the drifter tracks.

thermohaline fluxes from Numerical Weather Prediction (NWP) products would improve the results. The inflow prescription is however problematic. Without long term observations in the Korea/Tsushima Straits, it is nearly impossible to prescribe correct inflow conditions.

Improvement can also be made in the assimilation method. In this study, we used one relationship for the conversion of altimetry anomaly into vertical temperature anomaly profile for the whole ES region. It might therefore be desirable to divide the ES at least into

two regions; northern half and southern half of Polar Front because they have different TS characteristics; the southern warm water has a salinity maximum layer due to the inflow of warm and saline Tsushima Current while the northern cold water does not have this feature. However, the results depend very much on the data density. Since the data are concentrated in regions south of the Polar Front, the result will be biased towards this relatively data-rich region.

Another significant problem we do not have a solution to, is how to derive the true reference state for the assimilation of temperature anomalies. This is simply because we can derive only the SSH anomalies from altimetry. It is not yet possible to separate the predominant geoid in altimetry accurately enough, and a global along-track mean must be subtracted out from each along-track observation. This means that the reference state of the altimetric SSH anomalies remains unknown. In this study, we used monthly mean temperatures from the model run with no assimilation but, this may not represent the true monthly mean values. It is possible to improve results somewhat through iteration by updating the reference temperature using the result from the previous run.

The only other routine observation being made is by the IR sensors on NOAA polar-orbiting operational satellites. MCSSTs form the most prolific data set available. Normally, MCSST only describes the temperature of the mixed layer and is therefore not generally very useful, especially during summer, when the mixed layer is shallow. However, for the ES, where the variability is principally in the upper 200 m, of which the mixed layer is a significant fraction, assimilation of MCSST in combination with altimetric data is perhaps the best strategy for a nowcast/forecast system. MCSSTs are being assimilated routinely in an operational nowcast/forecast system in the Mediterranean (Horton et al., 1996). Our future work will involve extension of the nowcast/forecast system in the ES to include MCSSTs. The boundary conditions imposed at the inflow and outflow ports are another crucial detail that need revisiting and refinement.

Acknowledgments.

LHK acknowledges with great pleasure the support by NAVO under contract IPA-OCG 0800 B. Support was also provided to LHK by the NOMP program of the Office of Naval Research under contract N 00014-92 C-6011, administered by Tom Curtin, and the Coastal Sciences Section of the Office of Naval Research under contract N00014-92-J-1766 administered by Thomas Kinder.

References

- BLUMBERG, A. F. and G. L. MELLOR (1987): A description of a three-dimensional coastal ocean circulation model. *In* Three-Dimensional Coastal Ocean Models, (Heaps, N. ed.) American Geophysical Union, 1-16.
- CHOI, J. -K., L. H. KANTHA, R. R. LEBEN and C. HORTON (1996): A nowcast/forecast experiment in the Gulf of Mexico. To be submitted to *J. Atmos. Ocean. Technology*.
- HELLERMAN, S. and M. ROSENSTEIN (1983): Normal monthly wind stress over the world ocean with error estimates. *J. Phys. Oceanogr.*, **13**, 1093-1103.
- HORTON, C., M. CLIFFORD, J. SCHMITZ and L. KANTHA (1996): A real-time nowcast/forecast system for the Mediterranean Sea. Submitted to *Dyn. Atmos. Oceans*.
- INOUE, N., T. MIITA and S. TAWARA (1985): Tsushima Strait II: physics. *In* Coastal Oceanography of Japanese Islands, (KUNISHI H. et al., ed) Tokyo Univ. Press, 914-933.
- ISOBE, A., S. TAWARA, A. KANEKO and M. KAWANO (1994): Seasonal variability in the Tsushima Warm Current, Tsushima-Korea Strait. *Continental Shelf Res.*, **14**, 23-35.
- ISODA, Y. and S. SAITOH (1993): The northward intruding eddy along the east coast of Korea. *J. Oceanogr.*, **49**, 443-458.
- KANTHA, L. H. and C. A. CLAYSON (1994): An improved mixed layer model for geophysical applications. *J. Geophys. Res.*, **99**, 22535-25266.
- KANTHA, L. H. and S. PIACSEK (1993): Ocean Modeling. *In* Computer Science Education Project Electronic Book, Department of Energy, pp. 73.
- KANTHA, L. H. and S. PIACSEK (1996): Computational Ocean Modeling. To appear in CRC Handbook of Computer Science and Technology.
- KIM, C. (1993): A study on the meso-scale warm eddy in the southwestern part of the East Sea. Res. Rep., BSPN 00187-611-1, KORDI, Korea.
- KIM, C. -H., H. -J. LIE and K. -S. CHU (1991): On the intermediate water in the southwestern East Sea (Sea of Japan). *In* Oceanography of Asian Mar-

- ginal Seas, (Takano, K. ed.) Elsevier, 129-141.
- KIM, C. -H. and J. -H. YOON (1994): A numerical study on the seasonal variation of the Tsushima Warm Current along the coast of Japan. Abstract of Third Workshop of Circulation Research of the East Asian Marginal Seas, November 7-8, Seoul, Korea.
- KIM, K. and J. Y. CHUNG (1984): On the salinity-minimum layer and dissolved oxygen - maximum layer in the East Sea (Japan Sea). *In* Ocean Hydrodynamics of the Japan and East China Seas, (Ichiye, T. ed.) Elsevier, 55-65.
- LEVITUS, S. (1981): Climatological atlas of the world ocean, NOAA Professional Paper No.13, U. S. Govt. Printing Office, pp. 173.
- LIE, H. -J., S.-K. BYUN, I. BANG and C. -H. CHO (1995): Physical structure of eddies in the southwestern East Sea. *J. Oceanol. Soc. Korea*, **30**, 170-183.
- MELLOR, G. L. (1992): User's guide for a three-dimensional, primitive equation, numerical ocean model. Program in Atmospheric and Oceanic Sciences Report, Princeton University, pp. 35.
- MORIYASU, S. (1972): The Tsushima Current. *In* Kuroshio, (Stommel, H. and K. Yoshida, ed.) Univ. Tokyo Press, 353-369.
- NA, J. Y., J. W. SEO and S. K. HAN (1992): Monthly-mean sea surface winds over the adjacent seas of the Korean Peninsula. *J. Oceanol. Soc. Korea*, **27**, 1-10.
- SEKINE, Y. (1988) On the seasonal variation in in and out-flow volume transport of the Japan Sea. *Prog. Oceanogr.*, **21**, 269-279.
- SENJU, T. and H. SUDO (1993): Water characteristics and circulation of the upper portion of the Japan Sea proper Water. *J. Mar. System*, **4**, 349-362.
- SEUNG, Y. -H. and K. KIM (1993): A numerical model of the East Sea Circulation. *J. Oceanol. Soc. Korea*, **28**, 292-304.
- SHIN, H. -R., S. -K. BYUN, C. KIM, S. HWANG and C. -W. SHIN (1995): The characteristics of the structure of warm eddy observed to the northwest of Ullungdo in 1992. *J. Oceanol. Soc. Korea*, **30**, 39-56.
- TAKEMATSU, M., A. G. OSTROVSKII and T. KITAMURA (1994): Current feature in the Japan Sea's proper water. Abstract of Third Workshop of Circulation Research of the East Asian Marginal Seas, November 7-8, Seoul, Korea, 1994.
- YOON, J. -H. (1991): The branching of the Tsushima Current. Report, Res. Inst. Appl. Mech., Kyushu Univer., **38** (108), 1-21.

Received December 12, 1995

Accepted March 22, 1996

Comparison of seawater carbonate parameters in the East China Sea and the Sea of Japan

Shu-Lun WANG* and Chen-Tung Arthur CHEN*

Abstract: During the Kuroshio Edge Exchange Processes-Marginal Sea Studies expedition (KEEP-MASS) in the summer of 1992, three parameters of the carbonate system were measured—pH, total alkalinity (TA) and total carbon dioxide (TCO₂). All measurements were made by two independent methods. The pH values based on the NIST phosphate buffers were lower than those based on the Tris buffer by 0.004 ± 0.014 pH unit ($n=210$). The TA determined from the potentiometric Gran titration was about $6.5 \pm 5.0 \mu\text{mol/kg}$ ($n=154$) lower than that determined by the single-point indicator method. The TCO₂ determined from the coulometry method was about $17.8 \pm 6.1 \mu\text{mol/kg}$ ($n=139$) lower than that determined by the potentiometric Gran titration. Typical distributions of these parameters in the East China Sea and the Sea of Japan are presented.

1. Introduction

Recently, the fate of fossil fuel CO₂ and the carbon cycle in the ocean have promoted much interest in the study of carbonate chemistry in the oceans (CHEN and DRAKE, 1986; CHEN, 1993). The carbonate system can be characterized by measuring two of the four parameters, pH, TA (total alkalinity), TCO₂ (total carbon dioxide) and pCO₂. The other parameters can then be calculated using the thermodynamic constants. However, when the measured values are compared with the calculated values, discordant results are often found (BROECKER and TAKAHASHI, 1978; BRADSHAW and BREWER, 1988; MILLERO *et al.*, 1993a).

The rate of increase of TCO₂ in the surface ocean is about $1 \mu\text{mol/kg/yr}$. In order to detect such a small change and to assure the internal consistency in the CO₂ system, it is necessary to make reliable and precise measurements of the parameters. The purpose of this article is to present the intercomparison results of 3 carbonate parameters during the Kuroshio Edge Exchange Processes-Marginal Sea Studies (KEEP-MASS) expedition (CHEN, 1992).

2. Method

In 1992, a multinational, multidisciplinary study of the West Philippine Sea (WPS), the East China Sea (ECS) and the Sea of Japan, called the KEEP-MASS, was conducted aboard the Russian R/V Academic Alexander Vinogradov. The ship departed Kaohsiung, Taiwan on 10 July, and returned to Vladivostok on 5 August. During the expedition 71 hydrographic stations were occupied: 11 in the WPS; 49 in the ECS and 11 in the Sea of Japan. The pH, TA and TCO₂ were measured as follows:

We used the NIST (National Institute of Standards and Technology, U.S.A.) 4.006 and 7.415 phosphate buffers to calibrate the Radiometer GK 2401C combination electrode at 25°C. The reproducibility of the pH measurements was better than ± 0.001 units for replicate samples. All measurements were performed within 30 minutes of sampling. The electrode drift (assumed to be linear) was determined at approximately 10 day intervals. The drift was approximately 0.0018 unit/day and the correction was made to the measured values. Altogether 534 samples were measured. Independent pH measurements on 210 samples were made by a Russian group using Tris (2-amino-2-hydroxymethyl-1, 3-propanediol) seawater buffer to calibrate the glass and

* Institute of Marine Geology and Chemistry, National Sun Yat-Sen University, Kaohsiung, Taiwan, R.O.C.

reference electrodes (CHEN *et al.*, 1992). The composition of the artificial seawater buffer was the same as used by MILLERO (1986). The reproducibility of the pH measurements was ± 0.009 units for replicate samples.

We determined the alkalinity of 373 samples by the Gran titration at $25 \pm 0.05^\circ\text{C}$ with a PC-controlled titration cell (CHEN and WANG, 1993). These measurements have a precision of $\pm 0.05\%$ and were performed within 12 hours of sampling. The accuracy of this method shown in HUANG and CHEN (1995) is $\pm 3 \mu\text{mol/kg}$. The Russian team measured 154 TA samples using the single-point indicator method following Bruevich's procedure (IVANENKOV and LYAHIN, 1978). The end-point was decided by eye with an accuracy of about $\pm 5 \mu\text{mol/kg}$ at room temperature (CHEN *et al.*, 1992).

The TCO_2 measurements were conducted by us with two independent methods. The SOMMA (single-operator multiparameter metabolic analyzer) system first extracted CO_2 gas from acidified seawater and subsequently the CO_2 gas was measured by UIC (Coulometrics, Inc.) model 5011 coulometric detector (DICKSON and GOYET, 1991). One hundred fifty two samples were performed within 12 hours of sampling, and the precision was $\pm 0.025\%$. The Centre for Ocean Climate Chemistry (COCC) in the Institute of Ocean Sciences, Canada, prepared the TCO_2 standard seawater for us as the running standard. The reference material could be traced to the standard material from the Scripps Institution of Oceanography, U.S.A. with the accuracy of about $\pm 1 \mu\text{mol/kg}$. Three hundred seventy three TCO_2 samples were also determined by the Gran titration at $25 \pm 0.05^\circ\text{C}$. The accuracy was $\pm 4 \mu\text{mol/kg}$.

3. Results and Discussion

When all the pH values based on the Tris buffer were changed to the NIST scale (MILLERO, 1986), these two sets of data agreed to within 0.004 ± 0.014 pH unit based on 210 measurements (Table 1). The Russian data were a little higher than ours, but the agreement was much better than the combined precision of ± 0.01 pH unit. A 1985 SCOR report stated that "the usual reproducibility of ocean pH measurements is not better than ± 0.02 pH units". The present results and the results of BYRNE *et al.* (1988) and CHEN (1994) clearly nullified that statement. Indeed these studies indicate that the usual reproducibility of ocean pH measurements is now about ± 0.003 pH units.

Figure 1 shows the vertical profiles of θ , S and pH in the Sea of Japan. The vertical temperature gradient was very large in the surface water, about 20°C in a matter of 100m. The salinity was lower for surface water then gradually increased with depth. In the deep water the water was very homogeneous and had a salinity of about 34.07. The pH data showed a large decrease with depth in the surface water and a minimum was found at about 1800m.

The pH minimum is shown more clearly when our data from several stations are plotted with depth (Fig. 2). This minimum, an indication of the presence of older water, is shown even more dramatically when plotted vs. θ (Fig. 3). CHEN *et al.* (1995a) also found an AOU maximum in the deep water, corresponding to the pH minimum. It should be pointed out that the magnitude of the pH signal was only 0.02 pH unit. High precision of the data is needed in order to detect it.

The comparison of TA data collected at the

Table 1. Comparison of the carbonate parameters during the KEEP-MASS Expedition

	pH	TA	TCO_2
ROC	NIST buffers	potentiometry	potentiometry, coulometry
Russia	Tris buffer	single-point	—
Δ	0.004 ± 0.014 (Russia-ROC)	6.5 ± 5.0 (Russia-ROC)	$17.8 \pm 6.1^{\#}$
n	210	154	139

$\#$ potentiometry-coulometry

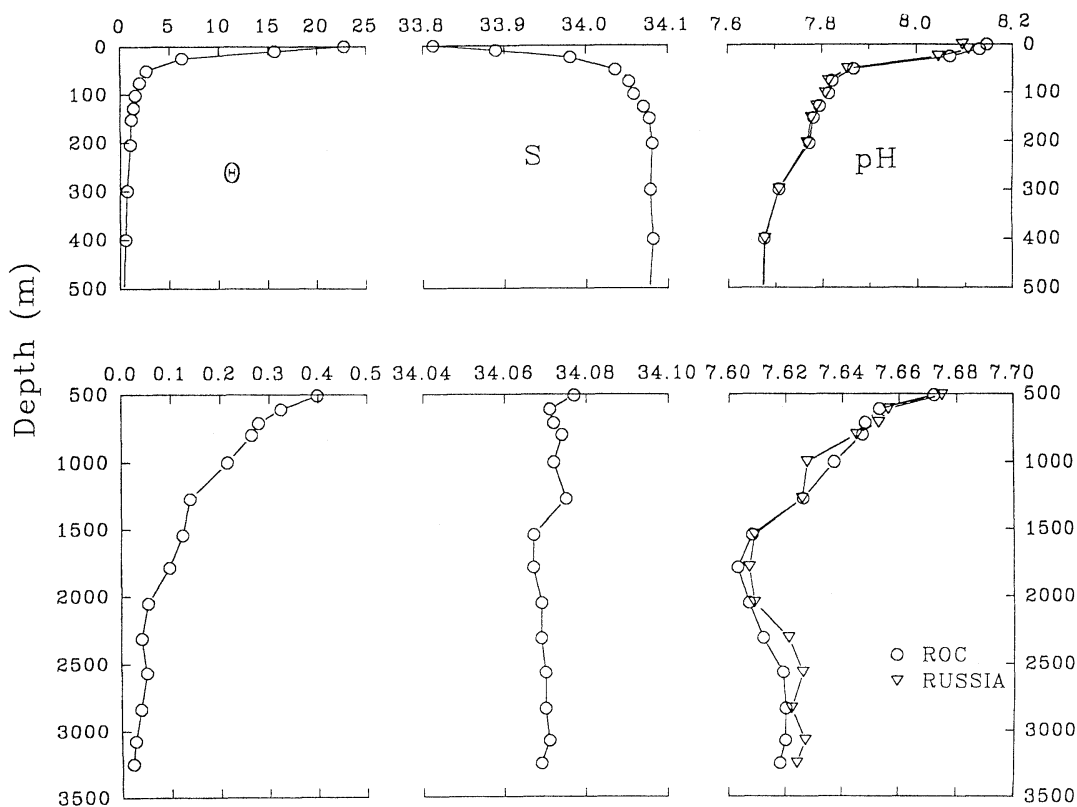


Fig. 1. The vertical profiles of θ , S and pH (25°C) at station 10 (40°56.3'N, 133°01.2'E) in the Sea of Japan.

same locations showed that our TA values were about $6.5 \pm 5.0 \mu\text{mol/kg}$ ($n=154$) lower than that determined by the single-point indicator method. The vertical profile of the normalized alkalinity ($\text{NTA} = \text{TA} \cdot 35/\text{S}$) in the Sea of Japan shown in Fig. 4 indicates that both methods gave reliable results, but the single-point method was less precise. The NTA increases steadily with depth below 500m. In the whole water column the NTA values varied less than $40 \mu\text{mol/kg}$ in the Sea of Japan.

The NTA is a useful tool for studying the mixing processes on the shelf (CHEN, 1985). The NTA data in the ECS are plotted vs. salinity in Fig. 5. In the shelf area, the NTA-S correlation falls into a linear trend with NTA shooting up at lower salinity, reflecting the alkalinity input of the river water (CHEN *et al.*, 1995b). The bottom water of shelf area in the northern ECS falls into a different trend which indicates a different water source. The Kuroshio has a

very different correlation with salinity as compared to the ECS shelf water.

The TCO_2 determined from the coulometry method was about $17.8 \pm 6.1 \mu\text{mol/kg}$ ($n=139$) lower than that determined by the potentiometric Gran titration (Table 1), similar to that reported by BRADSHAW and BREWER (1989). The vertical distributions of normalized total CO_2 ($\text{NTCO}_2 = \text{TCO}_2 \cdot 35/\text{S}$) is shown in Fig. 6. The difference between these two methods has been attributed to the presence of unknown protolytes in seawater (BRADSHAW and BREWER, 1988) but MILLERO *et al.* (1993b) suggested that the offset in the TCO_2 is due to deviations in the slope of the electrode from the Nernstian behavior. It suggests that the TCO_2 measured by the potentiometric method needs more attention vis-a-vis the condition of the electrode. Fig. 7 shows the pH- NTCO_2 correlation and clearly indicates the pH minimum but the quality of the NTCO_2 data is not sufficient

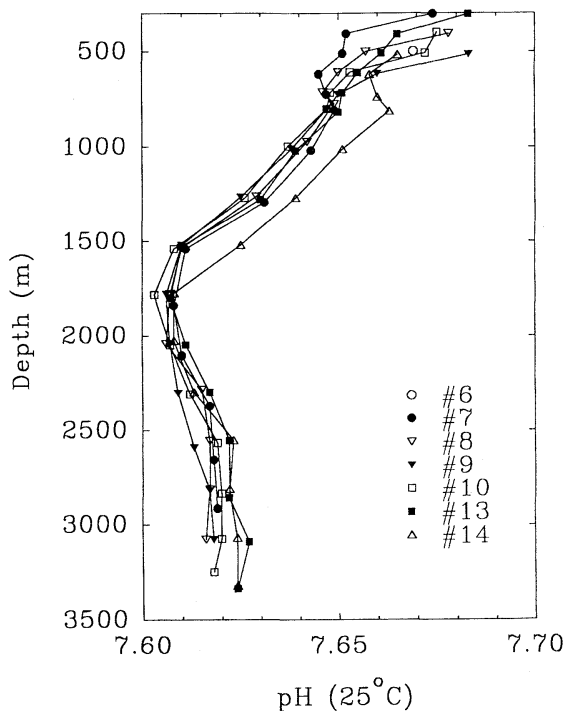


Fig. 2. The vertical profiles of pH (25°C) below 300m in the Sea of Japan.

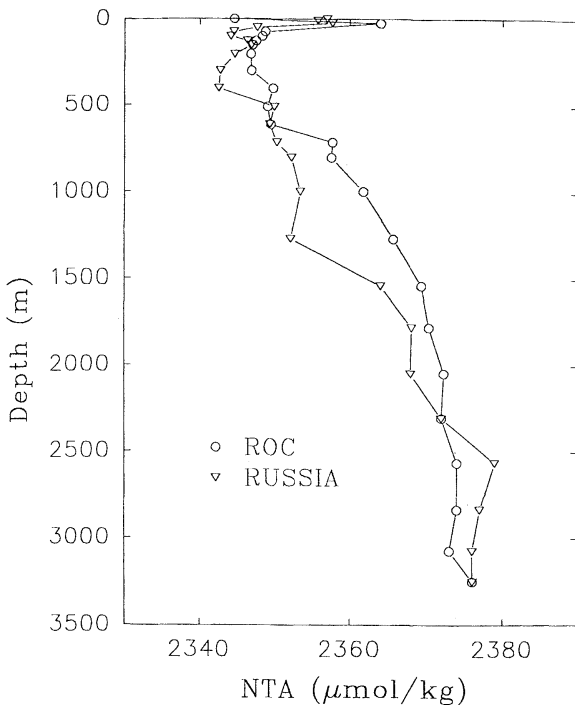


Fig. 4. The vertical profiles of NTA at station 10 (40°56.3'N, 133°01.2'E) in the Sea of Japan.

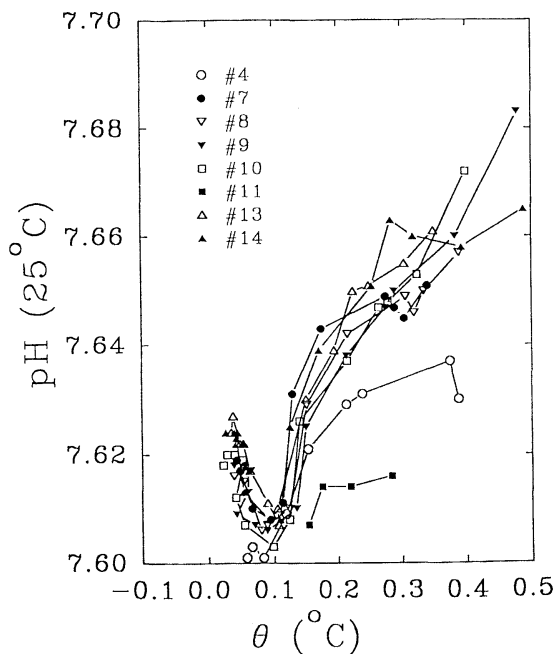


Fig. 3. The correlation of pH (25°C) with θ in the Sea of Japan.

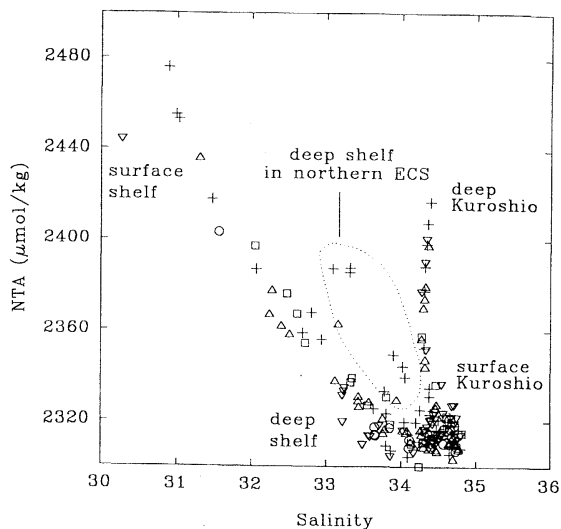


Fig. 5. The NTA vs. S diagram in the East China Sea. Enclosed area with dotted line indicates the deep shelf water in the northern ECS.

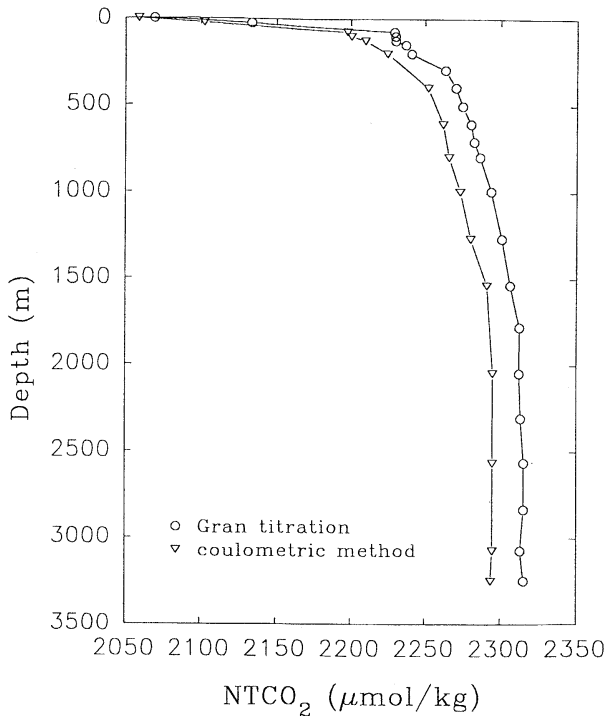


Fig. 6. The vertical profiles of NTCO_2 at station 10 ($40^\circ 56.3' \text{N}$, $133^\circ 01.2' \text{E}$) in the Sea of Japan.

to tell whether there is a NTCO_2 maximum.

4. Conclusion

The pH measurements based on the NIST and Tris buffers agreed to within 0.004 ± 0.014 pH unit during the KEEP-MASS expedition. The TA measurements showed that both of the potentiometric Gran titration and the single point method could give reliable results but the potentiometric Gran titration is more precise. The TCO_2 values determined by the potentiometric Gran titration apparently had a systematic shift compared with those determined by the coulometry method.

Acknowledgements

This research was supported by the National Science Council (NSC 85-2611-M-110-006 K2). We thank Alexander S. Bychkov of the Pacific Oceanological Institute, Russia for assistance at sea. An anonymous reviewer provided constructive criticisms.

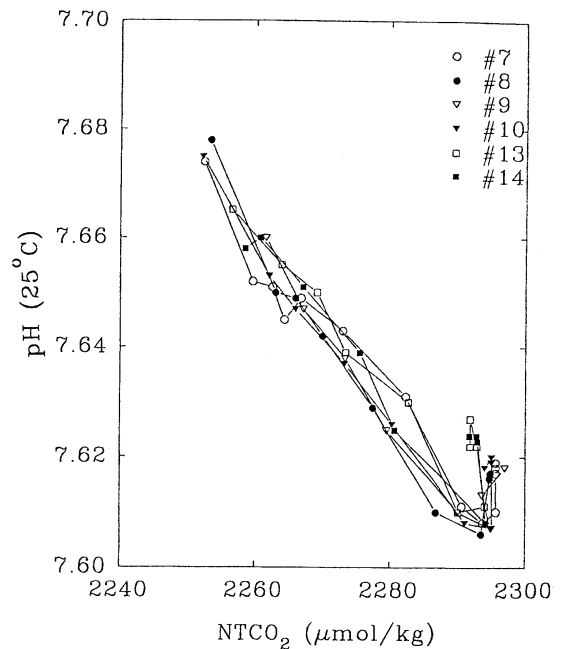


Fig. 7. The correlation of pH (25°C) with NTCO_2 in the Sea of Japan.

References

- BRADSHAW, A. L. and P. G. BREWER (1988): High precision measurements of alkalinity and total carbon dioxide in seawater by potentiometric titration-1. Presence of unknown protolyte(s) ? *Mar. Chem.*, **23**, 69-86.
- BRADSHAW, A. L. and P. G. BREWER (1989): High precision measurements of alkalinity and total carbon dioxide in seawater by potentiometric titration-2. Measurements on standard solutions, *Mar. Chem.*, **24**, 155-162.
- BROECKER, W. S. and T. TAKAHASHI (1978): The relationship between lysocline depth and in situ carbonate ion concentrations, *Deep-Sea Res.*, **25**, 65-95.
- BYRNE, R. H., G. ROBERT-BALDO, S. W. THOMPSON and C. T. CHEN (1988): Seawater pH measurements: an at-sea comparison of spectrophotometric and potentiometric methods, *Deep-Sea Res.*, **35**, 1405-1410.
- CHEN, C. T. (1985): Preliminary observations of oxygen and carbon dioxide of the wintertime Bering Sea marginal ice zone, *Cont. Shelf Res.*, **4**, 465-483.
- CHEN, C. T. A. (1992): A preliminary multination

- multidisciplinary study of the western marginal seas in the North Pacific, *Bull. Mar. Sci. Tech.*, **11**, 4-33.
- CHEN, C. T. A. (1993): The oceanic anthropogenic CO₂ sink, *Chemosphere*, **27**, 1041-1064.
- CHEN, C. T. A. (1994): Vertical distributions of pH and fluorescence in the western tropical Indian ocean-the INDIGO 2 expedition, *TAO*, **5** (1), 77-90.
- CHEN, C. T. and E. T. DRAKE (1986): Carbon dioxide increase in the atmosphere and oceans and possible effects on climate, *Annu. Rev. Earth Planet. Sci.*, **14**, 201-235.
- CHEN, C. T. A. and S. L. Wang (1993): International intercalibration of the CO₂ parameters, *Acta Oceanol. Sin.*, **15**(6), 60-67. (in Chinese)
- CHEN, C. T. A., S. L. WANG and A. S. BYCHKOV (1995a): Carbonate chemistry of the Sea of Japan, *J. Geophys. Res.*, **100**, C7, 13737-13745.
- CHEN, C. T. A., R. RUO, S. C. PAI, C. T. LIU and G. T. F. WONG (1995b): Exchange of water masses between the East China Sea and the Kuroshio off northeastern Taiwan, *Cont. Shelf Res.*, **15**, 19-39.
- CHEN, M. P., C. C. HUANG, F. L. LIN C. C. LIU, H. W. LI, G. C. GONG, J. J. HUNG and Y. L. LEE (1992): The KEEP-MASS data report, 728pp., NSC R. V. Ocean Researcher 1, Reg. Instrum. Cent., Taipei, Taiwan.
- DICKSON A. and C. GOYET (eds) (1991): DOE Handbook of Methods for the Analysis of the Various Parameters of the Carbon Dioxide System in Sea Water, 104pp., U. S. Department of Energy, Washington, D. C.
- HUANG, M. H. and C. T. A. CHEN (1995): Carbonate chemistry in northeast South China Sea, *J. Oceano. in Taiwan Strait*, **14**, 2, 124-134. (in Chinese).
- IVANENKOV, V. and Y. LYAHIN (1978): The determination of the seawater alkalinity. Methods of hydrochemical investigation of seawater, *Science, Moscow*, 110-114. (in Russian)
- MILLERO, F. J. (1986): The pH of estuarine waters, *Limnol. Oceanogr.*, **31**, 839-847.
- MILLERO, F. J., J. Z. ZHANG, S. FIOLE, S. SOTOLONGO, R. N. ROY, K. LEE and S. MANE (1993a): The use of buffers to measure the pH of seawater, *Mar. Chem.*, **44**, 143-152.
- MILLERO, F. J., J. Z. ZHANG, K. LEE and D. M. CAMPBELL (1993b): Titration alkalinity of seawater, *Mar. Chem.*, **44**, 153-165.
- SCOR (1985): Oceanic CO₂ measurements. Rep. 3rd Meet. Working Group 75, Les Houches, France, October 1985.

Received December 25, 1995

Accepted May 31, 1996

Mode of mud deposition on shelf to basin area off Akita, northeast Japan Sea

Ken IKEHARA*, Hajime KATAYAMA* and Takeshi NAKAJIMA*

Abstract : Akita shelf is a typical muddy shelf around the Japanese Islands. To clarify dispersal and depositional patterns of terrigenous materials, observations for concentration of suspended materials, analyses of sediment grain size and of coarse fraction compositions of sediments, and of seismic records were carried out. As the result, most of terrigenous fine materials had been transported through bottom nepheloid layers and deposited in shelf-slope area off Akita. Based on spatial distribution of plant debris, biotite and pumice in coarse fraction, terrigenous materials derived from Omono River had been transported westward and then southward.

Because concentration area of plant debris was well-concordant with the area of silt distribution, sand-sized plant debris was thought to be a useful tracer of terrigenous fine silt. Deposition of terrigenous organic materials in silty sediments formed high C/N ratio sediments along the outer shelf to slope area. High rate of organic material supply resulted in low oxidation-reduction potential. Total 1.56 million tons of fine grained materials had been deposited in shelf-slope basin area in a year.

Compared with annual mean discharge from major rivers around this area, almost of all materials supplied from Omono and Koyoshi Rivers and 40-50% of annual discharge from Mogami and Aka-gawa-shin-kawa Rivers had been deposited in this area. On the basis of annual mean volume of sediment accumulation and organic carbon content of surface sediments in several basins of Japan Sea, shelf-slope mud is very important for consideration of material cycles in Japan Sea.

1. Introduction

Dispersal and depositional patterns of terrigenous materials are a big problem on marine sedimentology as well as material transport and cycle in marine environments. Therefore, sedimentological studies have been carried out on the shelves near the river mouths (MILLIMAN *et al.*, 1987; ALEXANDER *et al.*, 1991; PUJOS and JAVELAUD, 1991; LESUEUR and TASTET, 1994; DÍAZ *et al.*, 1996). MILLIMAN and SYVITSKI (1992) and MILLIMAN (1995) indicated the importance of geomorphic and tectonic control for sediment discharge to the ocean. Japan is a typical example of tectonically active area in the world, where high mountains are located near the shores. Then, it is important to clarify sediment budget around the Japanese islands and to compare it with

those from the other tectonic or geomorphic settings.

Bottom sediments have recorded the long-term, averaged history of deposition and erosion, and of dispersal pattern of materials, which is difficult to detect by usual oceanographic measurements, because sediments are final state of transported materials. As materials derived from rivers have been transported according to water circulation, it is possible to infer the water circulation pattern in an area from sedimentological data. Therefore, sediment analysis is an important tool to clarify transport of materials and water circulation pattern, in particular, in an area where current measurement data are very limited (IKEHARA, 1992, 1993).

Akita shelf is a typical muddy shelf around the Japanese Islands. There are two slope basins (Tobishima and Oga Basins) which are isolated from offshore deep-sea trough

* Marine Geology Department, Geological Survey of Japan, Tsukuba, Ibaraki, 305 Japan

(Mogami Trough) by a north-south trended topographic high. Under these topographic conditions, almost of all terrigenous fine grained materials have been deposited on shelf-slope-basin setting. Therefore, it is a preferable area to consider material transport from land to coastal sea. To clarify the above mentioned problems, we would like to reexamine our sedimentological data. As the result, we clarified dispersal and depositional pattern of terrigenous fine particles, origin of high C/N ratio sediments at the outer shelf to upper slope, oceanographically controlled sedimentation, which was highly influenced by land and submarine topography, and sediment budget in this area.

2. Physiography and oceanography of study area

There are three large coastal plains in the study area (Fig. 1A). That is, Akita Plain at the north, Honjo Plain at the central, and Shonai Plain at the south. Major rivers in each plain are Omono river (annual mean water discharge; $243.50 \text{ m}^3/\text{sec}$) at Akita Plain, Koyoshi River ($72.77 \text{ m}^3/\text{sec}$) at Honjo Plain and Mogami River ($358.50 \text{ m}^3/\text{sec}$) and Aka-gawa-shin-kawa River ($74.40 \text{ m}^3/\text{sec}$) at Shonai Plain. Water discharge from these rivers showed seasonal variability and higher in early spring when snow was melted and in rainy season (late spring to early summer). These rivers and the other small rivers have transported sand and mud to the plains.

The major submarine topographic features in the study area are the north-south trended topographic highs from Tobishima Island at the south to Oga-muko-se Bank at the north, two slope basins (Tobishima Basin and Oga Basin) and wide shelf at the south of Oga Peninsula and the Mogami Trough (Fig. 1A). Shelf in the study area is wider in the northern (around Oga Peninsula) and the southern (Yamagata) area than in the central area (off Honjo to Mt. Chokai-san). There are two slope basins, Tobishima (447 m at the deepest position) and Oga Basins (537 m), between shelf and the topographic highs from Tobishima Island through Shin-guri Bank (135 m at the shallowest position) to Oga-muko-se Bank (96

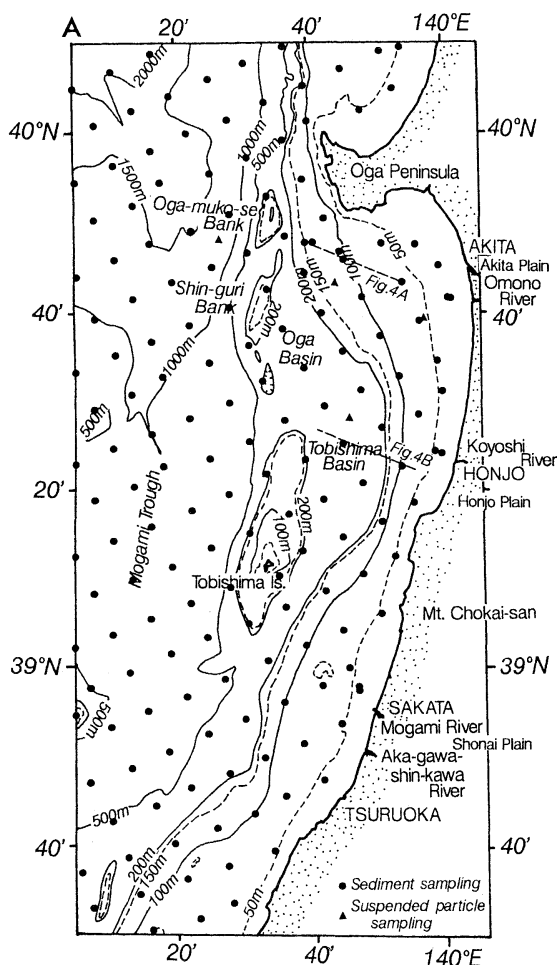


Fig. 1. Sampling stations of bottom sediments (solid circles) and of suspended particles (solid triangles) with bathymetry (A) and seismic survey lines (B).

m). They are separated by a small topographic high with NE-SW trend from Tobishima Island. Mogami Trough is the north-south trended trough with the water depth deeper than 800 m.

The Japan Sea water is divided into the surface and deep waters at the water depth of around 100–200 m. Surface water with high temperature, high salinity and low oxygen concentration originated from the Tsushima Current. The Tsushima Current inflows through the Tsushima Strait and flows northeast to northward in the region of the present study. Current velocities are higher in summer

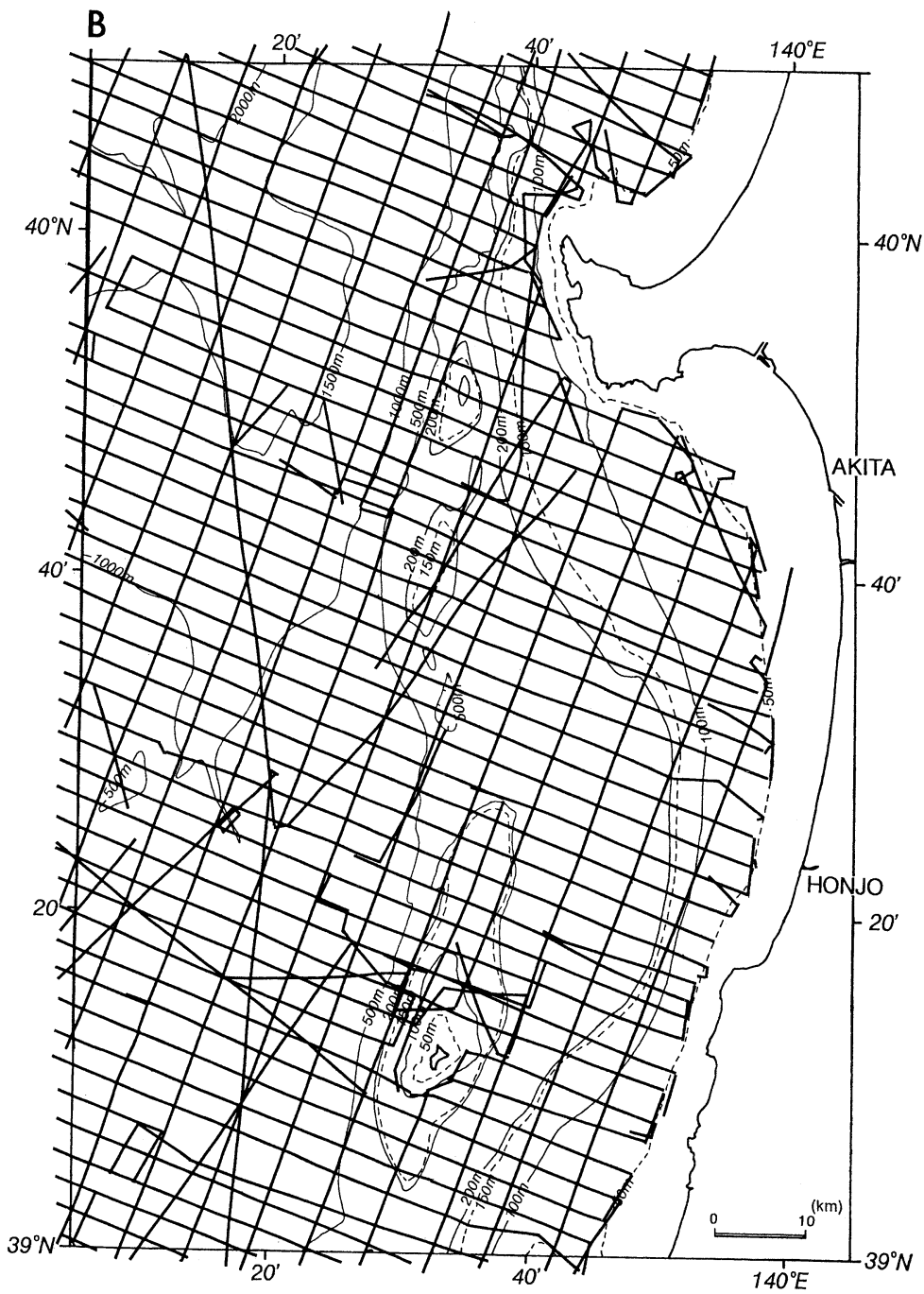


Fig. 1 B.

(0.1–0.9 knots in vector mean velocity) and in the north of Oga Peninsula (0.5 knots) than in winter (0–0.6 knots) and in the southern area (0.1–0.3 knots) (Japan Oceanographic Data Center, 1979, 1991). Temperature and salinity of surface water change seasonally (YAMAMOTO and IMAI, 1990). Surface temperature becomes higher, and salinity becomes lower landward. Remarkable decrease of surface water salinity is found in spring corresponded to large input of snow melt fresh water. Deep water, which called the Japan Sea Proper Water (JSPW), has low temperatures (0–1°C), rather low salinities (34.0–34.1 PSU) and high oxygen concentration (5.0 to more than 7.0 ml/l) (SUDA, 1932; NITANI, 1972).

3. Materials and methods

Total 130 of surface sediment samples from Akita area and 39 samples from Niigata-Yamagata area, both of which included more offshore area such as Mogami Trough and Sado Ridge, were collected by a Kinoshita-type grab sampler (Fig. 1A) during the cruises of GH89–2 (May–July, 1989), GH90 (June–July, 1990) and GH91 (June–July, 1991) of R/V Hakurei-Marui by the Geological Survey of Japan. Sediment grain size of surface sediments was determined by sieve analysis for sand fraction (coarser than 4.5ϕ ($44\mu\text{m}$) and hydrometer analysis for mud fraction (finer than 4.5ϕ). Composition of coarse fraction (1.75ϕ (0.3 mm)– 2ϕ (0.25 mm) and 0.75ϕ (0.6 mm)– 1.0ϕ (0.5 mm) fraction) were counted under a binocular. More than 200 grains were counted for each sample.

Seismic reflection survey by using high frequency (3.5 kHz) sub-bottom profiler was conducted along the 1.7 mile intervalled NW-SE and the 3 mile intervalled NE-SW survey lines (Fig. 1B). Acoustic facies analysis was conducted for the records and thickness of the uppermost sediment layer was measured.

Temperature and salinity of surface and bottom (1.5 m above the sea bottom) water was measured by using a thermometer and bathythermograph and digital salinometer (Tsurumiseiki E-202) at the same time and station of sediment sampling to understand oceanographic background of sedimentation.

Turbidity (light transmission values) was measured by using a Sea Tech transmissometer (ST025-D) along two survey lines in June–July, 1992 during the cruise of GH92 (Fig. 2). Compositions of suspended particles collected at four stations (solid triangles in Fig. 1A) were observed by using scanning electron microscopy. Oxidation-reduction potential (ORP) of surface sediments has also measured at all stations of sediment sampling by using a digital pH meter (Denki-kagaku Co. HPH-22) with an ORP electrode.

4. Results

4-1 Oceanographic and environmental aspects of study area

Salinity and temperature of surface water became lower in coastal area than in offshore area. Distribution of surface and bottom water salinity showed wide cover of low salinity coastal water on the inner and mid shelf, especially at the northern part, indicating the influence of riverine fresh water from the Omono River. On the basis of sea bottom photography, suspended particles were higher content in coastal area. Profiles of light transmission values across shelf indicated higher concentration of suspended particles in coastal water than in offshore water (Fig. 2). Profiles also indicated the occurrence of three layers of high suspended particle concentration. The first one is a surficial layer mainly found in the inner to mid shelf. Second one is an intermediate layer located at the water depth of 60–80 m. Third one is found at the just above the sea floor. On the basis of preliminary observations of grain compositions of each layer by using electron microscopy, grains in surficial and intermediate layers were mainly composed by biogenic grains but those in bottom layer were composed by mineral grains.

Oxidation-reduction potential (ORP) of surface sediments became lower values in muddy sediments than in sandy sediments and showed minus values, indicating reduction conditions, in muddy basin sediments in Tobishima Basin. Also, ORP was higher in deeper trough, because of the influence of the Japan Sea Proper Water (JSPW) containing higher concentration of oxygen.

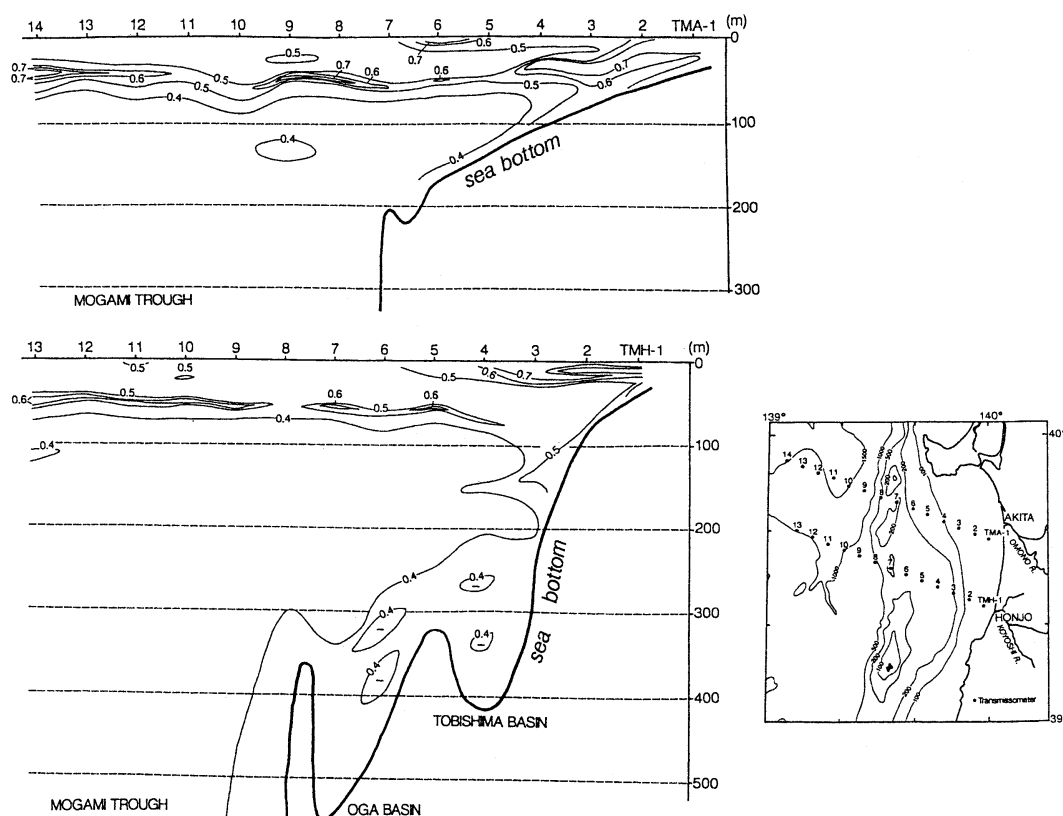


Fig. 2. Distribution of beam attenuation coefficient (C) values across the shelf. Three high concentration layers were recognized. Relation between C and S (suspended material concentration) is: $S = 1.15 (C - 0.358)$ (BISHOP, 1986).

4-2 Sediment grain size and compositions

Spatial distribution of sediment grain size (Fig. 3) indicated that Akita shelf was a typical graded-shelf where sediment grain size became finer offshoreward with increasing water depth. That is, well-sorted fine sand indicating wave effects distributed at the water depth shallower than 40 m. Coarser medium sand and gravels and rock exposures were found along the southern coast of Oga Peninsula and on a north-south trended topographic high from Tobishima Island to Oga-muko-se Bank. Grain size became finer offshoreward, and very fine sand and silt widely covered the mid-outer shelf. Finer clay was deposited in Tobishima and Oga Basins and Mogami Trough. Only the exception of graded-shelf in this area was found on the outer shelf at the south to southwest of Oga Peninsula, where very fine sand was distributed. This sand contained high

percentage of mud and was poorly sorted.

Surface sediments of Yamagata shelf just south of Akita shelf were mainly composed of sandy sediments. That is, well-sorted fine sand distributed in coastal area and fine-medium sand widely covered the mid-outer shelf. Fine grained sediments such as very fine sand and silt were only found at the mid shelf off Kisakata and at just offshore of Mogami River mouth.

Compositions of coarse fraction of sediments indicated that quartz, lithic fragments, pumice and biotite were dominant in sandy coastal sediments. Glauconite pellets (TRIPLEHORN, 1966) were commonly found in sandy sediments on the outer shelf off Akita. Silty sediments at the outer shelf to upper slope contained a large number of plant debris and pumice. Sand grains were very few and its compositions showed very wide diversity in

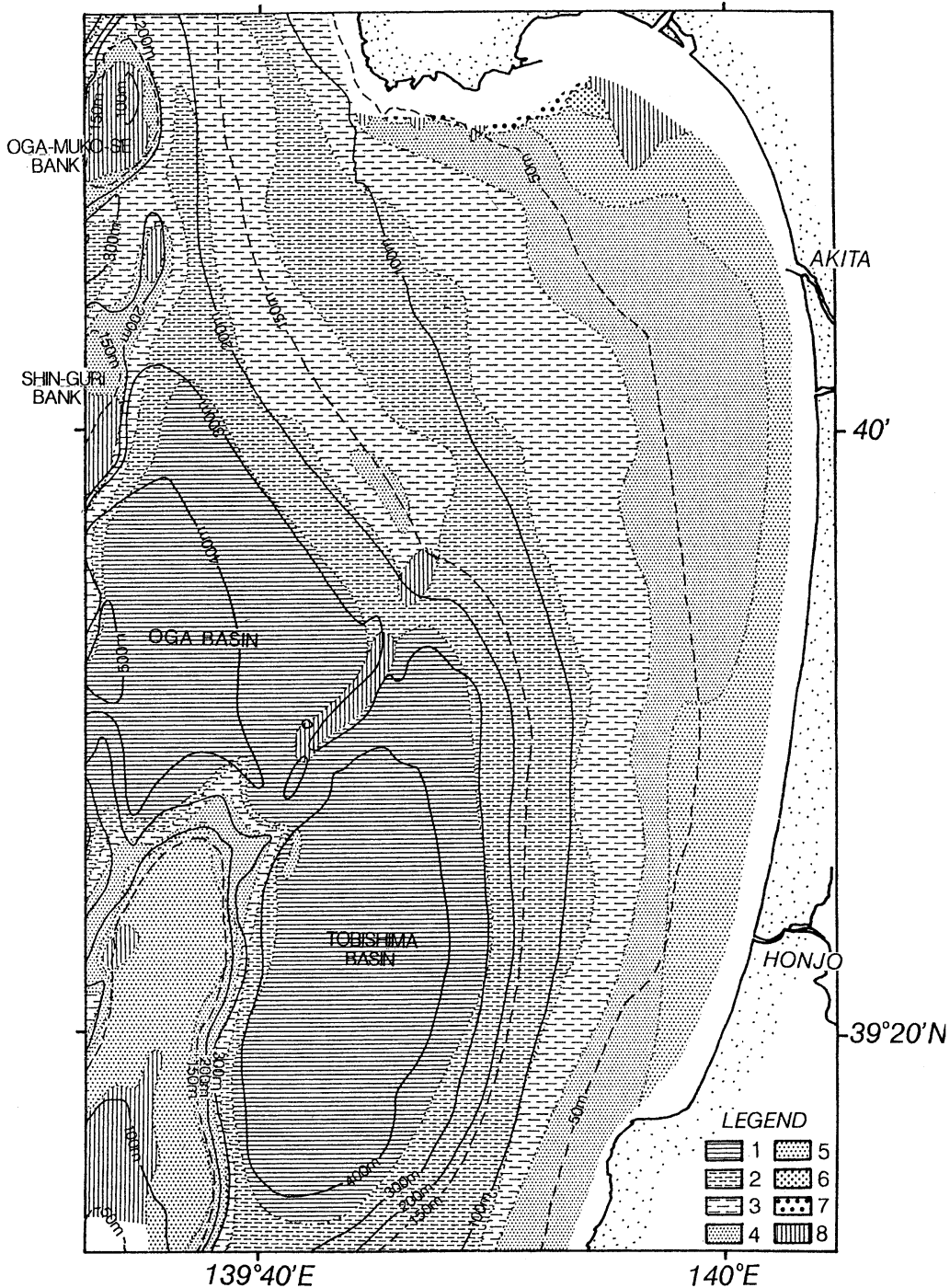


Fig. 3. Sediment distribution off Akita. 1; clay ($Md \phi > 8$), 2; fine silt (6-8), 3; coarse silt (4-6), 4; very fine sand (3-4), 5; fine sand (2-3), 6; medium sand (1-2), 7; gravel (< -1), 8; rocky bottom.

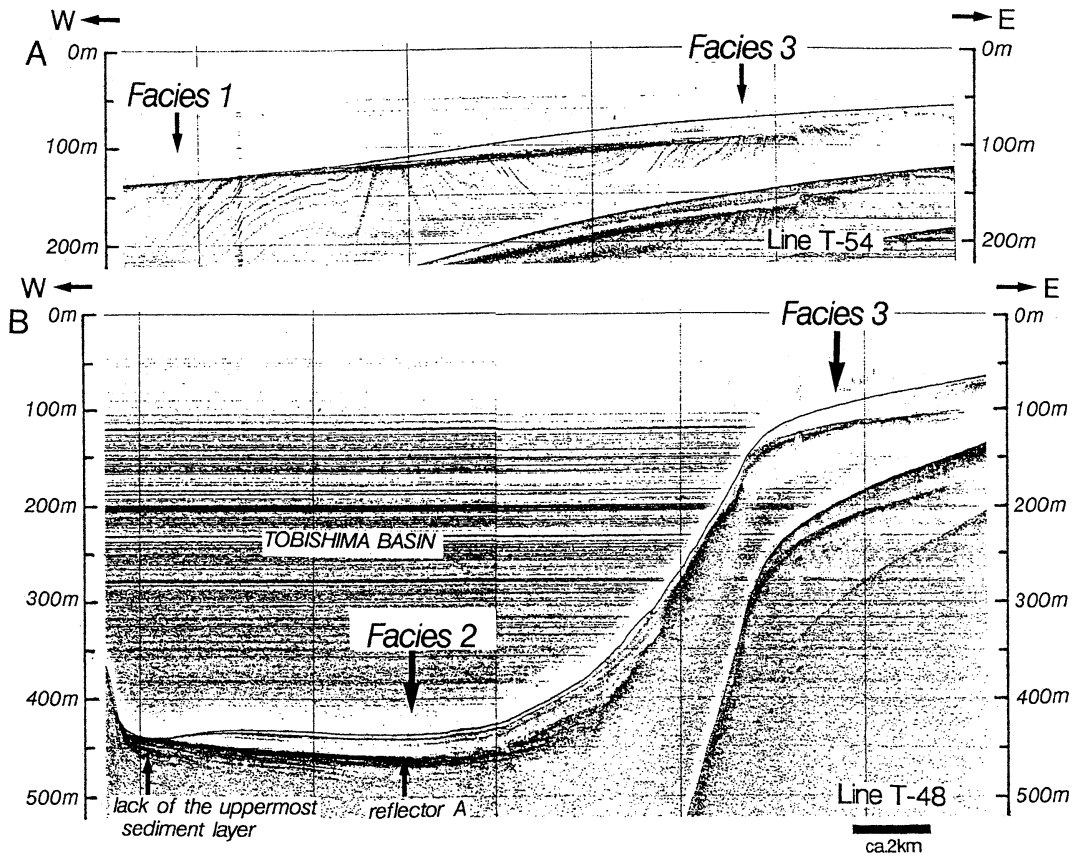


Fig. 4. Seismic (3.5kHz) profiler records on the shelf off Akita (A) and at the shelf-slope off Honjo (B). A: The uppermost sediment (transparent) layer becomes thinner offshoreward and absent at the outer shelf indicating no or very low sedimentation rate. Tilted and folded sediment layers are observed below the transparent layer. B: The transparent layer on the shelf continues to the uppermost sediment layer in Tobishima Basin. Stratified or prolonged facies was found below reflector A.

clayey sediments.

4-3 Acoustic facies and sediment thickness

Three acoustic (seismic) facies in high frequency (3.5kHz) sub-bottom profiler records were recognized in the study area. The characteristics of acoustic facies were influenced by grain size and degree of consolidation of sediment layers, and by morphology of sea bottom and boundaries between sediment layers (NARDIN *et al.*, 1979). Also, some acoustic facies were formed by a specific sedimentation process such as slope failure. Therefore, distribution of acoustic facies gives us good information on sedimentation.

Acoustic characteristics and spatial distribu-

tion of each acoustic facies were described below. On the shelf, distinct (Facies 1), which showed strong bottom return, and transparent facies (Facies 3) were found. Facies 1 was corresponded to sandy or gravelly or rocky bottoms. This facies was found in the inner shelf and at the outer shelf of the south to southwest of Oga Peninsula and on the topographic highs from Tobishima Island to Ogamuko-se Bank. Stratified facies (Facies 2) was commonly found in basins and trough where hemipelagic muddy sediments and some turbidites were deposited. The other acoustic facies was transparent facies (Facies 3), which had no or very poor internal reflectors and with weak bottom return. This facies was

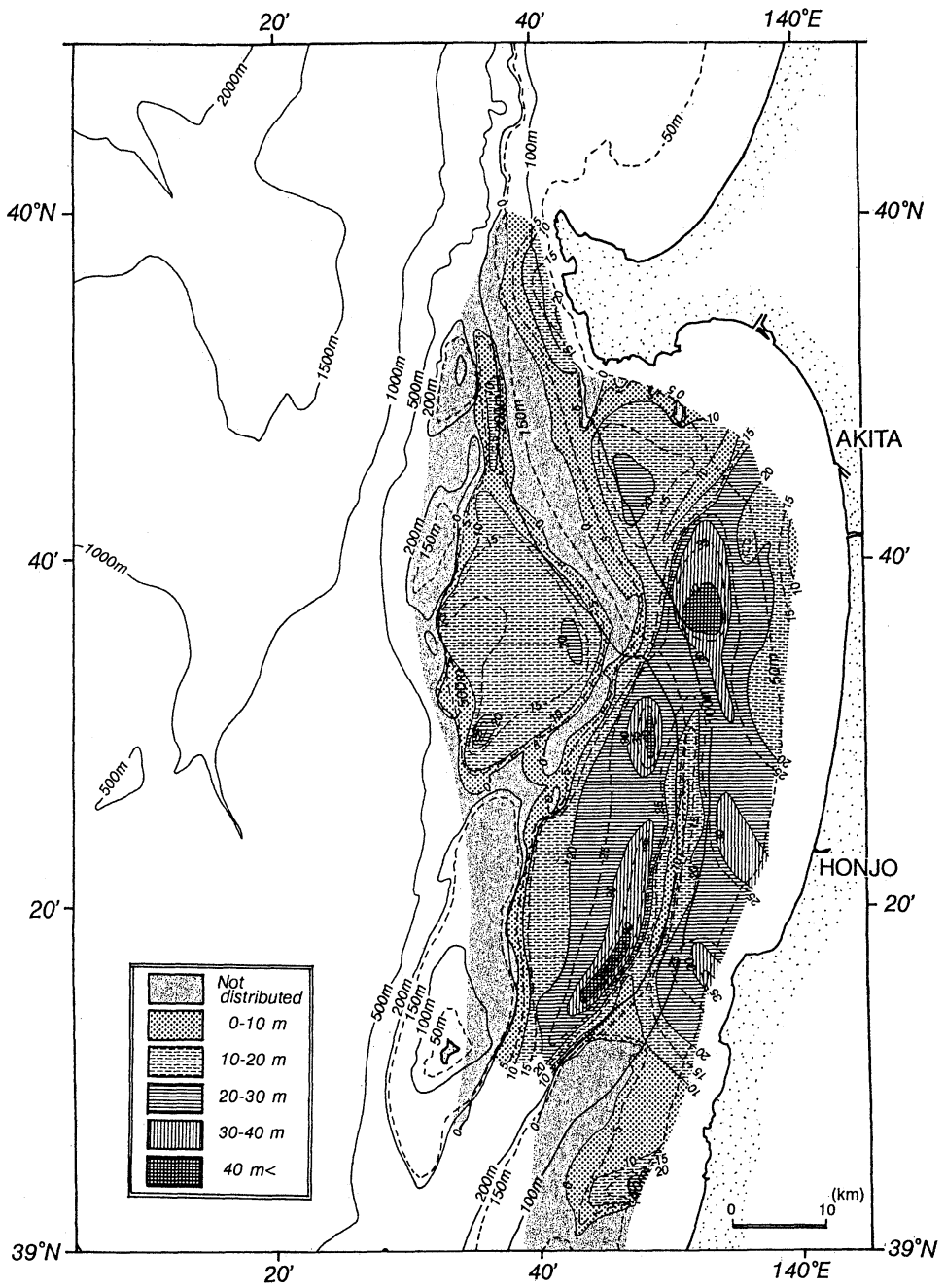


Fig. 5. Thickness distribution of the uppermost sediment layer based on seismic (3.5kHz) profiler records.

widely recognized in shelf to slope areas.

An acoustically transparent layer on the shelf (Fig. 4A) could be traced to the uppermost sediment layer in Tobishima Basin (Fig. 4B). The uppermost sediment layer showed acoustically transparent facies and overlaid the sediment layer with well stratified or prolonged acoustic facies indicating occurrence of coarser sediments. Spatial distribution of the thickness of transparent layer was shown in Fig. 5. The map showed a thickly deposited sediment belt from the west of Akita to the northern part of Tobishima Basin and thicker deposition on the outer shelf at the west of Akita (thickness; more than 40 m). Western end of the belt was limited by a NNE-SSW trended topographic high, but some of sediments flowed over the high and deposited more westward. Seismic records (Fig. 4A) clearly indicated that the layer covered the older and inclined sediment layer at the shelf and the older layer exposed sea floor at the outer shelf of the southwest of Oga Peninsula. Thickness became thinner at the outer shelf to upper slope area off Honjo (Fig. 5). Thickest distribution was found at the eastern foot of slope area of the southern Tobishima Basin (thickness; more than 50m).

5. Discussions

5-1 Mode of transport of terrigenous fine grained materials to offshore

Profiles of light transmission values across the Akita shelf (Fig. 2) clearly indicated the occurrence of three high suspended particle concentration layers. Because higher concentration is found coastal area than in offshore area, source of suspended materials was located coastal side. Grain compositions of each layer suggested that terrigenous fine materials had been transported through the high concentration layer just above the sea floor (bottom nepheloid layer).

Bottom nepheloid layer sometimes burdicate or detached from sea floor near the inflection points of bathymetry (water depth was around 150 m; Fig. 2). Major thermocline, which was boundary between surface water and deep water (the Japan Sea Proper Water), located almost the same water depth. As

salinity of bottom water was not changed largely between the water mass boundary, the thermocline formed density boundary. A part of bottom nepheloid layer detached from sea floor and flowed offshoreward along the surface of the density boundary.

Suspended material concentration and thickness of high concentrated layer was higher in Tobishima and Oga Basins than in Mogami Trough (Fig. 2). Therefore, most of terrigenous fine grained particles were trapped and deposited in two basins.

5-2 Dispersal pattern of terrigenous fine grained materials from Omono River

Larger grains with lower specific gravities than mineral grains such as plant debris were transported with smaller mineral grains. Also, easier transported particles such as biotite were transported with smaller grains, because of their specific morphologies (IKEHARA *et al.*, 1988). Therefore, concentration of these grains indicated the depositional areas and transport directions of smaller mineral grains. Especially, plant debris was a clearly land source component (IKEHARA *et al.*, 1988; IKEHARA, 1991). Then, there is a possibility that the distributions of each component showed the transport paths of sediment particles from land to offshore.

On the basis of relation between spatial distributions of composition of coarse fraction and sediment grain size, some of sand-sized components were used for tracers of transport of finer grains. For example, plant debris was concentrated in silt (Fig. 6), then plant debris was used for a tracer of terrigenous silt grains. Similar concentration of plant debris in silty sediments was also found at the sediments of Niigata shelf (IKEHARA *et al.*, 1994a). HOSHINO (1958) showed that plant debris was concentrated along the boundary of water masses. But at the offshore of Akita, there was no relation between water mass boundary shown in salinity distribution and concentration of plant debris. On the other hand, biotite grains were dominant in very fine sand-coarse silt, especially at the west of older Omono River mouth (Fig. 6). Biotite has nearly the same specific gravity (2.7-3.3) as quartz (2.65). Biotite, however, is easily transported by currents, because

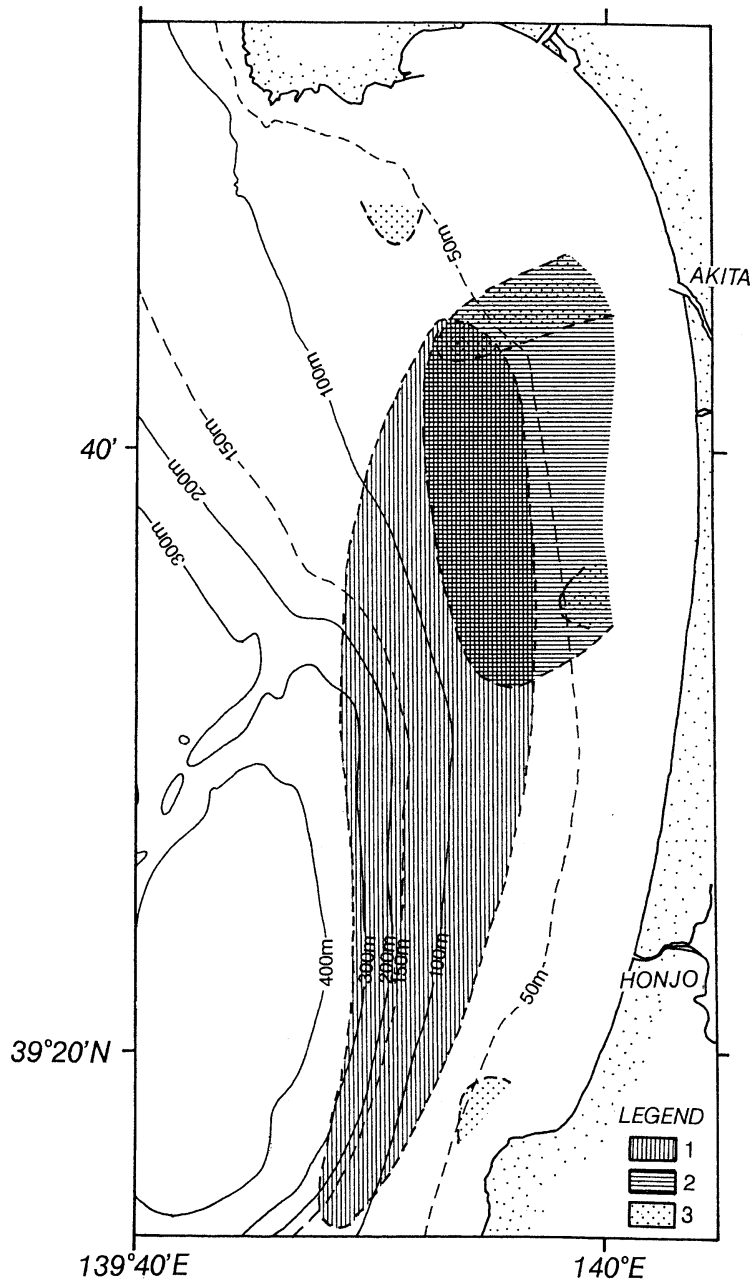


Fig. 6. Spatial distribution of concentrated areas of plant debris, biotite and pumice in coarse fraction (0.25–0.3mm in diameter). 1; plant debris (higher than 30% in composition of coarse fraction), 2; biotite (higher than 10%), 3; pumice (higher than 30%).

of their specific morphology (planar shape). And there are some reports on relation between biotite concentration and current systems (IKEHARA, 1991). Boundary in grain size between suspended load and traction load in state of sediment transport was found in very fine sand. Therefore, biotite concentration was a tool for tracing the transport path of the coarsest suspended particles. Concentration of pumice grains of the same size fraction were higher in very fine to fine sand, and very low in finer than very fine sand (Fig. 6). Distribution of pumice indicated that the grains were not supplied through the air (air fall pumice), but through the rivers or coastal erosion.

Judging from distribution patterns of coarse fraction of these three components (Fig. 6), sediment particles discharged from Omono River were transported westward and then southward. As mentioned earlier, terrigenous fine grained materials were transported offshoreward through the bottom nepheloid layers. Because directions of particle transport were controlled by those of bottom currents and sediments recorded the long-term averaged oceanographic conditions which were difficult to observe by normal oceanographic observations (IKEHARA, 1992), sediment transport paths showed the long-term averaged directions of bottom currents in this area.

Reported values of C/N ratio of surface sediments in this area (NOMURA, 1992) indicated high ratio (around 12 in weight ratio) for silty sediments at the outer shelf to upper slope. That means higher supply of terrigenous organic matter to the outer shelf-upper slope. As shown in Fig. 6, plant debris was dominant in coarse fraction in this area. Combined with above mentioned sediment transport path, terrigenous organic matters from Omono River and surrounding areas were transported and deposited at the outer shelf to upper slope and formed the sediments with high C/N ratio. Oxidation-reduction potential indicated minus values in this area showing reductional conditions. Decomposition of terrigenous organic matter supplied to the area used oxygen in bottom water and made a reductional condition.

5-3 Oceanographic control of modern sedimentation

Sediment grain size was affected by the oceanographic conditions such as currents, waves and water mass distribution (HOSHINO, 1958; IKEHARA, 1993). Although deposition of muddy sediments was controlled by the amount of supply and of removal to and from an area, muddy sediments were generally distributed under lower energy environments. On the contrary, sandy sediments were distributed along the current path (IKEHARA, 1992, 1993). Because muddy sediments were predominant at the offshore of Akita except of the outer shelf at the southwest-west of Oga Peninsula (Fig. 3), Akita area is thought to be under low energy environments. On the other hand, sandy sediments widely covered Yamagata shelf just south of Akita shelf. There are some large rivers in Akita (Omono and Koyoshi River) and Yamagata (Mogami and Akagawa-shinkawa River) areas. Annual mean discharges of suspended materials from these rivers in Akita area were smaller than those in Yamagata area. Then, it is difficult to explain the difference in shelf sediment types by the difference in the supply of fine grained materials to the shelves. Currents and waves were major factors for sediment reworking. That is, strong currents and waves agitated sea bottom and reworked fine grained sediments to downstream or offshore direction. Therefore, there is a possibility that difference of sediment types between two areas has been controlled by the intensity of currents and/or waves.

Two topographic effects controlling current and wave conditions are thought to be occurred in these areas. First effect is the occurrence of offshore topographic highs. There is a north-south trended topographic high from Oga-muko-se Bank to Tobishima Island off Akita shore, but no topographic high at the outer shelf off Yamagata shore. The topographic high will play a barrier to intrude currents and large waves from offshore and make a low energy and stagnant condition at the back of the barrier. Under such condition, riverine fresh water easier extended and formed low salinity coastal water in the inner shelf. Because coastal water, as mentioned

earlier, contained higher amount of suspended materials, muddy sediments were deposited.

Shoreline morphology was another topographic effect (IKEHARA, 1993). That is a large projection, Oga Peninsula, is located just north of Akita and forms an open bay (Akita Bay) between the Peninsula and Akita coast. Isobath contours curved into eastward. The bathymetric condition prevents the direct invasion of the currents to the bay and forms preferable condition to develop coastal water. The condition was corresponded to type A-1 or A-2 of modern mud deposition (effects of topographic barrier) of IKEHARA (1993). Occurrence of bedforms such as ripples, and of well-sorted sandy sediments and lack of modern muddy sediments was indexes for occurrence of bottom current along the shelf edge of San'in coast (IKEHARA, 1992). Although there were no ripples and well-sorted sediments on Yamagata shelf, surface sediments with low mud contents along the outer shelf off Yamagata indicated the occurrence of currents removing fine grained particles throughout the Yamagata shelf. On the other hand, lack of the uppermost sediment layer was found along the shelf edge of Akita coast (Fig. 4A). Glauconite pellets, which were autochthonous minerals and indicated non-deposition or very low sedimentation rates, were found in this zone. These facts indicated that the currents flowed over Yamagata shelf and along the outer shelf off Akita.

Major current system in Yamagata and Akita areas is thought to be the Tsushima Current. The Tsushima Current has flowed northward along the shelf edge. Therefore, fine grained particles, which did not deposit on Yamagata shelf and on the outer shelf off Akita, might be transported northward. A concentrated area of plant debris in surface sediments occurred along the west coast of Oga Peninsula. Thick mud deposition also found in this area. Because of no large source of plant debris and fine grained materials in Oga Peninsula, there is a possibility that some of terrigenous materials from Omono River have been transported northward through Akita shelf along the southern coast of Oga Peninsula.

5-4 Sediment accumulation and budget

On the basis of thickness distribution of the uppermost sediment layer (Fig. 5), volume of deposited sediments was calculated to be 15.6 billion tons. Judging from age estimation of underlined sediments of the uppermost sediment layer in Tobishima Basin (WATANABE, 1994) and depositional pattern in seismic records, the uppermost sediment layer was thought to be deposited after the last glacial maximum and during latest Pleistocene-Holocene ages. To calculate annual volume of sediment deposition, we used 10,000 years for duration of sediment formation. Therefore, 1.56 million tons of sediments per year were deposited in the survey area.

By the way, there was a higher sea level stage at 5,500–6,000 years before present (the Jomon Transgression), when the sea level was 2–6 m higher than the present level (OTA *et al.*, 1982). At the Akita Plain, the shoreline retreated 3.5 km from the present shoreline at 5,500 years before (MORIWAKI, 1982). During the higher sea level stage, location of river mouths retreated to landward and terrigenous muddy sediments deposited at more inshore area (below the present coastal plains) (MORIWAKI, 1982; Geological Research Group of Akita University on the Nihonkai Chubu Earthquake 1983, 1986). In this study, because of lack of enough data for calculation of sediment volume deposited under modern coastal plain, we can know only the volume of sediments deposited offshore area. Therefore, true volume of deposited sediments was larger than the value mentioned above.

Values of annual mean water discharges and suspended sediment content of each major river in the study area during 1969–1973 were edited by Japan Rivers Association (1974). By using these data, total amount of suspended sediment supply to this area was considered to be 0.78 million tons/year from Omono River and 0.05 million tons/year from Koyoshi River. Including with discharge from small rivers and coastal erosion, suspended sediments of around 0.8–0.9 million tons/year had been transported to this area and deposited. Because of the occurrence of topographic highs from Tobishima Island to Oga-muko-se Bank and of slope

Table 1 Sediment and Organic Carbon Accumulation in the Japan Sea

Area ($\times 10^{10} \text{m}^2$)	Averaged Sed. Rate ($\text{cm}/10^3 \text{y}$)	Sediment Accuml. Rate ($\times 10^{-3} \text{g}/\text{cm}^2/\text{y}$)	Sed. Volume with water ($\times 10^6 \text{m}^3/\text{y}$)	Sediment Accuml. Volume ($\times 10^6 \text{t}/\text{y}$)	Organic-C Content (wt.%)	Org-C Mass Accuml. Rate ($\times 10^{-5} \text{g}/\text{cm}^2/\text{y}$)	Organic-C Accuml. Weight ($\times 10^4 \text{t}/\text{y}$)	
Tsushima Basin	3.85	14.7	5.88	5.66	2.26	1-2	5.88-11.8	2.26-4.52
SW Yamato Basin	4.47	12.8	5.76	5.72	2.57	1-2	5.76-11.5	2.57-5.14
Oki Trough	0.88	16.7	6.68	1.46	0.58	2	13.4	1.16
Toyama Deep-sea Fan	1.22	12	6	1.46	0.73	1-2	6-12	0.73-1.46
Marginal Terrace (off Tottori)		(10-45)	(8.6-38.7)	0.99	0.85	2	(17.2-77.4)	1.7
Toyama Bay	0.6	> 30 (35-40)	> 15 (17.5-20)	> 1.8 (2.1-2.4)	> 0.9 (1.05-1.2)	1-2	> 1.8-3.6 (2.1-4.8)	> 0.9-1.8 (1.05-2.4)
Sado Basin	0.1	> 30 (140-200)	> 17 (77-110)	> 0.3 (14-20)	> 0.17 (7.7-1.1)	1.7	> 0.5 (1.3-1.9)	> 0.29 (13-18.7)
Niigata Shelf				1.56	1.33	1.5		1.99
Off Akita (shelf-basin)	0.4			2.6	1.56	1.5-2		2.34-3.12

basins, almost of all terrigenous materials have been trapped to shelf to basin area. Then, around 0.7 million tons of sediments have been transported from the other area. There are two large sources near the study area; one is Noshiro River, which have supplied 0.6 million tons of sediments per year, located at the north of the study area, and another is Mogami River, which have supplied 2.4 million tons of sediments per year, located at the south of the study area. Major current system around the study area is controlled by the Tsushima Current, of which flow direction is northward. Then, it is hardly to transport fine grained materials southward from Noshiro River against the major current system. Therefore, most probable major source of terrigenous materials is Mogami River. Judging from the annual mean sediment discharge from Mogami River and the remain between sediment deposition and supply from Akita area, 40-50% of suspended sediments from Mogami River have been transported northward and deposited in the southern part of Tobishima Basin.

5-5 Significance of shelf-basin area in sediment budget of Japan Sea

Sedimentation rates in offshore basins of Japan Sea such as Tsushima and Yamato Basins and Oki and Mogami Troughs were considered to be 10-25 cm/1000 years (MASUZAWA, 1987; IKEHARA *et al.*, 1994b), and became higher landward (IKEHARA *et al.*, 1994b). Although eolian input has been an important factor for

sedimentation rates in Japan Sea (MASUZAWA, 1991), spatial difference in sedimentation rates was influenced by supply of terrigenous materials. By using the sedimentation rates and areas of each basin, annual accumulation of sediments was calculated in Table 1. On the other hand, IKEHARA *et al.* (1994a) inferred annual accumulation on Niigata shelf, which is another muddy shelf in Japan Sea, as 1.33 million tons per year from the thickness distribution of shelf sediments. Estimated value of sediment accumulation in Akita area was the same order as those of Niigata shelf and of large offshore basins such as Tsushima and Yamato Basins and a little larger than those of small offshore basins such as Oki Trough. That means high rate of material supply to the shelves and adjacent basins from land supported higher sedimentation rates and most of terrigenous fine particles were thought to be deposited in this area.

Reported values of organic carbon content in shelf-slope sediments (1.5-2 wt. %) were a little higher than those in offshore basin sediments (0.8-2 wt. %; HAMAGUCHI and OTA, 1953; HAMAGUCHI *et al.*, 1954; NOMURA, 1992). By using accumulated sediment volume and organic carbon content, 20-30 thousand tons of organic carbon had been deposited in an offshore large basin and on a muddy shelf-slope area in a year. Because of higher sedimentation rates, larger volume of organic carbon was deposited in shelf-slope mud is very important to consider material (carbon) cycles in Japan

Sea.

6. Conclusions

Profiles of concentration of suspended materials, spatial distributions of sediment grain size and of sediment compositions, and thickness distribution of the uppermost sediment layer suggested the following remarks.

- 1) Most of terrigenous fine grained materials had been transported through bottom nepheloid layer and deposited in shelf-slope area off Akita.
- 2) Concentration area of plant debris of 0.25–0.3 mm in diameter was well-concordant with silt distribution. Therefore, sand-sized plant debris was thought to be a useful tracer of terrigenous silt.
- 3) Deposition of terrigenous organic materials in silty sediments formed high C/N ratio sediments along the outer shelf to slope area. High rate of organic material supply resulted in low oxidation-reduction potential (reductional condition).
- 4) Land and submarine topography might be influenced to current systems and caused the difference in distributions of bottom sediment types between Akita and Yamagata shelves. The Tsushima Current, which flows along the shelf edge off Akita, has prevented mud deposition on Yamagata shelf and on the outer shelf at the southwest of Oga Peninsula.
- 5) Total 1.56 million tons of muddy sediments had been deposited in this area in a year. Compared with annual mean discharge from major rivers around this area, almost of materials supplied from Omono and Koyoshi Rivers and 40–50% from Mogami River had been deposited in this area.
- 6) Judging from annual mean volume of sediment accumulation and organic carbon content of surface sediments in several basins of Japan Sea, shelf-slope mud is very important for consideration of material cycles in Japan Sea.

Acknowledgements

We express our hearty thanks to officers, crew and scientists of the R/V Hakurei-Marui for their kind help throughout the surveys. Acknowledgements are due to Mr. Mahito WATANABE of the Geological Survey of Japan

and Mr. Masahiro NOMURA of Niigata University for providing us the results of diatom analysis and organic carbon content measurements. We are grateful to Drs. Masafumi ARITA and Yoshiki SAITO of the Geological Survey of Japan, Prof. Tetsuo YANAGI of Ehime University and Dr. Yutaka ISODA of Hokkaido University for their fruitful comments and suggestions. This work was supported by the special research program, marine geological investigation around the continental shelf areas in the central part of the eastern Japan Sea, of the Geological Survey of Japan.

References

- ALEXANDER, C. R., D. J. DEMASTER and C. A. NITTRouer (1991): Sediment accumulation in a modern epicontinental-shelf setting: The Yellow Sea. *Marine Geol.*, **98**, 51–72.
- BISHOP, J. K. B. (1986): The correction and suspended particulate matter calibration of Sea Tech transmissometer data. *Deep-sea Res.*, **33**, 121–134.
- DIAZ, J. I., A. PALANQUES, C. H. NELSON and J. GUILLÉN (1996): Morpho-structure and sedimentology of the Holocene Ebro prodelta mud belt (north-western Mediterranean Sea). *Continental Shelf Res.*, **16**, 435–456.
- Geological Research Group of Akita University on the Nihonkai Chubu Earthquake, 1983(1986): Late Quaternary geology and development of the coastal alluvial plain of Akita Prefecture, northeast Japan. *Mem. Geol. Soc. Japan*, **27**, 213–235.
- HAMAGUCHI, H. and N. OTA (1953): Chemical investigations of deep-sea deposits (XIV). On the chemical composition of deep-sea deposits from Japan Sea. *J. Chem. Soc. Japan*, **74**, 761–764.
- HAMAGUCHI, H., M. TATEMOTO and J. ITAYA (1954): Chemical investigations of deep-sea deposits (XIX). On the content of Ti, Fe, Mn, P and organic carbon in the sediments from Japan Sea (2). *J. Chem. Soc. Japan*, **75**, 119–121.
- HOSHINO, M. (1958): The shelf sediments in the adjacent seas of Japan. *Monogr. Assoc. Geol. Collab.*, **7**, 1–41.
- IKEHARA, K. (1991): Modern sedimentation off San'in district in the southern Japan Sea. In: *Oceanography of Asian Marginal Seas*, ed. K. Takano, Elsevier Oceanography Series, 57, Elsevier, Amsterdam, 143–161.
- IKEHARA, K. (1992): Influence of surface water circulations on the sea bottom in the southern Japan Sea. *La mer*, **30**, 105–118.

- IKEHARA, K. (1993): Modern sedimentation in the shelf to basin areas around southwest Japan, with special reference to the relationship between sedimentation and oceanographic conditions. *Bull. Geol. Surv. Japan*, **44**, 283-349.
- IKEHARA, K., D. BI, Y. KINOSHITA and T. SUZUKI (1988): Heavy mineral distributions in the surface sediments of the Osumi Strait, south of Kyushu, Japan. *J. Sed. Soc. Japan*, **29**, 9-18.
- IKEHARA, K., H. KATAYAMA and T. NAKAJIMA (1994a): Sedimentological map of the vicinity of Awashima (with explanatory notes). *Marine Geology Map Series*, 42, Geological Survey of Japan, Tsukuba, 56p.
- IKEHARA, K., K. KIKAWA, H. KATAYAMA, and K. SETO, (1994b): Late Quaternary paleoceanography of the Japan Sea; a tephrochronological and sedimentological study. *Proc. 29th Int'l. Geol. Congr. Part B, VSP, Utrecht*, 229-235.
- Japan Oceanographic Data Center (1979): *Marine Environmental Atlas, Currents-adjacent seas of Japan*. 71p.
- Japan Oceanographic Data Center (1991): *Statistic Atlas of Currents adjacent seas of Japan-seasonal characters*. JP011-91-1, 165p.
- Japan Rivers Association (1974): *Nihon Kasen Suishitsu Nenkan* (1974). Sankaido, Tokyo, 885p.
- LESUEUR, P. and J. P. TASTET (1994): Facies, internal structures and sequences of modern Gironde-driven muds on the Aquitaine inner shelf, France. *Marine Geol.*, **120**, 267-290.
- MASUZAWA, T. (1987): Early diagenesis in deep-sea sediments of the Japan Sea: Type, controlling factor, and diffusive flux. *J. Earth Sci., Nagoya Univ.*, **35**, 249-267.
- MASUZAWA, T. (1991): Bottom sediments around Japan and Kosa. In: *Kosa*, ed. Res. Inst. Water Sci., Nagoya Univ., Kokon-shoin, Tokyo, 216-225.
- MILLIMAN, J. D. (1995): Sediment discharge to the ocean from small mountainous rivers: The New Guinea example. *Geo-Marine Lett.*, **15**, 127-133.
- MILLIMAN, J. D., Y.-S. QIN, M.-E. REN and Y. SAITO (1987): Man's influence on the erosion and transport of sediment by Asian rivers: The Yellow River (Huanghe) example. *J. Geol.*, **95**, 751-762.
- MILLIMAN, J. D. and P. M. SYVITSKI (1992): Geomorphic/tectonic control of sediment discharge to the ocean: The importance of small mountainous rivers. *J. Geol.*, **100**, 522-544.
- MORIWAKI, H. (1982): Geomorphic development of Holocene coastal plains in Japan. *Geogr. Rep. Tokyo Metropol. Univ.*, **17**, 1-42.
- NARDIN, T. R., F. J. HEIN, D. S. GORSLINE and B. D. EDWARD (1979): A review of mass movement processes, sediment and acoustic characteristics, and contrasts in slope and base-of-slope systems versus canyon-fan-basin floor systems. In: *Geology of Continental Slopes*, ed. DOYLE L. J. and O. H. PILKEY, Soc. Econ. Paleontol. Mineral., Spec. Publ., **27**, 61-73.
- NIITANI, H. (1972): On the deep and bottom waters in the Japan Sea. In: *Research in Hydrography and Oceanography*, ed. SHOJI, D. Hydrographic Department of Japan, 151-201.
- NOMURA, M. (1992): Carbon and nitrogen contents of surface sediments off Yamagata and Akita Prefecture. In: *Preliminary Reports of Marine Geological Investigation around the Continental Shelf Areas in the Central Part of the Eastern Japan Sea, FY1991*, ed. OKAMURA, Y., Geological Survey of Japan, 197-202.
- OTA, Y., Y. MATSUSHIMA and H. MORIWAKI (1982): Notes on the Holocene sea-level study in Japan-On the basis of "Atlas of Holocene Sea-level Records in Japan". *The Quat. Res. (Daiyonkikenkyu)*, **21**, 133-143.
- PUJOS, M. and O. JAVELAUD (1991): Depositional facies of a mud shelf between the Sinu river and the Darien Gulf (Caribbean coast of Colombia): environmental factors that control its sedimentation and origin of deposits. *Continental Shelf Res.*, **11**, 601-623.
- SUDA, K. (1932): On the bottom water in the Japan Sea (preliminary report). *J. Oceanogr.*, **4**, 221-241.
- TRIPLEHORN, D. M. (1966): Morphology, internal structure, and origin of glauconite pellets. *Sedimentology*, **6**, 247-266.
- WATANABE, M. (1994): First occurrence levels of *Pseudoemotia doliolus* in gravity cores (preliminary report). In: *Preliminary Reports of Marine Geological Investigations around the Continental Shelf Areas in the Central Part of the Eastern Japan Sea, FY1991*, ed. Y. OKAMURA, Geological Survey of Japan, 203-205.
- YAMAMOTO, K. and M. IMAI (1990): Physical oceanography, off Ou coast. In: *Coastal Oceanography of Japanese Islands, Supplementary Volume*, ed. Coastal Oceanography Research Committee, Oceanographic Society of Japan, Tokai Univ. Press, 805-819.

Received January 13, 1996

Accepted May 20, 1996

Separation of the Tsushima Current from the Kuroshio: A numerical study with an idealized geometry

Soo Yong NAM*, Moon-Sik SUK*, Inkwon BANG*, Kyung-II CANG*
and Young-Ho SEUNG**

Abstract: The dynamics on the separation of the Tsushima Current from the Kuroshio is studied using a three dimensional primitive equation model with an idealized domain which consists of a continental shelf and a marginal sea in the north and a deep ocean in the south with a stepwise topographic change between them. The model ocean is vertically stratified initially and a sinusoidal wind stress is applied only over the deep ocean to establish an anticyclonic circulation. For a weakly inertial case with a zonally oriented shelf break, a part of the western boundary current is separated in the eastern part of the continental shelf, the western rim of an island which the marginal sea enters the marginal sea, which differs from a barotropic model result predicting the separation along the western wall of the continental shelf. Numerical experiments show that the branching position is controlled by the orientation of the shelf break and the nonlinearity of the western boundary current. On the other hand, the volume transport of the inflow into a marginal sea is little affected by the nonlinearity of the WBC, the orientation of the shelf break and the specific topographic features of the shelf break, but by the transport of the western boundary current and the depth ratio between the marginal sea and the deep ocean as other studies suggested.

1. Introduction

The Kuroshio flows northeastward along the continental slope of the East China Sea (ECS henceforth) and part of it overruns the shelf break to form the Tsushima Current (TC henceforth) which enters the East Sea (or Sea of Japan, ES henceforth) through the Korea Strait. Its volume transport through the Korea Strait is estimated to be less than 4.0 Sv (MORIYASU, 1972; YI, 1966; MIITA and OGAWA, 1984) That is only 10% of the Kuroshio Transport in the ESC (CHIKAWA and BEARDSLEY, 1993).

There seems to be two different views about the origin of the TC; one suggests that the TC originates from the northeastern area of Taiwan and/or the Taiwan Strait (BEARDSLEY *et al.*, 1985; GUAN, 1986; HSUEH, 1986; CHAO, 1991) and the others show that it comes from the west of Kyushu Island (GUO *et al.*, 1990; LIE and

CHO, 1994; LIE *et al.*, 1993; LIM, 1971) by analyzing the hydrographic and satellite-tracked drifter data observed in the local area west of Kyushu Island. Barotropic model results show that all of the TC water comes from the northeast of Taiwan and/or the Taiwan Strait as the Kuroshio impinges on the sloping topography (CHANG, 1993; SEUNG and NAM, 1992), which seems to support the former view. A similar penetration of the Kuroshio takes place in a primitive equation model of the North Pacific (TAKANO and MISUMI, 1990), which has $1^\circ \times 1^\circ$ resolution in the horizontal and 6 levels in the vertical.

The penetrative flux into a marginal sea (MS henceforth) from the western boundary current (WBC henceforth) has been shown to be dependent on various factors. MINATO and KIMURA (1980) first quantified the flux in an idealized domain analytically using a linear frictional model. SEUNG and NAM (1992) examined the factors affecting the volume transport of the TC using a barotropic numerical model. The influx to a MS is dependent on the

* KORDI, Ansan P. O. Box 29, Seoul 425-600, Korea

** Dept. of Oceanography, INHA University, Incheon 402-751, Korea

transport of the WBC, depth ratio between a MS and a deep ocean and frictional parameterization but little affected by local winds over the continental shelf according to the above studies. CHANG (1993) pointed out that the changes in the wind stress over the deep ocean also influence the amount of influx using a barotropic model. NOF (1992) further showed analytically that the flux is a function of the latitude of the inflowing gap, the separation latitude of the Kuroshio and the stratification in the Pacific using a inviscid, inertial reduced-gravity model. No attempt has been made to investigate factors affecting the influx under a continuously stratified condition. The topographic and baroclinic influences play an important role in increasing the transport of the WBC (HOLLAND, 1973), hence likely affect the generation and the volume transport of the TC.

Although a primitive equation model (TAKANO and MISUMI, 1990) includes the ECS and the ES in its model domain the model resolution is not enough to examine the circulation in the above areas in detail. This study aims to examine the factors affecting the branching area of the WBC and the influx to a MS under a continuously stratified condition using a three dimensional numerical model. The model domain is simplified and thus made feasible to parameter studies. Model description and details of numerical experiments are described in Chapetr 2. Results of the each experiment are discussed in Chapters 3 and 4 focusing on the branching of the WBC and factors affecting the transport into a MS in Chapter 4 respectively. Chapter 5 provides a summary and discussions.

2. Model description

The numerical model used for the study is a primitive equation model by Cox (1984). The governing equations are given by the continuity and conservation of momentum and density. The rigid-lid, hydrostatic and Boussinesq approximations are used for the fomulation of the equations. Under the Boussinesq approximation, variations in density are ignored where ρ appears as a coefficient but is taken into account in the gravitational buoyancy force.

High speed external gravity waves are filtered out due to the rigid-lid approximation. The model uses the B-grid configuration and the finite differencing is such that mass, heat, salt, variances of temperature, salinity and total energy are conserved in the model domain. Under the rigid-lid approximation, the external mode of momentum may be represented by a volume stream function ψ . A prognostic equation for ψ can be obtained by the vertical average of the momentum equations. This vorticity tendency equation is solved by successive-over-relaxation method and stream function over islands are obtained using the Hole Relaxation Method (TAKANO, 1974). Other detailed descriptions about the model are referred to COX (1984). where τ^x is the zonal wind stress, τ^y the meridional wind stress, τ_0 the maximum wind stress, L the meridional distance of the model domain, and l_1 the distance between the southern boundary and the separation latitude of the WBC.

The model ocean consists of a deep ocean in the south and a continental shelf and a MS in the north as shown in Fig. 1. The model domain covers 15°N - 42°N , 120°E - 150°E . The MS is connected with the deep ocean to the north and with the shelf to the south through two 100 km (north) and 200km (south) wide straits respectively. The bottom of both the continen-

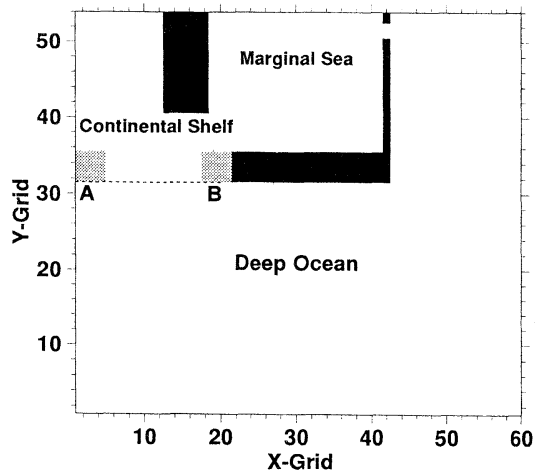


Fig. 1. Model domain. A and B denote areas where the branching of the WBC occurs depending on some parameters. The dashed line shows the location of step-like shelf break.

tal shelf and deep ocean is flat and the depths of both regions are 100m and 500m respectively. The depth of the MS is set to be the same as the depth of the continental shelf and there is no topographic irregularity within the MS, since a detailed circulation feature within the MS is beyond the scope of this study. However, the depth of the deep ocean is taken variable to examine the effect of depth difference between the two regions. The depth change between the deep ocean and the continental shelf takes place over one grid spacing so that it has a step-like character. The shelf break is placed in the east-west direction unless otherwise stated. Shaded parts in Fig. 1 on the continental shelf denote the areas where the branching of the WBC occurs depending on some parameters and will be referred to as an area A and area B respectively. Horizontally, the model domain is divided into $0.5^\circ \times 0.5^\circ$ grids, and there are 13 levels in the vertical as shown in Table 1. Salinity is held constant throughout the integration in all experiments and water density is calculated using a Knudsen's formula. The initial temperature profile increases linearly from 8°C at the bottom to 20°C at the surface of the deep ocean as shown in Table 1. Higher surface temperature (26°C) is imposed along the southern boundary of the model during time integration in order to maintain the vertical stratification. Without the supply of high temperature surface water, the stratification weakens and the model ocean is gradually cooled during time integration due to the advection and diffusion of upwelled cold water along the boundaries.

The values of lateral viscosity (A_m) and diffusivity (A_h) are taken as $1 \times 10^8 \text{ cm}^2/\text{sec}$ and $5 \times 10^7 \text{ cm}^2/\text{sec}$ respectively, unless stated otherwise, and we use constant values of vertical viscosity and diffusivity of $1 \text{ cm}^2/\text{sec}$. The model domain is closed and no slip condition is imposed along all solid boundaries. The normal gradients of T and S are set to zero on the side of walls, at the surface and at the ocean bottom so that there are no heat and salt fluxes across these boundaries. The bottom stress is parameterized by the quadratic drag law with a drag coefficient of 0.0015. A simple type of wind-stress is applied only over the deep ocean

Table 1. Level thicknesses and initial temperatures and salinities

No. of Level	Thickness (m)	Temperature ($^\circ\text{C}$)	Salinity (psu)
1	10	20.0	34.5
2	10	19.7	34.5
3	10	19.0	34.5
4	20	18.3	34.5
5	25	17.5	34.5
6	25	16.7	34.5
7	25	16.0	34.5
8	25	15.0	34.5
9	50	14.0	34.5
10	50	13.0	34.5
11	50	12.0	34.5
12	100	10.0	34.5
13	100	8.0	34.5

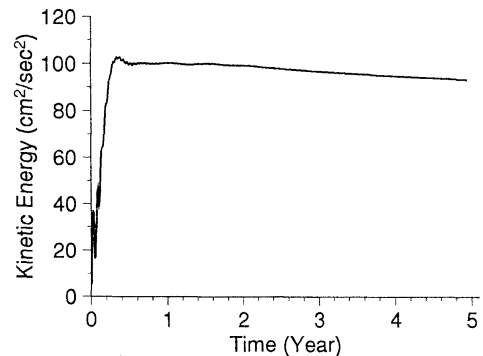


Fig. 2. Time series of total kinetic energy

to establish an asymmetric double gyres (e.g. subtropical and subpolar gyre), i.e.,

$$\tau^z = \tau_0 \cos\left(\frac{\pi(y-l_1)}{l_1}\right), \tau^y = 0, \text{ where } 0 \leq y \leq L$$

Elven numerical experiments are conducted to study the variation of the branching area of the WBC and the transport of an inflow into the MS as listed in Table 2. Additionally, barotropic versions of EXP 8 are carried out to identify the role of stratification. For these barotropic versions the wind stress is applied in a depth-independent manner like a body force so the flow is two-dimensional. Fig. 2 shows an example of a time series of total kinetic energy averaged over the whole volume. The kinetic energy changes little after one year though it slightly decreases afterwards. In all experiments, numerical integrations are carried out for five years and the results of year five are presented since we are only interested

Table 2. Description of numerical experiments

	τ_0 (dyne/cm ²)	D (m)	A_m (cm ² /sec)	AA ($^\circ$)
EXP 1	2	500	1×10^8	
EXP 2	1			
EXP 3	4			
EXP 4				deep trough in area A
EXP 5				deep trough in area A
EXP 6			5×10^7	
EXP 7			1×10^7	
EXP 8				30
EXP 9		250		
EXP 10		700		
EXP 11		1000		

* D denotes the depth of the deep ocean and AA the angle of the shelf break measured in the anticlockwise direction from the east.

in the steady solution.

EXP 1 is a nonlinear standard experiment, in which the shelf break is oriented in a purely zonal direction. The maximum wind stress applied over the deep ocean is halved (EXP 2) or doubled (EXP 3) in order to decrease or increase the volume transport of the WBC, respectively, and to examine the resultant changes in the branching position of the WBC and the transport of the inflow into the MS. A rectangular deep trough is introduced in area B (EXP 4) in Fig. 1 as like the deep trough west of Kyushu and in area A (EXP 5) to see whether it affects the branching of the WBC. OEY and CHEN (1991) suggests that the deep trough west of Kyushu Island contributes to the variability of the TC. In EXP 6 and EXP 7, the nonlinearity of the WBC is made to increase by decreasing the horizontal eddy viscosity coefficient. The orientation of the continental shelf break northeast of Taiwan is not zonal but tilted in the northeast direction, hence the Kuroshio is incident on a sloping shelf break northeast of Taiwan. The influence of the sloping topography on the penetration of the WBC is examined in EXP 8. Effects of the depth ratio between the deep ocean and the shelf are investigated in EXP 9 to EXP 11.

3. Separation of the Tsushima Current

Figure 3 shows streamlines of EXP 1 and its barotropic version. An anticyclonic gyre is established south of the grid point 40 in the deep ocean and a much weaker cyclonic subpolar gyre north of it. The separation latitude of the

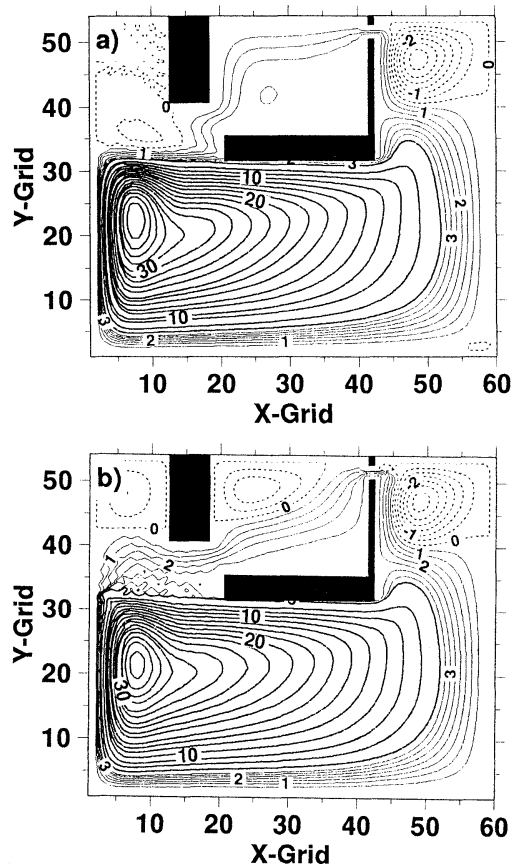


Fig. 3. Contours of streamfunction in Sv ($\times 10^6$ m³/s) unit for a) EXP 1 and b) the barotropic version with all parameters the same as in EXP 1. The contour intervals are 0.5 Sv between -4 Sv to 4 Sv and 2 Sv elsewhere. The dashed lines denote the negative values of streamfunction.

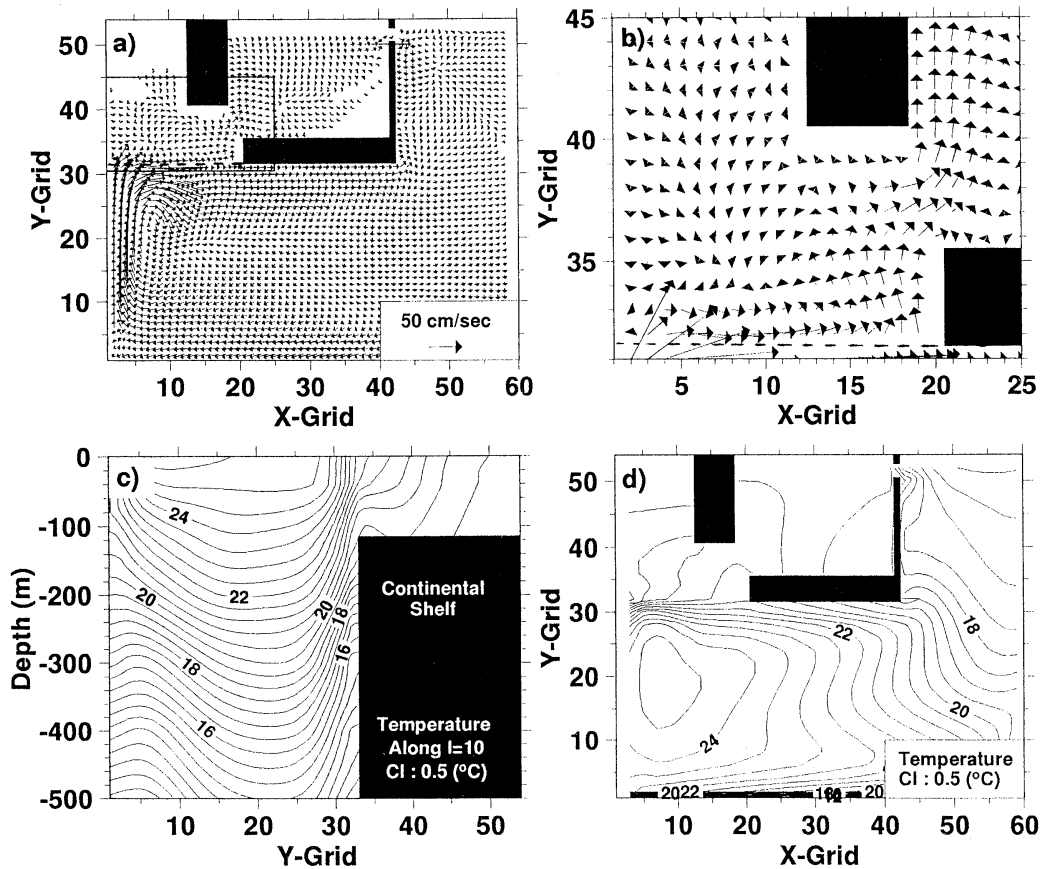


Fig. 4. Plots of a) currents at 75 m in whole basin, b) enlarged currents at 75 m in the continental shelf region, c) the vertical profile of temperature along $i=10$ in Fig. 1 and d) the horizontal distribution of temperature for EXP 1. The dashed line denotes the shelf break.

WBC coincides with the zero wind curl latitude. The WBC the subtropical gyre due to the planetary β -effect is formed in the deep ocean, the maximum volume transport of which is about 40 Sv in EXP 1 and is about 36 Sv in the barotropic version respectively. The stratification acts to increase the transport of the WBC. The WBC in the standard experiment is weakly inertial with the Reynolds number, $R_e = VW / A_m \approx 9$, where $V \approx 60 \text{ cm/sec}$ is the maximum northward velocity along the western wall of the deep ocean (Fig. 4a), and $W \approx 150 \text{ km}$, half-width of the WBC. Most of the WBC flows eastward along a zonally-oriented shelf break in both EXP 1 and the barotropic version.

Remarkable changes in the penetration of the WBC and the circulation on the shelf can be seen in both experiments. For a stratified case

of EXP 1, part of the WBC is separated in area B (Fig. 3a) and enters the MS, and a weak and isolated cyclonic circulation cell is induced on the continental shelf just north of the shelf break. On the other hand for the barotropic version, the separation takes place in area A and most of the WBC which penetrates onto the shelf enters the MS after turning anticyclonically in the shelf, while part of it rejoins the WBC. The cyclonic circulation cell on the shelf is located farther to the north in the barotropic experiment than in the baroclinic one. The cyclonic circulation on the shelf seems to result from the diffusion of the positive vorticity along the inshore part of the WBC. The volume transport into the MS is 1.86 Sv in EXP 1 and 2.8 Sv in the barotropic version, hence the stratification reduces the

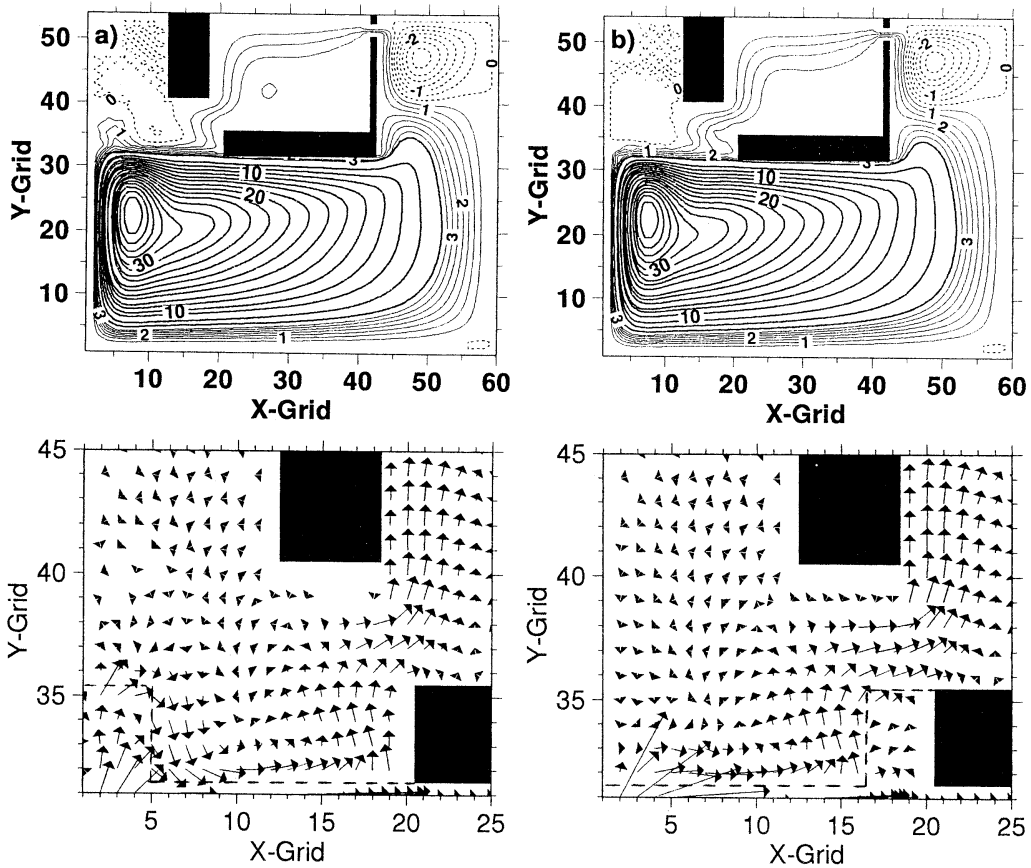


Fig. 5. Contours of streamfunction in Sv ($\times 10^6 m^3/s$) unit for a) EXP 4 and b) EXP 5. Here the rectangular-shaped deep trough is introduced in area A (EXP 4) and are B (EXP 5). Lower panels are enlarged currents in the continental shelf region. The dashed line denotes the shelf break.

transport into the MS while it acts to increase the transport of the WBC.

The horizontal temperature distribution in Fig. 4d shows much the same large scale features as the streamfunction plot. High temperature core is located just offshore of the WBC where the local recirculation gyre appears, and temperature is low in the subpolar region and along the southern boundary due to the upwelling of the cold water from the lower layer. A thermal front is formed along the shelf break and the intrusion of warm water to the MS can be seen in area B. Vertical profile of temperature along a meridional section also shows the shelf break frontal structure (Fig. 4c). The shelf water becomes vertically homogeneous despite the initial stratification. The

computed vertical profile of temperature is similar to published observations in the ECS in winter.

A rectangular-shaped deep trough is introduced in area A (EXP 4) and area B (EXP 5). Although the deep trough acts to guide part of the WBC onto the shelf in area A in EXP 4, the inflow into the MS originates from the area B as in the standard experiment (Fig. 5b). When the trough is located in area B like the trough west of Kyushu Island, the separation mainly takes place along the left flank of the trough and the flow inside the trough is weak and directed to the north (Fig. 5a). Recent ARGOS drifter trajectories clearly showed that the TC branches off the western flank of the deep trough west of Kyushu Island (LIE and CHO,

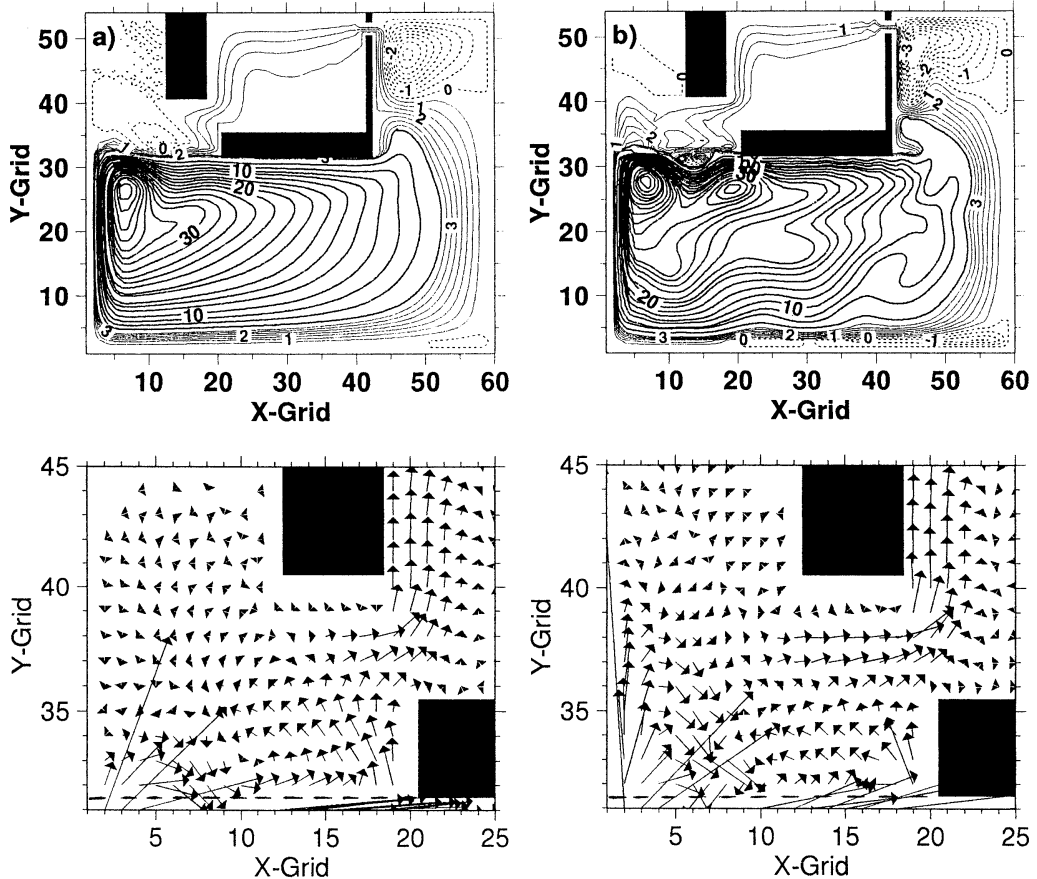


Fig. 6. Contours of streamfunction in Sv ($\times 10^6 \text{ m}^3/\text{s}$) unit for a) EXP 6 (eddy viscosity coeff. : $5 \times 10^7 \text{ cm}^2/\text{sec}$) and b) EXP 7 (eddy viscosity coeff. : $1 \times 10^7 \text{ cm}^2/\text{sec}$). Lower panels are enlarged currents in the continental shelf region. The dashed line denotes the shelf break.

1994). This study, however, suggests that the existence of the deep trough west of Kyushu Island does not result in the branching from the Kuroshio, but acts to shift the separation position to the west of the trough.

To investigate any changes in the separation position of the WBC as the WBC becomes more inertial, the horizontal eddy viscosity is reduced in EXP 6 and EXP 7 to an half and one tenth the standard value, respectively, with other conditions the same as in EXP 1. As the inertial effect increases the recirculating subgyre in the northwestern corner of the deep ocean is intensified and moves further to the north. For a highly inertial case of EXP 7, two sub-gyres emerge south of the shelf break in the deep ocean as in Fig. 6b. The WBC becomes

stronger and narrower and its transport is larger than the results of the standard experiment. The penetration of the WBC in EXP 6 takes place in area B nearly the same position as that in the standard experiment but in two areas in EXP 7; the area A and B. As the WBC becomes more inertial, the meridional scale of penetration of the WBC onto the shelf increases and the WBC reaches further to the north along the western wall of the shelf. This branch sharply turns anticyclonically over the shelf and part of it enters the MS while part of it returns to the WBC. The branching of the WBC also occurs in area B, hence the inflowing water into the MS comes from two areas in EXP 7. Observations show that part of the Kuroshio overruns the shelf break northeast of

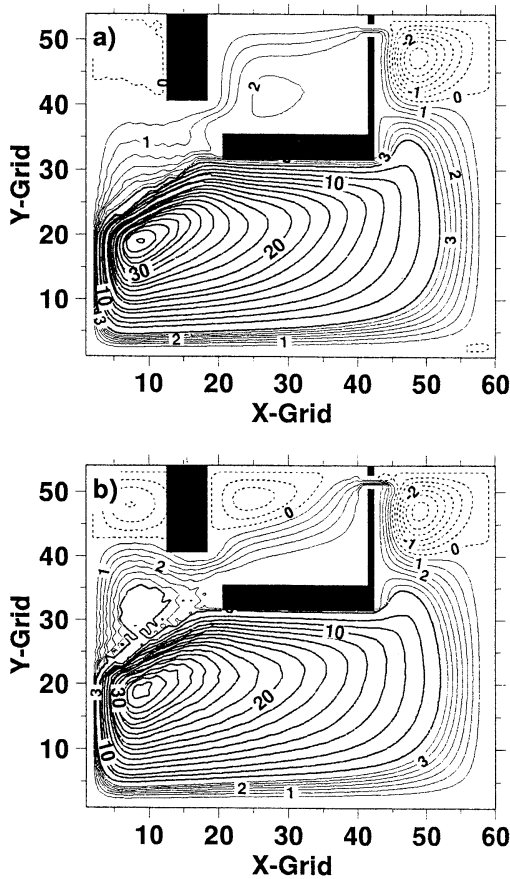


Fig. 7. Contours of streamfunction in Sv ($\times 10^6 \text{ m}^3/\text{s}$) unit for a) EXP 8 and b) the barotropic version with all parameters the same as in EXP 8. The contour intervals are 0.5 Sv between -4 Sv to 4 Sv and 2 Sv elsewhere. The dashed lines denote the negative values of streamfunction.

Taiwan and turns anticyclonically as it impinges upon the continental slope (e.g. GUO and LIN, 1987), which is similar to the result of EXP 7. The result of EXP 7 is similar to that of the barotropic version of EXP 1 in that the penetration of the WBC onto the shelf takes place in area A. However, two different features also emerge; the penetration of a part of the WBC also takes place in area B and there exists a cyclonic circulation between area A and B.

Within the parameter range in Table 2 (EXP 2, 3, 9, 11) the separation position of the WBC is not affected by the maximum wind stress in the deep ocean and the depth ratios between the deep ocean and the shelf (not shown), it

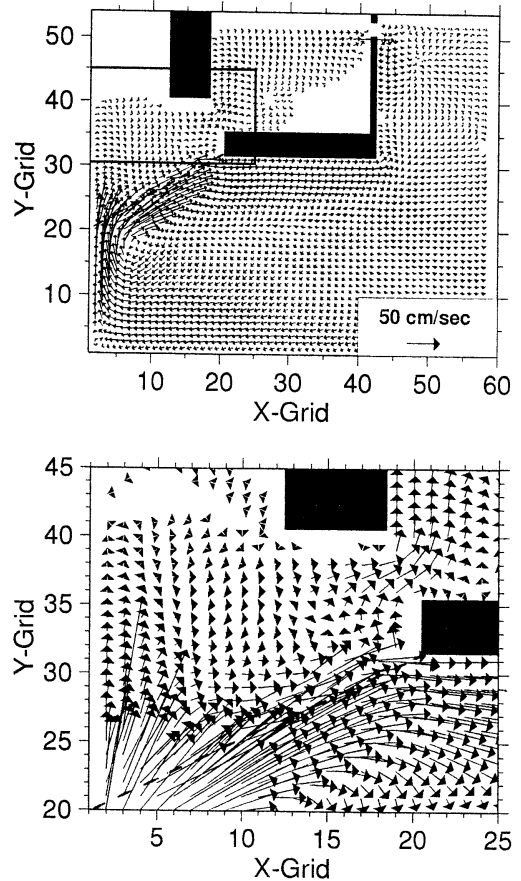


Fig. 8. Plots of currents at 75 m in EXP 8. Lower panels are enlarged currents in the continental shelf region. The dashed line denotes the shelf break.

takes place in area B the same as the result of EXP 1. However, it should be noted that the separation position would be changed as the wind stress in the deep ocean further increases since the nonlinearity of the WBC depends on the wind stress applied as well as the eddy viscosity.

When the orientation of the shelf break is horizontally inclined (EXP 8), the stream line penetrates onto the continental shelf along the western boundary (area A). Part of it returns to the WBC and others flows into the MS. We can find the stream line which joins with the WBC and separates at the southwestern tip of the island again in Fig. 7 and the northward flow along the western boundary of the island (area B) in Fig. 8. The separation from the

WBC takes place both in area A and area B as shown in Fig. 8, which is markedly different from the result of the standard experiment with a zonally oriented shelf break. The flow pattern on the shelf is more or less similar to the result of a highly inertial case of EXP 5 and the inflow into the MS comes from both area A and area B except that the cyclonic recirculation between area A and B cannot be seen in Exp 8 (Fig. 7a).

The stratification acts to decrease the influx to the MS the same as in the zonally-oriented shelf break case. The flow on the shelf has a broad feature for the stratified case, while the streamlines are more closely spaced for the homogeneous case.

4. Volume transport of the inflow into the MS

The transport of the WBC is increased by the vertical stratification of the WBC, but the transport into the MS is inversely decreased as mentioned previously. The volume transports of the WBC in EXP 1 and its barotropic version about 40 Sv and 36 Sv, respectively. The volume transports into the MS in EXP 1 and its barotropic version are about 1.86 Sv and 2.8 Sv, about 4.7% and 7.8% of the volume transport of the WBC respectively.

Figure 9 shows the dependence of the influx into the MS on some factors. Numerical experiments indicate that the influx is little sensitive to the orientation of the shelf break and the existence of the deep trough west of the MS. Instead, it is sensitive to the maximum wind stress in the deep ocean (or the volume transport of the WBC) and the depth ratio between the deep ocean and the shelf. The influx into the MS increases linearly as the transport of the WBC increases and the depth ratio decreases as shown in Fig. 9a and 9c, which has been also shown in previous barotropic model results (MINATO and KIMURA, 1980; SEUNG and NAM, 1992; CHANG, 1993). As the nonlinear effect of the WBC increases, the WBC becomes narrower and stronger as can be seen in Fig. 6. The influx into the MS, however, changes only a little as the nonlinearity of the WBC increases. As the eddy viscosity decreases the influx slightly increases as shown in Fig. 9b.

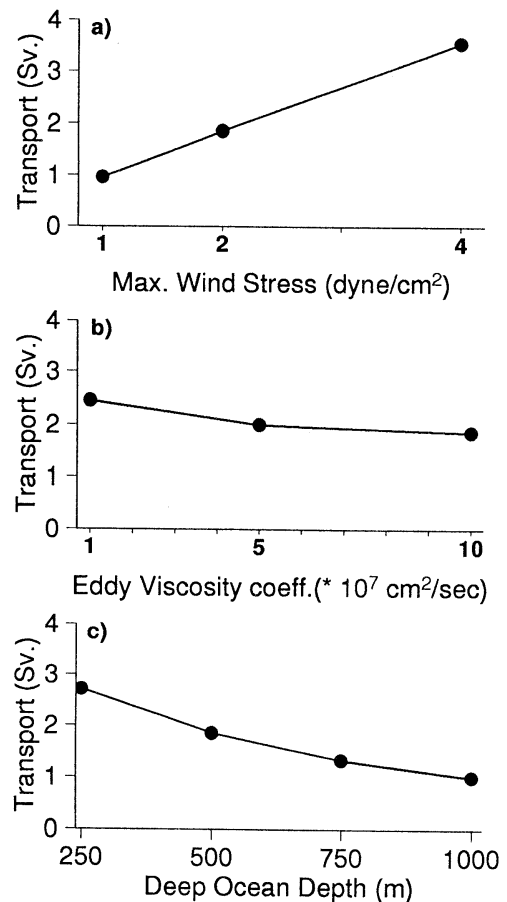


Fig. 9. Dependences of transport into the MS on a) the maximum wind stress applied over the deep ocean, b) the eddy viscosity coefficient, and c) the depth of the deep ocean.

5. Summary and Discussion

This study attempts to investigate the circulation of a continental shelf and a marginal sea driven by the WBC and highlights the variability of their circulation depending on the stratification, nonlinearity of the western boundary current and the orientation of the shelf break. The major circulation feature is such that part of the western boundary penetrates onto the shelf and enters the marginal sea while most of it follows the shelf break. The resulting shelf circulation and the influx to the marginal sea are dependent on various factors

For a zonally oriented shelf break, the separation from the WBC takes place in the eastern part of the shelf (area B) and the circulation on

the continental shelf is characterized by a weak cyclonic circulation, which differs from the result of the barotropic version of the standard experiment where the branching occurs in the western part of the shelf and the shelf circulation is anticyclonic. The separation, however, takes place along the western wall of the continental shelf even for the stratified case when the western boundary current becomes highly inertial, similar to the barotropic case. The branching position is also changed by the orientation of the shelf break. When the shelf break is oriented in the northeast direction, the separation occurs at two positions; one is area A and the other is area B. The definite dynamics for the alteration of the separation position of the western boundary current is left unexplained.

The amount of the inflow into the marginal sea is about 2 Sv, approximately 5% of the total volume transport of the western boundary current. It has been shown that the total volume transport of the western boundary current increases when the stratification is taken into account. On the other hand, the stratification acts to decrease the amount of the inflow to the marginal sea. According to the result of the standard experiment, an anticyclonic circulation and a weak cyclonic circulation are established in the deep ocean and the continental shelf respectively with the thermal front in between them. The thermal front and stratification seem to play a role in blocking the penetration of the deep ocean water onto the shelf and the marginal sea in area A.

Numerical experiments show that the amount of the inflow to the marginal sea increases as the transport of the western boundary current increases and the depth ratio between the deep ocean and the shelf decreases as other studies suggested (SEUNG and NAM, 1992; MINATO and KIMURA, 1980; CHANG, 1993). The influx is only a little affected by the eddy viscosity. The orientation of the shelf break and specific topographic features of the shelf break like the deep trough west of Kyushu do not affect the influx to the marginal sea.

It can be suggested from the present study that the branching of the Tsushima Current in the East China Sea can take place in the two

regions; the western region of Kyushu and the northeastern region of Taiwan since the shelf break in the East China Sea is oriented in the northeast direction and the Kuroshio is likely to be inertial.

Acknowledgments

This study is mostly supported by grants from the Ministry of Science and Technology and the Ministry of Environment of Korea (PN00271-2) and partly supported by the Ministry of Science and Technology of Korea (PN00281-2, PN00278-7, PN00520).

Reference

- BEARDSLEY, R. C., R. LIMBURNER, H. YU and G. A. CANNON (1985): Discharge of the Changjiang into the East China Sea. *Continental Shelf Res.*, **4**, Nos 1/2, 57-76.
- CHANG, K.-I. (1993): The shelfward penetration of western boundary currents. Ph.D. thesis, dept. of oceanography, Southampton University.
- CHAO, S.-Y. (1991): Circulation of the East China Sea, A Numerical Study. *J. Oceanogr. Soc. Japan*, **46**, 273-295.
- COX, M. D. (1984): A primitive equation three-dimensional model of the ocean, Tech. Rep. 1,250pp., Geophys. Fluid Dyn. Lab., NOAA Princeton Univ., Princeton, N.J.
- HSUEH, Y. (1986): The intrusion of the Kuroshio across the continental shelf northeast of Taiwan. *J. Geophys. Res.*, **97** (C 9), 14323-14330.
- GUAN, B. (1986): On the Circulation in the East China Sea. *Studia Marina Sinica*, **27**, 1-21.
- GUO, B. and K. LIN (1987): Characteristics of circulation in the continental shelf area of the East China Sea in winter. *Acta Oceanologica Sinica*, **V**, 6, Supp. I, 51-60.
- GUO, B., S. XIU, H. ISHII and Y. NAKAMURA (1990): Kuroshio warm filament and the source of the warm water of the Tsushima Current. Proc. of Japan China Joint Symp. of the Cooperative Study on the Kuroshio, 112-127.
- HOLLAND W. R. (1973): Baroclinic and topographic influences on the transport in the western boundary currents. *Geophys. Fluid Dyn.*, **4**, 187-210.
- ICHIKAWA, H. and R. C. BEARDSLEY (1993): Temporal and spacial variability of volume transport of the Kuroshio in the East China Sea. *Deep Sea Research*, **40** (3), 583-605.
- LIE H. J. and C. H. CHO (1994): On the origin of the Tsushima Current. *J. Geophys. Res.*, **99**, 25081-25091.

- LIE, H. J. *et al.* (1993): Study on oceanographic variability in the formation area of the Tsushima warm Current. KORDI, BSPN 00179-603-1, 193 pp.
- LIM D. B. (1971): On the origin of the Tsushima Current Water. *J. Oceanogr. Soc. Korea*, **6**, 85-91.
- MIITA T. and Y. OGAWA (1984): Tsushima Currents measured with current meters and drifters. In *Ocean Hydrodynamics of the Japan and East China Seas*. T. ICHIYE (ed.), Elsevier, 235-352.
- MINATO, S. and R. KIMURA (1980): Volume transport of the Western boundary current penetrating into a marginal sea. *J. Oceanogr. Soc. Japan*, **36**, 185-195.
- MORIYASU, S. (1972): The Tsushima Current. In *Kuroshio: Its physical Aspects*. by H. STOMMEL and K. YOSHIDA (eds), Univ. of Washington Press, 353-369.
- NAM S. Y. and Y. H. SEUNG (1992): A numerical model on the inflow into the Japan Sea: the formation and transport of the Tsushima Warm Current. *Bull. Korean Fish. Soc.*, **25**, 58-64.
- NOF, D. (1993): The penetration of Kuroshio into the Sea of Japan. *J. Phys. Oceanogr.*, **23**, 797-807.
- OEY, L.-Y. and P. CHEN (1991): Frontal waves upstream of a diabathic blocking: A model study. *J. Phys. Oceanogr.*, **21** (11), 1643-1663.
- SEUNG, Y. H., and S. Y. NAM (1992): A numerical study on the barotropic transport of the Tsushima Current, *La mer*, **30**, 139-147.
- TAKANO, K. (1974): A general circulation model for the world ocean. UCLA Dept. of Meteorology Tech. Rep. No.8.
- TAKANO, K and A. MISUMI (1990): Numerical simulation of the North Pacific circulation as a fundamental study on the Kuroshio power harnessing. *Proc. Japan-China Joint Res., STA (Japan) and SOA (China)*, 146-156.
- YI, S. U. (1996): Seasonal and secular variations of the water volume transport across the Korea Strait. *J. Oceanol. Soc., Korea*, **1**, 7-13.

Received January 9, 1996

Accepted March 11, 1996

Time variations of the current northwest of Tsushima

Takashige SHINOZAKI*, Akimasa TASHIRO*, Tomoki NAGAHAMA*,
Hideo ISHII*, Kouichi OMURA**, Yasunori OUCHI**,
Yoshio HASHIMOTO* and Kazuo KAWATATE*

Abstract: We measured current and temperature northwest of Tsushima. On the basis of records obtained from July 1991 to March 1995 we confirmed that in shallow and middle depth, all year round, the current goes northeast and the temperature is higher than 10°C; in deep depth, in spring, summer, and autumn, the current goes southwest and the temperature is about 5°C, in winter, however, the current northeast and the temperature higher than 10°C.

1. Introduction

It has drawn attentions of researchers in ocean that bottom water intrudes from north to south at a basin northwest of Tsushima.

NISHIDA (1927) reported, in northwest of Tsushima, existence of southward flowing phenomenon of the Japan Sea bottom cold water. CHANG and UDA (1968) also wrote about intrusion of the Japan Sea cold bottom water into the Strait of Korea. LIM and CHANG (1969) discussed water mass structure and proposed 10 °C as an index number of the cold water. MIITA (1976) made Eulerian measurements of the current for about ten days. OGAWA (1983) analyzed observation data along a line between Kawajiri and Ulsan. He pointed out that it is difficult to recognize the cold water clearly in winter. NAGATA (1985) wrote about forming of the cold water mass region along the Korean and the Japan shore lines. ISOBE (1993) discussed a relation between the cold water and the Tsushima current.

On the basis of these pioneering works, we made a plan to measure the current northwest of Tsushima and carried it out. Until now we showed data obtained in summer of 1991 (OMURA and KAWATATE, 1994).

2. Method

We have used three kinds of lines: 173, 40, and 25 m long. We show them schematically in Fig. 1, where a signal buoy, current meters (denoted by CM), floats, and an acoustic releaser (denoted by AR), a sinker, and an anchor are illustrated. The line of 173 m long is equipped with two current meters. We have used an iron sinker of 240 kgf in air. Each of the shorter two lines has one current meter and a sinker of 120 kgf.

We set mooring lines in a circle of a point 5 nautical miles (nm) radius with a center at 340 degrees (°) from north and 9.5 nm away from Mitsushima lighthouse, the northern extreme of Tsushima. Depth is about 220 m there. We show measuring stations in Fig. 2. We deployed eight lines, among which we retrieved five lines and lost three shown by solid circles.

We show items of lines used in Table 1, which includes mooring terms, measure interval, and positions. In 1991 the line was recovered safely. In 1992 we lost one short line with one current meter. A cluster of top floats was recovered in January 1993 at Murakami city on the coast of the Japan Sea, Niigata, Japan. In 1993 we lost one long line with two current meters. We had no news of this line until now. In 1994 we put two short lines. In February 1995 we found that one line was lost. In June we went the site to retrieve the remaining line. During three months and half, from February to June, the line was disappeared. We lost all

* Research Institute for Applied Mechanics, Kyushu University, Kasuga, 816 Japan

** Chikuzenkai Laboratory, Fukuoka Fisheries and Marine Technology Research Center, Imazu, Fukuoka, 819-01 Japan

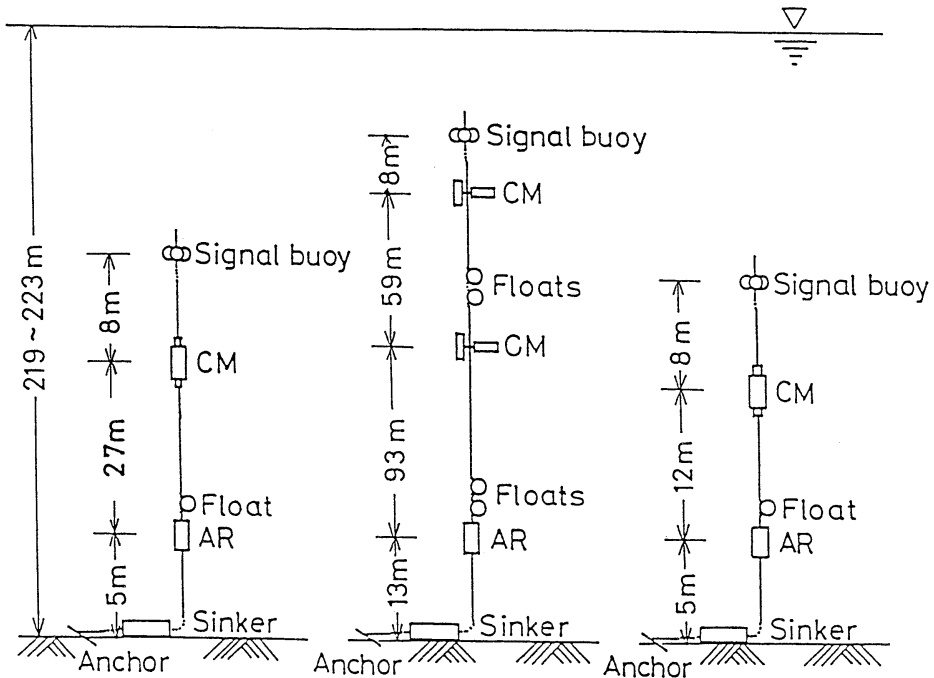


Fig. 1. Schematic mooring lines used northwest of Tsushima.

two lines at the measuring station. In May, however, a fisherman caught one line at Okinoshima in the Japan Sea, Shimane, Japan with one current meter, data of which will be shown later. As for the other one line we had no news until now.

In total we deployed eight lines. We lost three lines with four current meters. We retrieved five lines with six current meters.

3. Results

We show the current vector after taking 24 hours running average in Fig. 3 with an interval of 3 hours. Data obtained from six current meters are presented. We outline results in the following. In summer of 1991 at deep depth the current goes southwest. In summer of 1992 at shallow and middle depth the current goes northeast. In deep depth from the middle of May to the end of December 1993 the current goes southwest. From January to April 1994 the current goes northeast. From May to December 1994, it goes southwest again. Exceptionally we see northeastward currents in September and October 1994, which seem to be caused by passing of typhoons. From January to March 1995

the current goes northeast as in 1994.

Temperature records are shown in Fig. 4. In summer, in deep depth the temperature is low, 5°C or less; in middle and shallow depth the temperature is higher than 10°C. Turning to deep depth, we see as follows. From June to December the temperature is low, about 5°C. From January to April it is 10°C or higher. In May and June it is about 8°C. From July to January it is about 5°C. In February and March the temperature becomes higher.

Hereafter we examine the current and the temperature at deep depth. We calculated velocity components of northeast-southwest (NE-SE) and southeast-northwest (SE-NW). We show temporal variations of velocity (NE-SW) component and temperature from May 1993 to March 1995 with 1 hour interval in Fig. 5. Manners of both variations are different from each other. The velocity change is fast and the temperature slow. Examining data of May and June 1993, for example, we see that the current went southwest and the temperature was still higher than 10°C (more specific 13.6°C) at the end of May, for about 3 weeks the temperature decreased, then the temperature became the

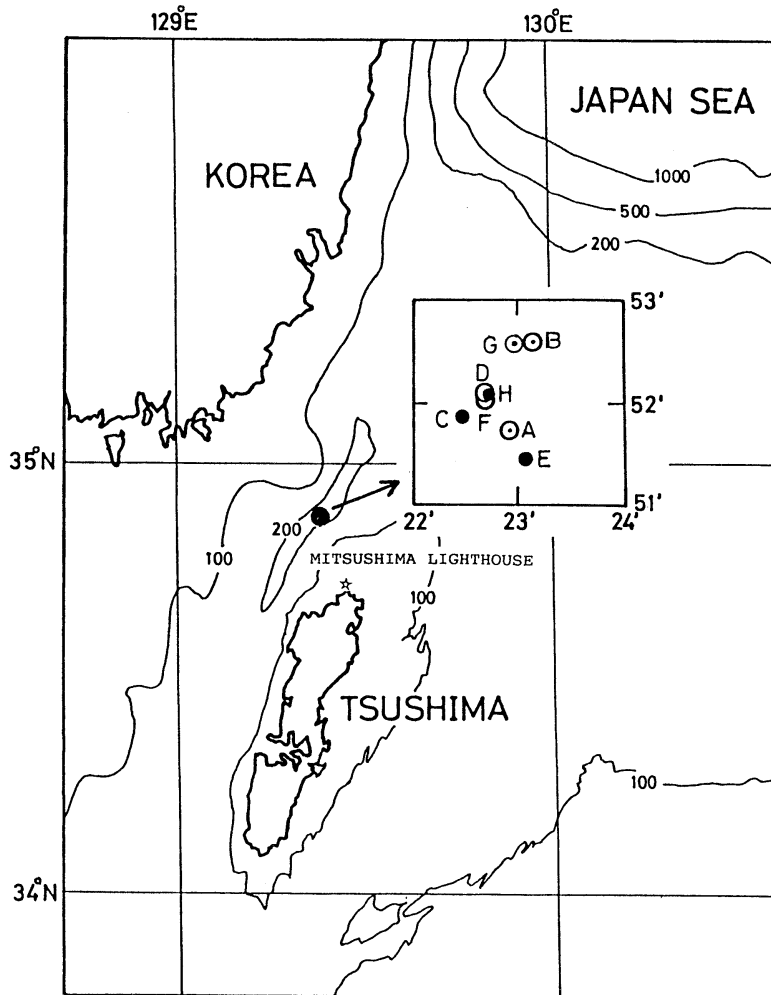


Fig. 2. Observation stations, solid circles demotes station where current meters were lost.

Table 1. Items of lines used northwest of Tsushima.

No.	From	To	Terms (day)	Bottom Depth (m)	Line Length (m)	Current Meters Number	Measure Interval (minute)	Site	
								Latitude (° ' N)	Longitude (° ' E)
A	11 Jul 1991	03 Oct 1991	85	221	40	1	30	34°51.73'	129°22.93'
B	07 Jul 1992	13 Nov 1992	130	219	173	2	20	34°52.604'	129°23.159'
C	07 Jul 1992	Lost		222	40	1		34°51.870'	129°22.460'
D	19 May 1993	05 Aug 1993	79	222	25	1	30	34°52.086'	129°22.687'
E	05 Aug 1993	Lost		220	173	2		34°52.434'	129°23.091'
F	05 Aug 1993	08 Jun 1994	308	223	25	1	60	34°52.034'	129°22.681'
G	08 Jun 1994	31 Mar 1995	297	219	25	1	60	34°52.568'	129°22.965'
H	08 Jun 1994	Los		222	25	1		34°52.097'	129°22.744'

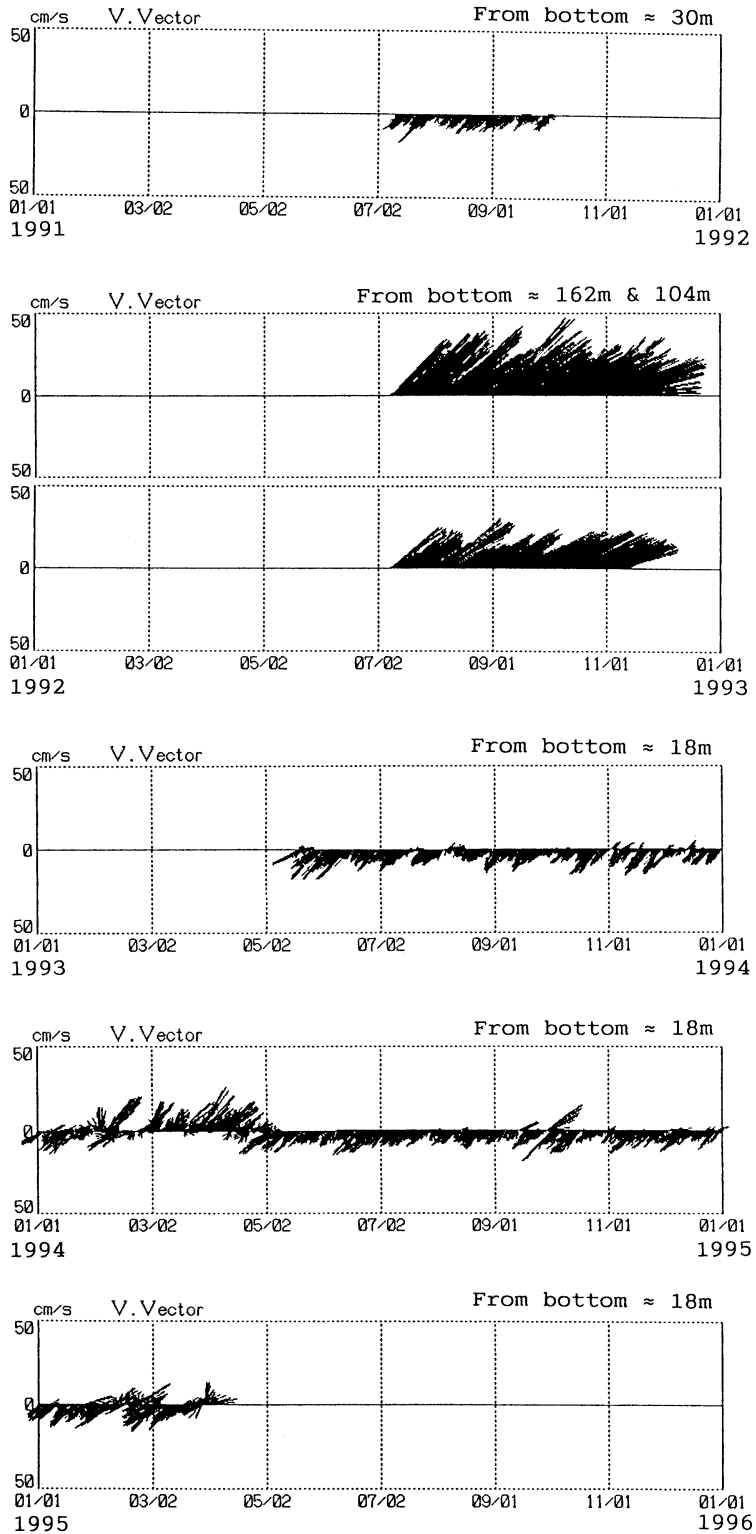


Fig. 3. Current vector, from July 1991 to March 1995.

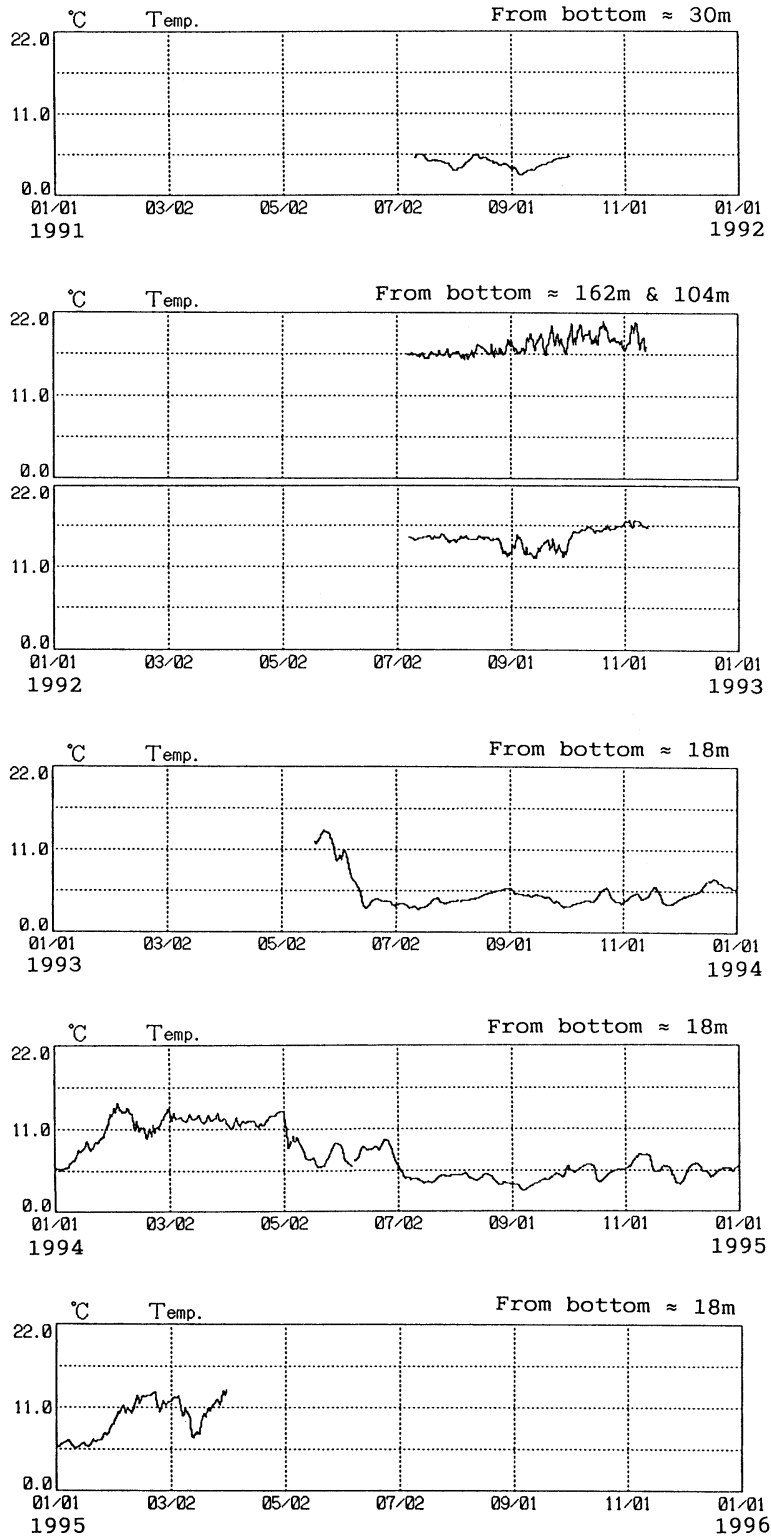


Fig. 4. Temperature, from July 1991 to March 1995.

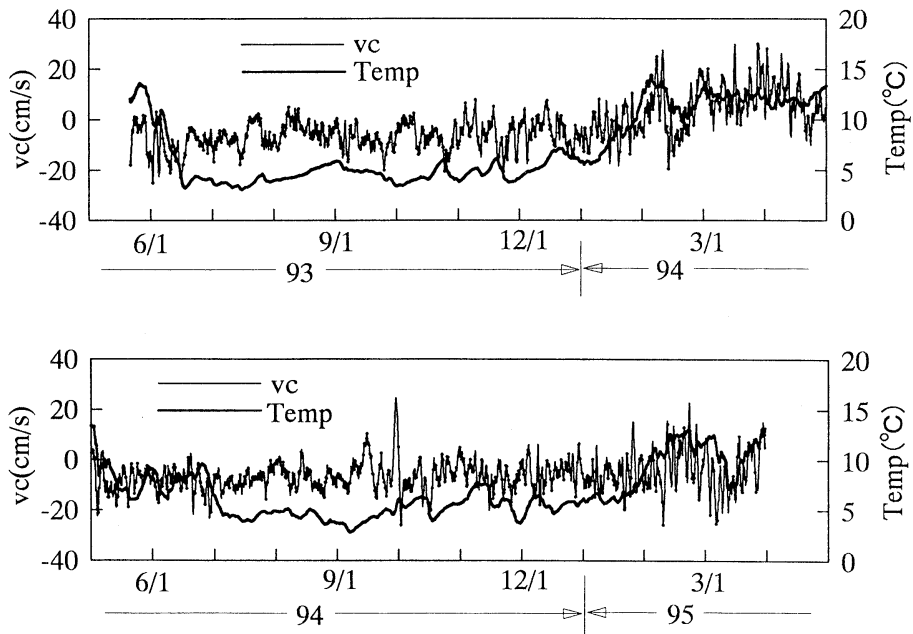


Fig. 5. Velocity component (NE-SW) and temperature, from May 1993 to March 1995.

minimum less than 5°C (3.2°C) in the middle of June. To explain the above, we use a primitive conjecture. Characteristics of current must reflect the properties of upstream. At steady state a property of downstream is the same as that of the upstream. At an instance when the current direction changes, the downstream turns to a new upstream, of which property remains as before. It needs time for the new upstream to get a new property. To confirm the conjecture or determine an extent of current source, such as area, depth, and duration, we need measurements in wider range and longer terms. It also attracts our attention to seek what is a mechanism of changing the current direction.

We took monthly averages of velocity components of NE-SW with SE-NW and temperature. Values of SE-NW components were at maximum $1/3$ or less of NE-SW components. We show changes of the velocity of NE-SW components and the temperature of 1991, 1993, 1994, and 1995 in Fig. 6. From the upper drawing we know that the both average values change from year to year. The yearly differences are large from February to June and they are small from July to December and January.

From the lower drawing we see as follows. When the current goes northeast, the temperature is higher than 10°C , the warm water; when the current goes southwest, the temperature becomes less than 10°C , the cold water. Three exceptions are pointed out: 1) in May 1993, the SW current velocity was 7.4 cm/s , the temperature was still 12.3°C , indicating the cold water intrusion delayed; 2) in February 1995, the SW current 1.9 cm/s , already the temperature 11.5°C ; and 3) in March 1995, the SW current 4.5 cm/s , already the temperature 10.6°C , showing that supply of the cold water already stopped. The exceptions are related to problems of transition process: from warm to cold and vice versa. To explain the first exception we used the primitive conjecture before. To cope with the second and third exceptions we perhaps need another conjecture, in which we assume an extent of source and an influence of surrounding environments. To polish and prove the conjecture we again need another measurements.

We made spectral analysis, by use of the fast Fourier transform (FFT) method and the auto-regression (AR) method. Both methods were applied under conditions: number of data

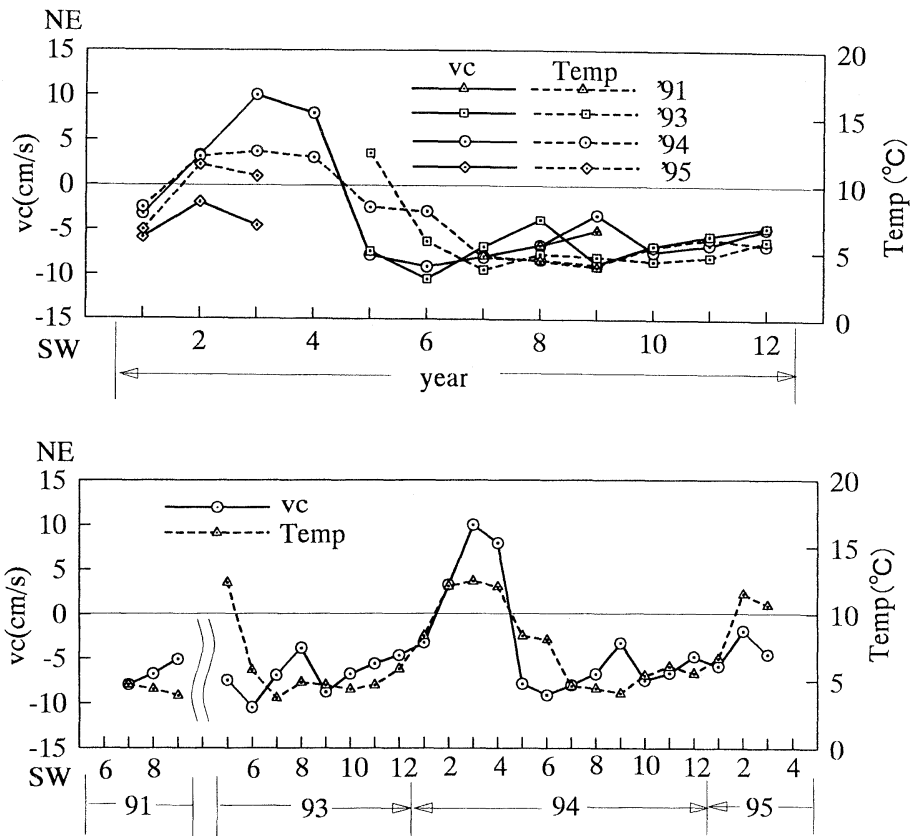


Fig. 6. Average values of velocity component (NE-SW) and temperature, in 1991, 1993, 1994, and 1995.

N is 1,024 and sampling interval ΔT is 1 hour. Thus, a fundamental frequency $f_0 = 1/(N\Delta T) = 0.000977$ cycles per hour (1/h) and the Nyquist limit $f_{N/2} = 1/(2\Delta T) = 0.5/h$. We sought linear trends for data by use of the least square method, subtracted them from the original data, and obtained series of data for analysis. On applying the AR method, we express a datum by a linear combination of the past M and the future M data. We choose M that makes Akaike's final prediction error $\{(N+2M)/(N-2M)\}^2 \times P$ minimum, where P is an auto-correlation of difference between the original and the auto-regressed data. We took data from 00:00 on 6 August 1993 to 15:00 on 17 September 1993. Both FFT and AR methods give similar results on the whole. Power spectrum becomes almost zero as the frequency goes high. We present results from 0 to 0.1/h in Fig. 7, where values obtained by the FFT method are shown by thin lines and those of

the AR method by bold lines. On applying the AR method we used $M=60$ for the velocity (NE-SW) component and $M=30$ for the temperature. The maximum appears in each spectrum at $0.000977/h$ (period 1,024 hours, which coincides with the length of data). It has no physical significance, probably being brought by a leakage effect of data truncation other than multiple of the period. For the velocity, we see local peaks at $0.0127/h$ (3.28 days), $0.0244/h$ (1.71 days), $0.0420/h$ (23.8 h), $0.061/h$ (16.5 h), and $0.0830/h$ (12.0 h). Shape of spectrum is round except around $0.0830/h$. Through a visual inspection of Fig. 5, we may predict existence of the peak at a period of about 3 days. Most energy is recognized in low frequency range. For the temperature, we see no appreciable peaks. Shape of spectrum is almost monotonous. These may also be expected by examining Fig. 5. Energy is contained in lower frequency range.

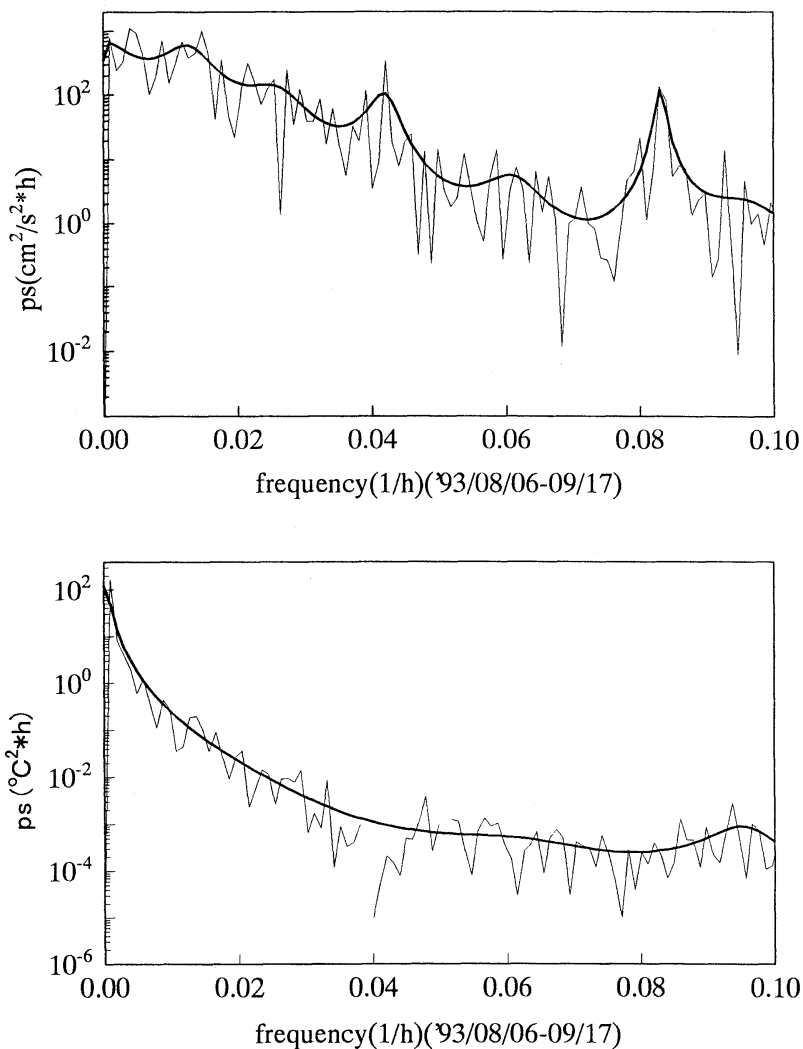


Fig. 7. Power spectrum of velocity component (NE-SW) and temperature, from 6 August 1993 to 17 September 1993

4. Conclusion

We have surveyed time variations of the currents northwest of Tsushima, in particular, relating to intrusion of the cold water. As seen in the above we learn that times for beginning, continuation, and stopping of the intrusion of the cold water change year by year.

After examining data obtained we have confirmed the following in outline. Where the depth is shallow or middle, all year round, the current goes northeast and the temperature is higher than 10°C. Where the depth is deep, in spring, summer, and autumn, the current goes

southwest and the temperature is about 5°C; in winter, however, the current northeast and the temperature about 10°C.

Acknowledgments

We express our sincere gratitude to Tsunehiko MIITA, the former director of Fukuoka Fisheries and Marine Technology Research Center, who proposed and promoted long term measurements at the basin northwest of Tsushima. Our thanks also go to Captain Shigemi YOSHIMURA of the Research Vessel Genkai and his crew for skills and

patients which they show in deploying and retrieving the lines. We are grateful to Dr. Hong-Ryeol SHIN, Korea Ocean Research and Development Institute, for his pointing out and reminding us of passing of Typhoons in September and October 1994. We are deeply thankful to Mr. Kiyoshi MAEKAWA, Okinoshima Ama Fishermen's Cooperative Society, for his kindness that he caught our line with one current meter and sent them back to us. The current meter contained data from June 1994 to March 1995.

References

- CHANG, S. and M. UDA (1968): Oceanic front in the western part of the Japan Sea, Summary Rept. Annual Meet. Oceanog. Soc. Japan, April, 5-9.
- ISOBE, A. (1993): The Seasonal variability of the Tsushima Warm Current (in Japanese), *Umi to Sora*, **69**, 35-60.
- KAWATATE, K. (1978): A comment on the auto-regression cross spectral analysis (Note in Japanese), *Bulletin of Research Institute for Applied Mechanics, Kyushu University*, **48**, 77-82.
- LIM, D. B. and S. D. CHANG (1969): ON THE COLD WATER MASS IN THE KOREA STRAIT, *The Journal of the Oceanological Society of Korea*, **4**, 71-82.
- MIITA, T. (1976): Transports of fish eggs and larvae in waters west of Kyushu, 2-2 Current structures observed by anchored measurements (in Japanese), *Bull. Japan. Soc. Fish. Oceanog.*, **28**, 33-58.
- NAGATA, Y. (1985): Water temperature measurement by a liner (in Japanese), *Mon. Mar. Sci.* **184**, 621-627.
- NISHIDA, K. (1927): Results of the current measurements in the adjacent seas of Tyosen (Korea) (in Japanese), 1923-1926. *Rep. Oceanog. Invest. Fish. Exp. Sta. Husan*, 2.
- OGAWA, Y. (1983): Seasonal Changes in Temperature and Salinity of Water Flowing into the Japan Sea through the Tsushima Straits (in Japanese), *Bull. Japan. Soc. Fish. Oceanog.*, **43**, 1-8.
- OMURA, K. and K. KAWATATE (1994): Hydrographic Features of the Bottom Cold Water in the West Tsushima Channel (in Japanese), *Bull. Fukuoka Fisheries Mar. Technol. Res. Cent. No. 2*, 93-101.

Received December 24, 1995

Accepted March 18, 1996

Seasonal variation of the East Korea Warm Current and its relation with the cold water

Yang-Ki CHO* and Kuh KIM**

Abstract: Hydrographic data and satellite images show the structure of the East Korea Warm Current (EKWC) and its seasonal variation. Satellite images taken in April with concurrent hydrographic data provide evidence of the branching of the Tsushima Current. However there is no evidence of branching in February. The EKWC flows north in summer when the cold water in the lower layer become thicker in the Korea Strait. Observed results and calculation of vorticity change suggest a possibility that the presence of the cold water, which can provide the negative relative vorticity for the EKWC, is more important than the planetary beta effect in the formation of the EKWC.

1. Introduction

The Tsushima Current (henceforth TC) carries heat and salt from the East China Sea to the East Sea throughout the year and determines the major hydrography in the East Sea (SVERDRUP, *et al.* 1942, p.734.)

UDA (1934) suggested that the TC leaving the Korea Strait splits into two branches (Fig. 1); one flows along the Japanese coast and the other along the Korean coast which is called the East Korea Warm Current (henceforth EKWC). Numerical experiments (YOON, 1982 *a, b, c*; KAWABE, 1982*b*) simulated the EKWC as a permanent feature due to the planetary beta effect and the branch along the Japanese coast due to the topographic effect.

Recently a couple of reports indicated the absence of the EKWC sometime. Firstly, based on satellite images and hydrographic surveys KIM and LEGECKIS (1986) showed that the EKWC was not formed in spring 1981 and suggested that the southward movement of the cold water was closely related with the branching of the TC. This suggestion is important, be-

cause in previous numerical models the cold water was assumed at rest as far as the branching was concerned.

Secondly, according to ISODA and SAITOH (1993) observation, the warm and saline water in the EKWC region is due to the seasonal episodic supply of the warm and saline waters through the northward intruding eddy process rather than the result of the persistent branching of the TC and they suggested the absence of the EKWC in winter. However they examined the data for only one year taken in 1987. Therefore it would be useful to examine the data for other years in order to understand whether the formation of the EKWC is indeed seasonal.

Most historical data were taken with bottle casts, so the depths of measurement were not accurate and it was often difficult to reveal the vertical structure of the EKWC. Moreover the meridional structure along the Korean coast was known poorly, because of inadequate spacing between stations.

The primary objective of this study is to understand the structure of the EKWC and its seasonal variation from recent CTD, hydrographic and satellite data.

2. Data

To understand the physical characteristics in the Korea Strait and neighbouring sea and their temporal variation, surveys were

* Research Institute for Basic Sciences, Seoul National University, Seoul, 151-742, Korea

** Present address: Faculty of Earth Systems and Environmental Sciences, Chonnam National University, Kwnagju, 500-757, Korea
e-mail: ykcho@chonnam.chonnam.ac.kr

** Department of Oceanography, Seoul National University, Seoul, 151-742, Korea

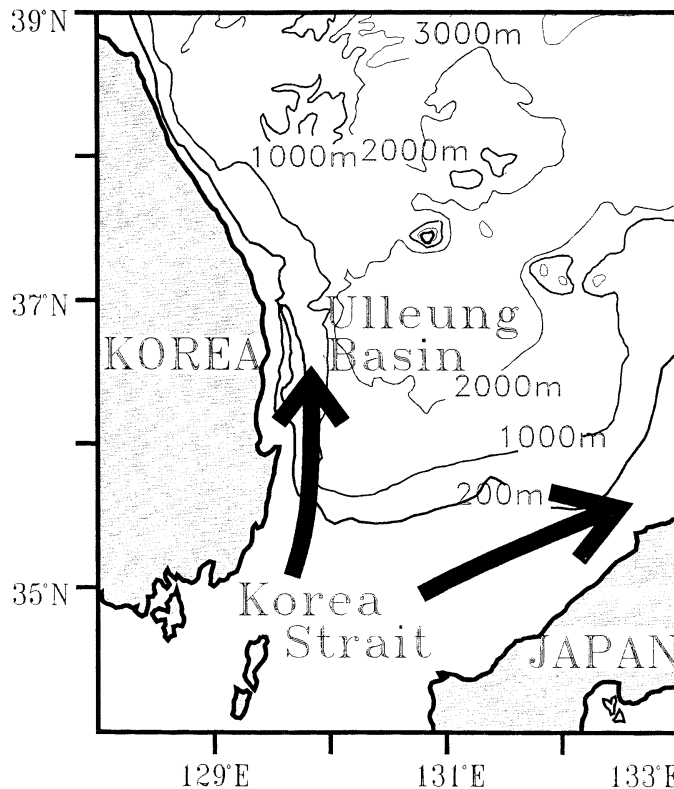


Fig. 1. Bathymetry of the East Sea. Arrows show schematically two branches of the Tsushima Current after Uda (1934). Depth are in meters.

conducted in April, June, August and October of 1991 and 1992 respectively, taking 60 CTD stations each time (Fig. 2). The stations are spaced every 10 miles approximately in the strait and CTD was lowered to near bottom at stations shallower than 500 m and about 500 m at stations deeper than 500 m. At each station SBE 19 profiler of Ser-Bird Electronics Inc. was lowered at a speed of 60 m/min approximately, taking two samples of temperature, conductivity and pressure in one second, which gives a vertical resolution of about 50 cm. Final data for analysis were obtained by averaging temperature and salinity data over two decibars.

To cover the eastern part of the strait, we used Japanese CTD data which were taken by Yamaguchi Prefectural Open-Sea Fisheries Experimental Station (\blacktriangle marks in Fig. 2). The routine hydrographic data taken by the Korean Fisheries Research and Development Agency in February of 1991 and 1992 were also used. Satellite infrared image data from the

Advanced Very High Resolution Radiometer on NOAA-9, NOAA-10 and NOAA-11 were processed at the Research Institute of Oceanography, Seoul National University to examine the branching of the TC.

3. Branching of the Tsushima Current

Since the sill depth of the Korea Strait is less than 150 m, the warm water flowing through the Korea Strait is limited to the upper layer as it spreads into the East Sea. Therefore, the major vertical and horizontal variation of temperature is also confined in the upper 200 m, which makes sea surface temperature (henceforth SST) particularly useful in investigating the branching. The path of the Tsushima Warm Water (henceforth TWW) is clear in winter and spring, because a thermal front is formed as the TWW meets the resident cold water. In summer and autumn, it is difficult to detect the path of the TWW by SST, because the surface front is not so clear due to the

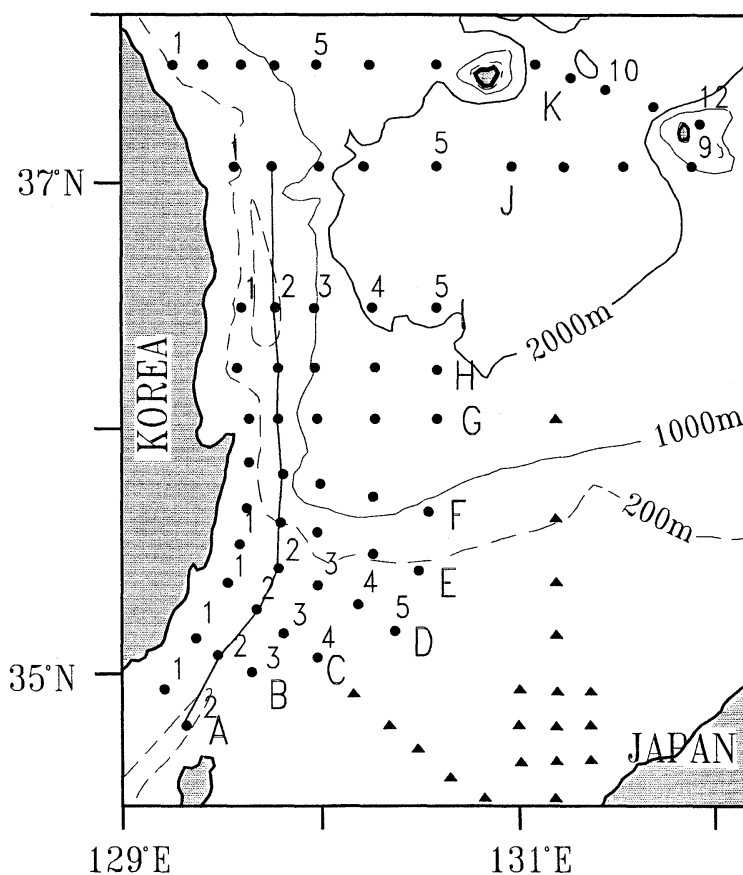


Fig. 2. CTD stations taken in April, June August, October, 1991 and 1992. Thick solid line represent the selected stations for vertical section. Depths are in meters. ▲ marks represent Japanese stations.

seasonal heating. Therefore satellite images of SST are useful in winter and spring only, illustrating nearly instantaneous distribution of the SST.

On February 25 1991, the SST was almost constant at 13°C over a wide area, including the western and eastern channels of the Korea Strait (Fig. 3a). This uniformly warm water and the cold water to the north make a distinct thermal boundary in the east-west direction at $35^{\circ}30' \text{N}$. Across this boundary temperature dropped to the north by $3\sim 5^{\circ}\text{C}$ in several kilometers. Similar front was reported previously by KIM and LEHECKIS (1986).

A partially cloud-free image taken on April 30 shows that warm inflow of $13\sim 14^{\circ}\text{C}$ through the Korea Strait splits into two parts as it left the strait (Fig. 3b). The branch along the

Japanese coast was similar to that observed in February. The other branch, the EKWC, flowed northward on separation, and part of it turned eastward at 38°N toward Ulleung Island.

On February 26 1992, the SST along the Korean coast was warmer than that on February 25 1991 (Fig. 3c). There is also thermal front in the east-west direction around $35^{\circ}30' \text{N}$.

The last image (Fig. 3d) taken on April 27, 1992 shows that the warm inflow of $13\sim 14^{\circ}\text{C}$ through the Korea Strait clearly splits into two parts, developing two branches. The branch along the Japanese coast was similar to that observed in February 1992. The EKWC flowed northward on separation as in April 1991, and at 37°N most of it turned sharply eastward toward Ulleung Island and small part of it flowed northward along the coast.

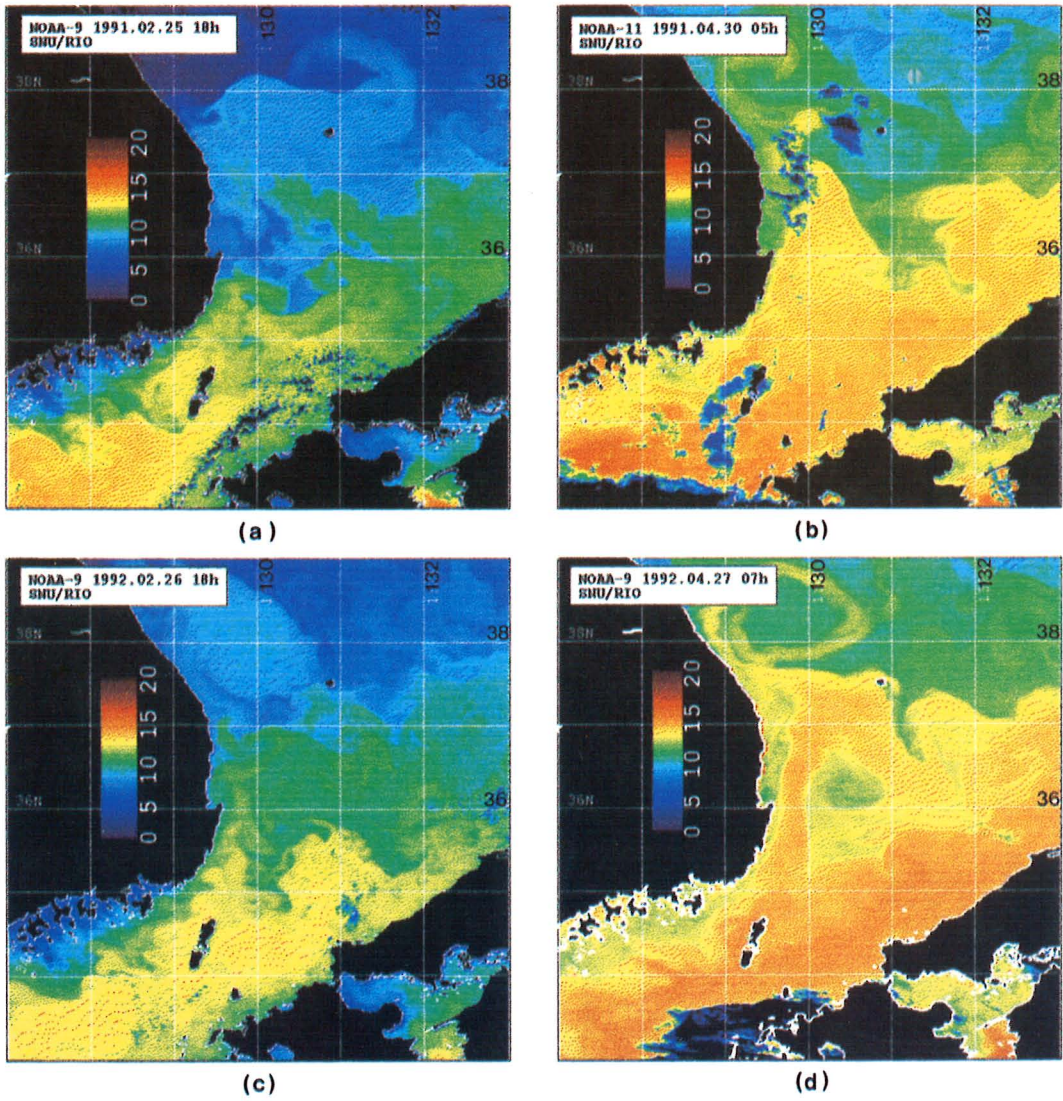


Fig. 3. SST images taken by satellite in (a) February 1991, (b) April 1991, (c) February 1992 and (d) April 1992.

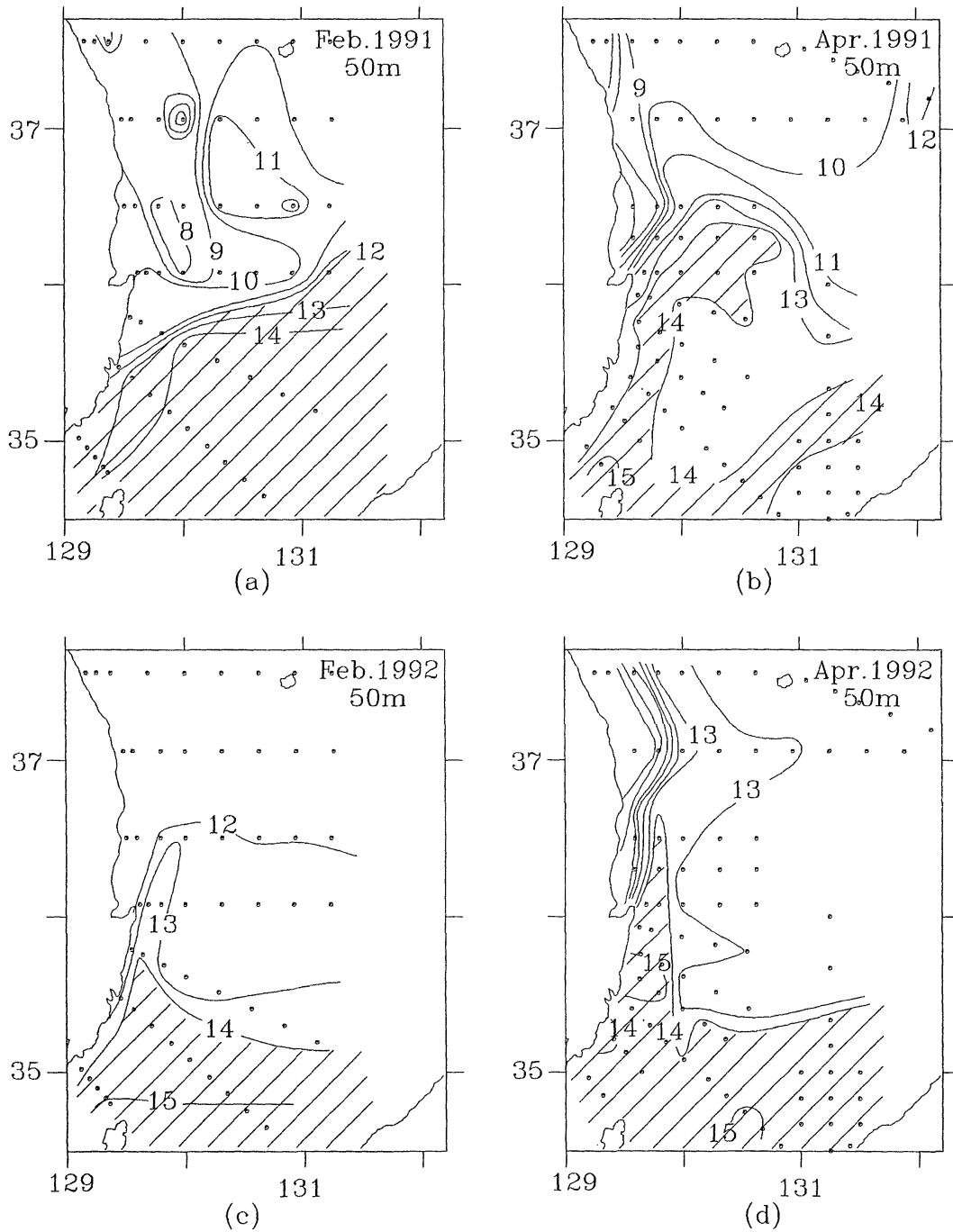


Fig. 4. Temperature distribution at 50 m depth from hydrographic survey in (a) February 1991, (b) April 1991, (c) February 1992 and (d) April 1992.

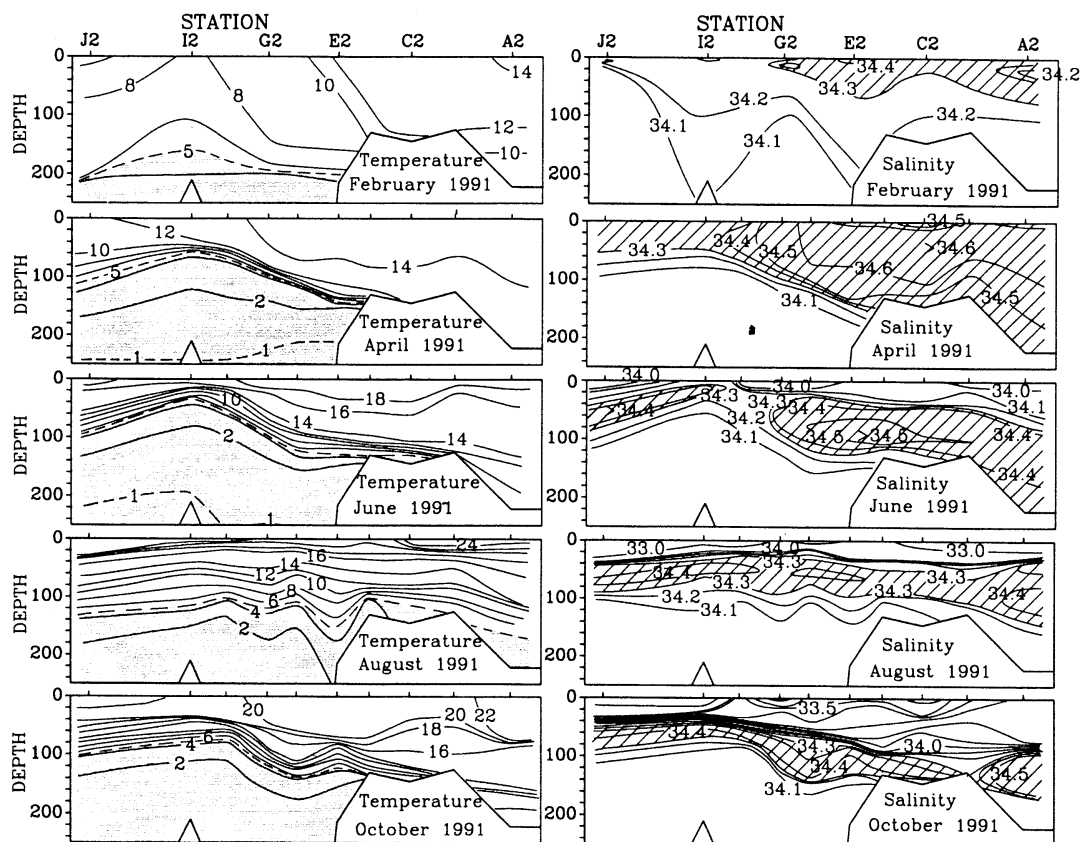


Fig. 5. Vertical sections of temperature and salinity along the Korean coast (see Fig. 2) in 1991. The waters colder than 5°C are shaded and saline more than 34.3 psu are hatched.

Development of branching can be found also at 50 m depth in hydrographic data taken on February 2~7, 1991 and February 17~23, 1992 by the Korean Fisheries Research and Development Agency. Hydrographic surveys were repeated on April 9~27, 1991 and from 8 April to 4 May 1992.

In February, the water warmer than 12°C in 1991 and 14°C in 1992, passing the Korea Strait, was not observed north 36°N along the Korean coast (Fig. 4a, c). Although the survey was not conducted at the same time, it provided invaluable data to confirm the presence of the front in the east-west direction around 36°N which implies the absence of the EKWC. The formation of the EKWC was clear (Fig. 4b, d). The water warmer than 14°C in 1991 and 15°C in 1992 splits clearly into two parts as leaves the strait. One of it flowed north 36°N along the Korean coast, the other was along the Japanese

coast as shown in SST (Fig. 3).

4. Vertical section along the Korean Coast

The section along the 2nd stations of each line was taken to examine seasonal variation of the EKWC (See Fig. 2 for stations). The most southern one is station A2 which is located at the deep trough of the Korea Strait. Those from B2 to D2 are on the sill whose depths are about 150 m (Fig. 5). Station E2 and I2 are on the southern slope and the bank respectively. The depth of the stations G2 and J2 is about 500m.

The cold water less than 5°C which is consisted of the East Sea Proper Water and the salinity minimum layer water (CHO and KIM, 1994) is shaded and the saline water more than 34.3 psu which represents the TWW are hatched. The strong permanent thermocline with 5~10°C in temperature between the TWW and the water colder than 5°C, deepens

towards the Korea Strait during entire period except February. In February, a mixed water with 8~10°C in temperature is well developed, separating the TWW and the cold water. The thermal front between the mixed and the TWW around station E2 suggests the absence of the EKWC north of the continental slope in February. The saline water more than 34.3 psu, which can be used as another criteria for the TWW, is not observed north of station G2.

In April, the depth of 5°C isotherm becomes shallow about 100 m in the Ulleung Basin, as the cold water expands into the Ulleung Basin from north. The isotherm of 12°C moved near station J2 and the saline waters greater than 34.3 psu are observed at all stations. This indicates the formation of the EKWC along the Korean coast. The TWW whose thickness is about 140 m in the Korea Strait becomes thinner (less 60 m) around station I2, which is about 150 km apart from the strait. In June, the isotherm of 5°C becomes further shallow and the cold water less than 5°C appears on the sill. The surface water less than 34.3 psu in salinity appears at the surface. Therefore the saline TWW is present in the middle layer. The TWW becomes thinner to north as in April. The slope of the 10°C isotherm is about 100 m/150 km from station C2 to I2.

The cold water moves further south in August. However the 5°C isotherm becomes deeper in the northern area, which reduces the slope of the 10°C isotherm. The temperature and salinity of the surface water is highest and lowest respectively during entire period. In October, the cold water on the sill retreats to slope, which increases the slope of the 10°C isotherm. The slope is about 70 m/150 km. However the cold water less than 8°C remains at station A2. The surface mixed layer is well developed, which makes the TWW deeper than in August. Although the surface layer becomes thicker than in August, it becomes colder and saline. Therefore the density increases compared with that in August. Salinity sections show that the EKWC which can be traced with the saline water more than 34.3 psu persists continuously except in February.

The same section in 1992 shows similar seasonal variation of the cold water and the

TWW, although it is not shown here. The cold water becomes thicker in the strait in summer and thinner in winter. The TWW is not observed north of station G2 in winter but appears in other seasons.

Although we examine only one section, the fact that the temperature at 200 m depth in the Ulleung Basin for 1931-1940 is lower in August than in February (KANG, 1992), indicates that the lower layer in the Ulleung Basin and the Korea Strait is colder in summer than in winter generally. The sea water gets heat from the atmosphere in summer in this area (KANG, 1984). Therefore the decrease of the temperature can be explained only by the southward flow of the cold water from the East Sea which is the only place where the cold water lower than 10°C is found. Directly measured results (ISOBE *et al.*, 1991; OMURA and KAWATATE, 1994) all show consistently southward flows of the cold water in the Korea Strait in summer.

5. Conclusion and Discussion

Satellite images taken in April of 1991 and 1992 with concurrent hydrographic data provide an evidence of branching of the TC. The distribution of SST clearly shows that the warm water flowing into the East Sea splits into two branches as it leaves the Korea Strait. One branch flows eastward along west coast of the Japan and the other one northward along the east coast of Korea, forming the EKWC. Contrast with April, non-branching were observed in February of 1991 and 1992.

ISODA and SAITOH (1993) suggests that the branching is not persistent, but episodic and the warm and saline waters are supplied by the northward intruding eddy process in spring and summer not in winter and autumn. Temperature distribution at surface in February of the 1989 and 1990 also show the absence of the EKWC (Fig. 6). Considering non-branching in February from 1989 to 1992 and the result of ISODA and SAITOH (1993) in 1987, it is believed that the absence of the EKWC is a permanent feature in winter.

Figure 7 shows schematically vertical distribution of the cold water (shadow area) and the TWW (hatched area) in each season. The cold water is defined by temperature lower than

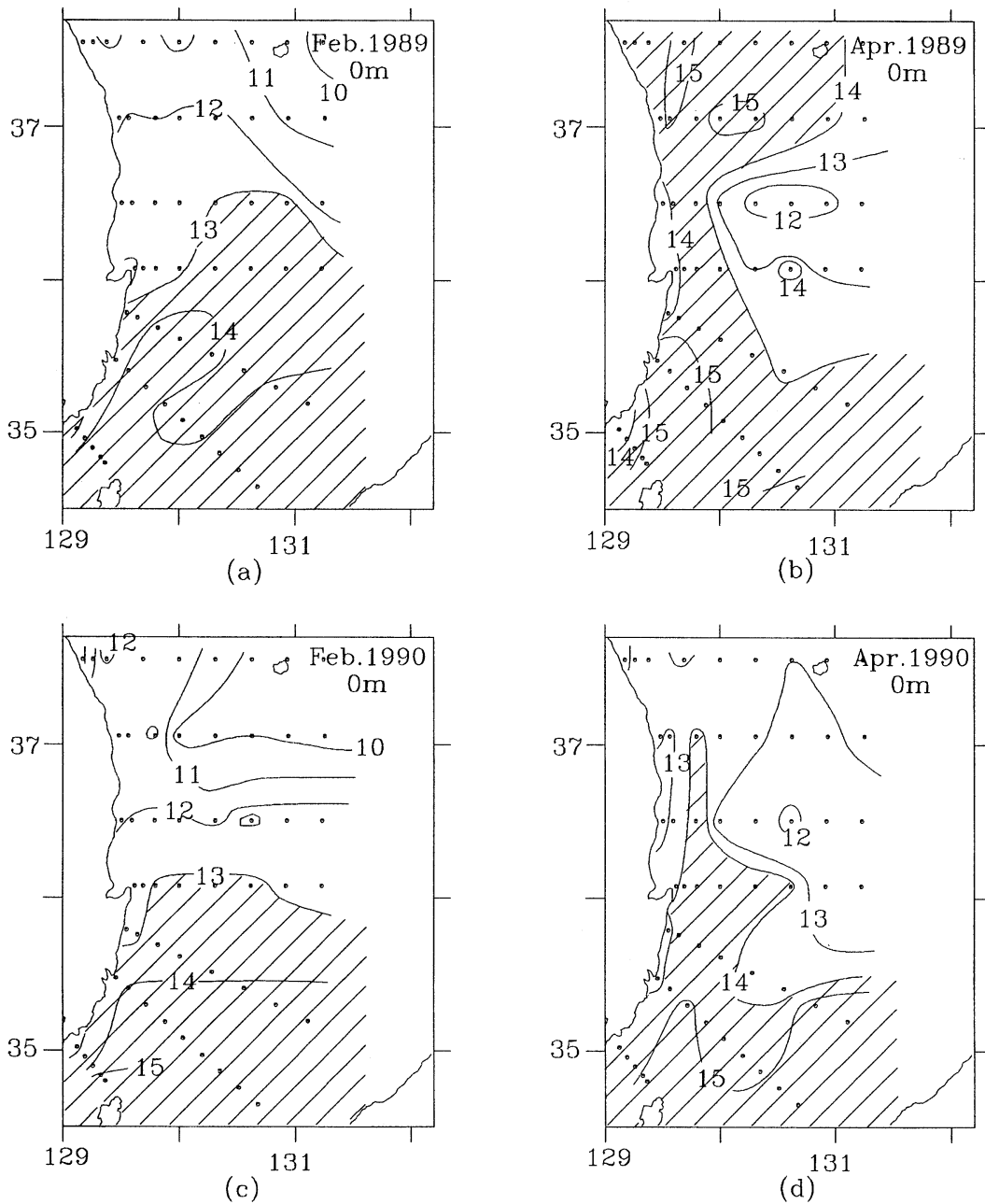


Fig. 6. Distribution of SST from hydrographic survey in (a) February 1989, (b) April 1989, (c) February 1990 and (d) April 1990.

5°C, the mixed water between 5°C and 10°C and the TWW higher than 34.3 psu and the surface water less than 34.3 psu. The cold water becomes thicker in the strait in summer when the density of the TWW decreases and retreats in

winter when it increases. Further studies are necessary to reveal that the southward extension of the cold water is related with the density of the TWW or not. This study shows that the EKWC is formed when the cold water

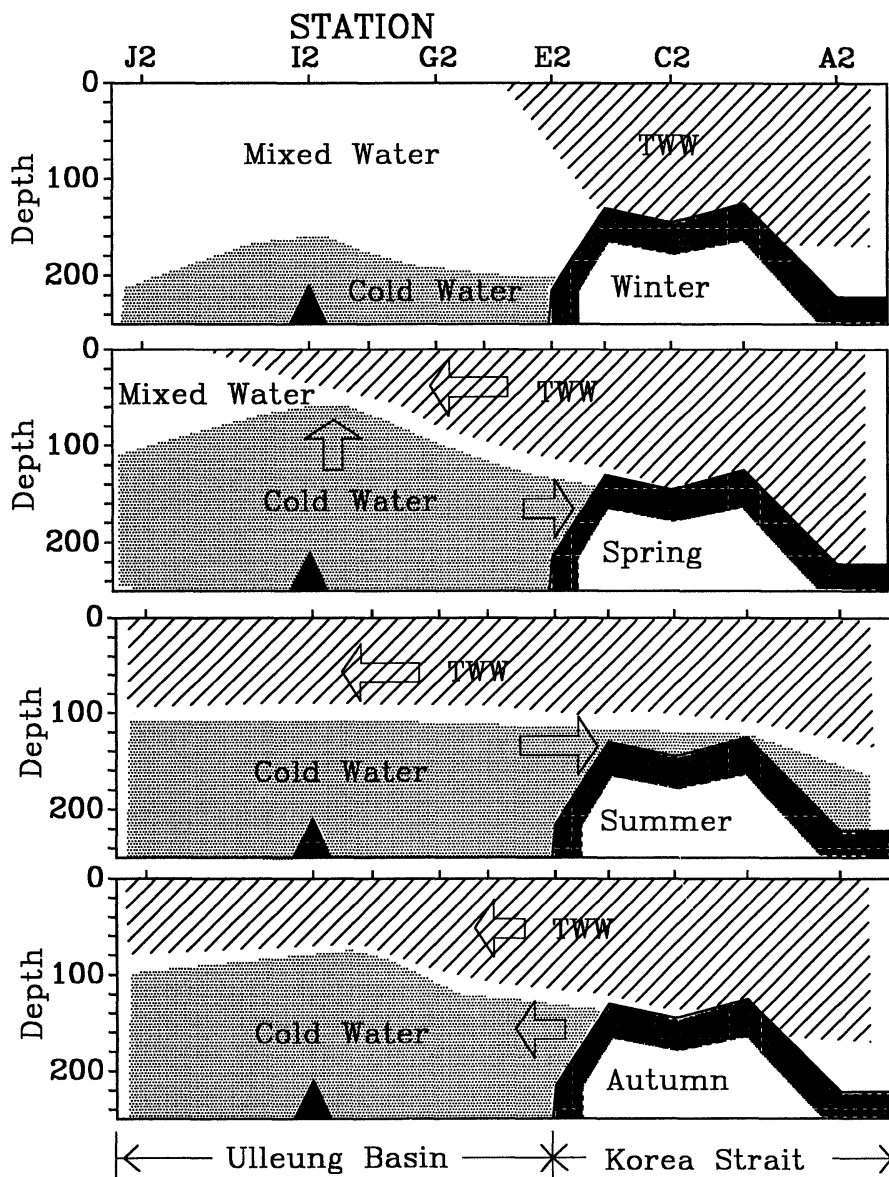


Fig. 7. Schematic distribution of the lower cold water (shadow area) and the Tsushima Warm Water (hatched area). Arrows indicate the direction of the water movement. The cold water represents the water colder than 5°C, and the TWW saline more than 34.3 psu and the surface water less than 34.3 psu.

becomes thicker in the strait and it is absent when the cold water is located at a deeper depth in the basin.

The absence of the EKWC bears an exceptional importance in terms of not only the branching mechanism but also the circulation in the East Sea. YOON (1982 *a, b, c*) and KAWABE

(1982b) treated the branching of the TC as dynamics of a warm current which is forced through a shallow strait into a deep basin of motionless cold water and reproduce the permanent branching numerically. However the absence of the EKWC in winter implies that the motion of the cold water is interlocked with

the branching.

Concerning the formation of the EKWC, the planetary beta effect has been recognized as the cause of it. However simple calculation shows that the change of potential vorticity due to the shrinking of the TWW along the Korean coast is greater than the planetary beta effect. Neglecting external forcing and friction, we can show that quasi-geostrophic motion of uniform upper layer conserves the potential vorticity such as

$$\frac{f}{H} = \frac{f_0}{H_0} \left(1 + \frac{\beta}{f_0} y - \frac{\alpha}{H_0} y \right) = \text{constant.}$$

Here β is the beta-effect, α is the slope of the bottom and H_0 is the mean thickness of the upper layer. In this case, let's assume the permanent thermocline as a bottom for the upper layer, because the upper TWW shrinks due to the presence of the lower cold water along the Korean coast. Locally $\frac{\beta}{f_0} = 10^{-9} \text{cm}^{-1}$ (Kim *et al.*, 1991) and $\frac{\alpha}{H_0} = 1.3 \sim 5.3 \times 10^{-8} \text{cm}^{-1}$ as the permanent thermocline changes 20~100 m over about 150 km as shown in along-strait section (Fig. 5). When the TWW experience shrinking due to the presence of the lower layer, it takes the negative relative vorticity which can induce the northward flow along the Korean coast. However the cold water which locates at deep depth in winter could not induce the negative vorticity. This simple calculation indicates that the effect of the cold water on the formation of the EKWC is important. Concerned with the effect of the cold water, Isobe (1994) argued that the Jebar effect in the Korea Strait which is mainly caused by the cold water along the Korean coast in summer, supplies the negative vorticity. His result in which the bottom cold water could supply the negative vorticity, is consistent with this study. However his interest is on the seasonal variation of the main axis of the TC in the strait. Our recent study to investigate the branching of the TC in the Korea Strait by the hydraulic model with two active layer, showed quantitatively the effect of the cold water in the formation of the EKWC (CHO, 1995).

Acknowledgement

The authors express thanks to captain,

officers and crew of the R/V Busan-802, Korea Hydrographic Office and graduate students in the Ocean Circulation Laboratory, SNU for collecting the hydrographic data. Mr. J. S. KIM helped to process IR images. This research was supported in part by the Basic Sciences Research Institute Program, Korea Ministry of Education, 1996. Ilju Academic and Cultural Foundation supported this research in 1995-1996. We also appreciate the support by the Korea Science and Engineering Foundation in 1993-1995.

References

- CHO, Y., -K (1995): Hydrography and hydraulic model of the currents in the Korea Strait. Ph. D. Thesis, Seoul National University, 142pp.
- CHO, Y. -K. and K. KIM (1994): Two modes of salinity minimum water in the Ulleung Basin. *La mer*, **32** (4), 33-40.
- ISOBE, A., A. KANEKO, S-K. BYUN, S. D. CHANG and S. TAWARA (1991): On the current structures in the western channel of the Tsushima/Korea Strait from the result of the ADCP survey in September 1989- Engineering Science Reports. Kyushu University **13** (1), 45-51 (in Japanese).
- ISOBE, A. (1994): Seasonal variation of the vertically averaged flow caused by the Jebar effect in the Tsushima Strait. *J. Oceanogr.* **50**, 617-633.
- ISODA, Y. and S. SAITOH (1993): The northward intruding eddy along the east coast of Korea. *J. Oceanogr.* **49**, 443-458.
- KANG, K, R, (1992): A study on the thermal structure of the East Coastal Water of Korea. M. S. Thesis, Pusan National University, 101pp. (in Korean with English abstract).
- KANG, Y. Q. (1984): Atmospheric and oceanic factors affecting the air-sea thermal interaction in the East Sea. *J. Oceanol. Soc. Korea*, **19** (2): 163-171.
- KAWABE, M. (1982a): Branching of the Tsushima Current in the Japan Sea, Part I. data analysis. *J. Oceanogr. Soc. Japan*, **38**, 97-107.
- KAWABE, M. (1982b): Branching of the Tsushima Current in the Japan Sea, Part II. numerical experiment. *J. Oceanogr. Soc. Japan*, **38**, 183-192.
- KIM, K., K.-R. KIM, J.-Y. CHUNG and H.-S. YOU (1991): Characteristics of physical properties in the Ulleung Basin. *Jour. Oceanol. Soc. Korea*. **26** (1), 83-100.
- National Fisheries Research and Development Agency, Korea (1992-1993): Annual report of oceanographic observation in 1991-1992, 40-41.
- OMURA, K, and K. KAWATATE (1994): Hydrographic

- features of the bottom cold water in the west Tsushima Channel. Bull. Fukuoka Fisheries Mar. Technol. Res. Cent. 2, 93-101 (in Japanese).
- SVERDRUP, H. U., M. W. JOHNSON and R. J. FLEMING (1942): The Oceans, their physics, chemistry and general biology, Prentice-Hall, New York, 1087 pp.
- UDA, M. (1934): Results of simultaneous oceanographic investigation in the Japan Sea and its adjacent waters during May and June, 1932. Jour. Imp. Fish. Exp. Station, 5, 57-190.
- YAMAGUCHI Prefectural Open-Sea Fisheries Experimental Station (1992-1993): Reports on Affairs for Forecasting Fishery and Oceanographic Conditions in the 1991-1992 Fiscal Years (in Japanese).
- YOON, J. H. (1982a): Numerical experiment on the circulation in the Japan Sea, Part I: Formation of the East Korean Warm Current. J. Oceanogr. Soc. Japan, 38, 43-51.
- YOON, J. H. (1982b): Numerical experiment on the circulation in the Japan Sea, Part II: Influence of seasonal variations in atmospheric conditions on the Tsushima Current. J. Oceanogr. Soc. Japan, 38, 81-94.
- YOON, J. H. (1982c): Numerical experiment on the circulation in the Japan Sea, Part III: Formation of the nearshore branch of the Tsushima Current. J. Oceanogr. Soc. Japan, 38, 119-124.

Received January 13, 1996

Accepted May 13, 1996

The stratification variations during spring and neap tidal periods in Deukryang Bay, Korea

Byung-Gul LEE*, Tetsuo YANAGI**, Hidetaka TAKEOKA**
and Kyu-Dae CHO***

Abstract: The stratification-destratification (SD) phenomenon in Deukryang Bay, Korea was studied based on the data of wind speed, heat flux through the sea surface and tidal current amplitude. To find out the main factors causing SD, we introduce the rate of energy balance of the surface heat flux, tidal and wind stirring proposed by SIMPSON and HUNTER (1974). The calculated energy of three terms are compared, in which energy of wind stirring effect was one order smaller than that of heat flux and the tidal stirring. Using the results, we implement time integration of the potential energy with the several ε values (tidal mixing efficiency) of 0.010~0.014 at interval 0.001 and with wind speeds of 1.5 and 2.0 times larger than observed values at land. It shows that the variation of SD phenomenon in the bay mainly depends on tidal stirring and sea surface heating in summer.

1. Introduction

Many oceanographers have studied stratification-destratification (SD) phenomenon during spring-neap tidal cycle (GRIFFIN and LEBLOND, 1990; MACKAY *et al.*, 1990; LARGIER and TALJAARD, 1991) since SIMPSON and HUNTER (1974) proposed the governing equation on the balance between the time rate of change of the potential energy in a unit water column.

Most of the study area, however, was confined in a coastal zone and estuaries associated with fresh river water discharge or high salinity area. Basically they tried to explain the temporal variation of a front formed by the horizontal juxtaposition of two distinct water masses and the interaction between the different water masses.

SAMARASINGHE (1989) pointed out temporal changes of salt-wedge movement of the whole domain during spring-neap tidal cycle at the Shark Bay in the Australian Bight, and explained such phenomena based on a density

current effect. However, he did not show the critical changes of stratification during spring and neap tidal periods in the day and did not estimate the relationship of other environmental factors.

In Korea, there are so many bays in the southern part of the country and their sizes are mostly less than 1000 km², where tidal current is predominant and affects oceanic phenomena in the whole domain of the bays. The Deukryang Bay, one of such bays is a semi-enclosed bay with three open channels. The area is approximately 374.4 km² and the average depth 7.5 m (Fig. 1). The eastern part of the bay dips steeply about 30 m while depth decreases slowly on the western part less than 5 m depth.

Tidal elevation ranges in the bay are less than 2 m and the tidal current amplitude from 0.2 m/sec in neap tide to 0.6 m/sec in spring tide in which semi-diurnal components are dominant (LEE, 1992).

The objectives of this paper are firstly to show the drastic changes of SD phenomena during short periods between spring-neap tidal cycle, and second we check the magnitudes and variations of wind speed, sea surface heat flux and tidal current amplitude. Finally, we estimate the budget of potential energy from

* Department of Civil Ocean Engineering, Cheju National University, Cheju 690-756, Korea

** Department of Civil and Ocean Engineering, Ehime University, Bunkyo 3, Matsuyama 790, Japan

*** RCOID, National Fisheries University of Pusan, Pusan 608-737, Korea

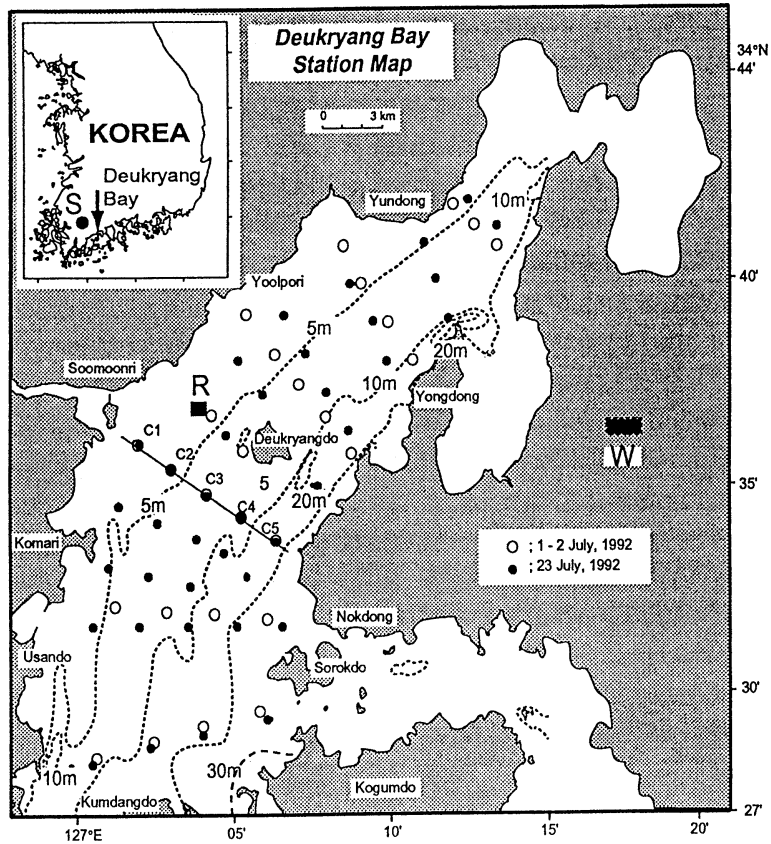


Fig. 1. Location of the Deukryang Bay and observation points in 1-2 July and 23 July, 1992. S denoted solar radiation station, R and W are current mooring and wind speed stations.

observed data, in addition to prediction the beginning and the ending time of SD phenomenon in summer.

2. Observation results during spring and neap tidal periods

We observed temperature and salinity twice in 1-2 July (spring) and 23 July (neap), 1992, respectively. Three selected stations were shown in Fig. 1 in which the first observation points were 27 and the second were extended to 37 for more detail observation so that the station positions between the first and the second were different except transect C. The mooring station of current meter was R and the wind speed was W, and the solar radiation S was observed at Kwangju City located for from the study area about 100 km since there is no meteorological observation center including the solar radiation data near the study area.

Figure 2 presents T-S diagrams for the observation data at all stations of surface and bottom during the spring and the neap tidal periods. In the figure, the salinity variations were less than 1 PSU at twice observations and appeared to be insignificant compared to the temperature ones. The temperature in spring tide, ranged from 19 to 25°C and the character of water mass in bottom and surface layers is almost the same while in neap tide the temperature from 20 to 27°C, water masses are separated into two parts. The intensities of the surface and bottom temperature gradients were so much different between neap and spring tidal periods.

Figure 3 was constructed to present vertical temperature, salinity and density distributions, along section C. The data indicated the drastic changes of vertical structures between two observation periods. From the figure, the vertical

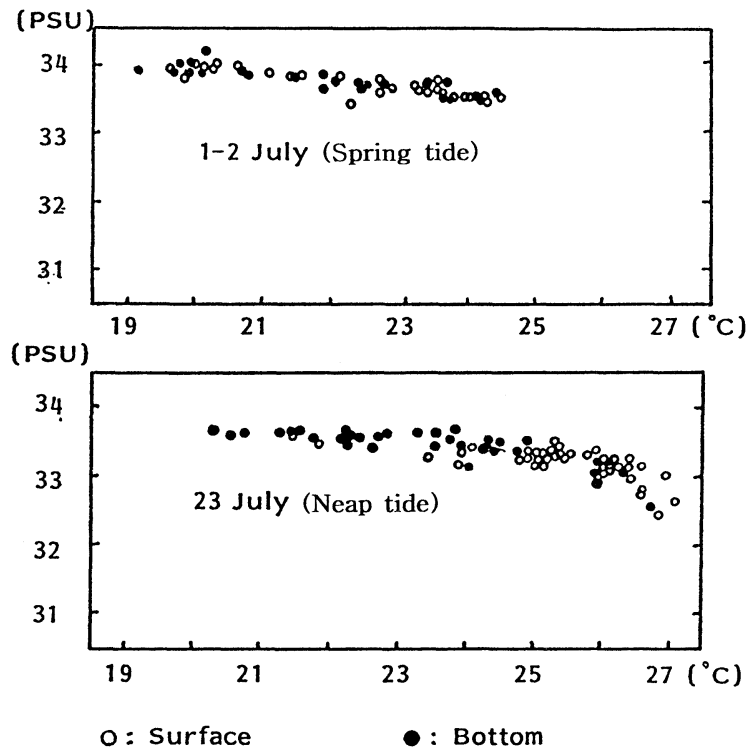


Fig. 2. The variations of temperature and salinity from bottom to surface (T-S diagram) during spring and neap tidal cycle.

temperature and density gradients in neap tide showed strong stratification while in spring tide vertically well mixed. The temperature variations at spring and neap tides are larger than the salinity ones so that the temperature is more effective to form vertical stratification in the periods. Although the partially mixed form at C1, C2, and C3 appeared during neap tide, it looks like local phenomenon since it occurred only in shallow region limited less than 5 m depth. Regarding this, SD characteristics in the bay can be mainly controlled by the the heat flux through the sea surface, tidal and wind stirring effects.

3. Heat Flux, Wind and Current Variations during Spring and Neap Tidal Periods

Oceanographical and meteorological data were compared for estimating the variability of SD phenomenon during spring-neap tidal cycle. Wind speed, surface heat flux, and tidal current variations are shown in Fig. 4.

The heat flux was calculated based on the method of YANAGI (1982) and GILL (1984), and daily mean variation of sea surface water temperature was calculated from linear interpolation and extrapolation methods using two times observation on 1-2 July and 23 July. In Fig. 4, the wind speed ranges approximately from 1 to 2 m/sec, the heat flux from 0 to 200 Watt/m², the tidal current amplitude from 0.1 to 0.6 m/sec. Wind speed from 21 June to 23 July are not strong and not changed comparing to other factors. Moreover, the wind in the period of strong stratification was stronger than that of vertically well mixed condition. It gives an account of that the wind stirring effect for the stratification may be not the main factor in the bay.

The fluctuation of the heat flux was very large in spite of monthly average of 124 Watt/m², sometimes zero values happened because of a lot of cloud that prohibits the solar heating through the sea surface.

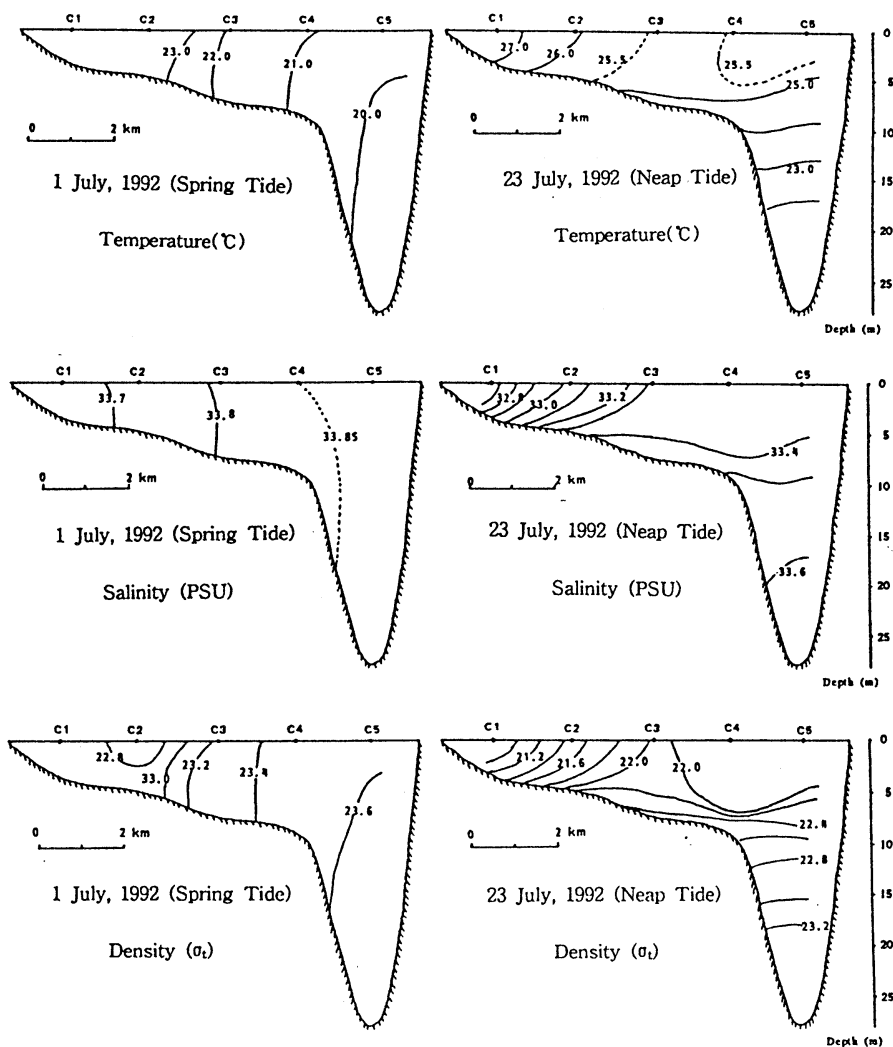


Fig. 3. hydrographic profile during spring and neap tidal cycle at typical central part of the Deukryang Bay along Section-C.

The stick current velocity diagram in the figure shows the manifest fluctuations of tidal current amplitude, particularly M_2 tidal current was dominated. The current amplitude was the largest in the first observation time while in the second the velocity was the lowest. From 13 to 20 July, the current was relatively weaker than that during the former spring period so that presumably comparatively low tidal mixing occurred at this period.

4. The budget of potential energy during spring and neap tidal periods

It was clear that the SD phenomenon during spring-neap tidal cycle existed in Deukryang Bay from previous results. We showed that is phenomenon as related to mostly the heat flux and the tidal current amplitude from data analysis.

To estimate the variation of stratification due to three factors, we used basically the simple potential energy arguments given by SIMPSON and HUNTER (1974), ELLIOTT (1991), and TAKEOKA *et al.* (1993) who studied at

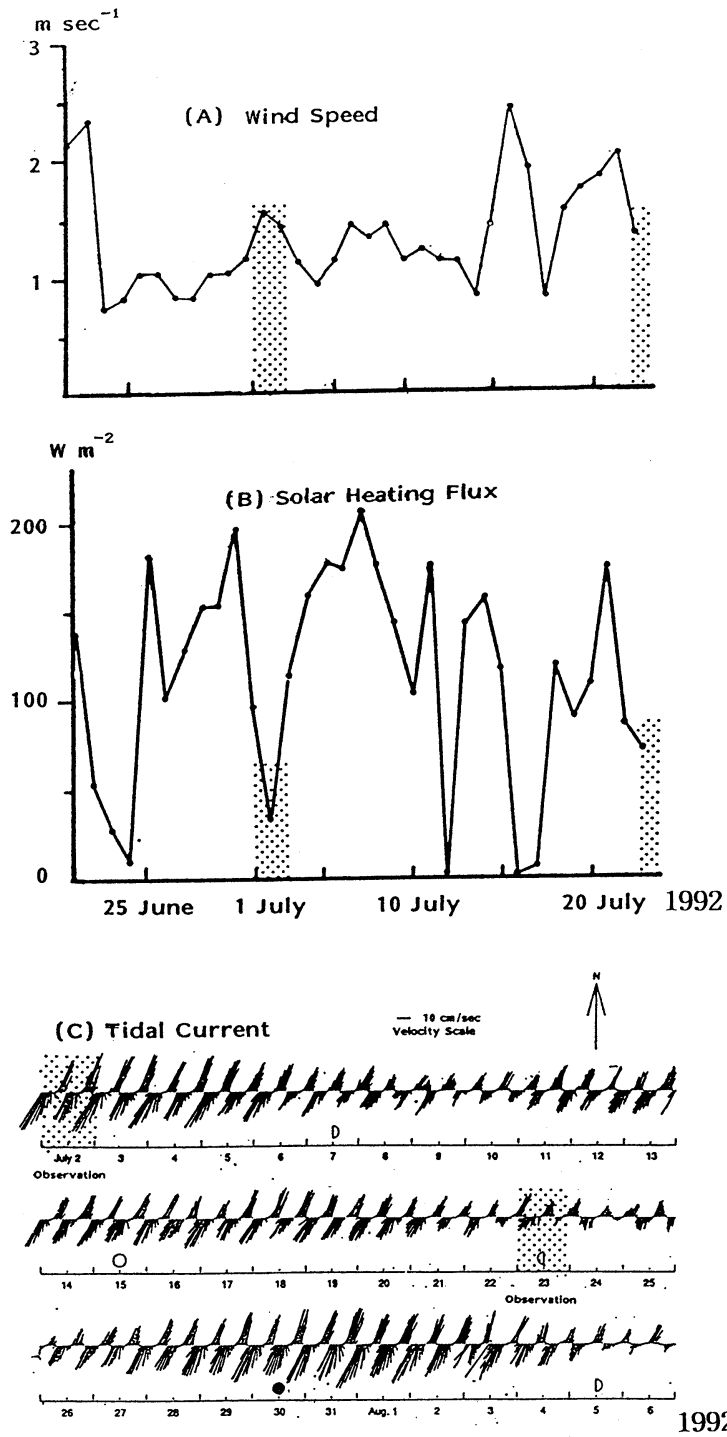


Fig. 4. The time variations of the wind speed, the heat flux and tidal current amplitude. \dots : Observation periods of hydrographic data.

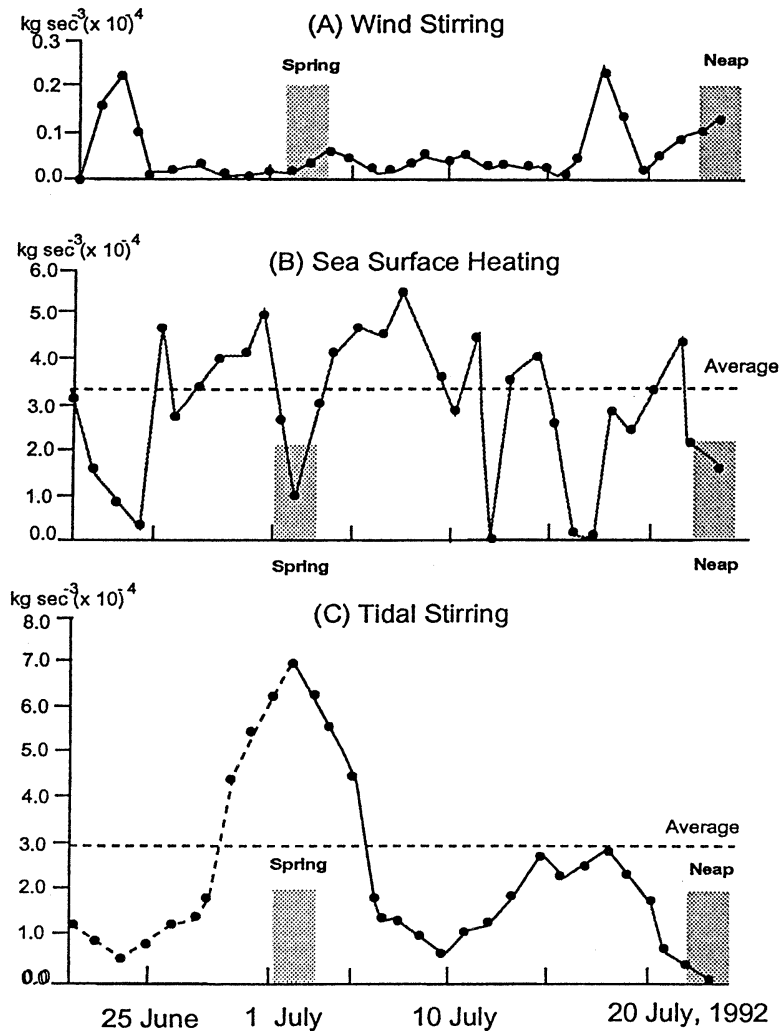


Fig. 5. The time variations of the rate of potential energy anomaly of a water column based on Fig. 4. ∴ : Observation periods of hydrographic data.

European Shelf and at Bungo Channel in Japan.

If we assume that the total rate of change in potential energy of a water column is only influenced by the wind and the tidal stirring and the sea surface heating, the daily mean rate of change in the energy will be given by (ELLIOTT, 1991)

$$\frac{dE}{dt} = \frac{g\alpha}{2C_\rho} Q_T H - e C_A \rho_a W^3 - \epsilon C_D \rho_w U^3 \dots (1)$$

Here, E is the potential energy of a water column. The first term in the right hand of

equation (1) is the loss of potential energy by the surface heating, the second and the third are the gain of potential energy by the wind and tidal current, where g is gravitational acceleration, α is thermal expansion coefficient, ρ_a and ρ_w are air and water density, e and ε are efficiencies of surface and bottom mixing process, C_A and C_D represent the surface and bottom drag coefficients. W is wind speed, U is the absolute tidal current speed. H is water depth (10 m). If the right side of equation (1) is positive, stratification is intensified, and if it is negative, the stratification is weakened.

In calculation procedure of above equation, we used tentatively 0.015 ϵ value proposed by YANAGI and TAMARU (1990) because they successfully applied this value to Bungo Channel, Japan. C_D and C_A are given as 0.0025 and 0.000065 by SIMPSON and BOWERS (1981). The tidal energy values from 20 to 30 June are extrapolated assuming that tidal change pattern from 20 to 30 June is the same as the pattern from 1 to 10 July because of the symmetric characteristics of tidal current amplitude in time.

The calculated results are shown in Fig. 5. As we expected previously, the wind stirring effect is approximately one order of magnitude smaller than the surface heating and the tidal stirring ones. As considering the rate of potential energy derived by wind stress, we argue that the wind effect in summer can be omitted for analyzing SD phenomenon during the observation period. Comparing the energy of the tidal stirring to the surface heating, during the first spring tidal period approximately from 27 June to 5 July, the tidal energy was larger than the heating energy while in the second spring tide of middle of July, the tidal energy was similar to the heating one in which it seems to be impossible to destroy the stratification already made by sea surface heating. Therefore, the stratification of the first neap tide from 7 to 13 July may also be weaker than that of second neap tide. Possibly, destratification sustained from end of June to early of July, and stratification became to be formed from early July if the surface heating was continually stable.

5. Discussion

Our hydrographic data of Deukryang Bay showed critical changes of vertical structure of temperature, salinity and density between spring and neap tidal periods. As we analyzed meteorological and oceanographical data using three energy equation, it was found that the tidal stirring and the sea surface heating played important roles for the stratifying and mixing processes while wind stirring effect was one order smaller than the previous two factors. However, for more accurate estimates of the effects of sea surface heating and wind and tidal stirring in the bay, we tried to

undertake integrate of the rate of potential energy variation between spring-neap tidal cycle, and then estimate the stratification intensity quantitatively.

The integral equation of (1) can be presented as following equation,

$$E_c = \int_{t1}^{t2} \left[\frac{ga}{2C_D} Q_{\tau} H - eC_A \rho_a W^3 - \epsilon C_D \rho_w U^3 \right] dt \dots\dots(2)$$

where $t1$ is the start time of observation, 1 July, and $t2$ is the end time of observation, 23 July. E_c is the calculated potential energy anomaly. In order to find out an optimal ϵ values for the Deukryang Bay, equation (2) following several ϵ values of 0.010~0.014 at 0.001 interval was calculated and its results were compared with the observed value in Table 1.

To compare the calculated result to the observed one, the potential energy anomaly E_0 of observation data was calculated by the following equation (Bowden, 1984) :

$$E_0 = \int_{-h}^0 [\rho - \bar{\rho}] g z \, dz \dots\dots\dots(3)$$

where $\bar{\rho} = \frac{1}{h} \int \rho dz$

ρ is a density at a depth z , $\bar{\rho}$ is averaged density of a total water column. In the calculation, the data of section C located at the nearest stations from the current meter mooring were averaged.

We also showed, in Table 1, the potential energy variations according to the several wind speed conditions, because following YANAGI (1980) and IMANUKI, the wind speed at the sea surface is larger than that at land by about 1.5 or 2 times due to surface roughness differences. In Table 1, W_f is the ratio of an presumed wind velocity at the sea (W_s) and an observed wind velocity at the land (W_M). In the table, the calculated potential energy was very similar to the observed one in the cases where $W_f=1.0$ and $\epsilon=0.014$, $W_f=1.5$ and $\epsilon=0.012$, and $W_f=2.0$ and $\epsilon=0.010$.

Figure 6 indicates the potential energy variation selected in the case of $\epsilon=0.014$. The start time $t1$ was 1 July. From the figure, we know that the heating energy was larger than the wind and tidal energy from 5 July. The figure also shows that the stratification gradually

Table 1. The Potential Energy Anomaly Changes for the Coefficients of Tidal Efficiency and Wind Speed (W_M is observation wind at land, W_S is assumed wind at sea)
Unit : kg sec^{-2}

ϵ Value	Model						Obser.	
	$W_f (= W_S/W_M)$	0.010	0.011	0.012	0.013	0.014		0.015
1.0		262.66	241.84	221.73	201.62	181.51	162.60	194.56
1.5		238.02	217.91	197.80	177.69	157.58	139.18	
2.0		191.43	171.32	151.21	131.10	111.11	93.56	

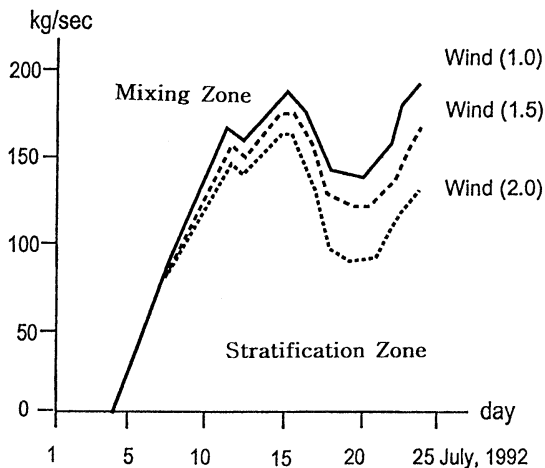


Fig. 6. Potential energy anomaly variation from 5 July to 23 July ($\epsilon = 0.014$). The number of () indicated wind speed intensity of ratio of wind at sea surface and wind at land.

increases until 15 July. However, during the second spring tidal period from 16 to 19 July, the stratification decreases by strong tidal current amplitude although the current energy could not overcome the total potential energy caused by the sea surface heating. From the figure, we found that stratification continually sustained in the observation period from 5 to 23 July. The patterns of other energy variations following other ϵ values, which were not shown in this paper, should resemble at of $\epsilon = 0.014$, although the amount of total energy might be different during the same periods.

From the results, we supposed that ϵ -value ranged from 0.010 to 0.014 and from 5 or 6 July and the stratification had been started by the sea surface heating. It was emphasized that the strong sea surface heating in summer permitted only a short time of the vertically well

mixed pattern and it might be less than one week based on the rate of energy variations.

Acknowledgements

This work was supported by Research Center for Ocean Industrial Development, National Fisheries Univ. of Pusan designated by KOSEF, in 1992.

References

- BOWDEN, K. F. (1983): Physical Oceanography of Coastal Water. John Wiley & Sons Inc., Brisbane, 302 p.
- ELLIOTT, A. J. and T. CLARKE (1991): Seasonal stratification in the northwest European Shelf Seas. *Continental Shelf Research*, **11**, 467-492.
- GRIFFIN, D. A. and P. H. Leblond (1990): Estuary/ocean exchange controlled by spring-neap tidal mixing. *Estuarine, Coastal and Shelf Science*, **30**, 275-297.
- GILL, A. E. (1982): Atmosphere-Ocean Dynamics. Academic Press, Oxford, 662 p.
- IMANUKI, A. (1982): Turbulence and Atmosphere. Tokyo Press, Tokyo, 191 p.
- LEE, J. C. (1992): Multidisciplinary oceanographic studies in Deukryang Bay, Korea. 2nd International Conference Reports, Research Center for Ocean Industrial Development, Korea, 3-4.
- LARGIER, J. L. and S. TALJAARD (1991): The dynamics of tidal intrusion, retention, and removal of seawater in a Bar-Built Estuary. *Continental Shelf Research*, **33**, 325-338.
- MACKAY, H. M. and E. H. SCHUMANN (1990): Mixing and circulation in the Sundays River estuary, South Africa. *Estuarine, Coastal and Shelf Science*, **31**, 203-216.
- SAMARASINGHE, J. R. de Silva (1989): Transient salt-wedges in a tidal gulf: criterion for their formation. *Estuarine, Coastal and Shelf Science*, **28**, 129-148.
- SIMPSON, J. H. and D. BOWERS (1981): Models of

- stratification and frontal movement in shelf seas. *Deep Sea Research*, **28A**, 727-738.
- SIMPSON, J. H. and J. R. HUNTER (1974): Fronts in Irish Sea. *Nature*, **250**, 404-406.
- TAKEOKA, H, H. AKIYAMA and T. KIKUCHI (1993): The Kyucho in the Bungo Channel, Japan "Periodic intrusion of oceanic warm water". *Journal of Oceanography*, **49**, 369-382.
- YANAGI, T. (1980): Variability of the constant flow in Osaka Bay. *Journal of the Oceanographical Society of Japan*, **36**, 246-252.
- YANAGI, T (1981): Heat budget of Uwajima Bay. *Umi to Sora (Sea and Sky)*, **58**, 13-20 (in Japanese).
- YANAGI, T and H. TAMARU (1990): Temporal and spatial variation in a tidal front. *Continental Shelf Research*, **7**, 61-627.

Received December 24, 1995

Accepted March 22, 1996

Tidal energy in Suyoung Bay, Korea

Dong-Sun KIM* and Tetsuo YANAGI*

Abstract: To investigate the characteristic of M_2 tide, tidal current and tidal energy in Suyoung Bay of Korea, we developed two-dimensional numerical model under the cartesian co-ordinate. The maximum speed of M_2 tidal current is about 30cm s⁻¹ at the north-eastern and south-western part of the bay. M_2 tidal energy flux in Suyoung directs from the north-east to the south-west. The maximum values of M_2 tidal energy flux are seen at the south-eastern and north-eastern part of the bay and M_2 tidal energy loss by bottom friction at unit area in Suyoung Bay is 34 ergs s⁻¹ cm⁻².

1. Introduction

Suyoung Bay is situated at the south-eastern coastal area of Korea where the topography gradually widens and deepens from the mouth of Suyoung River to off-shore. It is a coastal plain type estuary whose shape is nearly triangle. The inner bay water mass is directly subjected to the intrusion of the off-shore water mass (Fig. 1).

By the report of the Pusan City of Korea (1984), the semi-diurnal tidal component is distinguished and the tidal form number ($K_1 + O_1 / M_2 + S_2$) is 0.11~0.17 in Suyoung Bay. The average tidal range is about 101cm, 36cm in spring and neap tide, respectively. The amplitude of M_2 tide is 34.3cm and that of S_2 tide is 16.4cm.

Until now, the studies about tide and tidal current have been carried out by KIM and HAN (1982), JUNG and YOA (1992), KIM and LEE (1991, 1992) and HWANG (1993) but there has been no study on the tidal energy in Suyoung Bay. Therefore, in this study, we try to make clear the characteristic of M_2 tide, tidal current and to inquire about the M_2 tidal energy in Suyoung Bay.

2. Numerical model of tide & tidal current

The equations used in this numerical simula-

tion are the horizontal two-dimensional momentum and continuity equations for tide and tidal current in the homogeneous fluid under the cartesian co-ordinate which are as follows (YANAGI and OKAMOTO, 1985),

$$\frac{\partial \bar{u}}{\partial t} + (\bar{u} \cdot \nabla) \bar{u} + fK \times \bar{u} = -g \nabla \eta - \frac{\gamma_b^2 |\bar{u}| \bar{u}}{H + \eta} + \nu \nabla^2 \bar{u} \quad (1)$$

$$\frac{\partial \eta}{\partial t} + \nabla \cdot \{(H + \eta) \bar{u}\} = 0 \quad (2)$$

where \bar{u} is the depth-averaged velocity vector, t the time, ∇ the horizontal differential operator, $f (= 2\Omega \sin \Phi : \Omega = 7.27 \times 10^{-5} \text{sec}^{-1}$ and $\Phi = 35^\circ 07' \text{N}$) the Coriolis parameter, K the locally vertical unit vector, $g (= 980 \text{cm sec}^{-2})$ the gravitational acceleration, η the surface elevation above the mean sea level, $\gamma_b^2 (= 2.6 \times 10^{-3})$ the bottom frictional coefficient, H the local depth, $\nu (= 5.0 \times 10^5 \text{cm}^2 \text{s}^{-1})$ the horizontal eddy viscosity.

Equations (1) and (2) are approximated by finite-differences and are solved by the primitive method (YANAGI *et al.*, 1983). Depths used for this model were taken from Korean hydrographic chart No. 201C. The maximum depth is 54 m and the calculation grid size is 0.2 km \times 0.2 km. For the computational stability of numerical calculation, the time interval according to Courant-Friedrichs-Lewy criterion (MESINGER and ARAKAWA, 1976) is 5 sec in this study.

* Department of Civil and Ocean Engineering, Ehime University, Matsuyama 790, Japan

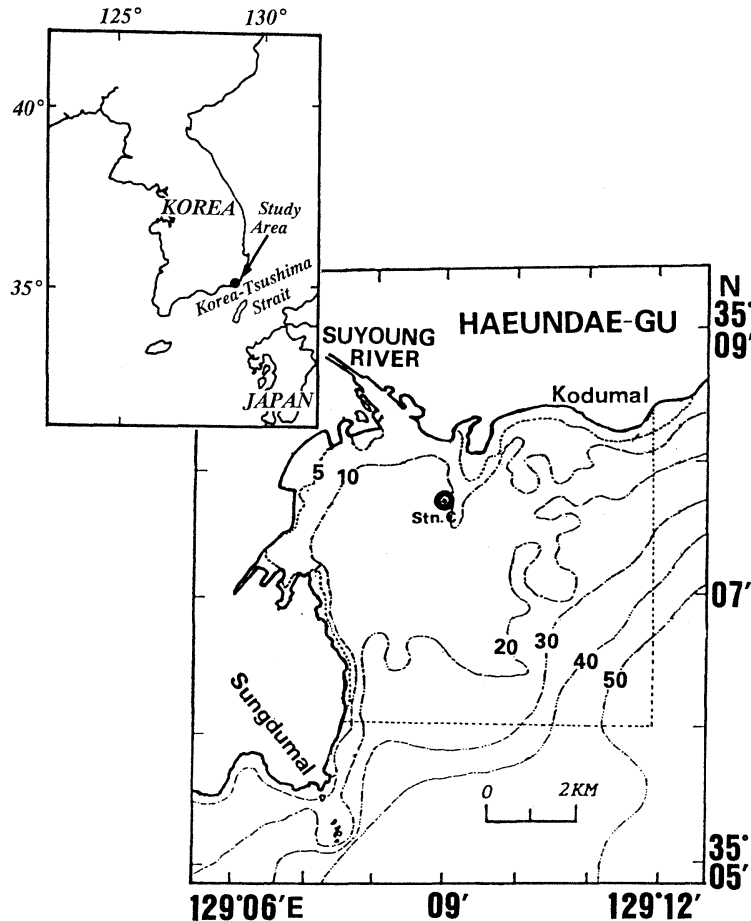


Fig. 1. Map of the study area where Stn. C is the current observation station. Broken line shows the open-boundary of numerical model. Numbers show the depth in meter.

Along the eastern open-boundary ($129^{\circ}12'E$), the M_2 tidal amplitude decreases from 34cm to 32cm toward the north and the phase decreases from 235° to 233° in the same direction. The phase at the southern open-boundary ($35^{\circ}06'N$) is 236° . As for the amplitude along the southern open-boundary, it decreases from 35cm to 34cm toward the east (ODAMAKI, 1989). M_2 tidal wave propagates from the north-eastern part to the south-western part of Suyoung Bay.

The quasi-steady state is obtained four tidal cycles after the beginning of the calculation and the harmonic analysis of sea surface elevation and current field is carried out at the 5th tidal cycle.

3. Results

The calculated results of amplitude and phase of M_2 tide and tidal current are shown in Fig. 2. The amplitude and phase of M_2 tide is about 34cm and 234° at the mouth of river, respectively. The amplitude of M_2 tidal current is about 40cm s^{-1} at the outer bay and about 1cm s^{-1} at the mouth of river. The phase of M_2 tidal current is 330° at the southern part of the bay and about 270° at the mouth of river. From this figure, we can understand that M_2 tidal wave behaves like a standing wave at the central part of Suyoung Bay because the phase difference between tide and tidal current is near 90° . The comparison of calculated M_2 tidal current ellipse and observed one (KIM *et al.*, 1991)

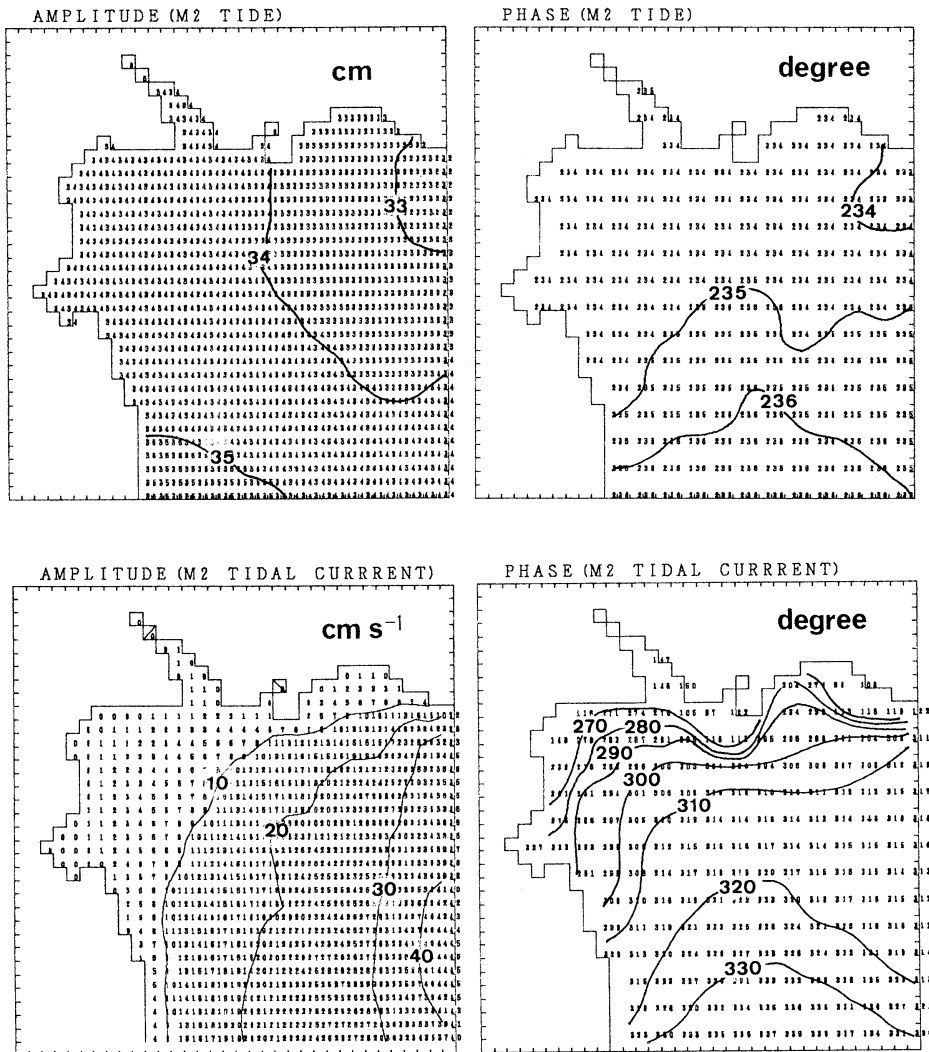


Fig. 2. Calculated amplitude (left) and phase (right) of M_2 tide (upper) and M_2 tidal current (lower). Phase is referred to the transit of Moon at 135°E .

at Stn. C (see Fig. 1) is shown in Fig. 3. The dotted circle shows the observed result 3 m below the surface of Stn. C, and the full circle the calculated one. The calculated M_2 tidal current ellipse by our model well reproduces the observed one in speed and direction.

The flow patterns of M_2 tidal current at the times of maximum flood and ebb at the central part of the bay are shown in Fig. 4. The M_2 tidal current at the maximum flood flows from the north-east toward the south-west. The tidal current at the inner bay flows parallel to the coastal line and the speed at the inner bay is

slower than that at the outer bay. Generally, the flow pattern of M_2 tidal current at the maximum ebb is opposite to that of maximum flood.

The calculated tide-induced residual current by M_2 tidal current, which is obtained by averaging calculated tidal current over one-tidal cycle, is shown in Fig. 5. Tide-induced residual current by M_2 tidal current makes two circulations in the bay, that is, one is the eastward flow at the north-eastern part and the other is the southward flow at the south-western part.

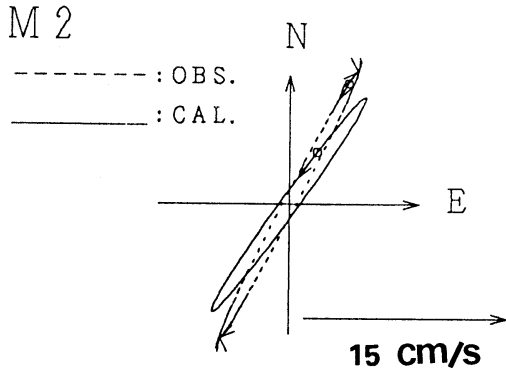


Fig. 3. Observed (full line) and calculated (dotted line) of tidal current ellipses at Stn. C.

4. Tidal Energy

The tidal energy flux through the n-th grid is estimated as follows (YANAGI *et al.*, 1982),

$$E_n = \frac{g}{2} V_n H_n \cos \Phi_n^{VH} \quad (3)$$

where V_n is the amplitude of tidal volume transport through the n-th grid, H_n the tidal amplitude at the n-th grid, and Φ_n^{VH} the phase difference between the tidal volume transport and the tidal elevation.

The vector average of tidal energy flux through each grid gives an indication of the direction and magnitude of tidal energy flow associated with M_2 tidal component. These vectors are shown in Fig. 6 (a). There is a noticeable reduction in tidal energy flux near the

shallower area. It is shown that M_2 tidal energy in Suyoung Bay is from the north-eastern part toward the south-western part and this is the same as the tidal wave propagation. Fig. 6 (b) shows the tidal energy flux which is intergrated at the eastern and southern boundaries. The tidal energy flux through the eastern boundary and that through the southern boundary are 4.69×10^{13} ergs s^{-1} , 3.11×10^{13} ergs s^{-1} , respectively. Therefore the tidal energy of 1.58×10^{13} ergs s^{-1} is lost in Suyoung Bay.

On the other hand, the M_2 tidal energy dissipation can be directly estimated by the following formula (TAYLOR, 1919),

$$E^f = \frac{4}{3\pi} \times \gamma_b^2 \times S \times \left(\frac{V}{A}\right)^3 \quad (4)$$

Here γ_b^2 is the bottom frictional coefficient ($= 2.6 \times 10^{-3}$), S the surface area of each grid, A the cross sectional area of each grid, V the amplitude of tidal volume transport across each grid. The application of this formula to the Irish sea (TAYLOR, 1919) demonstrated that the tidal energy flow from the ocean tides into a partially enclosed body of water was principally dissipated by the bottom friction. The distribution of M_2 tidal energy dissipation due to bottom friction in Suyoung Bay is shown in Fig. 7. The maximum values of M_2 tidal energy dissipation are seen around the south-eastern and the

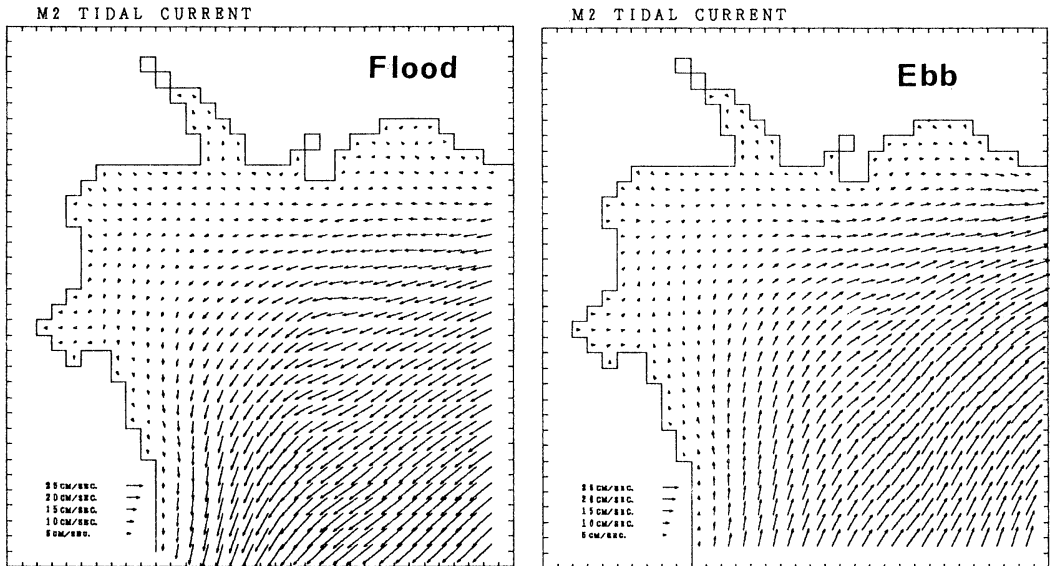


Fig. 4. Maximum flood (left) and ebb (right) M_2 tidal current.

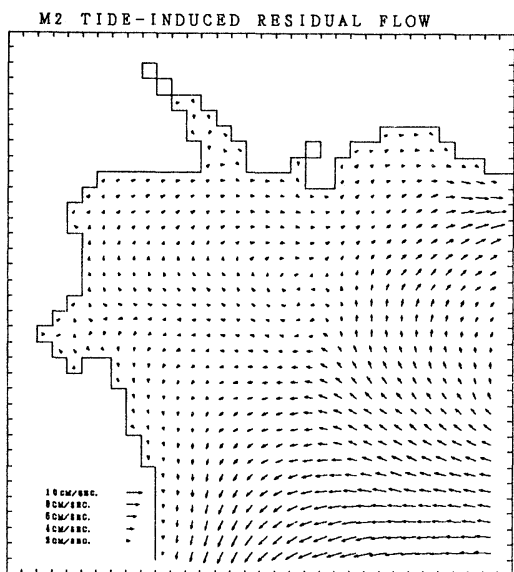
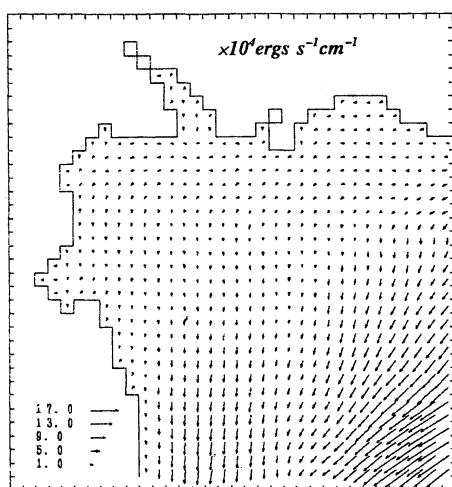


Fig. 5. Calculated tide-induced residual current by M_2 tidal current.

north-eastern part of the bay. The total M_2 tidal energy dissipation due to bottom friction is 1.03×10^{13} ergs s^{-1} in Suyoung Bay. The difference of M_2 tidal energy flux between the eastern and the southern boundaries (1.58×10^{13} ergs s^{-1}) is nearly the same as the calculated result ($=1.03 \times 10^{13}$ ergs s^{-1}) by Eq. (4). This fact shows the propriety of the M_2 tidal energy calculation of Eq. (3).



5. Discussion

We developed two-dimensional numerical model under the cartesian co-ordinate in Suyoung Bay of Korea, compared its results with that of field observation and calculated the M_2 tidal energy. The calculated M_2 tidal current by our model well reproduces the observed one in speed and direction. The tide-induced residual current, generated by the M_2 tidal current, is eastward and southward flow around the north-eastern and south-western part, respectively.

The comparison of M_2 tidal energy in Suyoung Bay, Korea and the Seto Inland Sea, Japan (YANAGI *et al.*, 1982) is shown in Table 1. The maximum values of M_2 tidal energy flux in Suyoung Bay are seen around the south-eastern and north-eastern part. The M_2 tidal energy flux in Suyoung Bay directs from the north-east to the south-west. On the other hand, local maximum values of M_2 tidal energy flux in the Seto Inland Sea are seen around the Sea of Iyo and Akashi Strait (YANAGI *et al.*, 1982). The topography of Suyoung Bay is monotonous that is gradually widens and deepens from the mouth of Suyoung River to off-shore (see Fig. 1). On the other hand, the topography of the Seto Inland Sea is very complicated (see Fig. 8) and that causes very strong tidal current, especially near the straits. The maximum

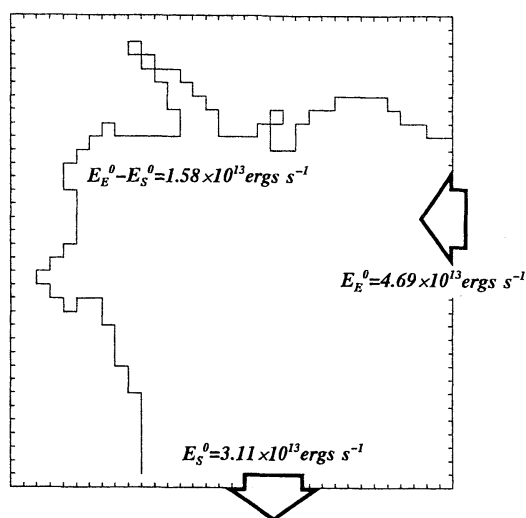


Fig. 6. M_2 tidal energy flux vectors (a) and the M_2 tidal energy flux at the eastern and the southern boundaries (b).

Table 1. M_2 tidal energy loss per unit area (E), M_2 tidal energy flux (E°), M_2 tidal energy dissipation due to friction (E^{**}), amplitude of tidal volume transport (V), and cross sectional area (A) in the Suyoung Bay and Seto Inland Sea.

	E ergs $s^{-1} cm^{-2}$	E° ergs s^{-1}	E^{**} ergs s^{-1}	V $cm^3 s^{-1}$	A km^2
Suyoung Bay	34	4.69×10^{13} (East Bound.)	1.03×10^{13}	3.26×10^9 (East Bound.)	0.17 (East Bound.)
		3.11×10^{13} (South Bound.)		3.17×10^9 (South Bound.)	0.16 (South Bound.)
Seto Inland Sea	189	37.4×10^{15} (Bungo Ch.)	41.6×10^{15}	15×10^{12} (Bungo Ch.)	12.5 (Bungo Ch.)
		9.5×10^{15} (Kii Ch.)		2×10^{12} (kii Ch.)	3.1 (Kii Ch.)

*Surface Area : Suyoung Bay ($30km^2$), Seto Inland Sea ($22,000km^2$)

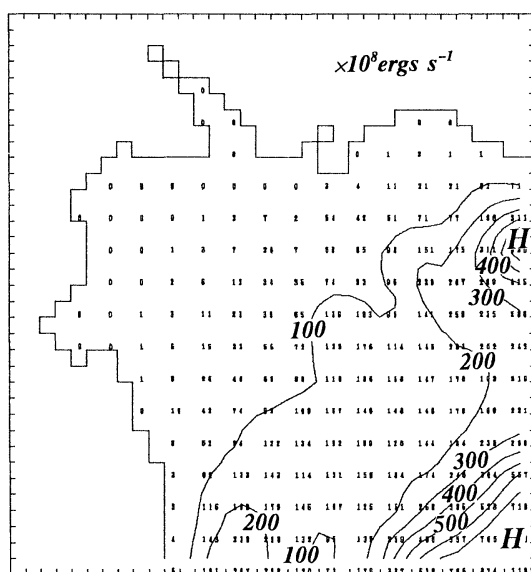


Fig. 7. Distribution of M_2 tidal energy dissipation due to bottom friction.

amplitude of M_2 tidal current in Suyoung Bay is about $40cm s^{-1}$ and that in the Seto Inland Sea is about $500 cm s^{-1}$ at Naruto Strait. The cross sectional area in Suyoung Bay is about 87 times smaller than that of the Seto Inland Sea. Hence the amplitude of tidal volume transport in Suyoung Bay is about 3 order of magnitude smaller than that of the Seto Inland Sea. The M_2 tidal energy loss per unit area is about $34 ergs s^{-1}cm^{-2}$ in Suyoung Bay and $189 ergs s^{-1} cm^{-2}$ in the Seto Inland Sea; the value of Suyoung Bay is about 5.5 times smaller than that of the Seto Inland Sea. The dissipation rate of tidal energy by bottom friction, which

represents the rate of work per unit area made by the flowing water column against bottom friction, is large at the limited area like straits. That is to say, the tidal energy loss per unit area near the straits, where a strong tidal current exists, is larger than elsewhere. In the Seto Inland Sea, the tidal energy loss per unit area is about $400 ergs s^{-1}cm^{-2}$ at the vicinity of Tsurushima Strait, about $411 ergs s^{-1}cm^{-2}$ at the southern area of Naruto Strait and about $532 ergs s^{-1}cm^{-2}$ at the western part of Akashi Strait, especially a local maximum value about $17,021 ergs s^{-1}cm^{-2}$ around the Kurushima Strait (YANAGI *et al.*, 1982). These values are about 2~90 times larger than the average M_2 tidal energy dissipation per unit area in the Seto Inland Sea.

Therefore, we consider that the difference of M_2 tidal energy loss per unit area due to bottom friction in Suyoung Bay and the Seto Inland Sea is produced by the interaction of tidal current with horizontal and bottom topography.

Acknowledgments

The authors express their sincere thanks Dr. H. TAKEOKA and Mr. H. AKIYAMA of Ehime University for their useful discussions. The calculation was carried out on a FACOM M770 of the Computer Center of Ehime University.

References

- HWANG, J. D. (1992): Dispersion of pollutant flowing into Suyoung Bay. Department of Oceanography, Graduate School, National Fisheries University of Pusan, 44p (in Korean).

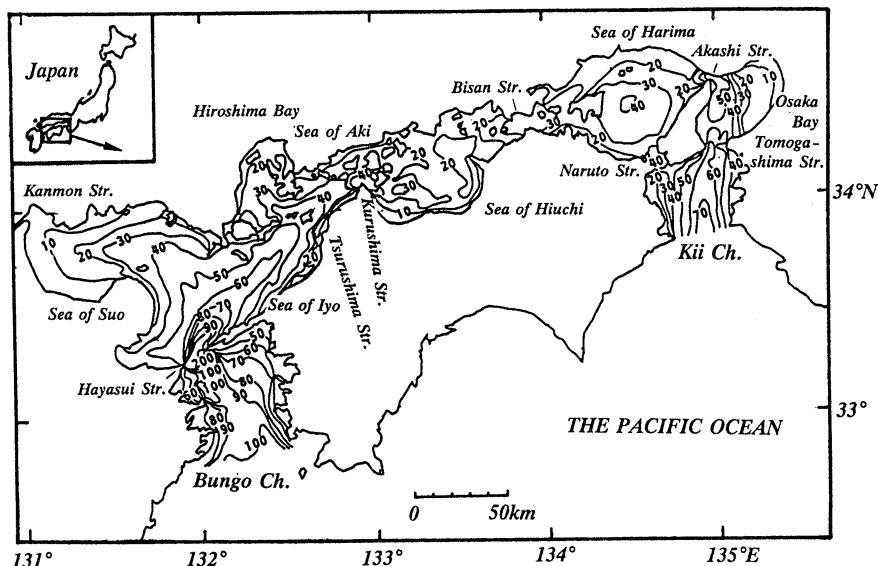


Fig. 8. Bathymetric map of the Seto Inland Sea, Japan. Numbers show the depth in meter.

- JUNG, Y. C. and S. J. YOA (1992): Numerical Modelling on Hydrodynamics and Diffusion in Suyeong Bay. *Bull. Korean Fish. Soc.* **25** (2), 133-143 (in Korean).
- KIM, C. J. and J. S. LEE (1991): A study on the flowing and diffusion of sea water by two-level numerical model in the estuary. *Bull. Korean Fish. Soc.* (1), **24**, 59-69 (in Korean).
- KIM, C. J. and J. S. LEE (1992): Distributions of Tidal Current, Salinity and Suspended Sediment in Suyeong Bay. *Bull. Korean Fish. Soc.* **25** (5), 359-370 (in Korean).
- KIM, D. S. and K. D. CHO and B. G. LEE (1991): Seasonal variation of oceanic conditions in Suyeong Bay. *Bull. Korean Fish. Tech. Soc.* **27**, 105-119 (in Korean).
- KIM, Y. S. and Y. H. HAN (1982): A study in the Characteristics of the Circulation and Diffusion in Suyeong Bay. *Bull. Korean Fish. Tech. Soc.* **18** (2): 55-61 (in Korean).
- MESINGER, F. and A. ARAKAWA (1976): Numerical Methods used in atmospheric Models. GARP (Global Atmospheric Research Programme) Publication Series No.14, WMO-ICSU Joint Organizing Committee, 64p.
- ODAMAKI, M (1989): Tides and Tidal Current in the Tsushima Strait. *J. Oceanogr.*, **45**, 65-82.
- Pusan City of Korea (1984): A report of numerical and mathematical model experiments of the development area in Suyeong Bay. 398p (in Korean).
- TAYLOR, G. I. (1919): Tidal friction in the Irish Sea, *Phil. Trans. Roy. Soc.*, **A220**, 1-193.
- YANAGI, T. and H. TAKEOKA and H. TSUKAMOTO (1982): Tidal Energy Balance in the Seto Inland Sea. *J. Oceanogr.* **38**, 293-299.
- YANAGI, T. TSUKAMOTO, H. INOUE and T. OKAICHI (1983): Numerical simulation of drift card dispersion. *La mer*, **21**, 218-224.
- YANAGI, T and Y. OKAMOTO (1985): A numerical simulation of oil spreading on the sea surface. *La mer*, **22**, 137-146.

Received January 5, 1996

Accepted March 29, 1996

Numerical modelling on atmospheric circulations over the eastern mountainous coastal seas of Korea

Hyo CHOI*

Abstract: By one way double-nested non-hydrostatic numerical model, wind fields in the high mountainous coastal region of Korea were three-dimensionally simulated from March 27 to March 28, 1994. Strong synoptic scale westerly winds blowing over the large steep mountains in the coastal region caused localized downslope wind storms and enhanced development of easterward internal gravity waves in the lee-side of mountain.

During the day a meso scale sea breeze circulation induced by thermal forcing due to temperature contrast of air over between land and sea progresses from sea toward inland. But it is impeded by eastward propagation of internal gravity waves and confines to the offshore side of the coast. Thus, two kinds of atmospheric circulations consist of an internal gravity wave circulation (westerly) and a sea breeze circulation (both easterly near the sea surface and westerly in the upper level). Air in the lowest atmospheric layer at Kangnung coastal site should be trapped by two opposite circulations and surface winds near the coastal seas are relatively weaker than those in the open sea or the inland sites, even if the upper level wind speeds were very strong. On the other hand, a nighttime land breeze from the inland toward the coastal sea could enhance development of existed eastward downslope wind storm and downward transport of momentum from the upper atmosphere toward the coastal surface due to disappearance of vertical thermal convection also makes a contribution to more intensification of westerly winds in the coastal region, increasing the surface wind speeds. Consequently, under the severe downslope wind storms induced by strong synoptic scale winds over the mountain toward the coastal sea, the surface wind speeds became much higher at night than in the daytime and caused much unstable sea states generated by the strong surface winds.

1. Introduction

In recent years, DURRAN and KLEMP (1987), KLEMP and DURRAN (1983), PELTIER and CLARK (1979) made numerical simulations on downslope winds, lee-side waves and up-stream blocking resulted from orographic effects in the inland mountain region. BOER *et al.* (1984), DAVIS (1987), LILLY *et al.* (1982), PALMER *et al.* (1986), SMITH (1978, 1989) and WMO (1986) carried out the theoretical and numerical studies on the surface pressure drag and wave momentum flux in the mountain ranges.

RAYNOR *et al.* (1979) and SETHURAMAN (1982) described boundary wind structure near land-sea interface and MCPHERSON (1970) mentioned distortion of sea breeze convergence zone from

the simulation of Galveston Bay in Texas due to the effect of irregularly shaped coastlines on predicted wind fields. SEGAL *et al.* (1982) identified calm wind zones in conjunction with sea breeze convergence front formed between nearly parallel coastlines through a three-dimensional simulation of sea breeze circulation. LANGLAND *et al.* (1987) demonstrated the result of numerical simulation on a satellite-observed calm zone over the curved coastline of Monterey Bay by using a meso scale marine boundary layer model, which is non-hydrostatic and anelastic without considering the effects of complex terrain.

In the mountainous coastal region, it is known that the patterns of atmospheric circulations are very complicated and are still unsolved problem (CHOI and CHOI, 1994; CHOI and CHOI, 1995; FRIEHE and WINANT, 1982; HSU, 1980, 1988; PLATE, 1971; SATOMURA and

* Department of Atmospheric Sciences, Kangnung National University, Kangnung, Kangwondo, 210-702 Korea

BOUGEAULT, 1992; SETHRAMAN, 1982). Along the coastal sea with high and steep mountains atmospheric circulations, which make a great influence upon waves and circulations, should be affected by sea-land breeze circulation and propagation of internal gravity waves in the lee-side of mountain (CHOI *et al.*, 1996; LEE, 1982; SMITH, 1989; SMOLARKIEWICZ and ROTUNNO, 1989)

In spring we often find that synoptic scale westerly winds with high wind speeds prevailed in north-eastern Asia and become enforced localized wind storms by Taegwallyang mountain near Kangnung city in the eastern coastal edge of Korea. When internal gravity waves with hydraulic jump motions, under downslope wind storms are rapidly developed in the lee-side of the coastal mountain, unusual high winds should be generated over coastal seas and resulted in high sea waves.

The purpose of this study is to explain atmospheric circulations by using a three-dimensional numerical model, which will have a great influence upon the formation of wind driven currents and wind waves and to find out mountain effects on forecasting coastal wind fields and sea states, when both downslope wind storms and sea breeze process exist.

2. Numerical method and data analysis

As shown in Fig. 1 and 2, the study area is located in the eastern coastal region of Korea (adjacent to Japan sea) with high and steep mountains, which lies from south to north parallel to coastal lines and consists of a complex terrain with sand, soil and forest in a high mountain called Mt. Taegwallyang near Mt. Whangbyung (1407m) (CHOI and CHOI, 1995). For investigating atmospheric circulations due to the rapid development of violent internal gravity waves and sea-land breeze circulation in Kangnung coastal region from March 26 through 29, 1994, a non-hydrostatic grid point model was adopted with some modification and one way double-nesting technique was used for precise simulation on coastal wind aspects.

We chose horizontal resolutions of the model as 20km in the coarse-mesh model and 7km in

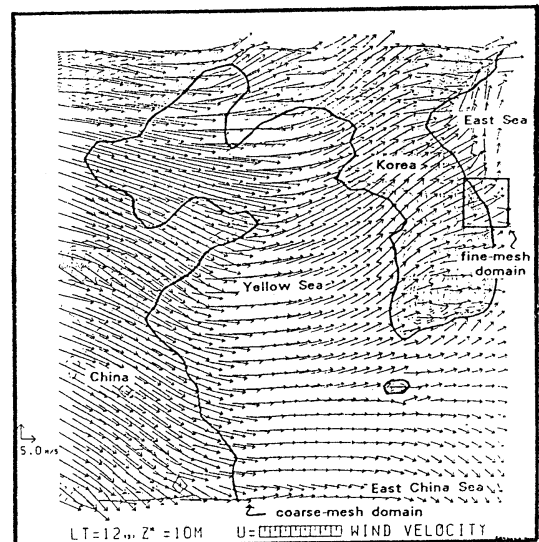


Fig. 1. Calculated wind speeds (m/s) at 10m height over the ground surrounding the Korean peninsula at 12 LST, March 27, 1994 in the coarse domain by using Global Analysis Data.

the fine-mesh for double nesting with the number of 34×34 grids. This model consists of 15 vertical levels from 10m to 6km over the ground such as 10, 45, 120, 235, 350, 500, 700, 900, 1100, 1400, 1800, 2400, 3200, 4200 and 5400m in z^* coordinate called a complex terrain-following coordinate, and the lowest model level is set at 10m, representing the depth of the surface layer.

In the coarse-mesh model, 12 hourly G-ANL (global analysis) data reanalyzed by Japan Meteorological Agency (JMA) are provided as initial data for lateral boundary of the model domain. The coarse-mesh model calculates meteorological variables at each grid point and predicted values on each variable were used again as lateral boundary data in the fine-mesh model. Through horizontal and vertical interpolations of the same global analysis data such as winds, potential temperature, specific humidity, modified data are provided as initial fields for all two models with different resolutions in this work. During the model experiment we found that horizontal gradient of sea surface temperatures on the coastal sea could also much affect the generation of coastal thermal winds comparable to horizontal gradient

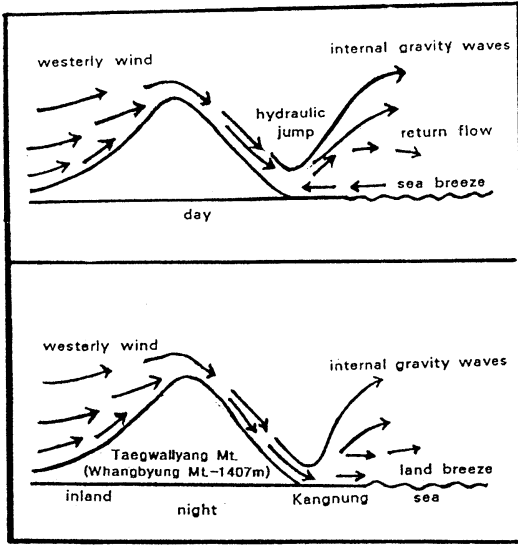


Fig. 2. Schematic profiles of air flows over the eastern mountainous coastal regions for day and night.

of air temperatures over land and sea surfaces. In order to consider effects of sea surface temperature on the coastal winds, initial temperatures of sea surface water were obtained from sea surface temperature data acquired by NOAA (National Oceanic Atmospheric Administration) satellite, which were analyzed by National Fisheries Research and Development Agency of Korea (CHOI and CHOI, 1995; 1995; NFRDA, 1994; ROLL, 1965).

A 30 hour numerical prediction experiment was carried out from an initial time, 09 LST (Local Standard Time=9h + Greenwith Mean Time), March 27 to the next day at 12 LST, March 28 by using HITACH super computer established at Meteorological Research Institute, JMA. After completing our numerical simulation for forecasting winds fields over the mountainous coastal seas, the simulated winds under the strong downslope wind storms were compared with observation ones measured by a pival balloon launched from Korean Air Force Base of Kangnung city at 09 LST, every day from March 27 through 29, 1994.

3. Numerical model

a. Governing equations

In the model formulae, the governing

equations consist of a terrain-following coordinate system called z^* coordinate with the assumption of Boussinesq and anelastic approximations (KIMURA, 1983 and KIMURA and TAKAHASHI, 1991). For the generalized vertical coordinate transformation (x, y, z^*) from the cartesian svstem (x, y, z) , the equations of motion can be derived as

$$d_t h u = f h v - h \Theta \partial_x \Pi + \Theta (z_T - z^*) \partial_x z_G \partial_z \Pi + z_T^2 / h \partial_z (K_m \partial_z u) \quad (1)$$

$$d_t h v = -f h u - h \Theta \partial_y \Pi + \Theta (z_T - z^*) \partial_y z_G \partial_z \Pi + z_T^2 h \partial_z (K_m \partial_z v) \quad (2)$$

$$d_t h w^* = -z_T \Theta \partial_z \Pi + g h \theta / \Theta \quad (3)$$

and

$$\begin{aligned} \Pi &= (P/P_{00})^{R/C_p} \\ \Theta &= T(P/P_{00})^{R_d/C_p} \\ z^* &= z_T(z - z_G)/h \end{aligned} \quad (4)$$

$$\begin{aligned} h &= z_T - z_G \\ d_t &= \partial_t + u \partial_x + v \partial_y + w^* \partial_z \\ h w^* &= z_T w + (z^* - z_T) (\partial_x z_G u + \partial_y z_G v) \end{aligned}$$

Here, u, v and w^* are velocity components in the x, y and z directions in the z^* coordinate and g is gravity (m/s^2). Θ, T, z, z_T, z_G and K_m are potential temperature (K), air temperature at a given height, actual height, height of upper boundary with its change for time and place in a model domein, height of topography and vertical diffusion coefficient for momentum (m^2/s), respectively. P, P_{00}, R, R_d and C_p are atmospheric pressure, atmospheric pressure at reference level, universal gas constant, gas constant for dry air and specific heat at constant pressure.

The first terms on the right hand side of eqs. (1) and (2) are Coriolis forces (f ; Coriolis parameter, $f = 2\Omega \sin \phi$, Ω ; angular velocity of the earth rotation, ϕ ; latitude), and the second, third and fourth terms are pressure gradient forces, adjusted terms on topography and vertical diffusion. The second and third terms of eq. (3) present vertical pressure gradient force and buoyancy.

Considering the thermodynamic equation and conservation of water vapor following equations are given by

$$d_t h \Theta = z_T^2 / h \partial_z (K_h \partial_z \Theta) + h Q_r \quad (5)$$

$$d_t h q = z_T^2 / h \partial_z (K_h \partial_z q) \quad (6)$$

where Q_r and q are Newtonian cooling due to long wave radiation and specific humidity of water vapor. Thus, the second term of eq. (5) implies radiative heating process. For the simplicity of our model, condensation processes such as microphysics of water are not considered. The continuity equation yields to

$$\partial_x hu + \partial_y hv + \partial_z hw^* = 0 \quad (7)$$

Euler-backward scheme is adopted for the time integration of eqs. (1), (2), (5), and (6) and for the vertical direction Crank-Nicholson scheme, respectively. z_G and z_T mean the ground surface level and top boundary level with a material surface in the model atmosphere (6000m), which can absorb gravity-wave energy generated in the lower layers and the radiation condition suggested by KLEMP and DURREN (1983) was adopted for upper boundary condition.

In general, horizontal scale of the phenomena is one order greater than vertical scale, and eq. (3) can be converted into the following equation for hydrostatic equilibrium as

$$\partial_z \Pi = h/z_T \cdot g/\Theta^2 \cdot \theta \quad (8)$$

Considering that the hydrostatic equilibrium can not exist, the pressure equation for non-hydrostatic state can be given by

$$\begin{aligned} & \partial_{xx} \Pi + \partial_{yy} \Pi + \{(z_T/(z_T - z_G))^2 \\ & + ((z^* - z_T)/h)^2 ((\partial_x z_G)^2 + (\partial_y z_G)^2)\} \partial_{zz} \Pi \\ & + 2(z^* - z_T)/h \partial_x z_G \partial_{xz} \Pi + 2(z^* - z_T)/h \partial_y z_G \partial_{yz} \Pi \\ & + \{(z^* - z_T)/h (\partial_{xx} z_G + \partial_{yy} z_G) \\ & + 2(z^* - z_T)/h^2 ((\partial_x z_G)^2 + (\partial_y z_G)^2)\} \partial_z \Pi \\ & = r(x, y, z^*)/(\Theta h) \end{aligned} \quad (9)$$

where r is the residual term and

$$\Pi = \pi - \pi_H \quad (10)$$

$$\partial_z \pi_H = gh \theta / (\Theta^2 z_T) \quad (11)$$

$$\begin{aligned} r(x, y, z^*) = & \partial_x ADVX + \partial_y ADVY \\ & + z_T/h \partial_z ADVZ + 1/h \partial_x z_G \partial_z (z^* - z_T) ADVX \\ & + 1/h \partial_y z_G \partial_z (z^* - z_T) ADVY \end{aligned} \quad (12)$$

and

$$\begin{aligned} ADVX = & -\partial_x huu - \partial_y huv - \partial_z huw^* \\ & + fhv - \Theta h \partial_x \pi_H - \Theta (z^* - z_T) \partial_x z_G \partial_z \pi_H \\ & + z_T^2/h \partial_z (K_m \partial_z u) \\ ADVY = & -\partial_x huv - \partial_y hvv - \partial_z hvw^* - fhu \\ & - \Theta h \partial_y \pi_H - \Theta (z^* - z_T) \partial_y z_G \partial_z \pi_H \end{aligned}$$

$$\begin{aligned} & + z_T^2/h \partial_z (K_m \partial_z v) \\ ADVZ = & -\partial_x huw - \partial_y hvw - \partial_z hww^* \end{aligned} \quad (13)$$

In the simulation processes of the model, the open boundary condition developed by ORLANSKI (1976) for u , v , θ and q was modified for the lateral boundary condition of the model domain.

b. Model formula in turbulent process

As suggested by YAMADA (1983) in the surface boundary layer the turbulent closure level-2 model is adopted for calculating turbulent diffusion coefficients, K_m and K_h for momentum and heat of eq.(1) through eq. (6) by

$$\begin{aligned} K_m = & S_m \cdot e \cdot \ell \\ K_h = & S_h \cdot e \cdot \ell \end{aligned} \quad (14)$$

where ℓ and e^2 imply turbulent length determined by diagnostic approaches and turbulent kinetic energy (m^2/s^2) as

$$\begin{aligned} \ell = & kz/(1 + \ell_0/kz) \\ \ell_0 = & 0.1 \int_{ez} dz/f \text{ edz} \end{aligned} \quad (15)$$

and the semi-empirical formulae between S_m , S_h and flux Richardson number, R_f in the surface boundary layer can be also evaluated by

$$\begin{aligned} S_m = & 1.76 (0.1912 - R_f) (0.2341 - R_f) / \\ & \{(1 - R_f) (0.2231 - R_f)\} = 0.085 \\ & \text{for } R_f \geq 0.16 \\ S_h = & 1.318 (0.2231 - R_f) / (0.2341 - R_f) S_m \\ = & 0.095 \quad \text{for } R_f \geq 0.16 \end{aligned} \quad (16)$$

R_f can be derived by the function of bulk Richardson number, R_i at each grid point (KIMURA, 1983; MELLOR and YAMADA, 1974; YAMADA and MELLOR, 1973) as

$$\begin{aligned} R_f = & 0.6588 \{R_i + 0.1776 - (R_i^2 - 0.3221R_i \\ & + 0.03156)^{1/2}\} \quad \text{for } R_i \leq 0.19 \\ R_i = & g/\Theta \cdot \Delta \theta \cdot \Delta z / \Delta U^2 \end{aligned} \quad (17)$$

From the balance between production of turbulent energy due to both shear and buoyancy and dissipation of turbulent energy, turbulent velocity, $e = (e^2)^{1/2}$ can be evaluated by

$$\begin{aligned} e^2 = & B_1 \ell^2 \{S_m (z_T/h)^2 \{(\partial_z u)^2 + (\partial_z v)^2\} \\ & - g/\Theta S_h (z_T/h) \partial_z \theta\} \\ B_1 = & 16.6 \end{aligned} \quad (18)$$

c. Radiation process

Long wave radiations are absorbed by water vapor and carbon dioxide in the lower atmosphere. Considering that flux from the ground surface toward the upper levels is regarded as positive, total net flux of long wave radiation, R_g yields to

$$\begin{aligned} R_g &= \sigma T_c^4 \tau_c + \sigma (T_{00}^4 - T_c^4) \tau_f(U_{00}) \\ &\quad + \sum \sigma (T_i^4 - T_{i+1}^4) \tau_f(|U_i|) \\ T_c &= 220\text{K} \end{aligned} \quad (19)$$

In the above, σ is Stefan-Boltzman's constant, and T_c , T_{00} and T_i are critical temperature, temperature at the top of model atmosphere and temperature at the i -th level, respectively. Here, transmission function, τ_f is derived as follows :

$$\begin{aligned} \tau_f &= \tau_{H_2O} \cdot \tau_{CO_2} \\ \tau_{H_2O} &= (1 + 1.746 U_*^{0.423})^{-1} \\ \tau_{CO_2} &= 0.93 - 0.066 \text{LOG}_{10}(U_*^{CO_2}) \\ \tau_c &= (1 + 3.0 U_*^{0.408})^{-1} \tau_{CO_2} \\ U_* &= 1/g \int q(p/p_0)^{0.6} dp \\ U_*^{CO_2} &= (p_0^2 - p^2)/p_0^2 \end{aligned} \quad (20)$$

where τ_{H_2O} , τ_{CO_2} and τ_c are the transmission functions for H_2O , CO_2 and critical temperature ($=220\text{K}$). U_* , q , p_0 and p are effective vapour amount, specific humidity (g/cm^2), pressure (mb) at the surface and at the arbitrary levels.

In this model, considering the absorption of solar radiation by water vapor due to Rayleigh scattering and the solar radiation toward the earth surface as a positive flux, total net solar radiation at the ground is given by

$$\begin{aligned} S_g &= (1 - \alpha_s) \{S_{os}(1 - \alpha_A)/(1 - \alpha_A \alpha_s) \\ &\quad + S_{oA}(1 - A(x))\} \\ S_{os} &= 0.651 S_o \cos \zeta \\ S_{oA} &= 0.349 S_o \cos \zeta \end{aligned} \quad (21)$$

and

$$\begin{aligned} \cos \zeta &= \cos \phi \cos \delta \cos h + \sin \phi \sin \delta \\ \alpha_A &= 0.085 - 0.247 \text{LOG}_{10}(p/p_0 \sec \zeta) \\ A(x) &= 0.273 x^{0.303} \\ x &= U_* \tau \sec \zeta \end{aligned} \quad (22)$$

where S_o , S_{os} and S_{oA} are solar constant, scattering part of solar radiation (wave length; $\lambda < 0.9 \mu$) and absorption one ($\lambda > 0.9 \mu$). ζ is solar zenith angle, which is a function of latitude (ϕ), declination (δ) and time angle (h). $A(x)$ is an absorbing function of solar radiation, and

α_s and α_A are albedos of atmosphere and earth surface, respectively.

Q_* , which is the heating rate of atmosphere can be approximated by the following Newtonian cooling due to long wave radiation as

$$Q_* = 10^{-5}(T_g - T) \quad \text{for } T > T_g \quad (23)$$

$$Q_* = 0 \quad \text{for } T \leq T_g \quad (24)$$

where T and T_g are air temperature and soil temperature at the ground level.

d. Similarity theory in the surface layer

Assuming that the lowest level of the model set at 10m in the surface layer is a constant flux layer and similarity theory can be applied to parameterize vertical turbulence. Considering energy balance near the surface momentum flux, τ , sensible heat flux H and latent heat flux, E are

$$\begin{aligned} \tau / \rho &= -(u_*)^2 = -k^2 u^2 / \phi_m^2 \\ H / (C_p \rho) &= -\theta_* u_* = -k^2 |u| (\theta_1 - \theta_g) / (\phi_m \phi_h) \end{aligned} \quad (25)$$

$$E / (L \rho) = -q_* u_* = -k^2 |u| (q_1 - q_g) / (\phi_m \phi_h)$$

ρ , q_* , u_* and k are the air density, the water vapor scale, friction velocity, θ_* the potential temperature scale and the Von Karman constant. The subscription 1 and g mean the lowest and ground level of the model domain.

BUSINGER (1973), HSU (1988), MONIN (1970), PANOFSKY and DUTTON (1984), PAULSON (1970) and WILLIAMS (1980) describe various kinds of formulae on the integrated universal functions, ϕ_m for momentum and ϕ_h for heat and we use the following formula suggested by KIMURA and TAKAHASHI (1991)

$$\begin{aligned} \phi_m &= \int \Phi_m / \zeta d\zeta \\ \phi_h &= \int \Phi_h / \zeta d\zeta \end{aligned} \quad (26)$$

here $\zeta = z/L$, $\zeta_0 = z_0/L$ and L is Monin-Obukhov length scale defined as

$$L = \rho C_p \theta_*^3 / kgH \quad (27)$$

Under unstable condition

$$\begin{aligned} \Phi_m &= (1 - 16 \zeta)^{-1/4} \\ \Phi_h &= (1 - 16 \zeta)^{-1/2} \quad \text{for } \zeta \leq 0 \end{aligned} \quad (28)$$

Under stable condition, two classifications for momentum and heat are given by

$$\Phi_m = 1 + 7 \zeta$$

$$\Phi_h = 1 + 7\zeta \quad \text{for } 0 < \zeta \leq \zeta_0 \quad (29)$$

and

$$\begin{aligned} \Phi_m &= 1 + 7\zeta_0 \\ \Phi_h &= 1 + 7\zeta_0 \quad \text{for } \zeta_0 < \zeta \end{aligned} \quad (30)$$

where

$$\begin{aligned} \zeta_0 &= z_0/L = 0.714 \\ \zeta &= R_i \phi_m^2 / \phi_h \\ R_i &= g / \Theta (\theta_1 - \theta_g) \Delta z_1 / |u|^2 \end{aligned} \quad (31)$$

For the prediction of earth surface temperature in the case of bare ground condition, a force restore method suggested by Deardorff (1978) are derived as

$$\partial t \theta_g = (S_g - R_g - H - E) / C_1 - (\theta_g - \theta_0) / C_2 \quad (32)$$

where θ_g and θ_0 are ground surface potential temperature and underground temperature. C_1 and C_2 can be evaluated by diurnal period, τ_d ($=24^h$), heat capacity of underground soil, C_g (cal/cm³/K) and heat conductivity, k_g (cal/cm/k/sec) as

$$\begin{aligned} C_1 &= 0.5 (\tau_d C_g K_g / 2\pi)^{1/2} \\ C_2 &= \tau_d / 2\pi \end{aligned} \quad (33)$$

and π is pi.

If evaporation coefficient, B_g at the ground is treated as constant, specific humidity at the ground surface, q_g yields to

$$\begin{aligned} q_g &= B_g q_s(T_g) + (1 - B_g) q_1 \quad \text{for } q_s(T_g) \geq q_1 \\ q_g &= q_s(T_g) \quad \text{for } q_s(T_g) < q_1 \end{aligned} \quad (34)$$

wetness of bare ground, w_g ($=0.2$ cal/cm³/k), which is defined as the ratio of available water content to maximum available water content has different value depending upon season. In this study w_g is treated as 0.2 for the spring time as CHOI and CHOI (1995) and can be predicted as

$$\begin{aligned} C_g &= 0.2(1 + w_g) \\ k_g &= (0.386 + 0.15w_g) 10^{-2} \\ B_g &= \min(1, 2w_g) \end{aligned} \quad (35)$$

4. Result of numerical simulation

a. Horizontal surface winds

The model forecasting of the wind in the

mountainous coastal region is of primary interest in explaining atmospheric circulations over the eastern coastal seas of Korea. In the case of prevailing strong synoptic scale westerly winds blowing over the north-eastern Asian counties such as China, Korea and Japan from March 26 through 28, 1994. we three-dimensionally simulated coastal wind fields by using a non-hydrostatic numerical model. On March 26, that is, one day before carrying out numerical simulation the surface winds were generally moderate and the wind fields had typical wind patterns like sea and land breeze in the Kangnung coastal region.

At 12 LST on March 27, 1994 strong westerly winds penetrate into Korean peninsula and pass by eastern coastal mountain regions (Fig. 1). At the same time strongly enforced local winds are detected near Kangnung coastal regions (Fig. 3-a). In Fig. 3a the surface winds at 12 LST, March 27, 1994 in the eastern mountainous coastal region of Kangnung city, adjacent to East Sea (The Sea of Japan) consist of two different kinds of coastal winds such as synoptic scale westerly and meso scale easterly. Along the coastal line, which lies from south to north-west, strong westerly winds with a speed more than 18m/s blow over the inland high mountains (Mt. Taegwallyang) toward East Sea, but easterly winds with a speed of 7m/s in the coastal sea also approach to inland of the coast. Since these two different kinds of winds in the opposite directions are in the confront each other, and the surface winds at 10m height are very weak, especially 2m/s near the surface at the edge of lee side of Taegwallyang mountain, but the surface wind speeds with easterly in the Kangnung city are in the range of 3m/s to 5m/s. These westerly winds were modified from original synoptic scale winds, which were enforced by flowing over the large steep mountains (Mt. Taegwallyang or Mt. Whangbang) like a wind storm. On the other hands, the easterly winds are caused by a sea-breeze due to the meso-scale thermal forcing from the difference between the air temperature over the ground and that over the sea surface in the daytime.

At 15 LST, as daytime goes on, the sea breeze was more intensified and the easterly wind

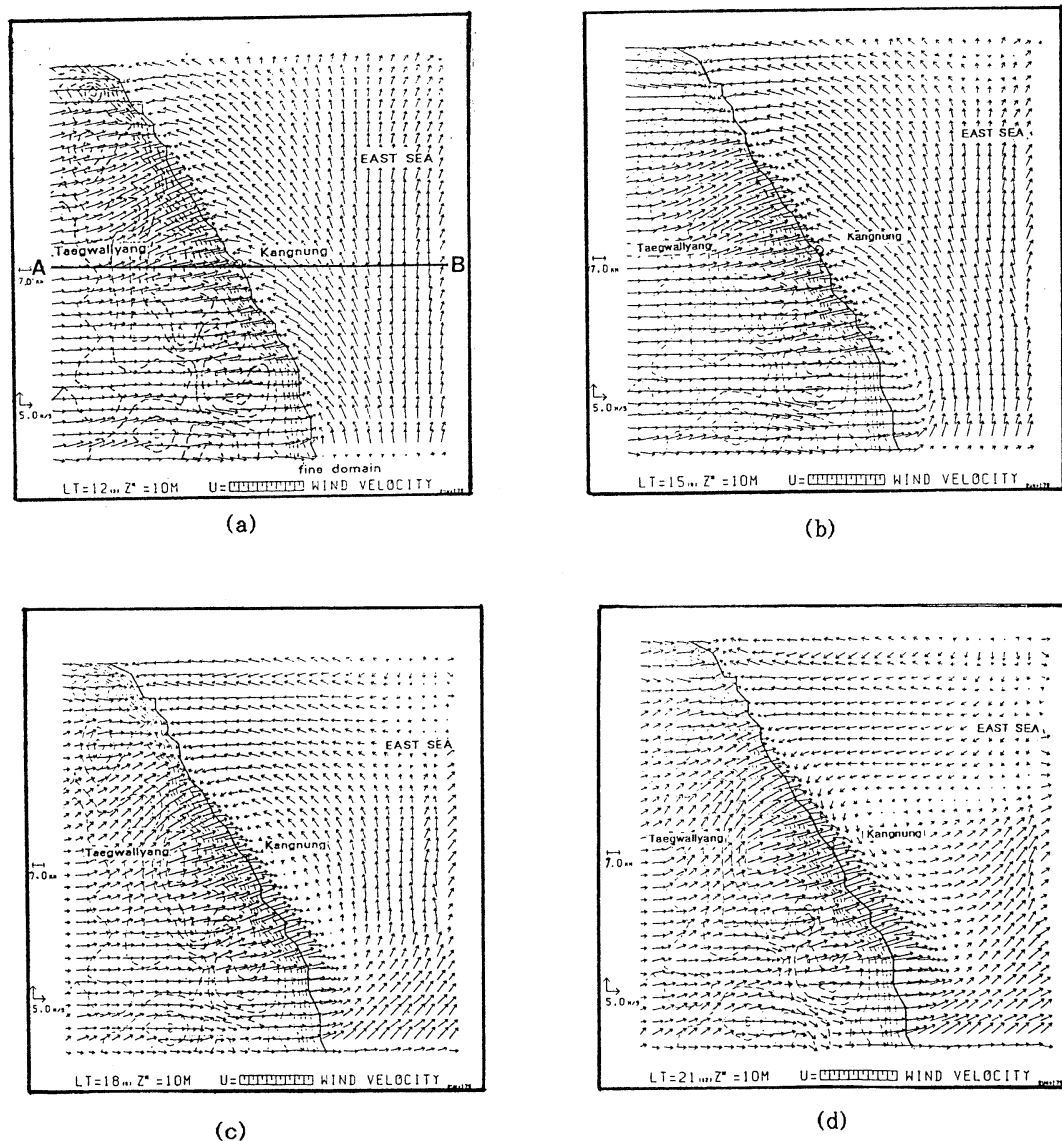


Fig. 3. Surface winds (m/s) at 10m height over topography near Kangnung coastal regions of Korea (—means coast line) at 12 (a), 15 (b), 18 (c) and 21 (d) LST, March 27, 1994.

speeds became slightly higher than that of 12 LST (Fig. 3b). At the same time, as the synoptic scale inland westerly winds in front of the mountains became stronger and stronger, they could be downslope wind storms along the eastern slope of the mountains. Under this situation the surface winds in the Kangnung area between lee side of the mountain and coastal sea became weaker and weaker, and reached to 2m/s.

Similar to 15 LST, the sea breeze cycle at 18 LST, just before sunset became smaller and shallower, and the surface wind patterns still show easterly with the more wide area of weak winds over the coastal sea surface in offshore sides of Kangnung city (Fig. 3-c). This feature is attributed to the intrusion of more intensified westerly winds toward the coastal sea, as the sea breeze was weakened with a shortage of solar radiation. In the simulation, a zone of the

minimum wind speed appears near the shoreline.

After sunset such as 21 and 00 LST, there was no sea breeze near the coast and the meso-scale forcing in the opposite direction due to surface cooling of ground could induce a land breeze from inland toward sea (Fig. 3-d, 4-a). The existed westerly winds in the inland sides was associated with the land breeze and could be more intensified with a higher speed at night. Especially, from 03 through 09 LST, March 28, strong westerly surface winds with speeds of 18m/s can stretch out to 200km off coast and from those points to open sea sides, the westerly surface winds could not be affected by orographic features. So the surface winds near Kangnung were not over the limit of 5m/s.

In the present work, a localized wind generated a circulation was detected with width of 110km (east-west) and 80km (north-south) in the coastal sea near Kangnung and rotated in an cyclonic direction (counter-clockwise). These circulations over the coastal sea surface, which tend to be smaller and smaller, exist until next day morning 09 LST (Fig. 4-b, 4-c, 4-d). These localized wind circulations over the sea surface may considerably affect formations of coastal oceanic circulations.

At 09 LST the surface winds continue to be eastward over both inland and sea surfaces. In the lee-side of mountains the strong downslope wind storms continuously prevail throughout the coastal region and the extension of localized westerly winds remains in the coastal sea (Fig. 4-d). In the open sea, the relatively weak surface winds induced by land breeze have the same eastward direction, because the surface cooling on the inland ground continues to exist. After 09 LST the surface wind pattern becomes similar to 12 LST, March 27. On March 29 the winds near Kangnung mountainous coastal region become moderate again with the similar structure of wind on March 26.

b. Vertical profiles of winds

Vertical profiles of wind vectors with speed and direction on 15 levels over the east-west straight cutting line from Kangnung (east) to Mt. Taegwallyang (west) (A-B line in Fig. 3-

a) in the fine-mesh model domain (Fig. 5~Fig. 8). As the synoptic scale westerly winds in the eastern coastal region rapidly flow over the large steep mountains, they can be localized to be strong downslope winds and changed to be internal gravity waves generated in the lee-side of mountain and over coastal seas. Hence, from the vertical profiles of horizontal wind speed at each level of 15 levels, the downslope winds get hydraulic jump motions with bounding forward, and the enhancement of downslope winds could produce wind storms along the east slope of the mountain, which move toward the eastern coastal sea (Fig. 2).

At 12 and LST, March 27 during the daytime a sea breeze circulation takes a place from sea toward inland sites, but the sea breeze circulation can stretch out to just coastal site due to the eastward propagation of internal gravity waves (Fig. 5a and 5b). It is not easy to find an upslope wind in the eastern side of coastal mountains, which can be often observed under the easterly synoptic wind or meso-scale sea breeze. It means that the sea breeze could not penetrate into the top of the mountain and be limited to the inland coast. As the westerly downslope winds confront the easterly sea breeze in Kangnung city, the some amount of air should be isolated, but the others move upward, blowing toward the sea side. Thus, the surface winds at inland coastal sites were relatively weaker than those in the open sea or the further inland sites from the coast.

Through the our numerical simulation, two different kinds of atmospheric circulations (two eddies) in the lee side of the mountain were detected such as an internal gravity wave circulation with westerly wind and a sea breeze circulation with both easterly wind near the sea surface and westerly in the upper level such as a circular flow pattern (Fig. 7a and 7b). Under the existence of two kinds of atmospheric circulations, the air near Kangnung coastal region should be trapped by the two circulations in the opposite directions, and the horizontal surface wind speed of the downslope wind near coast should be reduced to be about 2.0 m/s, that is, relatively weak by the intrusion of sea breeze. Fig. 7a and 7b show that as the westerly wind storms can drive out

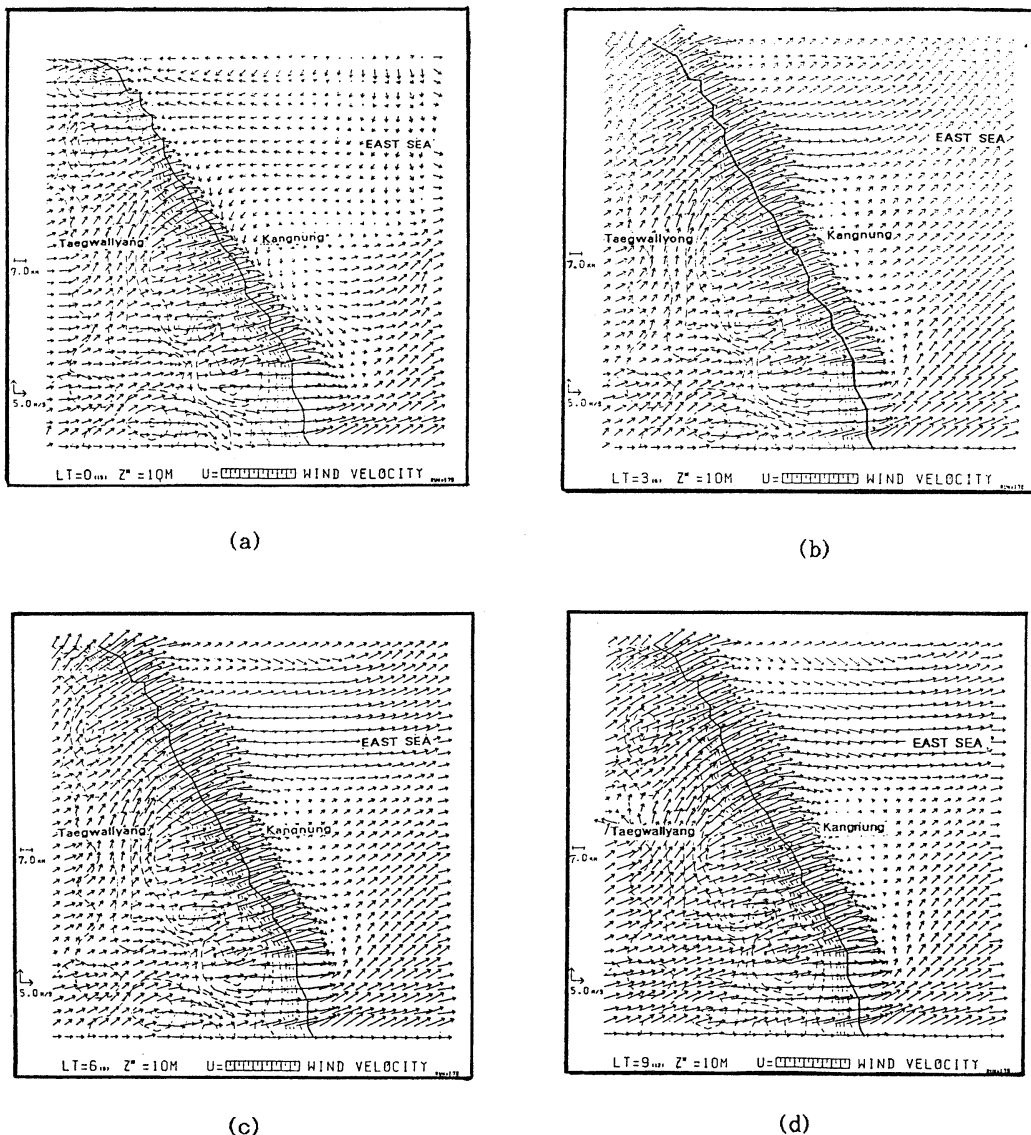


Fig. 4. As shown in Fig. 3 expect for 00 (a), 03 (b), 06 (c) and 09 (d) LST March 28, 1994.

the meso scale easterly winds such as sea breeze to the coast, the positions of minimum wind speed lie in lower and lower levels along the eastern slope of the mountain and eventually moves to the coastal sea. Of course, the wind at Kangnung city are easterly with 3 m/s under the influence of the sea breeze circulation.

At 18 LST, near sunset the wind pattern was similar to that at both 12 LST and 15 LST, but

the depth of the sea breeze circulation became shallower and shallower with weak wind speeds (Fig. 5c, 7c). As the nighttime went on, that is, from 21 LST, March 27 through 06 LST, March 28, the vertical convection of air from the earth surface should be suppressed due to the disappearance of solar radiation, and then, the momentum could be transported from the strong upper level winds toward the surface, enhancing the existed daytime downslope

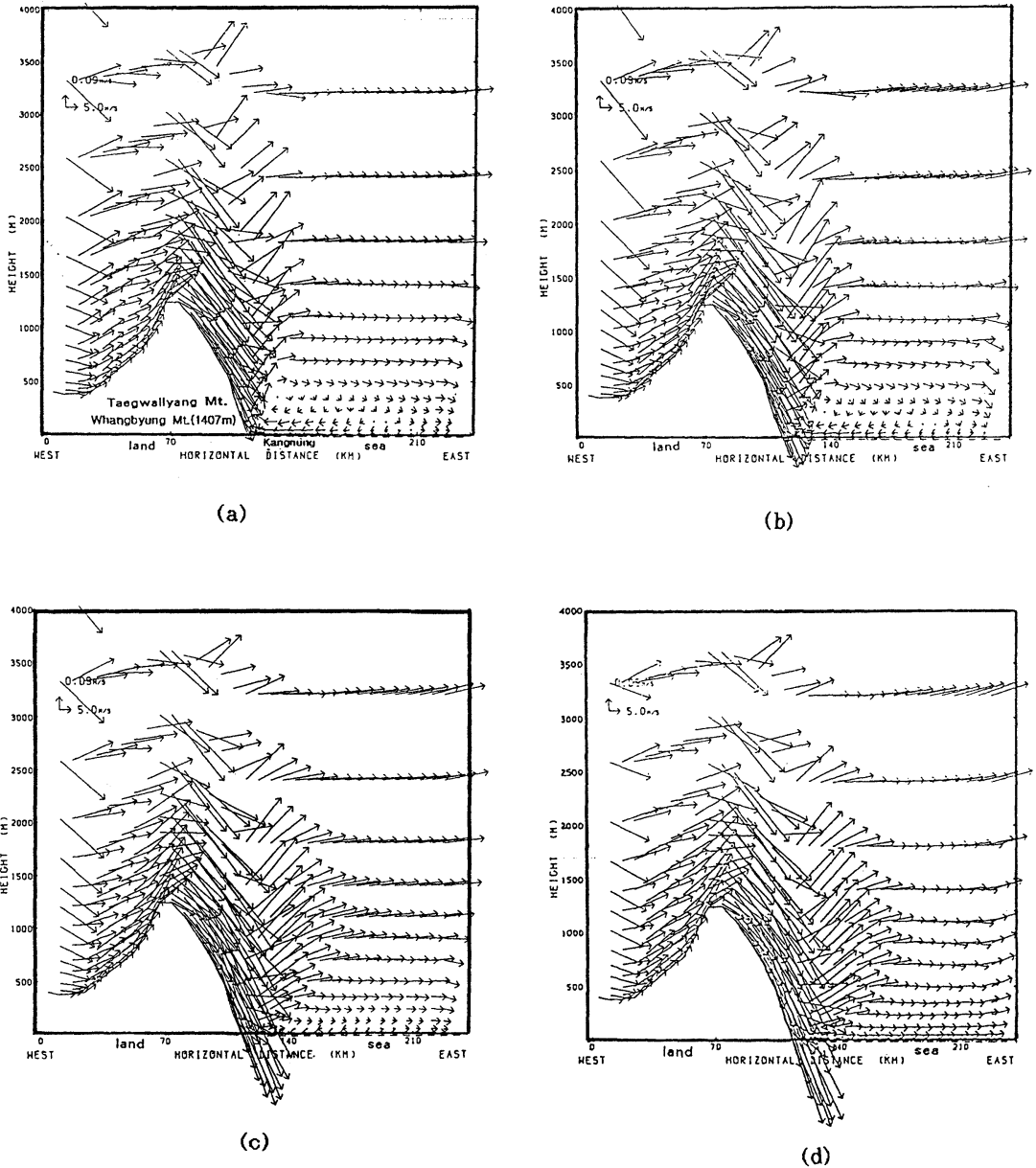


Fig. 5. Vertical profiles of wind vectors (m/s) on 15 levels over the east-west straight cutting line from Kangnung near to Mt. Taegwallyang (A-B line in Fig. 3a) at 12 (a), 15 (b), 18 (c) and 21 (d) LST, March 27, 1994.

wind storms to be more intensified at night than in the daytime (Fig. 5d, 6a, 6b). As mentioned above, in Fig. 7d, 8a, 8b and 8c the centers of wind storms with maximum wind speeds over 28m/s take positions lower and lower toward the ground surface and come

down to the height of 200m over the ground at 06 LST just before sunrise.

Furthermore, during the night the air over the inland surface was much cooler than that over sea surface, due to the cooling of ground surface and then, the meso-scale temperature

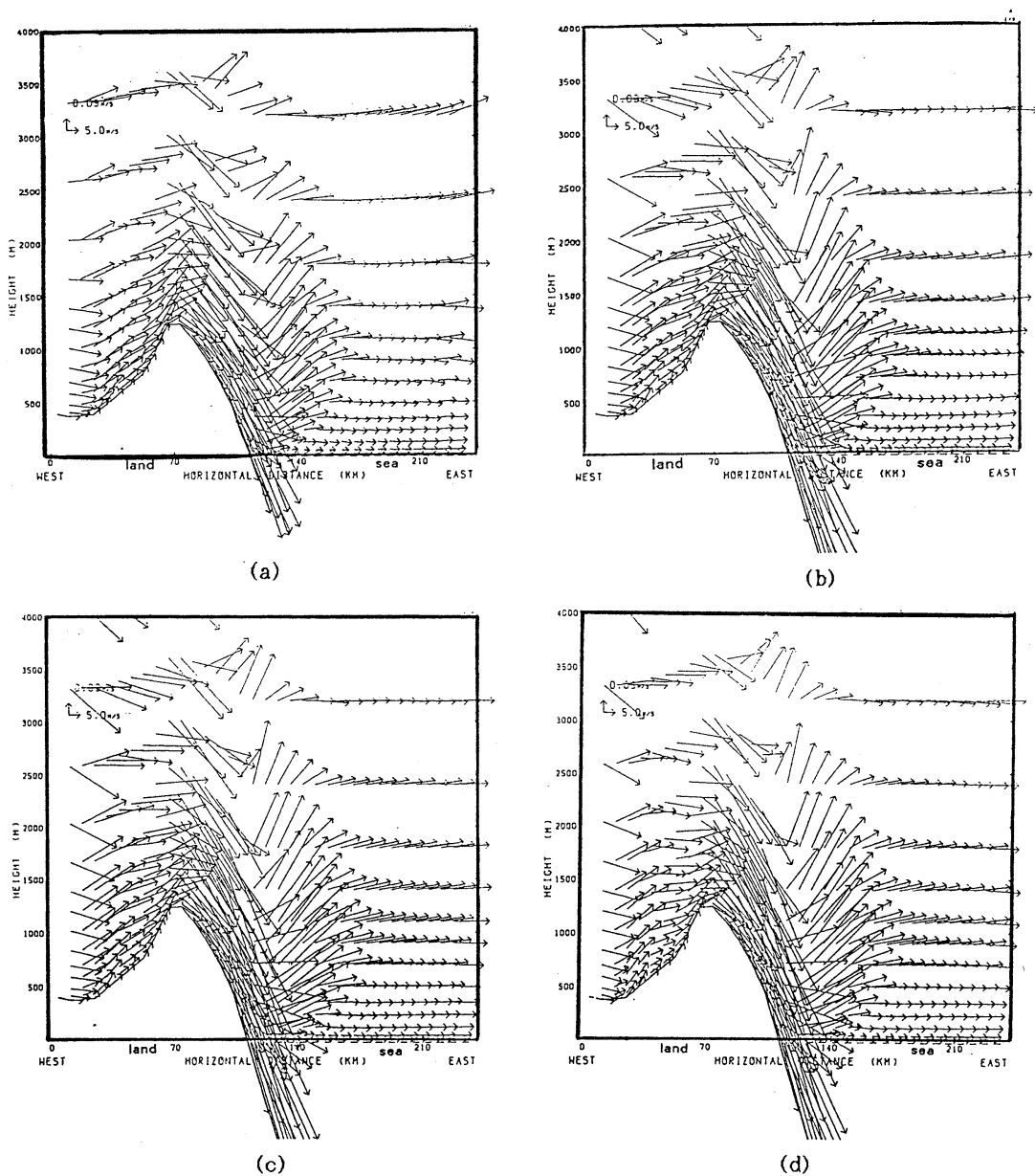


Fig. 6. As shown in Fig. 5 expect for 00 (a), 03 (b), 06 (c) and 09 (d) LST March 28, 1994.

contrast between air over the ground and that over the sea surface occurs, resulting in generating a land breeze from inland toward sea. Thus, the surface winds near the Kangnung city became strong. So, since the westerly downslope wind storms intensified by both orographic feature with a sharp inclination and momentum transfer from the strong upper

level winds toward the ground surface, after sunset, can be associated with the land breeze blowing from inland toward sea, they produce one atmospheric circulation (one cell) in the coastal region and enhance the surface winds near the Kangnung city to be stronger and stronger (7d and 8a).

At 06 lst on the next day morning, that is,

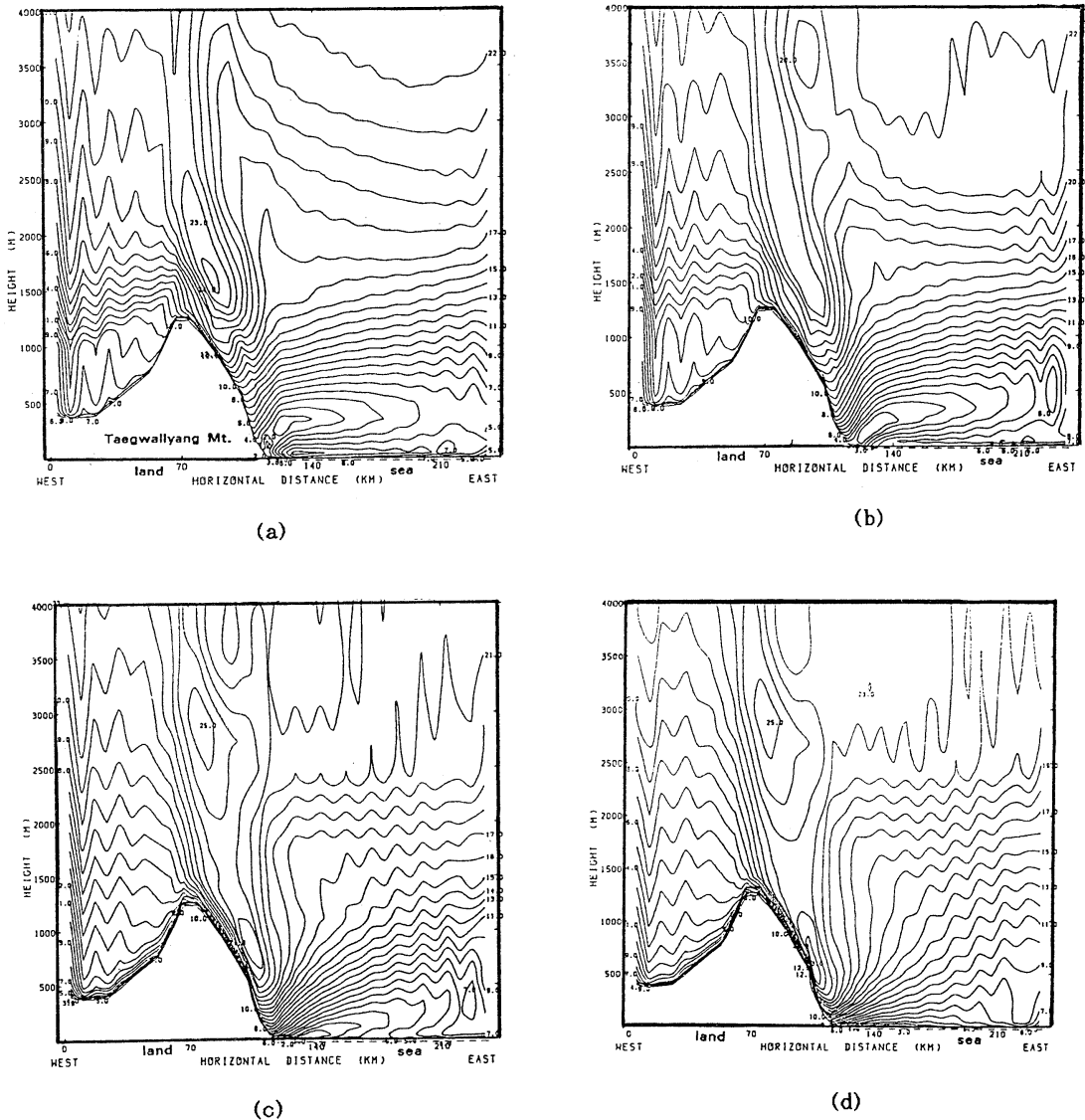


Fig. 7. Vertical profiles of horizontal wind speeds (m/s) on 15 levels over the east-west straight cutting line from Kangnung near to Taegwallyang Mt. (A-B line in Fig. 3a) at 12 (a), 15 (b), 18 (c) and 21 (d) LST, March 27, 1994.

sunrise time, as the center of the wind storm was located in the lowest level near the surface, due to both maximum momentum transfer from the upper layer and maximum effect of land breeze, the surface winds induced by the strong downslope wind storms were still westerly. Because it takes more time to excite air by solar radiation and sea breeze can just start to be generated at this time (Fig. 6c and 8c). The

center of the wind storm at 09 LST was located at the slightly higher position than at 06 LST, as the sea breeze started, and the strong westerly winds could suppress the easterly sea breeze, showing the resultant westerly surface winds near Kangnung city (Fig. 6d and 8d).

During the day, on March 28, the wind patterns were very similar to those on March 27. After 09 LST March 28, especially under the

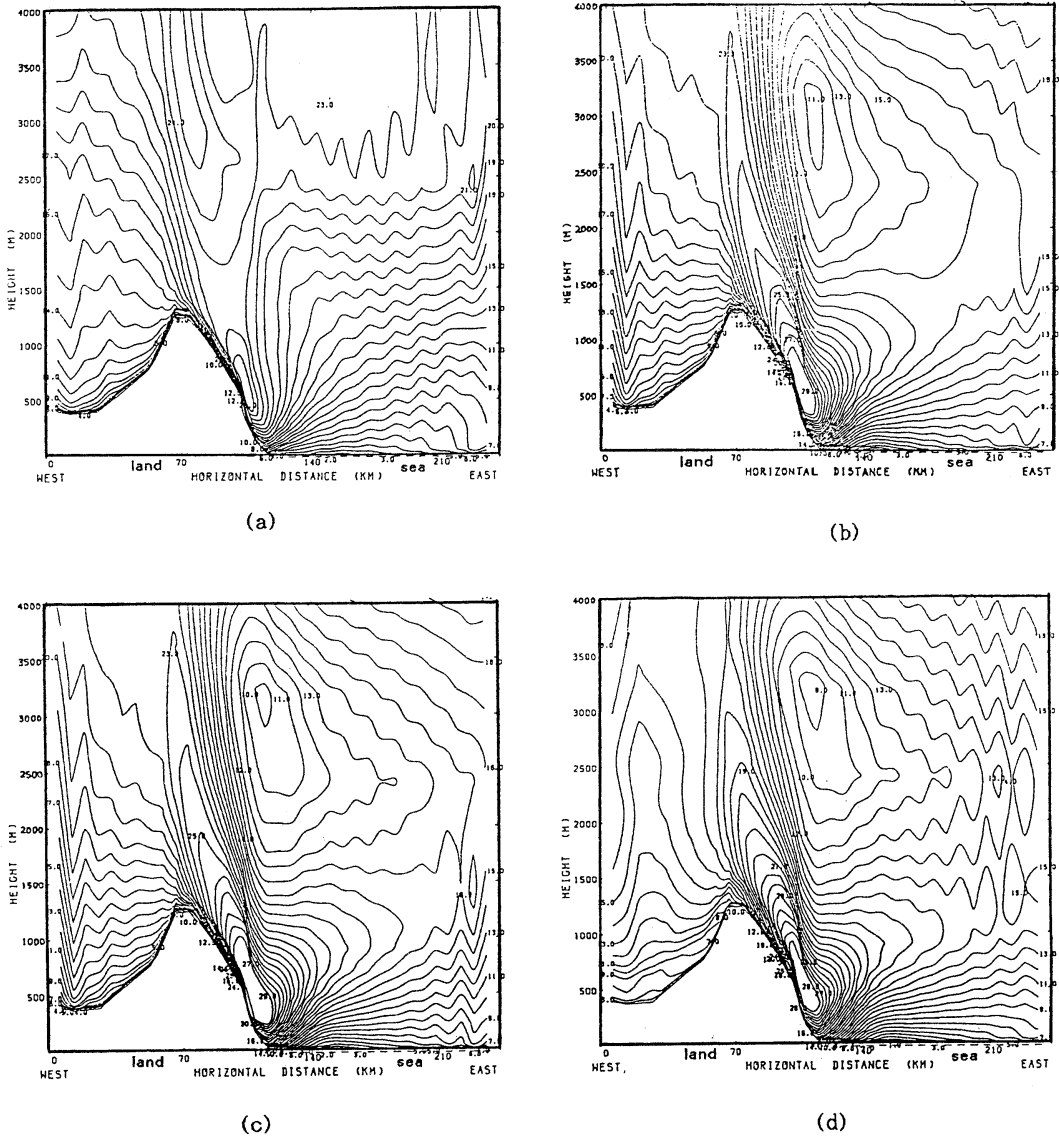


Fig. 8. As shown in Fig. 7 expect for 00 (a), 03 (b), 06 (c) and 09 (d) LST March 28, 1994.

strong development of downslope wind storms along the east slope of the mountain and in the lower layer over the coastal region, two kinds of circulations induced by both internal gravity waves and sea breeze should be produced again at Kangnung city and the surface wind speed was 18 m/s. The wind patterns in the coastal region on March 28 was similar to the previous daytime case. On March 29, the winds became moderate again and a typical wind

pattern controlled by only sea-land breeze was observed in the coastal region of Kangnung.

c. Comparison of simulated winds to measured ones

Under the severe downslope wind storms in the mountainous coastal region of Kangnung, the comparison of simulated winds to the observed one was made by using a pival balloon launched from Korean Air Force Base of

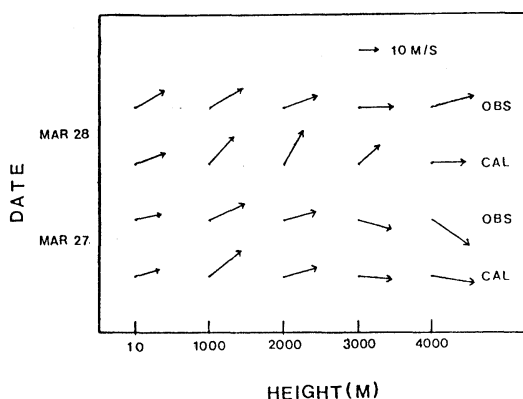


Fig. 9. Comparison of calculated wind vectors with observed ones at Korean Air Force Base of Kangnung from March 27 through March 28, 1994.

Kangnung city at 09 LST, every day from March 27 through 29, 1994. The measured height were 10m, 1000m, 2000m, 3000m and 4000m (Fig. 9). On March 27, the simulated wind speed and directions (measured wind speed and directions) at 10m height over the ground of Kangnung Air Force Base was 13m/s, 255° (14m/s, 260°) at 10m, 22.5m/s, 230° (21m/s, 245°) at 1000m; 18m/s, 256° (18m/s, 255°) at 2000m, 18m/s, 275° (18m/s, 285°) at 3000m and 24.1m/s, 278° (24m/s, 305°) at 4000m, respectively. At 09 LST on the next day morning, March 28, they are 17.5m/s, 250° (18m/s, 240°) at 10m, 20m/s, 225° (21m/s, 240°) at 1000m, 20m/s, 220° (19m/s, 250°) at 2000m, 15.6m/s, 230° (19m/s, 270°) at 3000m, 18.5m/s and 280° (24m/s, 265°) at 4000m under the existence of wind storms. Even if there were, in part, a little differences between the simulated winds and the observed ones, they well agreed each other. Thus, when the severe downslope wind storm and sea-land breeze occur over complex terrain near the coast, the numerical forecasting for atmospheric circulations can be expected to play a significant role in prediction of wind driven currents and wind waves on the mountainous coastal seas and it is very useful to operate a non-hydrostatic numerical model for the prediction of coastal sea states.

5. Summary

Numerical experiments of atmospheric

circulations were performed under the downslope wind storms generated in the lee-side of mountainous coastal region. In the daytime we have two different kinds of atmospheric circulations, which consist of an internal gravity wave circulation with westerly wind and a sea breeze circulation with both easterly wind near the sea surface and westerly in the upper layer. The internal gravity waves toward sea and the sea breeze circulation toward inland caused an isolation of air at Kangnung coastal site. Thus, surface winds near the coastal seas were relatively weaker than those in the open sea or inland.

On the other hand, at night under the intensification of westerly downslope wind storms associated with land breeze toward sea and the momentum transfer from the upper level toward the coastal surface, the surface winds became much stronger at night than during the day in the coastal region. Consequently, when the downslope wind storms were strongly developed, the surface wind speeds at Kangnung city also became higher and it might excite the severe sea states in the coastal regions.

Acknowledgements

For the successful execution of this coastal experiment, the author would like to express much thanks to Mr. S. TAKAHASHI, Dr. T. YOSHIKAWA and Dr. T. HANAFUSA of Meteorological Research Institute, Japan Meteorological Agency for using computer facility and technical assistance with helpful discussions. He is also grateful for oceanographical data provided by Korea Oceanographic Data Center, National Fisheries Research and Development Agency. This paper was supported in part by NON DIRECTED RESEARCH FUND, Korea Research Foundation, Ministry of Education in 1995, under grant for "Variation of atmospheric pollution concentrations due to the development of internal gravity waves in Kangwondo coastal regions". Another financial aid was provided by Ministry of Environment and Ministry of Science & Technology in 1995 for "Regional climate modelling-research and development on technology for global environmental monitoring and change prediction".

References

- BOER, G. J., N. A. McFARLANE and R. LAPRISE (1984) : The climatology of Canadian climate center general circulation model as obtained from a five-year simulation. *Atmos. Ocean*, **22**, 430-473.
- BUSINGER, J. A. (1973) : Turbulence transfer in the atmospheric surface layer, *In* Workshop on Micrometeorology, Haugen, D. A. (ed). Amer. Meteor. Soc., 67-100.
- CHOI, H. and J. CHOI (1994) : Characteristics of onshore winds in the coastal thermal internal boundary layer. *J. Korean Meteor. Soc.*, **30**, 1-11.
- CHOI, H. and J. CHOI (1995) : Atmospheric pollutant concentrations under the influence of internal gravity wave and sea-land breeze circulations in the mountainous coastal regions. *Korean J. Geophys. Res.*, **23**, 18-33.
- CHOI, H., J. CHOI, S. TAKAHASHI and T. YOSHIKAWA (1996) : Three dimensional numerical modelling on the growth of coastal thermal internal boundary layers in the Cheju island of Korea. *J. Korean Meteor. Soc.*, **32**, 1-16.
- DAVIS, H. C. (1987) : Observational studies and interpretation of the mountain pressure drag during ALPEX, in observation, theory and modelling of orographic effects, ECMWF. Reading, **113**, 136pp.
- DURRAN, D. R. and J. B. KLEMP (1987) : Another look at downslope wind storms, Part II : Non linear application beneath wave overturning layers. *J. Atmos. Sci.*, **44**, 3402-3412.
- DEARDOFF, J. W. (1978) : Efficient prediction of ground surface temperature and moisture with inclusion of a layer of vegetation. *J. Geophys. Res.*, **38**, 659-661.
- FRIEHE, C. A. and C. D. WINANT (1982) : Observation of wind and sea surface temperature structure off of the northern California coast. 1st International Conference on Meteorology and Air/Sea Interaction of the Coastal Zone, Hague, Amer. Meteor. Soc., 209-214.
- HSU, S. A. (1980) : Research in the coastal meteorology: basic and applied. 2nd Conference on Coastal Meteorology, Los Angeles, Amer. Meteor. Soc., 1-7.
- HSU, S. A. (1988) : Coastal Meteorology. Academic Press. 260pp.
- KIMURA, F. (1983) : A numerical simulation of local winds and photochemical air pollution (I) : two dimensional land and sea breeze. *J. Meteor. Soc. Japan*, **61**, 862-878.
- KIMURA, F. and S. TAKAHASHI (1991) : The effects of land-use and anthropogenic heating on the surface temperature in the Tokyo metropolitan area : numerical experiment. *Atmos. Environ.*, **25**, 155-164.
- KLEMP, J. B. and D. R. DURRAN (1983) : An upper condition permitting internal gravity wave radiation in numerical mesoscale models. *Mon. Wea. Rev.* **111**, 430-440.
- LANGLAND, R. H., P. M., TAG and R. W. FETT (1987) : Numerical simulation of a satellite-observed calm zone in Monterey Bay, California. *Mon. Wea. Rev.*, **2**, 261-268.
- LEE, Y. (1982) : The prediction of thermal internal boundary layer growth and fumigation. 1st International Conference on Meteorology and Air/Sea Interaction of the Coastal Zone, Hague, Amer. Meteor. Soc., 83-86.
- LILLY, D. K., J. M. NICHOLLS, R. M. CHERVIN, P. J. KENNEDY and J. B. KLEMP (1982) : Aircraft measurements of wave momentum flux over the Colorado Rocky mountains. *Q. J. R. Meteor. Soc.*, **108**, 625-642.
- MCPHERSON, R. D. (1970) : A numerical study of the effect of a coastal irregularity on the sea breeze. *J. of App. Meteor.*, **9**, 767-777.
- MELLOR, G. L. and T. YAMADA (1974) : A hierarchy of turbulence closure models of planetary boundary layers. *J. Atmos. Sci.*, **31**, 1791-1805.
- MONIN, A. S. (1970) : The atmospheric boundary layer. *Annual Review of Fluid Mechanics*, **2**, 225-250.
- NFRDA. (1994) : Analyzed NOAA satellite pictures on the sea surface temperatures in the East Sea (Japan Sea). National Fisheries Research and Development Agency.
- ORLANSKI, I. (1976) : A simple boundary condition for unbounded hyperbolic flows. *J. Comp. Phys.*, **21**, 251-269.
- PALMER, T. N., G. J. SMITH and R. SWINBANK (1986) : Alleviation of a systematic westerly bias in general circulation and NWP models for trough and orographic gravity wave drag parameterization. *Q. J. R. Meteor. Soc.*, **112**, 1001-1039.
- PANOFSKY, H. A. and J. A. DUTTON (1984) : Atmospheric Turbulence. John & Wiley, New York, 1-100.
- PAULSON, C. A. (1970) : The mathematical representation of wind speed and temperature profiles in the unstable atmospheric surface layer. *J. App. Meteor.*, **9**, 857-861.
- PELTIER, W. R. and T. L. CLARK (1979) : The evolution and stability of finite amplitude mountain waves. Part II : Surface wave drag and severe downslope windstorms. *J. Atmos. Sci.*, **36**, 1498-1529.
- PLATE, E. J. (1971) : Aerodynamic characteristics of atmospheric boundary layers. U. S. Atmospheric Energy Commission, 190pp.
- RAYNOR, G. S., S. SETHURAMAN and R. M. BROWN (1979) : Formation and characteristics of coastal

- internal boundary layer during onshore flows. *Boundary Layer Meteor.*, **16**, 487-514.
- ROLL, H. V. (1965) : Physics of the marine atmosphere. Academic press, New York, 426pp.
- SATOMURA, T. and P. BOUGEAULT (1992) : Orographic wave drag during PYREX experiment. *In* Spring Meeting of the Meteorological Society of Japan, Tsukuba, 282pp.
- SEGAL, M., R. T. MCNIDER, R. A. PIELKE and D. S. McDOUGAL (1982) : A numerical model simulation of the regional air pollution meteorology of the greater Chesapeake Bay area—summer day case study. *Atmos. Environ.*, **16**, 1381-1397.
- SETHURAMAN, S. (1982) : Observation of the boundary layer wind structure near land-sea interface. 1st International Conference on Meteorology and Air/Sea Interaction of the Coastal Zone, Hague, Amer. Meteor. Soc., 4-7.
- SMITH, R. B. (1978) : A measurement of mountain drag. *J. Atmos. Sci.*, **35**, 1644-1654.
- SMITH, R. B. (1989) : Hydrostatic airflow over mountains. *Adv. Geophys.*, **31**, 1-41.
- SMOLARKIEWICZ, P. K. and R. ROTUNNO (1989) : Low Froude number flow past three dimensional obstacles. Part I : Baroclinically generated lee vortices. *J. Atmos. Sci.*, **46**, 1154-1164.
- WILLIAMS, R. G. (1980) : A procedure for wind field construction from measured data which utilizes local surface roughness. 2nd Conference on Coastal Meteorology, Los Angeles, Amer. Meteor. Soc., 307pp.
- WMO. (1986) : Scientific results of the Alpine experiment. GARP publication series, 27, WMO, Geneva.
- YAMADA, T. (1983) : Simulation of nocturnal drainage flows by a q^2-1 turbulence closure model. *J. Atmos. Sci.*, **40**, 91-106.
- YAMADA, T. and G. L. MELLOR (1973) : A numerical simulation of the BOMEX data using a turbulence closure model coupled with ensemble cloud relations. *Q. J. R. Meteor. Soc.*, **105**, 95-944.

Received January 4, 1996

Accepted March 18, 1996

ERS-1 SAR observations of dynamic features in the southern East-China Sea

L. M. MITNIK^{1,2}, M. -K. HSU¹ and C. -T. LIU³

Abstract : ERS-1 SAR images covering the southern East-China Sea near Taiwan are analyzed together with relevant remote and *in situ* data to interpret the variations of their brightness (NRCS). A wealth of the oceanic and atmospheric phenomena of different scales were revealed on the SAR images : packets of internal waves, eddies and mushroom-like structures north and east of Taiwan, western Kuroshio front, natural and artificial slicks, island wakes, surface manifestations of bottom topography, cell and roll convection, atmospheric gravity waves, etc. Part of them had never been studied near Taiwan.

1. Introduction

The features of bottom topography in the southern part of the East-China Sea, vicinity of the vast Asia continent with full-flowing rivers, influence of Kuroshio, tide driven flows, indented coast line and coastal mountains disturbing wind field predetermine the complicated space-time structure of oceanic and atmospheric processes. Remote and *in situ* techniques, field and computer simulations are used to investigate these processes.

In spite of numerous efforts both the oceanic and atmospheric phenomena and processes are still not well known. This is particularly evident, when new devices and techniques are applied to study them. The primary attention in our research was concentrated on analysis of data obtained by a Synthetic Aperture Radar (SAR) from European ERS-1 satellite. Ground receiving station of the Center for Space and Remote Sensing Research at National Central University receives and processes the ERS-1 SAR images since October, 1993.

The active (different kinds of radars) and passive (radiometer) microwave techniques allow us to collect information about the ocean

surface parameters and phenomena under cloud conditions. It is a great advantage for the areas where the probability of cloudiness is high. Radar images provide better resolution in comparison with microwave radiometric data. It allowed us to study the fine details of the oceanic phenomena. They manifest themselves as anomalous states of the sea surface as opposite to "normal" states when roughness is determined by surface wind only. Appearance of these states results from modulation of small scale wind waves by the variable currents directly and/or indirectly, for example, through redistribution of surface films. The atmospheric mesoscale phenomena (roll vortices, cell convection, gravity waves, wind shadows, etc.) are also imprinted in the surface roughness field due to modulation of horizontal surface wind.

The objective of this study is to interpret the brightness patterns observed on the ERS-1 SAR images collected over the southern East-China Sea to extract qualitative and quantitative information about phenomena in the ocean-atmosphere system. Processing of the SAR images and geographical distribution of the ERS-1 SAR-observed oceanic and atmospheric phenomena are described in section 2. Imprints of the roll vortices and the atmospheric gravity waves on the SAR images are considered in section 3. Surface manifestations of the Kuroshio front, upwelling, internal

¹ National Taiwan Ocean University, Keelung, Taiwan, R. O. C.

² Pacific Oceanological Institute, Vladivostok, Russia

³ National Taiwan University, Taipei, Taiwan, R.O.C.

waves and other oceanic features are discussed in section 4.

2. Processing of SAR data. Map of dynamical phenomena

In image mode the SAR obtains strips of high resolution imagery approximately 100 km in width, 250 km to the right of the sub-satellite track. A spatial resolution is 26 m in range (across track) and between 6 m to 30 m in azimuth (along track) (VASS and BATTRICK, 1992). A SAR maps the surface roughness through Bragg scattering from the short gravity waves with a wavelength of $\Lambda = \lambda / (2 \sin \theta)$, where λ is the wavelength of radar and θ is local incidence angle. ERS-1 SAR ($\lambda = 5.66$ cm, $\theta = 19.5\text{--}26.6^\circ$, VV polarization) is sensitive to waves of about 8.3–6.5 cm long. For surface waves with crest at an angle ϕ to the radar line-of-sight, the Bragg scattering criterion is: $\Lambda' = \Lambda \sin \phi$. The differences in sea surface roughness are visible on the SAR images as tonal changes, with the light areas corresponding to stronger backscattering signals (to large values of normalized radar cross-section-NRCS). Backscatter increases with the increase of wind speed (stress) and depends on azimuthal angle (angle between wind vector and a plane of radar signal propagation). The threshold wind-speed value u_{\min} needed to form the resonant Bragg waves depends on radar frequency and sea surface temperature and for ERS-1 SAR the $u_{\min} \approx 3.2$ m/s at a height of 10 m above the surface (DONELAN and PIERSON, 1987).

Each SAR frame covers an area of about 100 km by 100 km. The SAR data are in binary form. The digital SAR image had 8002 pixels in column and more than 8000 pixels in row. To enhance the features on a SAR image, decrease noise and achieve a convenient size, at first the size of the data was reduced by an 8×8 averaging box. A surface resolution of about 100 m resulting from this averaging was adequate for our study. Then the histogram of gray level was calculated and displayed. The upper and lower bounds of gray level were determined manually to provide the best visibility of the details. Image file was obtained by conversion of the binary file. Finally, the images were

printed by a laser printer using commercial image process package.

We analyzed about 150 ERS-1 SAR images obtained over southern part of the East-China Sea since October, 1993. These were both the individual images and strips of several images. Most of them covered the waters surrounding Taiwan between $21\text{--}27^\circ$ N and $119\text{--}123^\circ$ E. The images were obtained at different seasons and at different weather conditions. The NOAA AVHRR images, weather maps of the Japan Meteorological Agency (JMA) and the Central Weather Bureau, wave analysis map of the JMA and other relevant data were used to interpret the brightness variations on the SAR images and separate the oceanic phenomena.

Our analysis revealed, in particular, that the SAR images with the mesoscale (over a range several hundreds meters to several kilometers) wave-like variations of the surface roughness are wide spread and common. They can be caused by both the oceanic and atmospheric phenomena and can confuse an oceanographic interpretation of the SAR imagery. For instance, horizontal roll vortices, open and closed convective cells and gravity waves in the atmospheric planetary boundary layer produce the quasiperiodic surface-wind-speed (surface roughness) fluctuations. To detect an atmospheric nature of the observed organized NRCS variations, correlation of cloud patterns on the visible and/or NOAA images and brightness distribution on the SAR images was used. Furthermore, SAR images of oceanic internal waves which also produce the mesoscale modulation of the NRCS, look different from SAR images of wind rolls and atmospheric gravity waves (see below 4.3, as well as ALPERS and BRÜMMER, 1993; MITNIK and VIKTOROV, 1990; VACHON, *et al.*, 1994, 1995).

We marked the areas where the surface manifestations of the following phenomena were observed: the changes of bottom topography (BT), coastal fronts (CF), eddies (E), internal waves (IW), island wakes (IsW), Kuroshio front (KF), mushroom-like structures (MS), slicks (s), unusual ship wakes (SW), upwelling (U) as well as the surface imprints of cellular convection (CC), roll

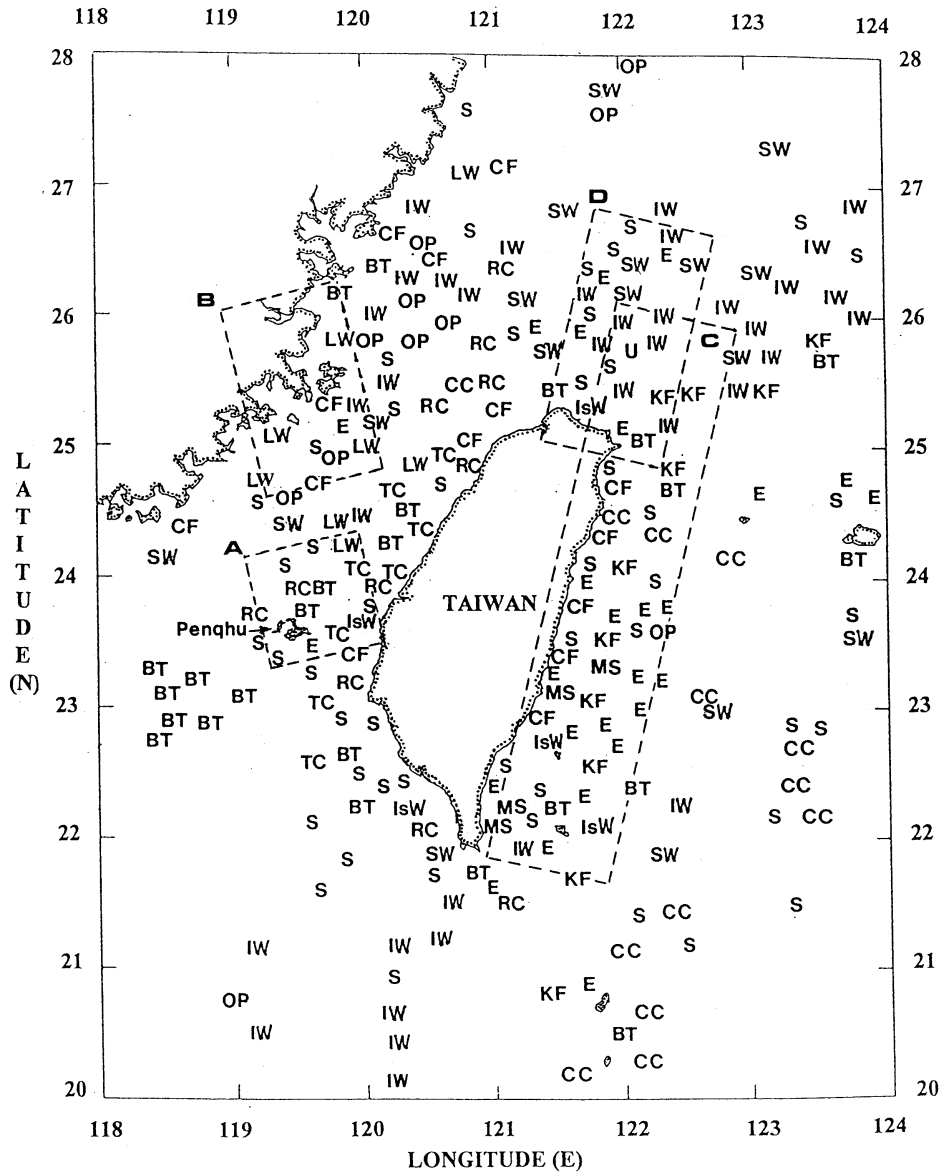


Fig. 1. Location of the features of sea surface roughness on the ERS-1 SAR images caused by the following oceanic and atmospheric phenomena near Taiwan: The changes of bottom topography (BT), coastal fronts (CF), eddies (E), internal waves (IW), island wakes (IsW), Kuroshio front (KF), mushroom-like structures (MS), slicks (S), unusual ship wakes (SW), upwelling (U), cellular convection (CC), roll convection (RC) and lee waves (LW). The dotted rectangles A, B, C and D show the locations of the SAR images used in the paper.

convection (RC) and lee waves (LW) (Figure 1). Several SAR strips were continued beyond the area under consideration. The mixed zone between Yangtze waters and waters of the East

China Sea and internal waves in the Luzon Strait and in the northern South-China Sea were registered on them.

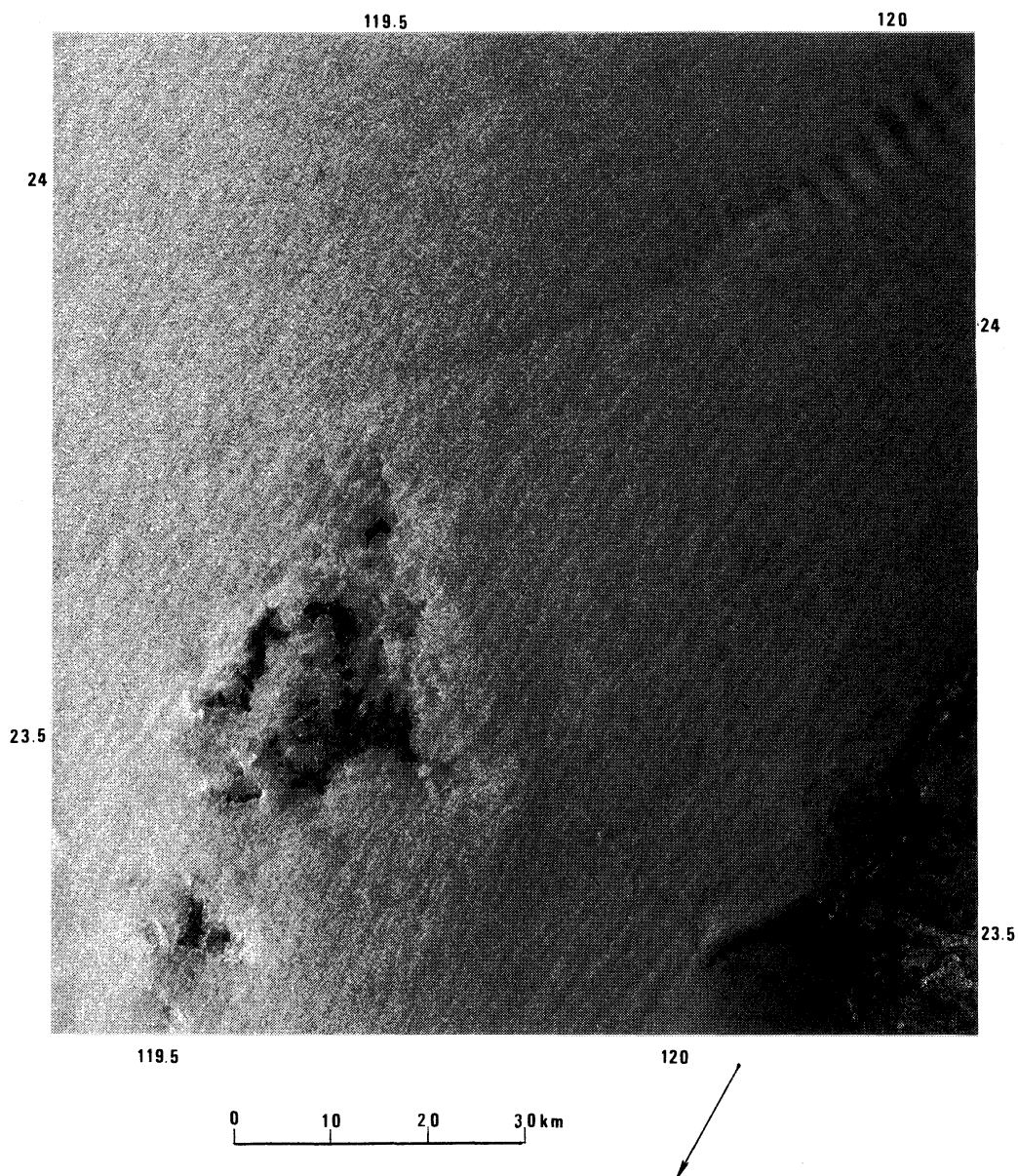


Fig. 2. ERS-1 SAR image of the Taiwan Strait, acquired on February 20, 1995, at 14 : 27 UTC (the original SAR image data is copyright ESA 1995). The image area is about 95 km x 100 km. Arrow shows mean wind direction derived from SAR image

3. Atmospheric phenomena

The oceanic phenomena can be detected with a SAR over a range of wind speed u from $u_{\min} \approx 3.2$ m/s to 8–10 m/s only. At $u \geq 10$ m/s the brightness variations on a SAR image are mainly due to the sea surface wind variability. Figure 2 depicts a section of an SAR image

taken over the Taiwan Strait near the Penghu (area A in Figure 1). From the weather maps of the JMA for 00:00 UTC on February 20 and 21, gale northeastern winds (prevailing during winter monsoon) and waves with a height of 3–4 m were observed at the time of the SAR pass. The increased brightness in the vicinity

of the Penghu was due to intensive wave breaking over shallow waters. It starts at a distance of about 8 km off northeastern coast. The boundaries of this area correlate well with isobaths and the results of Landsat image.

On the SAR image the alternating light and gray bands are surface expression of roll vortices in the marine boundary layer of the atmosphere. The surface waves that led to this streak-like pattern are formed primarily in response to variations in the surface wind caused by the rolls (ETLING and BROWN, 1993; ALPERS and BRÜMMER, 1993). The streak-like pattern has a mean orientation aligned with the north-northeastern wind (Figure 2). The distance between adjacent light lines determines a wavelength of the roll vortices. It varies between about 1.5 and 2.5 km. The difference of the NRCS values of light and gray bands depends on wind speed of the base flow, amplitude of mesoscale circulation, azimuthal angle and incidence angle (MITNIK *et al.*, 1994).

Additionally to the roll vortices, the quasiperiodic variations of the NRCS can be resulted from atmospheric gravity waves. They are internal waves for which gravity is the restoring force (MITNIK and VIKTOROV, 1990; VACHON, *et al.*, 1994; 1995). They modulate the horizontal surface wind speed and thus the surface roughness. A group of atmospheric gravity waves is seen in the upper right angle in Figure 2. Their wavelength is about 3.5 km and the wave crests are directed at a right angle to the bands, formed by the roll vortices.

At wind speed in the range of 3–10 m/s the variations of the sea surface roughness (NRCS) are due to both the oceanic and atmospheric factors. A strip of two SAR images covering the East-China Sea east of China coast (Figure 3, area B in Figure 1) shows three systems of the surface imprints of the lee waves. In the system 1 20 well-defined wave crests of 2.7-km wavelength, in the system 2 9 crests of 4.3-km wavelength and in the system 3 8 crests of about 2.0 km wavelength are readily apparent in Figure 3. They are oriented near parallel to the coastal mountain ridges and extend up 40–50 km offshore. Modulation of the surface wind was enough to decrease u below a threshold value u_{\min} needed to generate small gravity

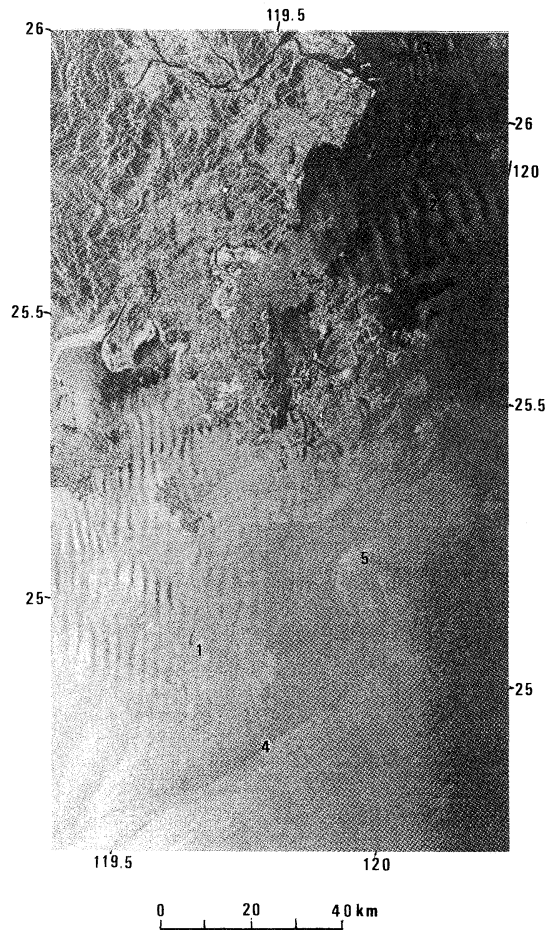


Fig. 3. ERS-1 SAR images of atmospheric lee waves east off China coast, acquired on December 8, 1994, at 14 : 26 UTC (the original SAR image data is copyright ESA 1994). The image area is about 100 km \times 160 km.

resonance waves with a wavelength of Λ . Amplitude of the modulation can be estimated with the CMOD IFR2 wind retrieval model for scatterometer (QUILFEN, 1995). From the model, it follows that the radar contrasts caused by the lee waves increase with the decrease of average wind speed.

A narrow contrast band 4 crossing part of the strip and ending by a cyclonic eddy 5 with size of about 10 km indicates, probably, a frontal boundary between the low-salinity China Coastal Current and the Taiwan Warm Current (GUAN, 1994).

4. Oceanic features

4.1 Kuroshio front

In the east Asia, the Kuroshio Current plays an important role in the local fishery, navigation and circulation. The season variations of the Kuroshio characteristics, such as location of axis, velocity, along-track width, flow separation, interaction with shelf of the East-China Sea, eddy formation, etc. are pronounced, especially northeast of Taiwan. These characteristics are studied with ships, drifters, NOAA AVHRR images, satellite altimeter data and computer simulation. The short time variability of the Kuroshio was explored to a significantly lesser degree. Only NOAA AVHRR images can cover the Kuroshio and surrounding waters, as opposite to altimeter and *in situ* measurements. However, a high probability of cloudiness coupled with thermal contrasts of the Kuroshio waters against a background in the area under consideration do not allow to use the IR images which proved to be a very effective in Kuroshio study east of Japan. The possibility of imaging radars to detect the dynamic phenomena can help us to understand better behavior of the Kuroshio front and, in particular, to clarify the main causes of its variability.

A strip of five SAR images obtained on April 23, 1995 covers a region approximately 100 km by 500 km off the east coast of Taiwan (Figure 4a, area C in Figure 1). The individual frames are marked by digits 1-5; the dotted lines show boundaries between them (Figure 4b). The SAR images of the same Kuroshio area were also acquired on November 26, 1993; May 28, July 2 and August 6, 1995. The coastal mountains and valleys are seen along the left-hand boundary of the strip. The strip is essentially an instant pattern showing surface expressions of interaction of northward Kuroshio flow with bottom topography and islands east of Taiwan coast. The complicated structure of the Kuroshio front is clear visible on the strip. The bright and dark bands of varying width represent the frontal boundary of the Kuroshio (Figure 4b). They are aligned parallel to the coast about 40-50 km away from it. It is suggested that the increased values of the NRCS (bright bands) are due to short gravity-wave/current

interaction along shear and/or convergence zones within the front. The reduced values of the NRCS (dark bands) are due to increased concentration of natural surface films aligned along frontal boundary (MARMORINO *et al.*, 1994; NILSSON and TILDESLEY, 1995; VESECKY and STEWART, 1982).

Cold front was north of Taiwan at approximately 27° N. It shifted to the south at the time of the SAR pass. Southerly winds of about 5-7 m/s and air temperature of 27-28°C were recorded by the coastal station at 24° 20' N, 123° 45' E (the JMA surface analysis at 00:00 and 00:06 UTC) and the JMA wave analysis map at 00:00 UTC (2.5 h before the SAR pass). Northward wind wave height was 1 m and westward swell height was 2 m and northward wind of 5 m/s were reported by ship at 24° N, 128° 30' E. In accordance with ten-day mean sea surface temperature (SST) of the JMA, the SST was 27°C south of 24° N. It decreased to 25°C near 26° N. In the NOAA-12 IR image for April 24 processed by the Fishery Research Institute, Keelung, the SST decreases from 29°C south of Taiwan to 27°C at about 23-24° N. Lack of *in situ* observation of atmospheric parameters hinders, however, the estimate of influence of the wind stress variations induced by the changes of atmosphere stability on radar contrast.

Eddy-like and wave-like disturbances of the boundary are caused by interaction of Kuroshio with islands, underwater ridges and mountains. Island wake was formed behind Lutao (frame 4). A shape of the individual eddies downstream Lutao was perturbed by current shift. Further north, an underwater mountain at about 23° 30', 121° 48' is a cause of the increased surface roughness (frame 3). The area over another bottom raising near 24° 40', 122° 20' is also characterized by increased backscatter (frame 2). North of this area the Kuroshio waters turn northeast. The small-scale linear striations north of the raising and around the right side of the boundary between the 1st and the 2nd frames are, probably, the surface effects of the adjustment of the bottom boundary layer to the changes in the interior flow. The similar SAR signatures were observed in the eastward deflection zone of the

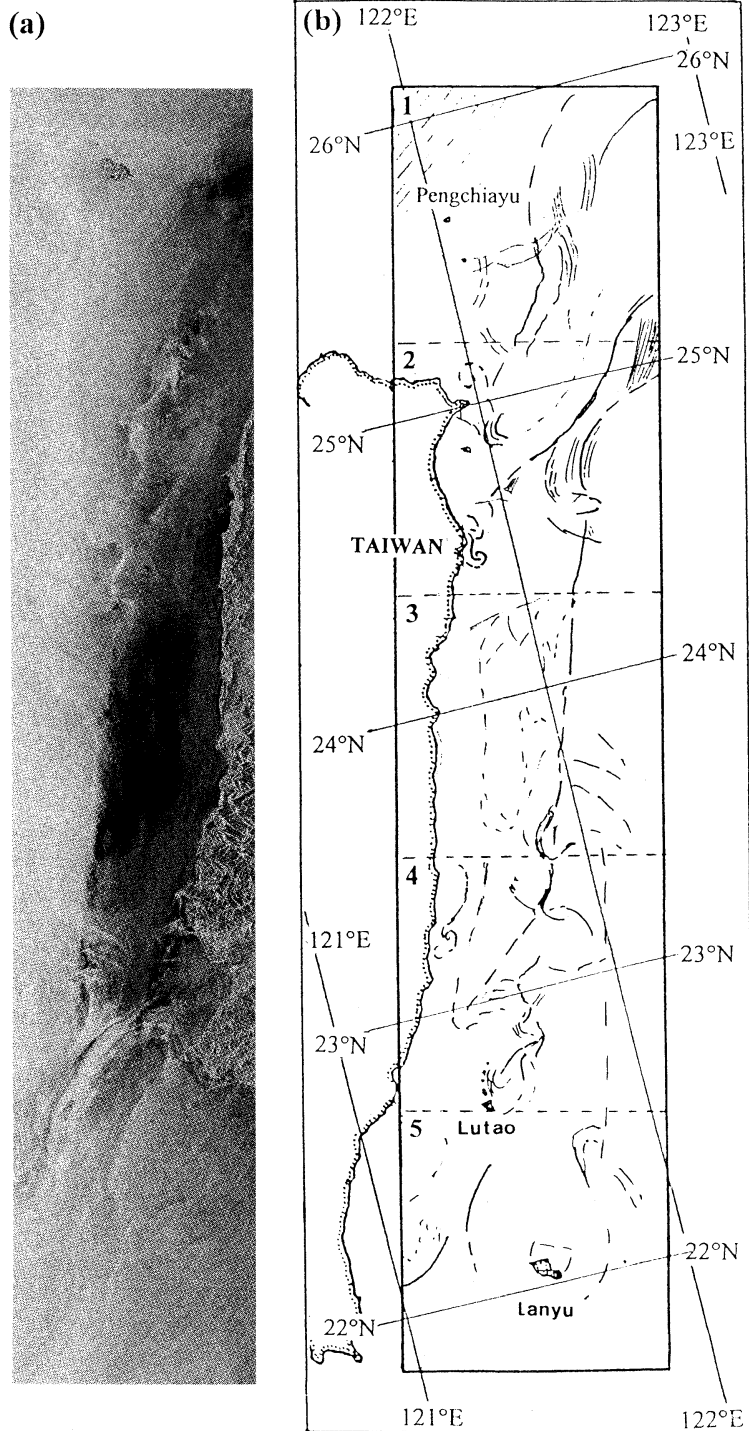


Fig. 4. SAR strip of five frames from ERS-1 on April 23, 1995, at 02 : 37 UTC (the original SAR image data is copyright ESA 1995) (a) and free-hand drawing of the contrast features (b), showing Kuroshio front, eddy-like structures along the front, packets of internal waves and surface manifestations of bottom topography.

Gulf Stream (FU and HOLT, 1982). Interaction of Kuroshio and tidal currents with shelf break causes generation of internal wave (IW) propagating both offshore and onshore (frame 1).

On the SAR images of Kuroshio acquired on other dates, several eddy-like structures behind Lanyu and Lutao as well as spiral eddies between these islands and over the underwater mountain at $23^{\circ}30'$, $121^{\circ}48'$ were observed. The possibility of eddy formation for currents flowing over topographic features was investigated theoretically by HUPPERT and BRYAN (1976). Intensive packets of the IW were observed in the area of frame 1 and further northeast. Their crests were directed approximately parallel to isobaths.

4.2 Upwelling

The region northeast of Taiwan is a region of the interaction between the Kuroshio and the East-China Sea waters. Satellite and ship observations were used to study upwelling (cold eddy) and the change of the western Kuroshio boundary in this area (CHEN, 1994; LIN, 1992). The upwelling was detected on Almaz-1 and ERS-1 SAR images as the area of reduced backscatter since 1992 (LIU *et al.*, 1992; HSU *et al.*, 1995).

Outlines of a large dark patch and the smaller dark features north of it on the SAR images (Figure 5, area D in Figure 1) agree with cold waters determined by NOAA-11 AVHRR (HSU *et al.*, 1995). The decrease of the SST was about $1-4^{\circ}\text{C}$. The cold waters are the upwelled subsurface nutrient-rich Kuroshio waters which impinge on the shelf break northeast off Taiwan. Damping of small scale roughness in this area may be caused by an increased surface film concentration and viscosity of slick-covered waters and by the more stable boundary layer of the atmosphere. Ship data collected during the Kuroshio Edge Exchange Program confirm both the SST decrease and the increased concentration of phytoplankton in the area of upwelling.

The scale, configuration, SST contrast and concentration of films vary here with time. Usage of SAR data can improve monitoring of upwelling. From the sequence of 23 SAR passes, collected in 1992-1995, evidence of

upwelling expressions assumed to be caused by the increased film concentration were clearly identified in 14 scenes out of 20 implying a capture rate of about 60%. During these 14 SAR overpasses the wind speed was between 2-3 and 10 m/s. The SAR images (Fig. 5) were taken at wind speed of 2-5 m/s. Swell with a wavelength of about 290 m from the strong tropical storm Walt with the center at 29.8°N , 133°E (1200km northeast of Taiwan) is clearly visible on the image.

4.3 Internal waves and eddies

Numerous packets of internal waves resulted from interaction of tidal current with the shelf break north of Taiwan were detected on the SAR images (Figure 1). Surface manifestations of several groups of the IW propagating to the east (at an almost right angle to swell) can be distinguished in Figure 5a. The crest lines are curved and their lengths decrease from the front to the rear. Their wavelengths decreased too due to the decrease of the amplitudes of the successive waves. The leading wave of a packet crossing the northeastern boundary of the dark patch has a large intensity: it is visible in the slick area due to surface wave breaking.

28 SAR images were collected in the southern East-China Sea. The packets of the IW propagating both offshore and onshore with an average group velocity of about 0.3-0.7 m/s were detected on 19 frames obtained at various environmental and tide conditions. A high probability of the IW detection denotes that the IW are a common phenomenon in the considered area. (The estimates of group velocity were obtained by measurements of the distance between packets of the IW identified in a particular SAR image. Analysis of the shape and the location of the packets allowed us to suggest that the packets were generated in the same sources by successive semidiurnal tidal cycles).

Eddies usually show up in SAR images as a result of wave/current interaction, which outlines the curved shape of the eddy, or are revealed indirectly through the presence of natural film trapped within spiraling lines associated with the eddy's orbital motion. The eddy having a large thermal contrast against a

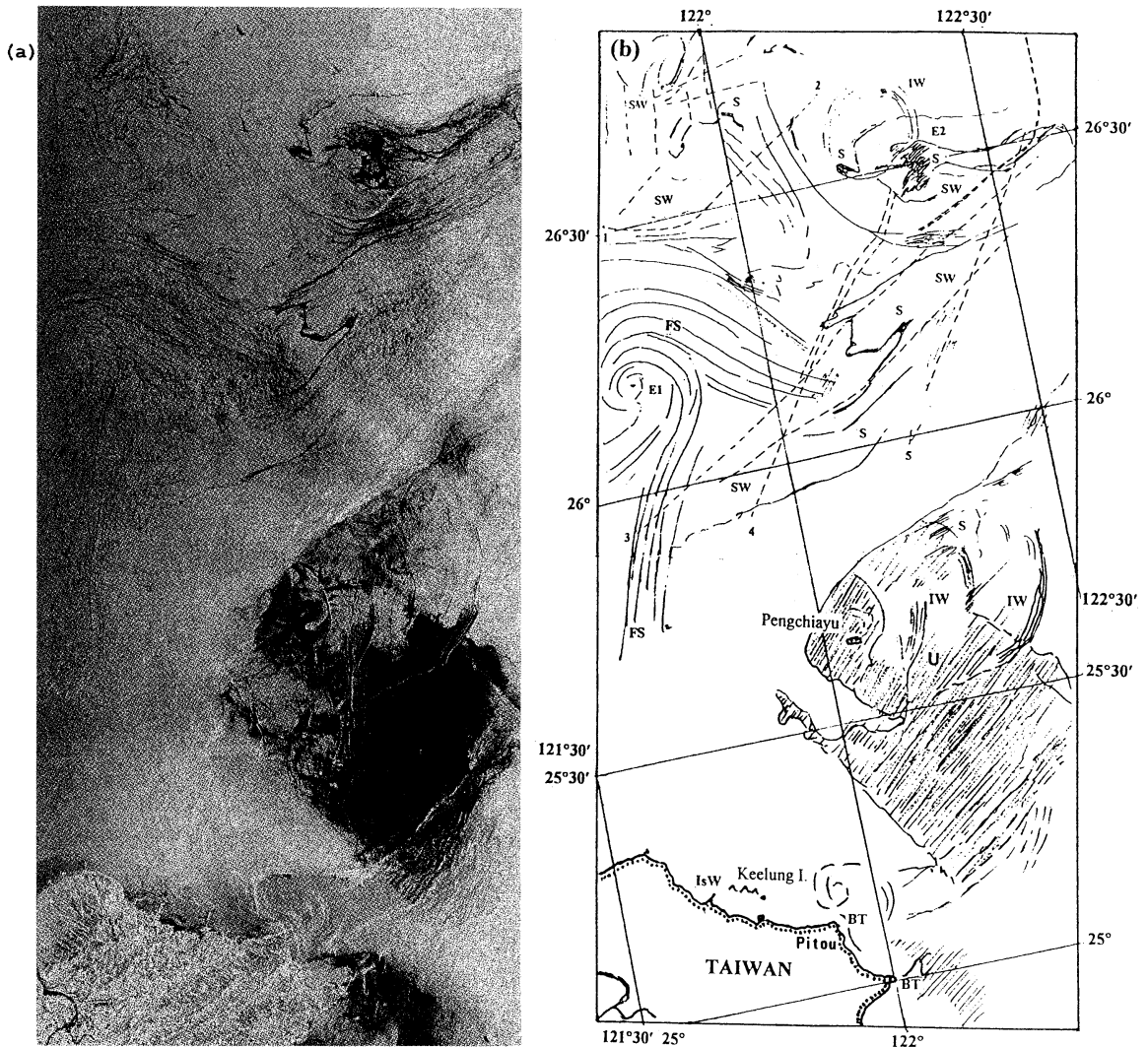


Fig. 5. SAR strip of two frames from ERS-1 on July 23, 1994, at 02 : 26 UTC (the original SAR image data is copyright ESA 1995) (a) and free-hand drawing (b), showing the location of upwelling (U), internal waves (IW), eddies (E1, E2), slicks (S), filamentary slicks (FS), surface manifestation of bottom topography (BT), island wake (IsW) and ship wakes (SW); ---- turbulent ship wake, ===== bright turbulent ship wake; 1-5-ships.

background can also be expressed by the change in wind stress across the temperature front (LICHY *et al.*, 1981; MITNIK and LOBANOV, 1991).

Mesoscale eddies E1 and E2 are made apparent in the SAR images by embedded narrow natural slicks (Figures 5a and 5b). These filamentary slicks (FS) aligned in spiral configuration reveal the E1 eddy. The spiral lines suggest convergence towards the eddy center.

Concentration of natural surfactants is higher in the area of the E2 eddy. The decreased SST (about 1-3°C) identifies this area in the IR image (Hsu *et al.*, 1995).

The variations of backscatter near Taiwan coast result from interaction of tidal current with the features of bottom topography (BT). A small-scale spiral eddy is seen north of Cape Pitou. An island wake (IsW) west of Keelung Island indicates the direction of the tidal

current (Figures 5).

5. Conclusion

This study has shown that under moderate (3–10 m/s) and strong (>10 m/s) winds the SAR can detect the imprints of the organized mesoscale structures in a field of horizontal sea surface wind caused by the wave phenomena in the boundary layer of the atmosphere: roll vortices, atmospheric gravity waves, etc. At high sea states the increased wave breaking (and thus, the increased values of the NRCS) marks the boundaries of the shallow waters.

Various oceanic phenomena manifest themselves under moderate winds only. These manifestations can have both positive and negative radar contrasts relative to the background. The narrow curved bright features sometimes in conjunction with the stretched slick bands and filamentary slicks allow to detect Kuroshio front, eddies of different sizes, mushroom-like currents, packets of internal waves, coastal fronts, etc. The upwelling north of Taiwan looks dark, likely, due to the increased concentration of natural surface films damping short gravity waves. The bright features arranging themselves into wave-like or eddy-like structures are also resulted from interaction of currents with underwater relief, islands and headlands.

These preliminary results demonstrated the potential of a satellite SAR for detecting and studying dynamical phenomena both in the atmosphere and in the ocean. With regular access to SAR observations, understanding of complex processes in air/sea system will be improved, especially in coastal region.

Acknowledgments

We thank the European Space Agency for ERS-1 and the staff at ESRIN and the Center for Space and Remote Sensing Research at National Central University in Taiwan for their enthusiastic help in data acquisition and processing. We are grateful to Maia Mitnik for figures' preparation and S. S. YU and S.-C. HUANG for assistance in processing of SAR images. This research was sponsored by the National Science Council through research grants NSC-82-0209-M002a-046W, NSC-83-0209-M019-010 and

NSC-84-2611-M019-009.

References

- ALPERS, W. and B. BRÜMMER (1994): Atmospheric boundary layer rolls observed by the synthetic aperture radar aboard the ERS-1 satellite. *J. Geophys. Res.*, **99**, 12613–12621.
- CHEN, Y.-L. L. (1994): The importance of temperature and nitrate to the distribution of phytoplankton in the Kuroshio-induced upwelling northeast of Taiwan. *Proc. National Science Council, ROC. Part B: Life Sciences.*, **18**, 44–51.
- DONELAN, M. and W. PIERSON (1987): Radar scattering and equilibrium ranges in wind-generated waves with applications to scatterometry. *J. Geophys. Res.*, **92**, 4971–5029.
- ETLING, D. and R. A. BROWN (1993): Roll vortices in the planetary boundary layer: a review. *Bound.-Layer Meteor.*, **65**, 215–248.
- FU, L.-L. and B. HOLT (1982): *Seasat Views Oceans and Sea Ice with Synthetic Aperture Radar*. JPL Publication 81–120, 200pp.
- HSU, M.-K., L. M. MITNIK and C.-T. LIU (1995): Upwelling area northeast of Taiwan on ERS-1 SAR images. *Acta Oceanographica Taiwanica*, **34**, 27–38.
- HUPPERT, N. E. and K. BRYAN (1976): Topographically generated eddies. *Deep-Sea Res.*, **23**, 655–679.
- LICHY, D. E., M. G. MATTIE and L. J. MANCINI (1981): Tracking of a warm water ring. *In: Spaceborne Synthetic Aperture Radar for Oceanography*, BEAL, R. C. P. S. DELEONIBUS and I. KATZ, (eds.), Johns Hopkins University Press, Baltimore, Md., 215pp.
- LIN, C.-Y., C.-Z. SHYU and W.-H. SHIH (1992): The Kuroshio fronts and cold eddies off northeastern Taiwan observed NOAA AVHRR imageries. *Terrestrial, Atmospheric and Oceanic Sciences (TAO)*, **3**, 225–242.
- LIU, C.-T., L. M. MITNIK, M.-K. HSU and Y. YANG (1994): Oceanic phenomena northeast of Taiwan from ALMAZ SAR image. *TAO*, **5**, 557–571.
- MARMORINO, G. O., R. W. JANSEN, G. R. VALENZUELA, C. L. TRUMP, J. S. LEE and J. A. C. KAISER (1994): Gulf Stream surface convergence imaged by synthetic aperture radar. *J. Geophys. Res.*, **99**, 18315–18328.
- MITNIK, L. M., C.-T. LIU, M.-K. HSU and K. S. CHEN (1994): Mesoscale atmospheric organized structures over the Asian marginal seas on satellite radar images. *Preprints of Second Intern. Conference on Air-Sea Interaction and on Meteorology and Oceanography of the Coastal Zone*. Lisbon, Portugal, 22–27 September 1994, 175.

- MITNIK, L. M. and V. B. LOBANOV (1991): Reflection of the oceanic fronts on the satellite radar images. *In: Oceanography of Asian Marginal Seas*, Takano, K. (ed.), Elsevier Oceanography Series, **54**, Elsevier, Amsterdam, P.85-101.
- MITNIK, L. M. and S. V. VIKTOROV (ed.) (1990) Radiolokatsiya Poverkhnosti Zemli iz Kosmosa (Radar Imaging the Earth's Surface from Space). *Gidrometeoizdat, Leningrad*, 200 pp. (in Russian).
- NILSSON, C. S. and P. C. TILDESLEY (1995): Imaging of the oceanic features by ERS 1 synthetic aperture radar. *J. Geophys. Res.*, **100**, 953-967.
- QUILFEN, Y. (1995): ERS-1 off-line wind scatterometer products. CERSAT, Ref.: C1-EX-MUT-CD0000-03-IF, 58 pp.
- VACHON, P.W., O.M. JOHANNESSEN and J.A. JOHANNESSEN (1994): An ERS 1 synthetic aperture radar image of atmospheric lee waves. *J. Geophys. Res.*, **99**, 22483-22490.
- VACHON, P. W., J. A. JOHANNESSEN and D. P. BROWNE (1995): ERS-1 images of atmospheric gravity waves. *IEEE Trans. Geosci. Remote Sensing*, **33**, 1014-1025.
- VASS, P. and B. BATTRICK (eds.), (1992): ERS-1 System ESA SP-1146, ESA Publications Division, c/o ESTES, Noordwijk, The Netherlands, 87 pp.
- VESECKY, J. and R. STEWART (1982): The observation of ocean surface phenomena using imagery from the SEASAT SAR: an assessment. *J. Geophys. Res.*, **87**, 3397-3430.

Received January 13, 1996

Accepted March 8, 1996

Variability of suspended particle concentration due to tidal influences in the shelf sea north of Taiwan

Cheng-Han TSAI* and I-Jiunn CHENG**

Abstract: This study investigated the time variation of the concentration of suspended particles in the shelf sea north of Taiwan due to tidal current. Waters from five tidal-cycle stations located on the shelf and the shelfbreak were sampled at various depths at a time interval of 2 hours. Suspended particle concentrations were determined, and currents were measured by a vessel mounted ADCP. It was found that for stations at the continental margin, the variation of particle concentration did not correlated well with the magnitude of the tidal current, but can change with the flow direction. Concentration was higher when the current flowed toward one direction and lower toward the other, which reflected the spatial variation of particle concentration. At the shelf stations, the concentration of the bottom layers increased with the flow velocity regardless of its direction, which may be due to the bottom resuspension and deposition or the convection of particle clouds caused by the tidal current, which in turn maintained a bottom nepheloid layer. The results also showed that the depth average of the ratio of maximum to minimum concentration in a tidal cycle ranged from 1.6 to 2.8, depending on the location, with a mean value of 2.3. That is, there is a factor of two's variation in concentration in a tidal cycle. It was also found that the time and depth mean concentration in the shelf sea was about 0.5 to 2 mg/l while in the shelfbreak region was 0.2 mg/l. The time mean concentration for shelf break station was constant along the depth, while that for shelf stations increased exponentially with depth. By analyzing the disaggregated suspended particles found at a shelf station it was found that 98% of the particle was less than 64 μ m with a median diameter about 6 μ m. That is, only the fine particles on the sediment surface were involved in the resuspension and deposition cycle.

1. Introduction

Suspended particles consist of terrigenous minerals and biogeneous particles, which are quite small in size and are light enough to move with the current. To study the transport of suspended particles or geochemical processes associated with particles in water environments, suspended particle concentration (or suspended particulate matter) needs to be investigated. This parameter can be easily measured by sampling the water and then determined gravimetrically or measured electronically using transmissometers or nephelometers. Suspended particle concentration, much like any other marine parameters, varies

according to several time scales, such as daily, tidal, seasonal etc. (KRANCK, 1980). Among them, tidal variation has received careful attention for studies carried out in coastal waters such as estuary, bay and inlet (e. g. POSTMA, 1965; KRANCK, 1980; KRANCK and MILLIGAN, 1992), since in these places the resuspension and deposition of the sediment due to tidal current are prominent. However, for related studies in the shelf, the tidal influences on the suspended particle concentration are often neglected. Particularly, during a survey of continental shelf, stations along one or more transects are often visited sequentially regardless of the tidal phase when the stations are visited. Due to large distance that has to be covered, the mapping of suspended particle by this method can be different from the real synoptic suspended particle distribution. The reasons for this are twofold. One, tidal current on

* Department of Oceanography, National Taiwan Ocean University, Keelung, Taiwan

** Institute of Marine Biology, National Taiwan Ocean University, Keelung, Taiwan

the shelf, which are the strongest current in the shelf sea, often traces out a tidal ellipse. Hence, the water sampled at a given location at different time can be different. Moreover, if there is a spatial variation of the particle concentration, the concentration will change with the current direction. Two, at places where depths are shallow enough and where bottom sediments are available for resuspension, the suspended matter would definitely vary with the tidal phase. Hence there is a need to establish the variability of this parameter due to tidal influences.

The objectives of this study are to measure the tidal variation of suspended particle concentration at various stations from the mid-shelf to the shelf edge north of Taiwan. These stations were occupied for 12 hours and current velocity and particle concentration were measured. The current velocity was used to determine the tidal phase. From results of this study, the maximum variability of particle concentration in a tidal cycle in this region was established. It is to note here that although some explanations on the temporal variation of the particle concentration are offered, they may be contested. Further investigation is necessary to clarify the reasons for variations.

2. Sampling locations and methods

The shelf sea north of Taiwan (Fig. 1) is a part of the marginal sea east of Chinese continent. Current field in this region includes Chinese continent coastal water, monsoon driven current, and Kuroshio, and they vary according to the summer and winter seasons (NIINO and EMERY, 1961). Along the coast of Chinese continent, the coastal water flows southward and enter Taiwan Strait in the winter when the northeasterly monsoon prevails. In the summer, the coastal water does not enter the Taiwan Strait, due to the opposing southwesterly monsoon, and turns eastward (THOMAS and PERRY, 1968). In the area north of Taiwan strait (or mid-shelf), the current is mostly monsoon-driven current. In the summer, the wind driven current combines with a branching Kuroshio in the strait flows northward. While in the winter, the current flows southward due to the northeast monsoon. At the lower shelf near the

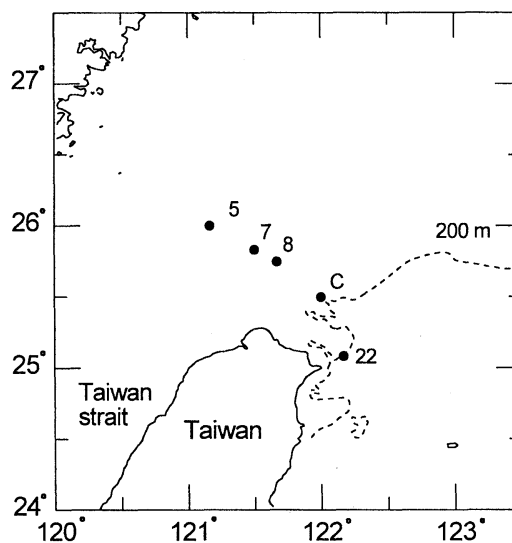


Fig. 1. Stations locations.

continental margin a complicated exchange process between the shelf water and Kuroshio exists (LIU *et al.*, 1992). Here, Kuroshio, skirting along the east coast of Taiwan, turns toward northeast as it encounters the continental edge located north of Taiwan, following the topography of the edge. Intrusion of Kuroshio water onto the shelf north of Taiwan has been reported by several researchers (e. g. LIU and PAI, 1987; CHERN and WANG, 1989).

Tidal current in the shelf sea north of Taiwan runs in the general direction of WNW and ESE, following the direction of the north coast of Taiwan. During the flood tide, tidal current flows from the offshore area toward the WNW direction and branches into Taiwan Strait. The current direction reverses during the ebb phase. The maximum speed of the current is one to three knts.

The bottom sediment on the shelf in this region has one of the typical distribution patterns on continental shelves as described by McCAYE (1972). Investigation conducted by BOGGS *et al.* (1974) indicated that close to the Chinese continental coast, the bottom are mainly fine-grained clay and silt particles deposits with traces of sand. This mud belt was suggested to be related to the input of the fine sediments from Chinese rivers (NIINO and EMERY, 1961). The percentage of fine particle deposits decreases and that of sand increases as

Table 1. Locations and depths of sampling stations and the time of sampling.

Station	Latitude	Longitude	Depth(m)	Cruise	Time
5	26°	121° 10'	83	389	4-5/6/94
7	25° 50'	121° 30'	78	352b	22/4/93
8	25° 45'	120° 40'	115	386	6/5/94
C	25° 30'	122°	120	365	29-30/8/93
22	25° 5'	122° 10'	205	352b	24/4/93

the distance from the continent increases. From the mid-shelf to lower-shelf, seabed changes from sandy mud to mostly sand and shell fragments. Sandy sediments in this area are of relic origin (NIINO and EMERY, 1961). On the continental slope fine-grained particles reappear with its size distribution closely resemble that found near the continental coast. The fine particle distribution pattern in this region seems to conform to the notion that sediment particles are transported from the continental coast toward the offshore water, and deposited on the slope and beyond, passing over the lower shelf (McCAYE, 1972).

Five tidal-cycle stations (Fig. 1) were occupied in four different cruises (Table 1) during spring and summer seasons. Since the purpose of this study is to look at the changes in the time scale of a tidal cycle, it does not matter whether experiments are conducted in various or in one cruise. Station 5, which has a depth of 83 m, was located at mid-shelf, while stations 7 and 8 at lower mid-shelf with depths of 78 m and 115 m respectively, and stations C and 22 were near the shelf edge with depths of 120 m and 205 m respectively. Each station was occupied for 12 hours. Since the research vessel was not anchored, it drifted with the tides. Hence, the vessel was always returned to the original position at the sampling time. Water samples from four to five levels, including one from the surface and one from the near bottom were collected every two hours by Go-Flo water bottles on a rosette sampler attached to a CTD. Four to eight liters of water, depending on the concentration, were filtered through preweighted Nuclepore polycarbonate filters for particle concentration determination. Multiple tests showed that the concentration measurements had a coefficient of variation about 10%.

In order to correlate the measured suspended particle concentration with the tidal current,

concurrent current data were obtained. The currents were measured by a vessel mounted Acoustic Doppler Current Profiler (from RD Instruments). The ADCP had a frequency of 150 kHz. Ten-minute-average of the ADCP data were obtained. Only the data corresponding to the time when water samples were collected were selected. Due to the limitation of the instrument, the topmost velocity was measured at 12m deep and the lowest layer measured was about 25% of the water depth above the sea bed. Hence, the bottom shear stress created by the current can not determined. The phenomenon of bottom resuspension is often discussed in terms of bottom shear stress. However, in this study only the current velocity is discussed. This is not really a problem, since this study does not investigate the quantitative relationship between the bottom resuspension and the bed shear stress.

Size distributions of disaggregated bottom sediment and suspended particles were also measured for some stations. Bottom sediments were obtained by a box core and pretreated by sodium hexametaphosphate (GALEHOUSE, 1971) for peptization. Wet sieving was used to separate sands and shells from silts and clays by a 64 μ m sieve. Particles larger than 64 μ m were then dry-sieved and silts and clays, mixed in DI water suspension, were analyzed by a laser based particle sizer (CIS-1 by Galai). This instrument determines particle size by scanning individual particles with a fine, rotating laser beam. Size information was determined by the time length of light obscuration by the scanned particle (AHARONSON *et al.*, 1986; TSAI and RAU, 1992). Suspended particles were obtained from the filters used for concentration determination by immersing them in DI water and in an ultrasonic bath. Their sizes were also measured by the CIS-1.

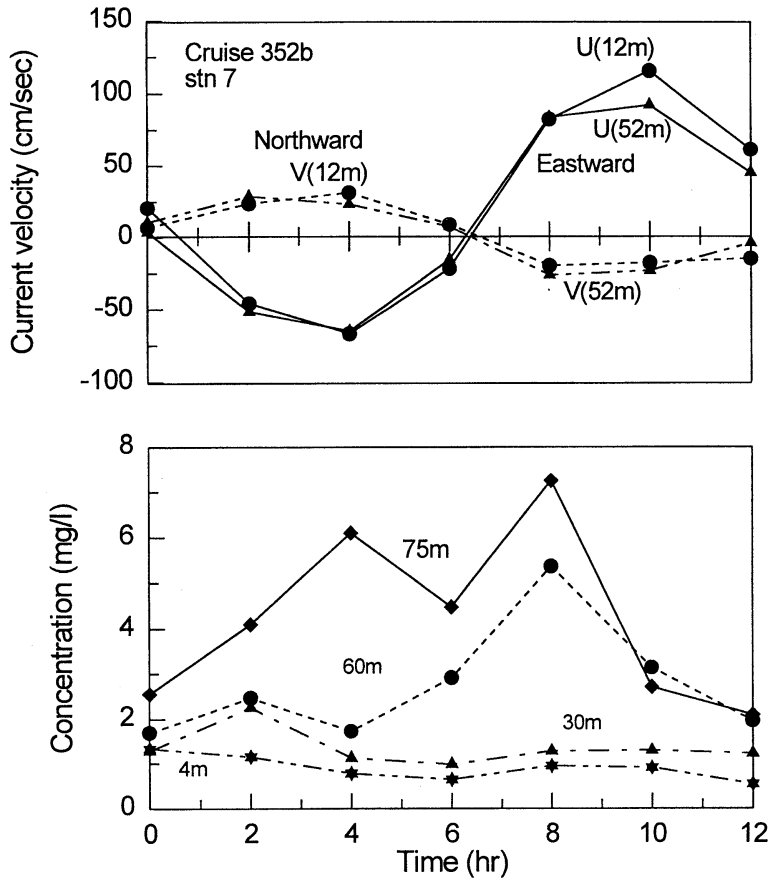


Fig. 2. Temporal variation of current velocity and concentration for the station 7 (U : east-west component and V : north-south component).

3. Results and discussion

3.1 Particle concentration and current velocity

For brevity, two examples are presented here: stations 7 and 22. At the lower-mid shelf station, the tidal current was uniform over the depth and was highly semidiurnal (Fig. 2). In the first half of the observation period, the current was in the direction of WNW and then turned ESE in the later half. The U component was not entirely symmetric between the flood and ebb phases though. The maximum eastward flow was over 100 cm/s while the westward current was only 70 cm/s. The north-south component of the current was, on the other hand, quite symmetric but only reached a maximum speed of 25 cm/sec.

The concentration at the upper layers (4 m and 30 m) was less than 2 mg/l and showed

slight increase when the tidal current was in the maximum flood and ebb stages. Since this station was only 78 m deep and the bottom current was quite strong, one would expect that bottom resuspension at the maximum current is important. This phenomenon can be seen from the suspended particle concentration. At 75 m the concentration increased from 2.6 mg/l to 6 mg/l as the current picked up from the slack tide at the hour 0 to maximum flood at the hour 4. At the hour 6 the tide slacked again. The concentration at the bottom decreased to 4.2 mg/l, and then increased to 7.2 mg/l at the hour 8 as the current turned east and accelerated. Then the bottom turbidity dropped sharply to 2.6 mg/l at the 10th hour; equal to its corresponding concentration at hour 0. At the 60 m level, the sediment concentration only

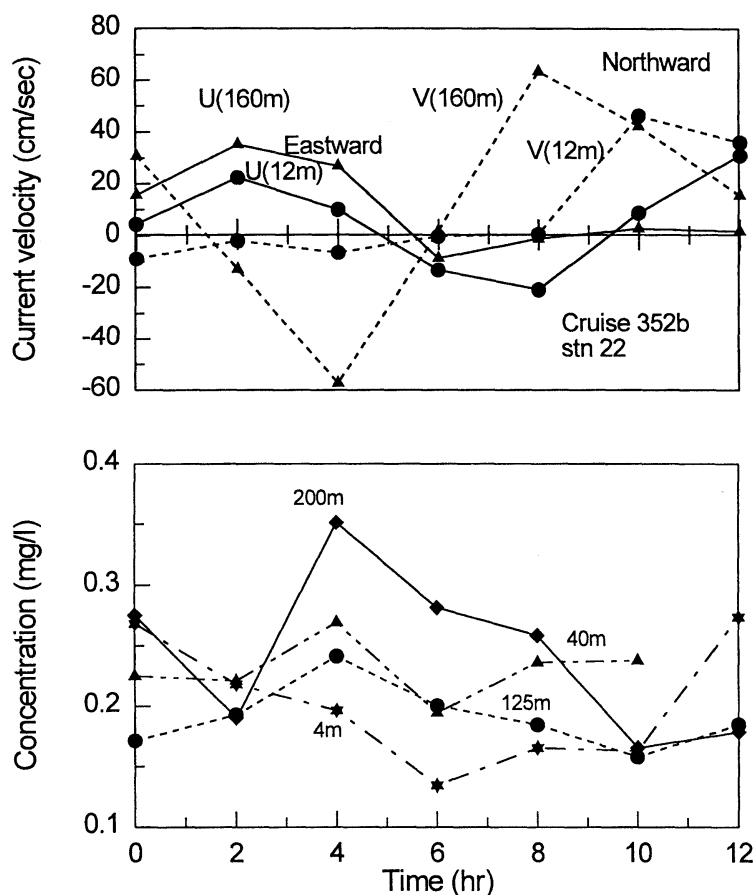


Fig. 3. Temporal variation of current velocity and concentration for the station 22.

increased slightly during the flood tide and then increased significantly as the current turned southeastward when the tide was strong enough to diffuse the particles upward to this level. The asymmetry in the flood and ebb velocity caused the maximum suspended concentration to be higher during the ebb phase than at the flood phase. This and the dip in the bottom concentration at the slack period seem to indicate that the bottom resuspension and deposition were responsible for the fluctuation in the particle concentration. However, the sharp decrease during the peak ebb current at hour 10 contradicts this explanation. This dip may be due to a possible depletion of a limited amount of bottom sediments which the flows are capable to resuspend. The whole temporal fluctuation of concentration may even be attributed to the movement of particle clouds

carried by the tidal current, and the sharp decrease of concentration at hour 10 can be explained by the departure of the cloud; or due to both particle clouds and bottom resuspension. Despite this fluctuation, there existed a bottom nepheloid layer at all time with a particle concentration of at least 2 mg/l.

Figure 3 is the current and concentration data obtained from the station 22. The current changed with depth rather significantly at this station. As can be seen from the figure, the magnitude of the surface current was often less than the bottom current. In the surface layer the current flowed towards E and turned towards W and then NE, while in the lower layer the V component exhibited a well defined semidiurnal variation. The east-west component at the 160 m level only showed a eastward flow in the first 6 hours and then it almost

Table 2. Coefficient of variation (CV) and ratio of maximum to minimum values (Cmax/Cmin) for suspended particle concentration for all stations.

Stn 5			Stn 7			Stn 8			Stn C			Stn 22		
Depth (m)	CV (%)	Cmax/Cmin	Depth (m)	CV (%)	Cmax/Cmin	Depth (m)	CV (%)	Cmax/Cmin	Depth (m)	CV (%)	Cmax/Cmin	Depth (m)	CV (%)	Cmax/Cmin
4	25	2.0	4	31	2.5	4	31	2.4	4	33	2.2	4	26	2.0
30	19	1.8	30	31	2.3	40	29	2.2	40	43	3.2	40	11	1.4
55	15	1.7	60	47	3.2	80	30	2.1	90	35	2.6	125	14	1.5
70	34	3.1	75	46	3.5	110	30	2.6	115	17	1.7	200	28	2.1
80	12	1.4												

vanished in the second. Clearly, the current pattern deviates considerably from that of tidal current found at the previous station. By comparing the velocities of the upper and lower levels, one can see that there was large disparity in the flow velocity between the two levels, showing baroclinic effects. This phenomenon may be attributed to the effect of internal tide, generated by the interaction of surface tide and the abrupt change in bottom topography, such as a continental edge (BAINES, 1982). MAEDA (1979) also suggested that internal tide is prevalent in the south East China Sea. The suspended particle concentrations were all quite low, between 0.35 to 0.15 mg/l. At each level, the suspended concentrations also showed variation with time. Noticeably, one can see that during southeastward (ebb) flow, the concentration were higher, and as the flow turned westward, the particle concentration decreased, despite the peaking of the bottom flow speed.

It is clear that there was no discernible bottom resuspension observed at the station near the shelf edge. Although there is no definite increase of concentration as the flow speed reached its peaks, there are indications that suspended particle concentration varies with the flow direction. Hence this phenomenon showed a spatial variation of particle concentration. That is the temporal variation of concentration may be due to convection. In order to clarify the mechanisms which caused the temporal fluctuation of particle concentration, more investigations are warranted. Self-recording transmissometers and current meters tethered on a mooring line or fixed on a tripod for a longer term measurement can be an option.

3.2 Range of variation of particle concentration

Since the suspended particle concentration varied with time, one can examine its range of variation within a tidal cycle. Listed in Table 2 are the statistics of the particle concentration for each depth level for all stations. The table includes : the coefficients of variation (CV), computed by dividing the standard deviation of concentration by the time mean concentration, and the ratios of maximum to minimum concentration measured in the tidal period. The CV value represents the variability relative to the time mean value, while the ratio stands for the maximum variability within the tidal cycle. Among all stations, the coefficient of variation ranged from 11% to 47%; all are larger than the variation due to the measurement itself. The ratio of maximum to minimum concentration varied between 1.4 and 3.5. As can be seen, these two parameters also varies with depth at each station. At the station 7, the CV and Cmax/Cmin increased towards the bottom, as there was large concentration variability due to resuspension and deposition. The variability for stations 5, C, and 22 also differed significantly with the depth, while that for station 8 was uniform with depth. Figure 4 plotted the envelopes of minimum and maximum concentration for all stations. The envelopes represent the band within which the concentration in the tidal cycle fall. By integrating the CV and the maximum to minimum concentration ratio with depth, their depth mean values for each station were obtained (Table 3). Among these five places, the depth mean CV changed from 17% to 37% and maximum to minimum ratio was in the interval of 1.6 to 2.8. As can be seen from the table, station 7 has the largest variability with station C the second, while

Table 3. Comparison of depth mean value of CV and the ratio of maximum to minimum value of particle concentration with that of water temperature and salinity.

	Stn 5		Stn 7		Stn 8		Stn C		Stn 22		Mean	
	CV (%)	max/min	CV (%)	max/min	CV (%)	max/min	CV (%)	max/min	CV (%)	max/min	CV (%)	max/min
Conc.	21	2.0	37	2.8	30	2.3	35	2.6	17	1.6	28	2.3
Temp.	0.61	1.02	5.56	1.19	2.78	1.07	7.28	1.23	7.16	1.21	4.68	1.14
Sal.	0.03	1.001	1.04	1.031	0.04	1.001	0.38	1.011	0.07	1.002	0.31	1.009

station 22 has the least. On average, the CV value for all stations was 28% and the ratio of maximum to minimum concentration was 2.3. The latter value is significant; It indicates that the maximum variability of particle concentration in a tidal cycles is at least 2.

It is well known that the suspended particle concentration is independent of the temperature and salinity of the water. However, for the purpose of comparison, the variability of the latter two parameters within a tidal cycle was investigated. Also listed in the Table 3 are depth mean of CV and maximum to minimum ratio for water temperature and salinity. It shows that their variability was quite small compared with that for the particle concentration. The highest variability for temperature was 7.3% and 1.23 for CV and maximum to minimum ratio, respectively, which occurred at the station C. The average among stations was 4.7% for CV and 1.14 for maximum to minimum ratio. Correspondingly, the largest variability for salinity occurred at the station 7 with a 1.04% for CV value and 1.03 for maximum to minimum ratio. The variability for salinity averaged among stations was only 0.31% for CV and 1.009 for maximum to minimum ratio.

3.3 Particle concentration profile

Also plotted in Fig. 4 are the time mean concentration profiles for all stations. As can be seen, the time mean surface concentrations were very close for all stations (between 0.2 and 0.3 mg/l) except at station 7, whose value was 0.9 mg/l. For stations on the shelf (5, 7 and 8), where there existed a bottom nepheloid layer, their time mean concentration exhibited an increasing trend towards the bottom. On the other hand, there was no definite trend for time mean concentration change over depth for stations C and 22, where there was no bottom

resuspension. Their profiles of time mean concentration can be approximated by a constant value. The depth averages of the time mean values were 0.5 mg/l for stations 5 and 8, 2 mg/l for station 7 and 0.2 mg/l for shelf edge stations C and 22. For the former three stations, their mean concentration correlate with their maximum tidal current speed, which is 70 cm/s for stations 5 and 8 and 100 cm/s for station 7. The low concentration for stations C and 22 can be attributed to no resuspension and their proximity to the deep ocean.

Sediment resuspended by the tidal current will diffuse upward by turbulence while the gravity will pull them downward. The net results is an exponential increase of sediment concentration toward the bottom (McCAYE, 1972). This type of concentration profile has been demonstrated by many measurements. For example, the temporal variation of particle concentration measured by POSTMA (1965) in the Guerrero Negro lagoon, Baja California, which is about 10 m deep, fits the exponential distribution very well. LICK *et al.* (1992) also showed this by solving the conservation of mass equation for vertical particle transport for steady state solution. The equation is

$$\frac{\partial}{\partial z}(w_s C) = \frac{\partial}{\partial z}\left(A_v \frac{\partial C}{\partial z}\right) \quad (1)$$

where z is the vertical distance measured from the water surface. C the concentration, w_s the settling velocity and A_v the eddy diffusivity. For an idealized case, assuming that w_s and A_v are independent of z , then the concentration C has the form

$$C = C_0 \exp(z_0 z) + F/w_s \quad (2)$$

where C_0 is a reference concentration, $z_0 = w_s/A_v$, and F an integration constant corresponding to the flux $w_s C$ specified at a large negative z distance. If the flux is set zero, the concentra-

tion profile became

$$C = C_0 \exp(z_0 z) \quad (3)$$

Which is an exponential function with C_0 represents the surface concentration, and z_0 is an coefficient indicating the degree of increase of the concentration with respect to depth.

Figure 4 shows that the time mean concentration profiles fit equation (3) well. Regression analysis showed the profiles fit exponential functions with correlation coefficient (R^2) better than 88%. A more closer examination also showed that the concentration profile for station 7 at each time step also fits the exponential profile well (Table 4). It is to note that the changes of C_0 value with time correspond well with the time variation of measured surface concentration. The z_0 value also varies in-step with resuspension activities.

3.4 Particle size distributions

Suspended particles exist in water as a flocculated particles, and they continue to aggregate and disaggregate due to particle collision and shear. In order to investigate the size of constituent particle (or so called primary particle) of these suspended particles, they have to be disaggregated. The size distributions of disaggregated suspended particles from the station 7 were analyzed, since this station exhibited the most active bottom resuspension. Shown in Fig. 5 are four suspended samples from various depth at different tidal phases. The figure indicates that these distributions are almost identical; although the largest median size is $6.2 \mu\text{m}$ obtained at the 75 meter depth during the highest resuspending activity and the smallest median diameter is $5.4 \mu\text{m}$ for the surface sample at hour 12. It can also be seen that 95% of the particles are fine-grained. This indicates that only the fine-grained portion of the sediments are being resuspended and deposited by the tidal current.

The stations on the shelf showed possible occurrence of resuspension, while the continental edge stations did not. The resuspension of bottom sediment depends on the magnitude of the current and the availability of sediment. Thus, it is of interest to determine the type of the sea bed. Shown in Fig. 6 are the sizes of sediments

from stations 5, 7 and 22. As can be seen, at station 5 (in mid-shelf), its bottom sediment contains about 30% mud and 70% of sand. The median size at this place is $90 \mu\text{m}$. Further outward, the median size at station 7 is $190 \mu\text{m}$ and only 1% is fine-grained. Although there was more mud found at station 5 than at station 7, since the maximum tidal current for the former station was 30% smaller than the latter, the former location had less suspended particles than the latter. The sediment at the station 22, located on the shelf edge, is coarser than that of stations 5 and 7. Its bottom sediment had a median diameter of $210 \mu\text{m}$ and contained a large percentage (about 30%) of particle larger than $500 \mu\text{m}$, which was observed to be shell fragments, while there was only 3% for the sediment found at the station 7. In general this size analysis conforms to the distribution of bottom sediment reported by BOGGS *et al.* (1974)

4. Summary

Water samples were obtained from five stations on the shelf and near the shelfbreak north of Taiwan. The particle concentrations were measured from various levels and their variation with time in a tidal cycle was examined. The current velocity was also measured concurrently. It was found that on the shelf particle concentrations were influenced by the speed of the current through bottom resuspension or convection of particle clouds, while near the continental margin the concentration was generally insensitive to the current speed, but can vary with the direction of the flow. This is an evidence that there is a spatial variation of particle concentration, and this causes the changes of concentration due to the tidal current. Within a tidal cycle, the highest particle concentration was 1.4 to 3.5 times as large as the lowest concentration, depending on the depth and location. In the bottom layer of the shelf station, where bottom resuspension was significant, the maximum to minimum concentration ratio was the highest. Taking average on this ratio over the water depth, it varied from 1.6 to 2.8 for various stations. On average, it can be said that the suspended particle concentration in a tidal cycle varied with a factor of no less than two. This is the error that can be expected

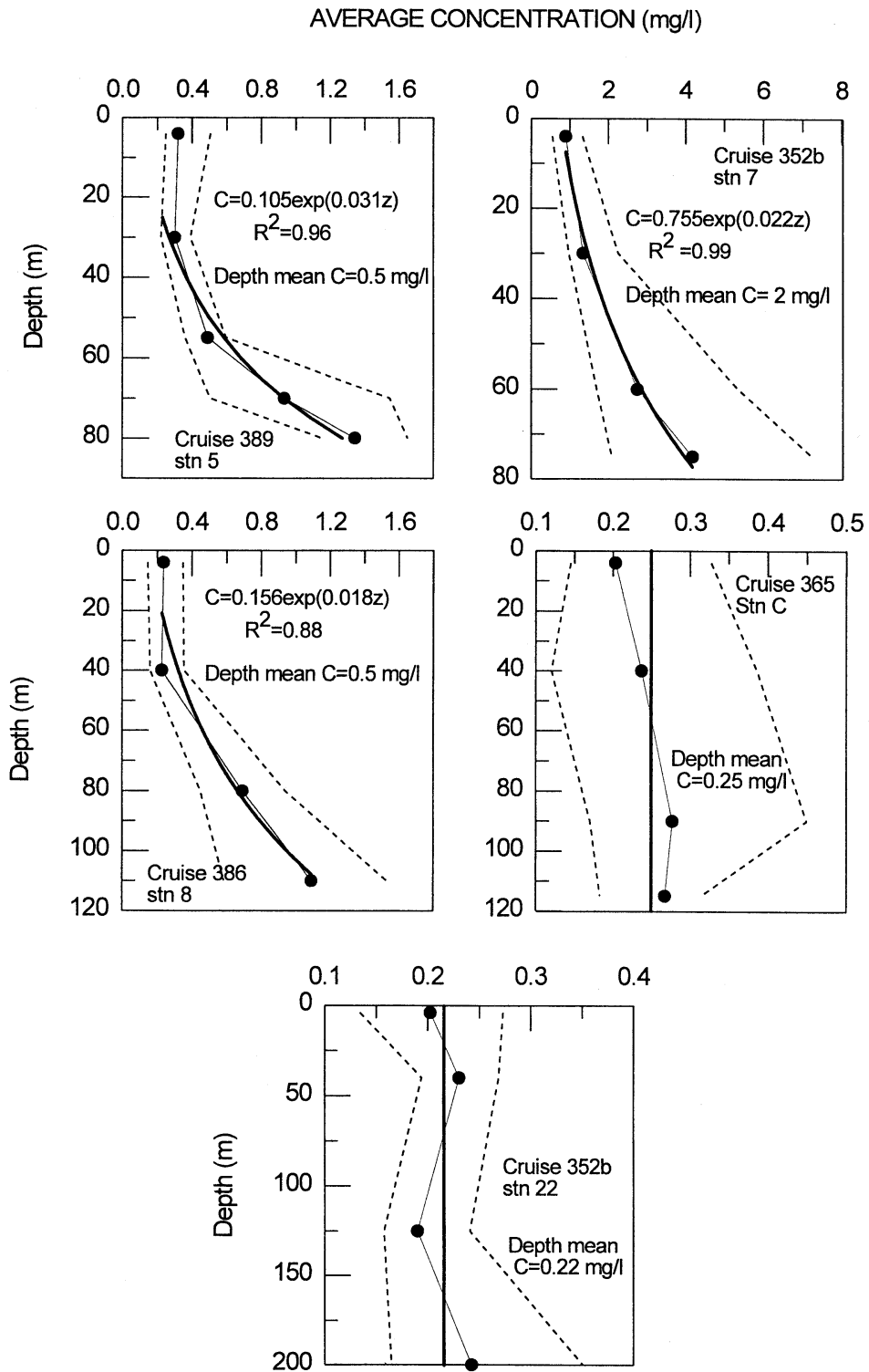


Fig. 4. Time averaged depth profiles of particle concentration (including the minimum and maximum envelopes) for all stations.

Table 4. Parameters of the concentration profile, $C=C_0 \exp(-z_0/z)$, and correlation coefficient R^2 for the station 7 at various sampling times.

	0h	2H	4h	6h	8h	10h	12h
C_0 (mg/l)	1.00	1.07	0.46	0.49	0.64	0.76	0.54
z_0 (l/m)	0.012	0.018	0.031	0.029	0.033	0.020	0.020
R^2	0.75	0.90	0.82	0.98	0.95	0.90	0.93

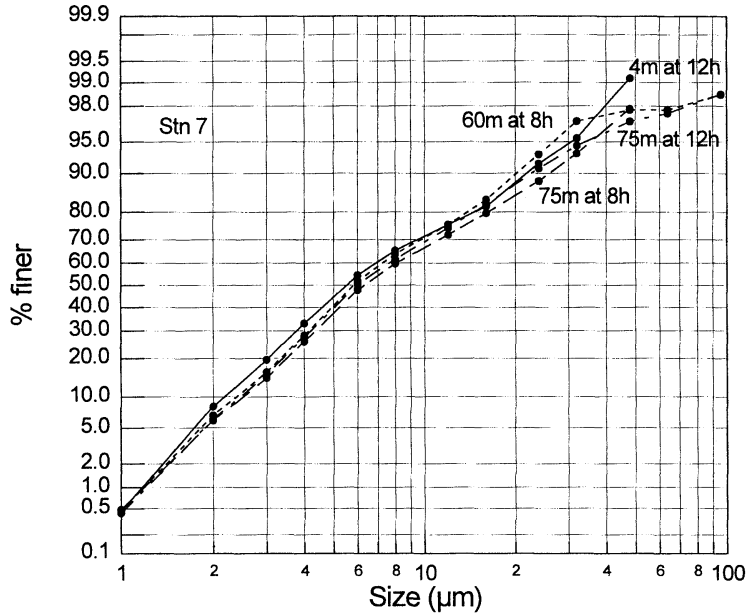


Fig. 5. Size distributions for disaggregated suspended particles obtained at various depths and times at the station 7 (in log-normal probability).

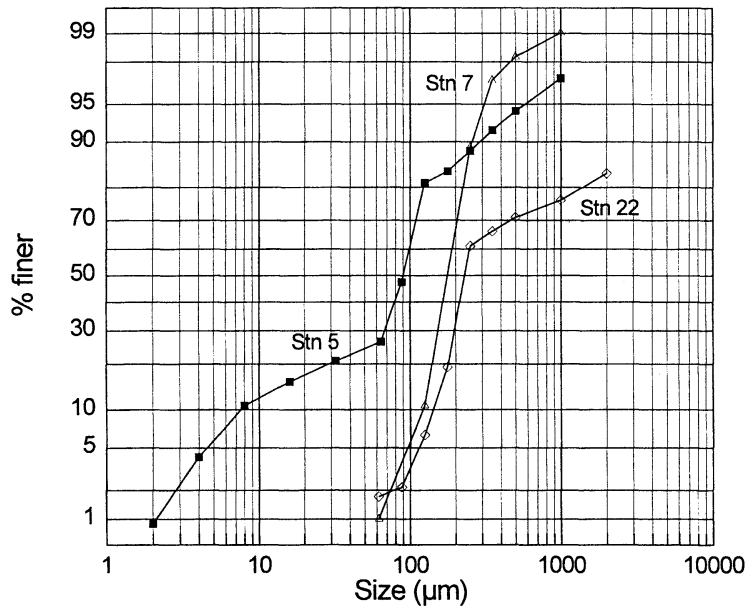


Fig. 6. Size distributions for bottom sediments (in log-normal probability).

in this region if the tidal phase is ignored when studying suspended particle distribution.

On the shelf the time mean (over a tidal period) concentration increased exponentially with depth. The depth mean value of the time mean concentration varied from 0.5mg/l to 2 mg/l, depending on the magnitude of tidal current. At two locations close to the continental margin no bottom resuspension was observed. Their depth profile of the time mean concentration can be approximated by a constant value of 0.2 mg/l. Particle size analysis performed on the resuspended particles revealed that the primary suspended particles were predominantly fine-grained particles with a median diameter of 6 μ m. This means that only the fine-grained particles are continuously being resuspended and settled on the shelf. Some of the resuspended particles are then transported to the deep ocean.

Acknowledgments

This study was supported in part by the National Science Council grants 82-0209-M-019-003-K and 83-0209-M-019-005-K.

References

- AHARONSON, E. F., N. KARASIKOV, M. ROITBERG, and J. S. HAMIR (1986): Galai-CIS-1: a novel approach to aerosol particle size analysis. *J. Aeros. Sci.*, **17**, 530-536.
- BAINES, P. G. (1982): On internal tide generation models. *Deep Sea Res.*, **29**, 307-338.
- BOGGS, S. Jr., W. C. WANG and J. C. CHEN (1974): Textural and compositional patterns of Taiwan shelf sediment. *Acta Oceanogr. Taiwan.*, **4**, 13-56.
- CHERN, C. S. and J. WANG (1989): On the water masses at northern offshore area of Taiwan. *Acta Oceanogr. Taiwan.* **22**, 14-32.
- GALEHOUSE, J. S. (1971): Sedimentation analysis. in *Procedures in Sedimentary Petrology*. Carver, R. E. (ed.), Wiley-Interscience, New York, 69-94.
- KRANCK, K. (1980): Variability of particulate matter in a small coastal Inlet. *Can. J. Fisheries and Aquatic Sci.*, **37**, 8, 1209-1215.
- KRANCK, K. and T. G. MILLIGAN (1992): Characteristics of suspended particles at an 11-hour anchor station in San Francisco Bay, California. *J. Geophys. Res.*, **97**, C7, 11373-11382.
- LICK, W., J. LICK and C. K. ZIEGLER (1992): Flocculation and its effect on the vertical transport of fine-grained sediments. *Hydrobiologia*, **235/236**, 1-16.
- LIU, C. T. and S. C. PAI (1987): As the Kuroshio turns, II, The oceanic front north of Taiwan. *Acta Oceanogr. Taiwan.*, **18**, 49-61.
- LIU, K. K., G. C. GONG, C. Z. SHYU, S. C. PAI, C. L. WEI and S. Y. CHAO (1992): Response of Kuroshio upwelling to the onset of the northeast monsoon in the sea north of Taiwan: Observations and a numerical simulation. *J. Geophys. Res.*, **97**, C8, 12511-12526.
- MCCAVE, I. N. (1972): Transport and escape of fine-grained sediment from shelf areas, in *Shelf Sediment Transport: Process and Pattern*. SWIFT, D. J. P. D. B. DUANE and O. H. PILKEY, (eds.), Dowden, Hutchinson and Ross, Pennsylvania, 225-248.
- MAEDA, A. (1979): Short internal waves on the margin of the continental shelf of the East China Sea. *La mer*, **17**, 18-27.
- NIINO, H. and K. O. EMERY (1961): Sediments of shallow portions of East China Sea and South China Sea. *Geol. Soc. America Bull.*, **72**, 731-762.
- POSTMA, H. (1965): Water circulation and suspended matter in Baja California lagoons. *Netherlands J. Sea Res.* **2**, 566-604.
- THOMAS, H. E. and W. L. PERRY (1968): Historical environmental data: East China Sea-Yellow Sea, Area 16. Naval Oceanographic Office, Washington, D. C., 213 pp.
- TSAI, C. H. and S. R. RAU (1992): Evaluation of Galai CIS-1 for measuring size distribution of suspended primary particles in the ocean. *TAO*, **3**, 2, 147-163 (Chinese Geoscience Union: Taipei, Taiwan).

Received December 24, 1995

Accepted March 7, 1996

A paleoenvironmental record during 7~21 Ka BP in the sediments off northeastern Taiwan

Jiann-Yuh LOU* and Chen-Tung Arthur CHEN*

Abstract: A sediment core collected from the western slope of the South Okinawa Trough off northeastern Taiwan recorded the last glacial/postglacial changes of paleoenvironments. The sediments that had higher content of biogenic material (CaCO₃ and opal), lower terrigenous/biogenic ratio and higher salinity in the last glacial period suggested lower river water input to the East China Sea shelf. On the contrary, the sediments in the postglacial period contained higher terrigenous detritus and organic matter, and might reflect the warmer and more humid climate or higher river discharge.

1. Introduction

The abundance of chemical elements in recent pelagic clays has been measured by many investigators in order to study their geochemical cycles and processes in the marine environment (GOLDBERG and ARRHENIUS, 1958; KRISHNASWAMI, 1976). The temporal changes of chemical compositions in the sediment are partly due to the diagenesis and partly due to the change in the source functions (e. g., terrigenous detritus, calcium carbonate, hydrogenous ferromanganese oxide, biogenic silica) and are considered to be an useful indicator of the paleo-depositional environment (GOLDBERG, 1961).

The western slope of the South Okinawa Trough off northeastern Taiwan is the transition zone between the shallow East China Sea shelf and the deep Okinawa Trough (Fig. 1). After turning northeastward here, the main current of the Kuroshio flows along the Okinawa Trough. UJIE *et al.* (1991) proposed that the main course of the present (post-glacial) Kuroshio was similar to that of the interglacial period, but the Kuroshio moved to the east of the Ryukyu Island Arc during the last glacial period. Thus, the mineral and chemical compositions of the sediments on the slope may change with flow patterns or the

input of the source material.

The purpose of the present study is to obtain the paleoenvironmental information concerning the glacial/postglacial changes based on the variations of chemical elements in the sediments.

2. Material and methods

A piston core was collected from the lower part (water depth: 1480 m; Lat. 25°00' N; Long. 122°42' E; Fig. 1) of the trough slope by R/V Ocean Researcher I on cruise 120 in 1987. The upper 370 cm segment of the core is the target of this study. Sampling was made at approximately 10 cm intervals.

The grain size distribution of the sediment was measured with a Coulter LS-100 Counter. The sediments were prepared for chemical analysis by washing three times with distilled water and then drying for several days at 50 °C. The desalted sediments were ground into powder in an agate mortar and the total carbon and total nitrogen (TN) contents were measured using an element analyser (LECO-CHN 932) calibrated with the NIST standard material (SRM-2704, C: 3.348 wt% and S: 0.397 wt%) and the LECO standard (EDTA, C: 41.1 wt% and N: 9.59 wt%). Dried samples were combusted at 450°C for 3 hours to remove the organic carbon and the inorganic carbon contents measured by the element analyser. The inorganic carbon was then subtracted

* Institute of Marine Geology and Chemistry, National Sun Yat-sen University, Taiwan, ROC

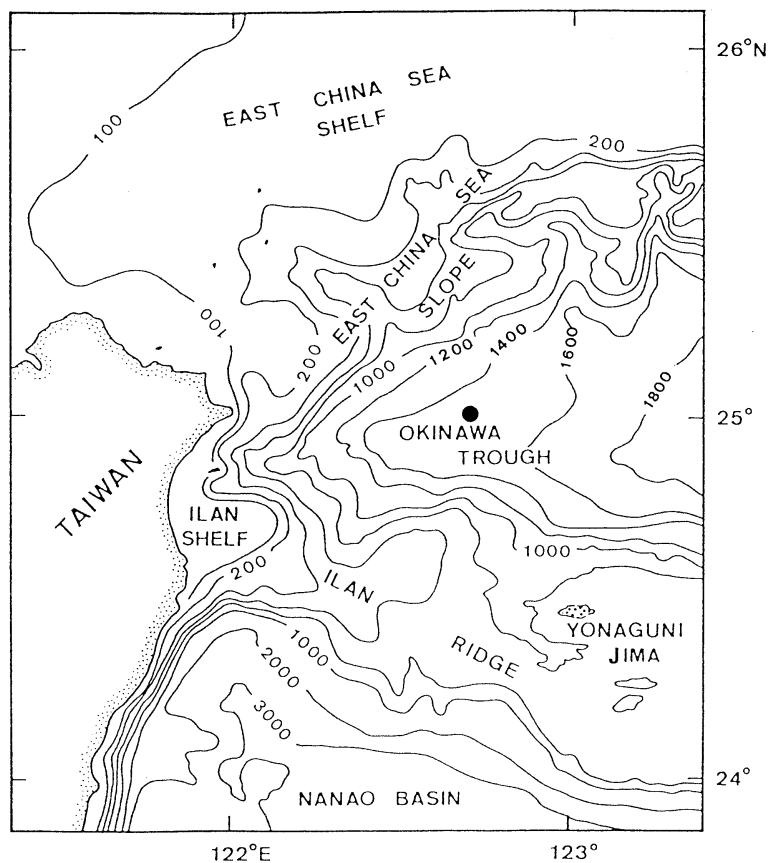


Fig. 1. Location map of the sampling site (●). (modified from Yu and Hong, 1992)

from the total carbon to obtain the total organic carbon (TOC).

For X-ray fluorescence (XRF) analysis, the sediment powder was palletized at 20 tons/30mm dia. to form a cake with cellulose as backing. The contents of 27 elements were measured using the Rigaku RIX-2000 XRF machine. Eight standard samples, including MAG-1, NIES (no.2), NIST (1646), NIST (2704), BCSS (BD001), MESS (MD001), PACS (PD004) and GBW (07314) were used for calibration. The precisions were within $\pm 5\%$ for Na, Mg, Al, Si, P, S, Cl, K, Ca, Ti, V, Cr, Mn, Fe, Ni, Cu, Zn, Br, Rb, Sr, Zr and Pb; $\pm 10\%$ for C, N, Ga, Cd and Ba; $\pm 30\%$ for Ce and As. The carbon-14 dating of bulk organic matter was done by both the AMS (accelerator mass spectrometry) method at the Institute of Geological & Nuclear Sciences in New Zealand and by the conventional method at the National Taiwan

University. The samples were sieved and treated consecutively with hot solution of acid, alkali, and acid before measurement. A conventional radiocarbon age implies correction for isotope fractionation through the normalization on $\delta^{13}\text{C}$ (PDB) value of -25‰ . We subtracted the reservoir correction of 400 years (BARD, 1988) from the conventional radiocarbon age, and then the age was transformed to the calibrated age with the formula of STUIVER and REIMER (1993). The quartz contents were measured using the SIEMENS D5000 X-ray diffraction with a Cu target tube at 40kV, 30mA.

3. Results and discussion

3.1 Chronology and organic matter stratigraphy

The core was dated as between 7 and 21 Ka BP (Fig. 2a), thus the last glacial/postglacial changes could be identified. Piston coring often loses the uppermost loose sediments because of

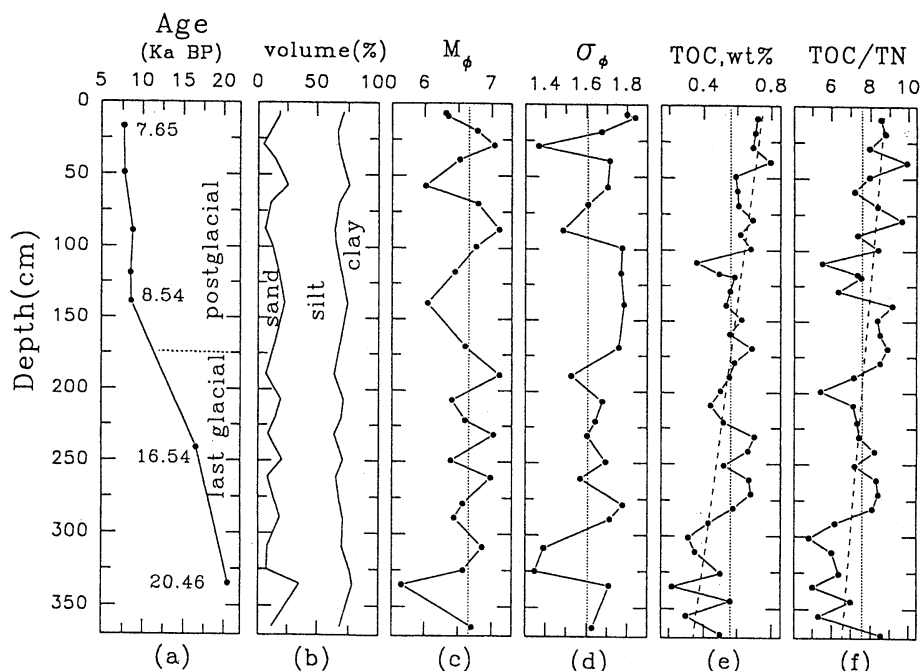


Fig. 2. The profiles of (a) C-14 dates, "●" denotes those measured by the AMS method and "▲" denotes the one measured by the conventional method; (b) sand, silt and clay contents; (c) mean grain diameters (M_ϕ); (d) sorting coefficients (σ_ϕ); (e) TOC (total organic carbon) contents, and (f) atomic TOC/TN (total organic carbon/total nitrogen) ratios. The dashes lines show the mean values and the broken lines show the trends.

wrong setting of corer. But CHUNG and CHANG (1995) studied some box cores and suggested that the surface sediments on the upper and middle slopes were too old to detect the excess ^{210}Pb activities. SHIEH (1993) also found that the age of the coretop sediments was about 5 Ka BP and the sedimentation rates varied in the ranges of 10~46 cm/Ka since 10 Ka BP from another core on the slope. It is possible that there is no recent sediments that cover the study area because of the erosion of bottom currents. If the sedimentation rate was constant in each segment, the rate of the upper 150 cm segment (140cm/Ka) would be about 8 times higher than that below (16.8 cm/Ka). The sedimentation rate of the upper segment is very high and the possibility of deposit by slumping could not be ruled out.

There is little fluctuation in the grain size distribution of the sediments throughout the core. The sediments contain about 55% silt, 30% clay and 15% sand (Fig. 2b). The mean diameter (M_ϕ) is in the range of 5.6~7.1 Φ (phi)

and belongs to the fine silt class (Fig. 2c). The sorting coefficients (σ_ϕ) calculated with the formula of Folk and Ward (1957) are in the ranges of 1.3~1.8, and suggest that all sediments are poorly sorted (Fig. 2d). The coarser sediments show poorer sorting than the finer ones.

The TOC contents and the atomic TOC/TN ratios seem to have slightly higher values in the upper segment than the lower one (Figs. 2e and 2f). Usually, older sediments lose more organic matter because of consumption by oxidation or decomposition by the microbials. Our TOC results (Fig. 2e) are consistent with this trend. The gradual diagenetic decomposition of sedimentary organic matter with preferential loss of nitrogen (RAISWELL and TAN, 1985) also should have resulted in a gradual increase in the C/N ratios with depth in the Recent sediments but Fig. 2f shows a reverse trend. The reason is as follows:

The C/N ratios of the marine phytoplankton are about 6. The TOC/TN ratios of the

Table 1 The elemental composition of the sediments

element	range	average	(1)	(2)	element	range	average	(1)	(2)
TC(%)	1.28-1.67	1.41	1.82	3.94	Mn(ppm)	377-471	434	520	2020
TOC(%)	0.22-0.79	0.55	0.61	0.97	Fe(%)	2.88-4.51	3.72	3.15	3
TN(ppm)	510-1100	870	615	1130	Ni(ppm)	38-50	42	25	36
Na(%)	1.19-1.76	1.43	1.33	1.93	Cu(ppm)	30-52	41	14	26
Mg(%)	1.37-1.52	1.47	1.07	1.15	Zn(ppm)	77-111	99	66	82
Al(%)	6.83-8.21	7.91	5.31	5.93	Ga(ppm)	15-21	18	13	14
Si(%)	26.7-28.5	27.3	29.2	19.2	As(ppm)	nd*-14	7	8	9
P(ppm)	500-563	525	500	630	Br(ppm)	12-44	26	13	39
S(ppm)	748-1394	1051	472	730	Rb(ppm)	101-143	127	93	87
Cl(ppm)	600-7400	2800	3000	5700	Sr(ppm)	160-208	180	269	415
K(%)	2.11-2.59	2.47	1.82	1.83	Zr(ppm)	178-397	220	180	120
Ca(%)	2.42-3.80	2.87	4.15	11.4	Cd(ppm)	nd*-4	2	0.07	0.16
Ti(ppm)	3800-4200	4000	3500	3100	Ce(ppm)	56-101	79	63	46
V(ppm)	90-121	107	71	78	Ba(ppm)	391-557	472	396	440
Cr(ppm)	70-95	81	61	58	Pb(ppm)	46-87	58	21	27

(1) Taken from Zhao (1983) for the East China Sea

(2) Taken from Zhao and Yan (1994) for the Okinawa Trough

*nd \leq 1 ppm

sediments in the core are mostly between 5~9, similar to those of the marine phytoplankton (KNAUER *et al.*, 1979; CHEN *et al.*, 1996). However, the trend of the TOC/TN ratios, decreasing with depth rather than increasing (Fig. 2f), is opposite to the effects of early diagenesis and seems to indicate the change of organic matter sources. The higher TOC/TN ratios in the upper segment of the core may reflect the slight increase of the terrigenous organic matter input in the postglacial period. MULLER (1977) found that in the case of most of continental margin sediments with 1~4% organic carbon, clay-bound nitrogen substances including inorganic ammonium does not significantly affect the C/N ratios. But in some deep sea sediments containing little organic matter as in our case, the effect of inorganic nitrogen on the total nitrogen is drastic and cannot be neglected as inorganic ammonium may represent 20~45% of the total nitrogen. Because the end product of the TOC decomposition may be lost to the overlaying water, yet the end product of decomposing organic nitrogen is bound to the clay particles, the TOC/TN ratios may decrease to below 6 (Fig. 2f).

3.2 Distribution of elements

The sediments deposited on the south East China Sea shelf are characterized as coarse-grained, mud-free, with high carbonate

contents and shell fragments. Quartz and feldspars are abundant in the shelf sand which are primarily discharged from mainland China (CHEN *et al.*, 1992). The terrigenous material of the muddy sediments in the South Okinawa Trough is also mainly derived from mainland China through the shelf but partly from Taiwan and the Ryukyu Island Arc (LIN and CHEN, 1983). These terrigenous and local biogenic material may control the elemental composition in the sediments.

Table 1 shows the abundance of the chemical elements in the core, and in the surface sediments of the East China Sea shelf (ZHAO, 1983) and the Okinawa Trough (ZHAO and YAN, 1994). The contents of most elements in the core are similar to those on the East China Sea shelf and in the Okinawa Trough. The major chemical components in the sediments are SiO₂ (59%), Al₂O₃ (15%), CaCO₃ (7%), Fe₂O₃ (5%), K₂O (3%), MgO (2.5%), Na₂O (2%), total organic matter (1.5%) and TiO₂ (0.7%).

The correlation coefficients of elements are shown in Table 2. Aluminum is a typical element from the aluminosilicate minerals and is considered as of terrigenous origin. Mg, K, Ti, V, Cr, Mn, Fe, Ni, Cu, Zn, Ga, Br, Rb and Ba all show strong positive correlation with Al, suggesting that they are essentially of terrigenous origin. Calcium and Sr are mainly from biogenic origin in the East China Sea (ZHAO

and YAN, 1994) thus Sr has a high correlation coefficient (0.91) with Ca, and both have strong negative correlation with the terrigenous elements. Although Si is largely from the aluminosilicate minerals, it has strong positive correlation with the biogenic elements (Ca and Sr) and has negative correlation with the terrigenous elements. The likely explanation is that the variation in the biogenic silica content is larger than the differences in the terrigenous silicate. As a result, the fluctuation of Si behaves as a biogenic element.

The TOC, TOC/TN ratio as well as the terrigenous elements have strong negative correlation with the biogenic elements such as Ca and Sr (Tab. 2). It may indicate that higher TOC amount was supplied by the land plants. The Al content decreases with depth, but the ratios of Sr, Ca and Si to Al increase with depth (Figs. 3a and 3b). It seems to reveal a higher detritus input and lower biogenic content in the postglacial period compared with the last glacial period.

Total silica is composed of a minerogenic/aluminosilicate component and a biogenic component. The large variation in the Si/Al ratios of the sediments seems to indicate the changes of these components or their sources. ZHAO (1983) proposed that the high Si/Al ratios were induced by the high quartz contents in the coarse sediments of the East China Sea. The input of volcanic glasses or eolian dust with high quartz content may also increase the Si/Al ratio. However, there are less than 5 wt% changes in quartz, equaling about 2.6 wt% changes in Si in the sediments. In addition, the higher Si/Al ratio in the lower segment of the core is not associated with the coarser material or higher quartz content (Figs. 2c and 3c), thus the higher ratio may be a result of an increase in the biogenic opal input during the last glacial period. Diatoms are the major source of biogenic opal in the marine sediments thus biogenic opal can be a proxy of local surface water productivity because its content in the sediments is an indicator of surface nutrients. Therefore, local paleoproductivity can be reconstructed with biogenic opal content in the sediments (BROECKER and PENG, 1982; CHARLES *et al.*, 1991). The portion of biogenic silica

(opal) was determined on the basis of the assumption that the Si/Al ratio in the aluminosilicate fraction of the sediments is about 3 (LEINEN, 1977). Thus we subtracted three times of Al content from the total Si and obtained the biogenic Si content. The contents of biogenic silica were calculated as between 5 and 17 wt%, higher during the last glacial period (Fig. 3d).

Assuming that Ca is mainly from the calcium carbonate, the content of CaCO₃, ranging between 7 and 10 wt% (Fig. 3d), is very close to the result from the measurement of inorganic carbon. The content of the total inorganic biogenic material (opal and calcium carbonate combined) ranges between 11 and 26 wt% and increases with depth (Fig. 3d). The T/B (terrigenous/biogenic) ratio rises gradually from around 4 at the bottom to ca. 8 at the surface (Fig. 3e).

3.3 Paleooceanographic significance

During the last glacial period, a growth of the continental ice sheets caused a global drop in sea level by 100~120m (FAIRBANKS, 1989). As a result, large parts of the modern East China Sea shelf were exposed, when the main course of the Kuroshio moved to the east of the Ryukyu Island Arc (UJIE *et al.*, 1991; AHAGON *et al.*, 1993). But SHIEH and CHEN (1995) suggested that the Kuroshio did not change its path flowing into the Okinawa Trough until about 7.5 Ka BP during the Holocene period. Nevertheless, these authors all agreed that the Kuroshio moved away from the current path during the last glacial period. The change of current patterns would affect the characteristics of the sediments.

The C/N ratios can assist in defining the nature of the organic matter. Although the TOC/TN ratios of the sediments are similar to those of the marine phytoplankton, the close relationships between the contents of TOC, terrigenous elements and the TOC/TN ratio in this core reflect the importance of terrigenous organic material input. If the sedimentation rate was indeed higher in the postglacial period, the higher values of these parameters presented seem to indicate higher terrigenous detritus/organic material inputs because of higher river discharge. We can not decide reliable flux

of biogenic materials without reasonable sedimentation rates. The organic carbon and the biogenic opal contents are directly related to the surface productivity (HEBBELN and BERNER, 1993). But the organic carbon in this core is partly mixed with the terrestrial organic material thus is not suitable for calculating the productivity. Higher productivity in the glacial time was found in the northwestern margin of the Pacific (YAN *et al.*, 1991; AHAGON *et al.*, 1993), in the Northeast Pacific (KARLIN *et al.*, 1992), and in the Equatorial Pacific (REA *et al.*, 1991), and was discussed in detail by HONDA (1994). AHAGON *et al.* (1993) considered that there was greater amount of particles and nutrients supplied from the more exposed land-areas in addition to increased production in the Okinawa Trough at that time. During the postglacial period, the sampling site was near

the main course of the Kuroshio which was characterized by its deficiency in nutrient and by the low primary productivity, thus contributing little biogenic material content. Meanwhile, the warmer/wetter climate triggers off higher river runoff, therefore more terrigenous organic/inorganic detritus is supplied to the ocean. On the other hand, the Kuroshio moved away during the last glacial period and the more eutrophic near-shore water enhanced the primary productivity which resulted in higher opal and CaCO₃ contents, and also lowered the T/B ratio in the sediments (Fig. 3e).

The concentration of Mg in the sediments may reflect the salinity of water in the sedimentary environment. The contents of Mg ion and Mg-containing substances increase with salinity in water (ZHANG, 1992). The Mg/Al ratio averaged 0.183 in the upper segment and

Table. 2 The correlation coefficients among the elements.

	TOC	TN	TOC/TN	Na	Mg	Al	Si	P	S	Cl	K	Ca	Ti	V	Cr
TN	0.74	1.00													
TOC/TN	0.83	0.26	1.00												
Na	0.16	-0.08	0.28	1.00											
Mg	0.61	0.73	0.33	-0.01	1.00										
Al	0.76	0.76	0.49	0.11	0.80	1.00									
Si	-0.75	-0.74	-0.48	-0.21	-0.82	-0.89	1.00								
P	-0.04	-0.17	0.03	0.23	-0.30	-0.26	0.09	1.00							
S	0.02	0.21	-0.09	-0.17	0.16	0.12	-0.03	-0.31	1.00						
Cl	0.38	0.15	0.40	0.90	0.20	0.35	-0.48	0.23	-0.29	1.00					
K	0.73	0.77	0.45	0.07	0.85	0.97	-0.91	-0.34	0.08	0.33	1.00				
Ca	-0.75	-0.72	-0.52	-0.09	-0.81	-0.89	0.85	0.27	0.01	-0.35	-0.93	1.00			
Ti	0.47	0.41	0.34	0.16	0.55	0.74	-0.63	-0.14	-0.06	0.28	0.70	-0.68	1.00		
V	0.58	0.58	0.35	-0.04	0.65	0.78	-0.71	-0.53	-0.09	0.17	0.84	-0.80	0.66	1.00	
Cr	0.64	0.58	0.45	0.14	0.60	0.75	-0.72	-0.02	-0.17	0.42	0.73	-0.78	0.52	0.60	1.00
Mn	0.47	0.42	0.33	0.14	0.45	0.55	-0.61	0.29	-0.10	0.36	0.51	-0.45	0.37	0.26	0.54
Fe	0.64	0.71	0.37	-0.10	0.83	0.75	-0.81	-0.30	0.00	0.17	0.85	-0.91	0.51	0.73	0.62
Ni	0.65	0.54	0.46	0.37	0.44	0.65	-0.70	0.19	-0.16	0.58	0.62	-0.59	0.37	0.45	0.74
Cu	0.56	0.58	0.30	-0.15	0.53	0.65	-0.57	-0.31	0.00	0.15	0.66	-0.53	0.28	0.61	0.54
Zn	0.78	0.75	0.52	0.17	0.75	0.92	-0.87	-0.20	0.03	0.40	0.92	-0.88	0.66	0.79	0.77
Ga	0.53	0.48	0.38	0.18	0.70	0.79	-0.71	-0.24	0.07	0.31	0.80	-0.74	0.58	0.72	0.60
As	0.10	0.23	-0.05	-0.13	-0.01	0.09	-0.04	-0.36	0.38	-0.09	0.10	0.08	-0.17	0.01	-0.13
Br	0.69	0.55	0.53	0.63	0.53	0.68	-0.81	0.13	-0.12	0.81	0.68	-0.70	0.54	0.48	0.65
Rb	0.67	0.77	0.37	0.02	0.67	0.81	-0.65	-0.50	0.35	0.16	0.81	-0.72	0.51	0.69	0.48
Sr	-0.59	-0.56	-0.41	-0.04	-0.75	-0.74	0.77	0.14	0.15	-0.31	-0.80	0.91	-0.59	-0.71	-0.75
Zr	-0.59	-0.57	-0.41	0.01	-0.57	-0.56	0.57	0.24	0.01	-0.21	-0.62	0.61	-0.02	-0.49	-0.56
Cd	-0.01	-0.11	0.08	-0.07	-0.14	-0.24	0.18	0.32	-0.09	-0.02	-0.24	0.15	-0.25	-0.36	0.02
Ce	0.22	0.08	0.23	0.22	0.32	0.15	-0.26	-0.06	0.07	0.20	0.17	-0.11	0.04	0.23	-0.03
Ba	0.58	0.64	0.33	-0.06	0.60	0.63	-0.56	-0.20	0.30	0.05	0.61	-0.54	0.36	0.50	0.40
Pb	0.32	0.37	0.14	-0.25	0.24	0.37	-0.34	-0.06	0.13	0.02	0.36	-0.26	0.00	0.23	0.40

0.188 in the lower segment (Fig. 3f), suggesting higher salinity during the glacial than during the postglacial period. The average Mg/Al ratio was 2.7% with a maximum of 10% higher during the glacial period (Fig. 3f). It means that the salinity of the water column might be on the average 1 unit and with a maximum of 3.4 units higher than the postglacial period. SHIEH (1993) suggested that the salinity of surface seawater was as high as 37.8 during the last glacial maximum period because of the low precipitation on land and the low river runoff. The surface salinity of the study site is presently at about 34.5. An increase of 1 to 3 would result in a good agreement with Shieh's data for the last glacial period.

Further, the salinity of the global seawater also increased during the last glacial period when fresh water was extracted from the ocean

and was locked up in the form of ice sheets. The present ocean has a mean depth of 3800 meters and a mean salinity of 34.7. The removal of a 120 meter thick layer of water would increase the salinity by about 1.1, in good agreement with our Mg data. The fluctuation of the river discharge might also influence the salinity of surface water. Although the sampling site was closer to the shore during the last glacial period, there was relatively lower fresh water input. As mentioned above, there was higher river discharge during the postglacial period, but the Kuroshio controlled the salinity. According to the distribution of the Mg/Al ratio, we conclude that the variations in the salinity in the South Okinawa Trough was mainly controlled by the global sea-level fluctuations during the glacial/postglacial period.

Table. 2 (continued)

	Mn	Fe	Ni	Cu	Zn	Ga	As	Br	Rb	Sr	Zr	Cd	Ce	Ba
TN														
TOC/TN														
Na														
Mg														
Al														
Si														
P														
S														
Cl														
K														
Ca														
Ti														
V														
Cr														
Mn	1.00													
Fe	0.42	1.00												
Ni	0.56	0.45	1.00											
Cu	0.41	0.48	0.54	1.00										
Zn	0.51	0.75	0.74	0.66	1.00									
Ga	0.45	0.61	0.57	0.48	0.75	1.00								
As	-0.08	-0.03	-0.15	0.41	0.00	-0.15	1.00							
Br	0.58	0.58	0.77	0.32	0.73	0.59	-0.12	1.00						
Rb	0.27	0.61	0.37	0.61	0.75	0.65	0.38	0.46	1.00					
Sr	-0.42	-0.88	-0.60	-0.44	-0.79	-0.66	0.33	-0.63	-0.43	1.00				
Zr	-0.21	-0.60	-0.50	-0.58	-0.59	-0.56	-0.15	-0.39	-0.56	0.53	1.00			
Cd	0.02	-0.17	0.02	-0.05	-0.19	-0.23	-0.06	-0.10	-0.28	0.08	0.05	1.00		
Ce	0.06	0.14	0.14	0.18	0.19	0.31	-0.07	0.20	0.18	-0.11	-0.21	-0.32	1.00	
Ba	0.18	0.49	0.38	0.47	0.63	0.55	0.12	0.33	0.68	-0.39	-0.51	-0.23	0.20	1.00
Pb	0.35	0.24	0.35	0.76	0.37	0.07	0.52	0.08	0.33	-0.19	-0.36	0.14	-0.03	0.19

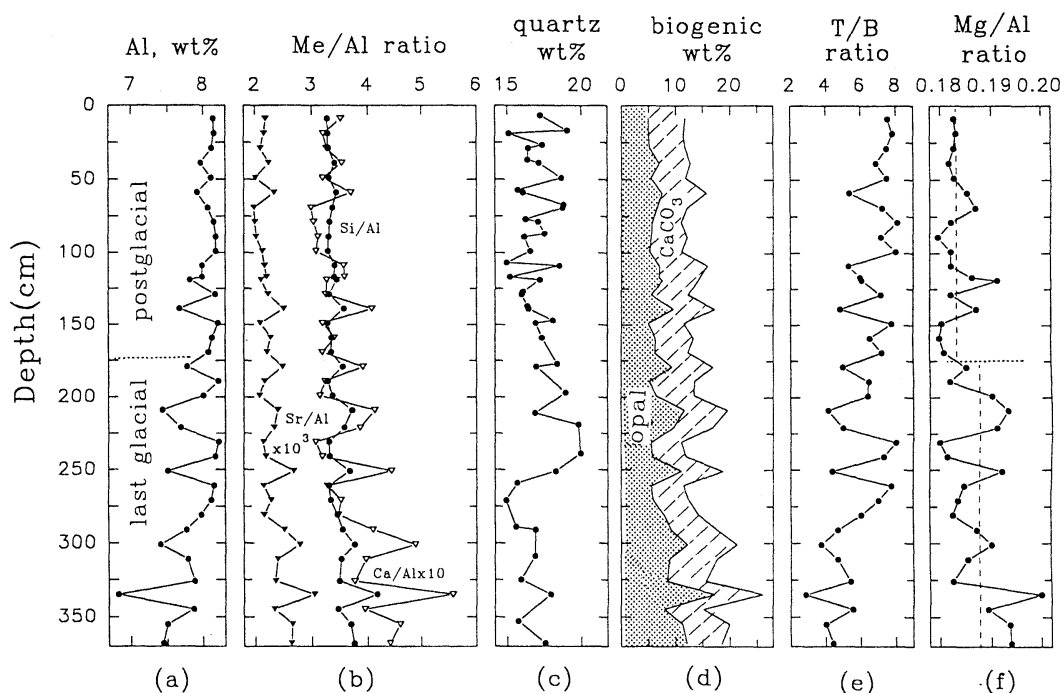


Fig. 3. The profiles of (a) Al ; (b) ratios of Sr/Al, Si/Al and Ca/Al ; (c) quartz ; (d) biogenic material (opal and CaCO_3) ; (e) T/B (terrigenous/biogenic) ratio ; and (e) Mg/Al ratio. The broken lines are average values for each segment.

4. Conclusions

The sediment core collected from the South Okinawa Trough revealed the last glacial/postglacial changes. The change in the relative abundance of the terrigenous and biogenic inputs was the major factor that controlled the distribution of these elements. There were about 74~89 wt% terrigenous and 11~26 wt% biogenic materials (including CaCO_3 and biogenic silica) in the sediments. The content of biogenic material in the glacial period was about 10 wt% higher than that in the postglacial period.

These data suggest higher terrigenous detritus/organic material input or higher river discharge in the postglacial period. The Mg/Al ratio indicated that the salinity of the seawater was related to the global sea-level fluctuation, and was on the average 1 unit higher in the last glacial period.

Acknowledgments

This research was supported by the National Science Council (NSC85-2611-M-110-003 GP).

We thank the assistance of the crew members of R/V Ocean Research I. We are also grateful to T. K. LIU, D. D. SHEU and Y. C. CHUNG for their valuable comments and assistance, and to B. J. WANG, Z. M. LIN, Y. P. LIN and M. J. CHEN for their assistance in the laboratory. Detailed constructive criticisms from an anonymous reviewer and from H. L. LIN strengthened the manuscript.

References

- AHAGON, N., Y. TANAKA and H. UJIE (1993): *Florisphaera profunda*, a possible nannoplankton indicator of late Quaternary changes in sea-water turbidity at the northwestern margin of the Pacific. *Marine Micropaleontology*, **22**, 255-273.
- BARD, E (1988): Correction of accelerator mass spectrometry C-14 ages measured in planktonic foraminifera: Paleocceanographic implication. *Paleocceanography*, **3** (6), 635-645.
- BROECKER, W. S. and T. H. PENG (1982): *Tracers in the Sea*. Eldigio Press, Columbia Univ., Palisades, New York, 690 pp.
- CHARLES, C. D., P. N. FROELICH, M. A. ZIBELLO, R. A. MORTLOCK and J. J. MORLEY (1991): Biogenic opal

- in southern ocean sediments over the last 450,000 years : Implication of surface water chemistry and circulations. *Paleoceanography*, **6**, 697-728.
- CHEN, M. P., S. C. LO and K. L. LIN (1992): Composition and texture of surface sediment indicating the depositional environments off northeast Taiwan. *Terrestrial, Atmospheric and Oceanic Sciences*, **3** (3), 395-418.
- CHEN, C. T. A., C. M. LIN, B. T. HUANG and L. F. CHANG (1996): Stoichiometry of carbon, hydrogen, nitrogen, sulfur and oxygen in the particulate matter of the western North Pacific marginal seas. *Mar. Chem.* (in press)
- CHUNG, Y. and W. C. CHANG (1995): Pb-210 fluxes and sedimentation rates in the lower slope between Taiwan and South Okinawa Trough. *Continental Shelf Research*, **15**(2/3), 149-164.
- FAIRBANKS, R. G. (1989): A 17,000-year glacio-eustatic sea level record : influence of glacial melting rates on the Younger Dryas event and deep-ocean circulation. *Nature*, **342**, 637-642.
- FOLK, R. L. and W. C. WARD (1957): Brazons River bar : a study in the significance of grain size parameters. *Jour. Sed. Pet.*, **27**, 3-26.
- GOLDBERG, E. D. (1961): Chemical and mineralogical aspects of deep-sea sediments. In : E. D. GOLDBERG (Editor), *Physics and Chemistry Aspects of Deep-sea Sediments*. *Phys. Chem. Earth*, **4**, 281-302.
- GOLDBERG, E. D. and G. O. S. ARRHENIUS (1958): Chemistry of Pacific pelagic sediments. *Geochim. Cosmochim. Acta*, **13**, 153-212.
- HEBBELN, D. and H. BERNER (1993): Surface sediment distribution in the Fram Strait. *Deep-Sea Research I*, **40** (9), 1731-1745.
- HONDA, M. (1994): Deep water circulation and ocean productivity in the last glacial period. *Sea Research*, **3** (3), 205-225. (in Japanese with English abstract)
- KARLIN, R. M. LYLE and R. ZAHN (1992): Carbonate variations in the Northeast Pacific during the late Quaternary. *Paleoceanography*, **7** (1), 43-61.
- KNAUER, G. A., J. H. MARTIN and K. W. BRULAND (1979): Fluxes of particulate carbon, nitrogen and phosphorus in the upper water column of the northeast Pacific. *Deep-Sea Research*, **26**, 97-108.
- KRISHNASWAMI, S. (1976): Authigenic transition elements in Pacific pelagic clays. *Geochim. Cosmochim. Acta*, **40**, 425-435.
- LEINEN, M. (1977): A normative calculation technique for determining opal in deep-sea sediments. *Geochim. Cosmochim. Acta*, **41**, 671-676.
- LIN, F. J. and J. C. CHEN (1983): Textural and mineralogical studies of sediments from the southern Okinawa trough. *Acta Oceanologica Taiwanica*, **14**, 26-41.
- MULLER, P. J. (1977): C/N ratios in Pacific deep-sea sediments : effect of inorganic ammonium and organic nitrogen compounds sorbed by clays. *Geochim. Cosmochim. Acta*, **41**, 765-776.
- RAISWELL, R. and M. Md. TAN (1985): Diagenesis of sediments beneath the Ross Ice Shelf and their sedimentary history. *Nature*, **315**, 483-485.
- REA, D. K., N. G. PISIAS and T. NEWBERRY (1991): Late Pleistocene paleoclimatology of the central Equatorial Pacific : Flux Patterns of biogenic sediments. *Paleoceanography*, **6**, 227-244.
- SHIEH, Y. T. (1993): The paleoceanography off Eastern Taiwan during late Quaternary. Ph. D. thesis, National Taiwan University, Taiwan R. O. C., 225pp. (in Chinese)
- SHIEH, Y. T. and M. P. CHEN (1995): The ancient Kuroshio current in the Okinawa Trough during the Holocene. *Acta Oceanographica Taiwanica*, **34** (4), 73-80.
- STUIVER, M. and P. J. REIMER (1993): Extended ¹⁴C database and revised CALIB radiocarbon calibration program. *Radiocarbon*, **35**, 215-230.
- UJIE, H., Y. TANAKA and T. ONO (1991): Late Quaternary paleoceanographic record from the middle Ryukyu Trench slope, Northwest Pacific. *Mar. Micropaleontol.*, **18**, 115-128.
- YAN, J., L. J. HE and S. G. XUE (1991): Characteristics of elements in marginal-sea strata of the West Pacific Ocean and their paleo-oceanological significance. *Marine Geology & Quaternary Geology*, **11** (2), 57-67. (in Chinese with English abstract)
- YU, H. S. and E. HONG (1992): Physiographic characteristics of the continental margin, northeast Taiwan. *Terrestrial, Atmospheric and Oceanic Sciences*, **3** (3), 419-434.
- ZHANG, S. S. (1992): Mg-Al ratio in sediment and paleoclimate. *Collected Oceanic Works*, **15** (1), 52-61.
- ZHAO, Y. Y. (1983): Geochemical modes in sediments of the China Shelf Sea. *Geological Science*, **4**, 307-314. (in Chinese with English abstract)
- ZHAO, Y. Y. and M. C. YAN (1994): Geochemistry of sediments of the China Shelf Sea. Science Press, 203pp. (in Chinese)

Received December 25, 1995

Accepted March 30, 1996

Some aspects on the circulation in the northern South China Sea

Joe WANG* and Ching-Sheng CHERN*

Abstract: The circulation pattern of the northern South China Sea (SCS) had long been a controversial topic for the regional oceanography. The results from recent multi-vessel surveys, over the northern and central SCS, show that the surface layer of the region to the northwest or west of north Luzon is mainly occupied by cyclonic flows during spring and summer; this is quite discordant with our past knowledges on the circulation pattern of the northern SCS. Moreover, these cyclonic flows are composed principally of SCS water masses, and in summer they could extend further northwards to the areas from the west of the Luzon Strait to the southwest of Taiwan. However, the aforementioned areas are flowed principally by Kuroshio intrusion waters and associated with anti-cyclonic flows in winter. Details of the seasonal alternation of such flow fields could be inferred from the differences of the monthly mean sea levels between Kao-Hsiung and Port Irene and between Kao-Hsiung and San Jose ($\Delta\zeta_{KS}$). The former is dominated by annual variations, low in summer and high in winter. The latter is principally biannual, whose two peaks, occurring in March to May and in August to September respectively, correspond likely to the sequential occurrences of anti-cyclonic and cyclonic flows in the Luzon Strait. Transitions of flow patterns may occur respectively in June to July and in October to November when $\Delta\zeta_{KS}$ is low. These particular periods, corresponding closely to the timings of alternation or onset of the regional monsoon, imply the significance of wind stress on the evolution of current fields in the SCS.

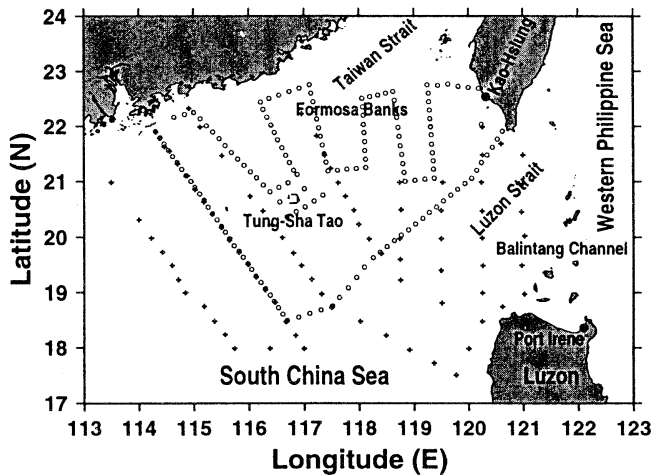
1. Introduction

For years, current fields in the northern South China Sea (SCS) had drawn a number of attentions; WYRTKI (1961) compiled bimonthly surface current charts of the SCS and his study enlightened the monsoon-driven behavior of the main flow of the SCS; others, like the CSK works of CHU (1970, 1972) and NITANI (1970), also posteriorly hydrographic surveys of FAN (1982) and SHAW (1989) in the Luzon Strait and nearby areas, CHAN (1970), QIU, YANG and GUO (1984) and WANG and CHERN (1987a) in the northern and the central SCS, etc., had improved or extended WYRTKI's (1961) results of the northern SCS because over which his data base is rather sparse and crude from a modern viewpoint. Several obscurities were illuminated by these later surveys indeed, however, more controversies had been

drawn by them too. For example, LI and WU (1989), based on NITANI's (1970) data, considered that the Kuroshio would form a loop current in the northeastern SCS, they also suggested that this is likely a typical pattern for summer. Their point of view, obviously, contravenes with what reported by CHU (1972) and FAN (1982), i.e., the southwesterly monsoon in summer drives the SCS surface waters flowing outward through the Luzon Strait to the Pacific. Moreover, Wang and CHERN (1987a) had reported that the northern SCS was occupied by anti-cyclonic flow systems during their spring survey, which they attributed to the intrusion of Kuroshio waters (WANG and CHERN, 1987b). Obviously, the anti-cyclonic pattern is absent in WYRTKI's (1961) current chart, so SHAW (1989) repelled it and he suggested the intrusion waters have to follow a cyclonic pathway. In our opinion, all of these controversies are simply the continuation of a long-standing question, i.e. the obscure behavior of

* Institute of Oceanography, National Taiwan University, Taipei, Taiwan, Republic of China

1992 3/8-3/27 ORI + SY3 CTD stations



1994 8/28-9/10 ORI+OR3+XYH14+YP2 CTD stations

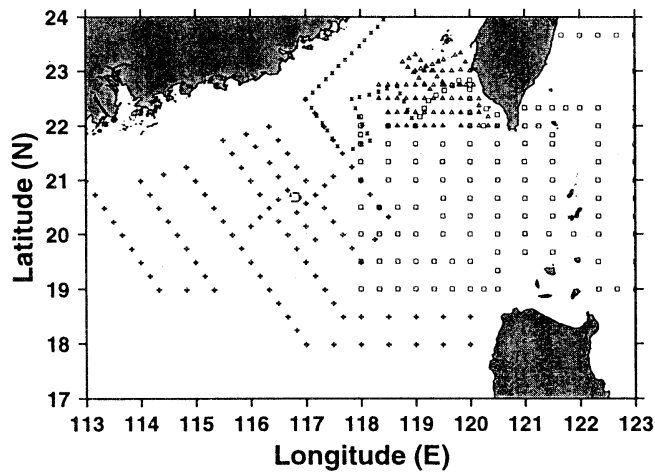


Fig. 1. Hydrographic stations of the joint SCS surveys ; (a) cruise 311, from March 8 to 27, 1992 ; where o signs denote (CTD) stations of ORI and + that of R/V SY3 (upper panel) ; (b) cruise 399, from August 28 to September 10, 1994 ; where □ CTD stations of ORI, △ OR3, × YP2, and + XYH14, respectively (lower panel).

the so-called SCS branch of Kuroshio (Wu, 1982). We are still lacking of enough observations in constructing a more comprehensive model capable of covering all of these disputes.

Recently, two larger-scale, multi-vessel surveys had been conducted in the northern and central SCS. The first was performed jointly by R/V Ocean Researcher I (ORI, managed by Institute of Oceanography, National Taiwan University) and by R/V Shi-Yan 3 (SY3, by South

China Sea Institute of Oceanology, Academia Sinica, SCSIOAS) from March 8 to 27, 1992 (Fig. 1a); the second, by four ships, i.e. ORI, R/V Ocean Researcher 3 (OR3, by National Sun Yat-Sen University), R/V Xian-Yang-Hong 14 (XYH14, by State Oceanic Administration) and R/V Yeng-Ping 2 (YP2, by Fujian Institute of Oceanography), was carried out from August 28 to September 10, 1994 (Fig. 1b). One of the purposes of these surveys is to present

Table 1. CTD data used.

Cruise #	Duration	Survey area	Note
283	1991 5/23-5/28	LS, NE SCS	ORI only
311	1992 3/ 8-3/27	LS, N SCS	With SY3
391	1994 6/14-6/20	LS, E Taiwan	ORI only
399	1994 8/28-9/10	LS, NE SCS	With OR3, XYH14, YP2
415	1995 4/ 4-4/13	LS, E Taiwan	ORI only

synoptic views of the distributions of water masses and current fields in the northern SCS under different seasons, which may fill in some of blanks in our past studies. In terms of this data base, we may identify several active flow-systems which are dynamically significant to the circulation pattern of the northern SCS. The evolution of such systems, however, could be inferred from the time series of Monthly Mean Sea Levels (MMSLs) of nearby tide stations. These, probably enlightening some of the aforementioned obscurities, are reported in the following sections.

2. Data base

Two kinds of data are used for the inspection on the seasonal behavior of large scale current fields of the northern SCS. The first is CTD data collected by ORI solely or by ORI and other research vessels¹ jointly, from which the spatial distribution of water masses and dynamic-height anomalies, thereby large scale motions, could be inferred. For later reference, informations of cruise number (of ORI only), duration and coverage of cruises are briefed in Table 1, where the abbreviation LS denotes the Luzon Strait, N northern, S southern, E eastern and NE northeastern, respectively. The second is the MMSL data of three tide stations, i.e. San

Jose, Port Irene and Kao-Hsiung (Fig. 1a; from January 1989 to December 1993)², from which the time series of the differences of MMSLs between any two of them, i.e. $\Delta\zeta(t)$, where t denotes time, is obtained readily. By geostrophy, $\Delta\zeta(t)$ is associated with the volume fluxes through the section between two stations, it is therefore an useful clue for reconstructing the temporal behavior of flow fields from few spatial snapshots by CTD surveys.

3. Spatial distribution of water masses

The SCS is a semi-enclosed ocean basin, whose exchanges of mass and salt with the western Philippine Sea are mainly by virtue of the flows in the Luzon Strait. WYRTKI (1961) had reported the seasonal behavior of the conveyance of high salinity North Subtropical Lower Water (LW) and less saline North Pacific Intermediate Water (IW) into the SCS. During the northeasterly monsoon, LW and waters above it flow into the SCS while IW flushes out in lower layers. However, it is in the reverse order during the southwesterly monsoon. The Kuroshio, being the major current system in the western Philippine Sea, is the principal conveyer for these waters. A massive part of sub-surface waters in the main stream of the Kuroshio belongs to the more saline LW, whose salinity maximum, S_{max} , is about 34.9psu (or higher) to the east of Luzon, while the salinity minimum, S_{min} , of IW is about 34.20–34.30psu in the same region. In the SCS, however, usually $S_{max} \sim 34.60$ psu and $S_{min} \sim 34.40$ psu (NITANI, 1970). It is these differences making S_{max} and S_{min} to be handy indexes for discriminating waters circulated in the SCS from that immigrated with the Kuroshio stream (CHU, 1972).

For the sake of later illustrations, spatial distributions of S_{max} in spring (ORI-311) and summer (ORI-399) are shown in Figs. 2 and 3,

¹ For the purpose of cross checking the quality of CTD data collected by different vessels, several common stations had been arranged during cruises; comparisons of T-S curves of common stations show no great deviations between each other (Xu and Su, 1993; Hu, 1995).

² The former two were retrieved via the anonymous ftp from the archives of British Oceanographic Data Centre (BODC), and the third one is provided by the Central Weather Bureau of the Republic of China (CWB). The location of San Jose (121° 5' E, 12° 20' N) is out of the range of Fig. 1a, so is not shown.

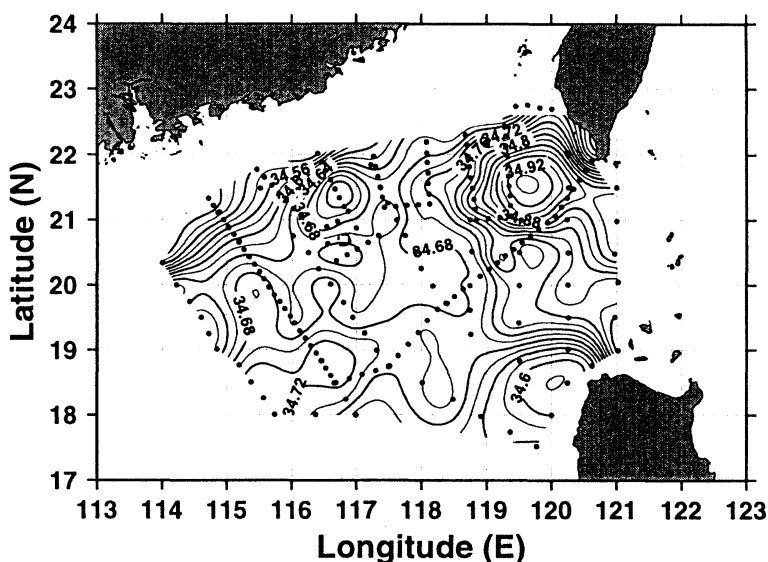


Fig. 2. The distribution of S_{max} (in psu) during ORI 311 from March 8 to 27, 1992.

respectively. A common feature, i.e. the tongue-like pattern of isohalines in the Luzon Strait, is clear in these figures. If the isohaline which is the closest to the Kuroshio front is chosen as the outer boundary of the intrusion water³, then we may infer that waters immigrated directly with the Kuroshio could reach to 118.7° E in spring of 1992 but merely to 119.8° E in summer of 1994. Along the rim of these tongues (in the SCS side) are circulating waters whose salinity is in between waters in the Kuroshio and that in the central SCS. Moreover, the orientation of isohalines in the Luzon Strait south of 21° N is worth noticing too; they are nearly meridional in summer, but mainly latitudinal during spring. This feature, associated closely with the variation of the path of the Kuroshio stream, is discussed next.

4. Spatial distribution of current fields

Horizontal distributions of dynamic height

³ Such as the S_{max} 34.8 psu and 34.9 psu for the cruise of ORI-311 and ORI-399, respectively, cf. Figs. 2 to 5.

⁴ It could extend vertically from the surface down to deeper layers, say more than 600 db.

⁵ The cyclonic flow in the northern SCS possesses a cold-cored structure, whose circulation sense could extend vertically to a much deeper layer, say more than 1500 db (Wang 1986).

anomaly, ΔD , (in *dynamic meter*) in spring and summer on 20 db (relative to 800 db), likely representing geostrophic streamlines in the surface layer, are shown in Figs. 4 and 5 respectively. The distribution of ΔD on 150 or 200 db (likely corresponding to the layer of S_{max} in the SCS) is quite analogous to the surface one in either season, so for the sake of brevity it is not shown. Apparently, there are several common as well as contrary features between both seasons, a brief of them is reported hereinafter.

The most striking feature is perhaps the cyclonic flows in the central to northern SCS (Figs. 4 and 5). The region south or southeast of Tung-Sha Tao (Pratas Islands) and west of northern Luzon, over which ΔD is always lower than its surroundings, no matter in spring or summer. This implies the region is occupied by a nearly-persistent cyclonic system. Though the feature is absent in WYRTKI'S (1961) flow chart of summer, but consistent with that reported by SCSIOAS (1985). On the other hand, the flow pattern northeast of this region varies greatly with seasons. During the spring cruise a consistently-northwestward flow⁴ emerged (Fig. 4) while in summer a pair of cyclonic⁵ and anti-cyclonic eddies were found (Fig. 5); these, especially the summer case, are not in accordance with WYRTKI'S (1961) charts.

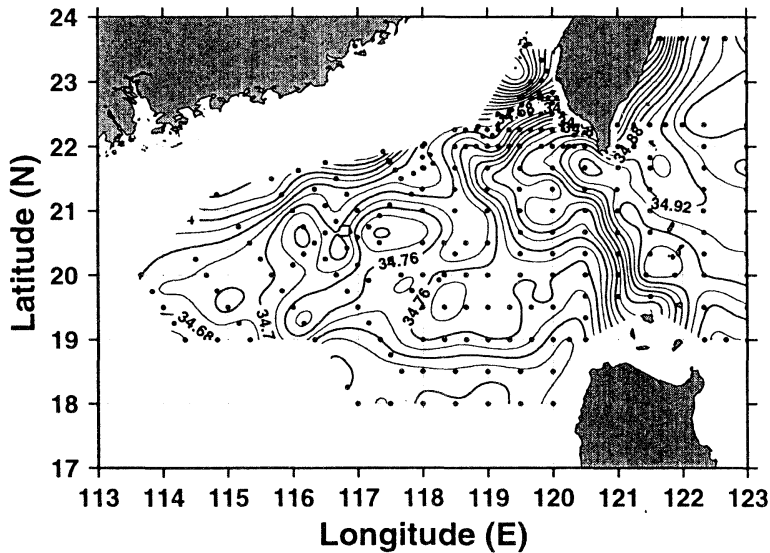


Fig. 3. The distribution of S_{max} (in psu) during ORI 399, from August 28 to September 10, 1994.

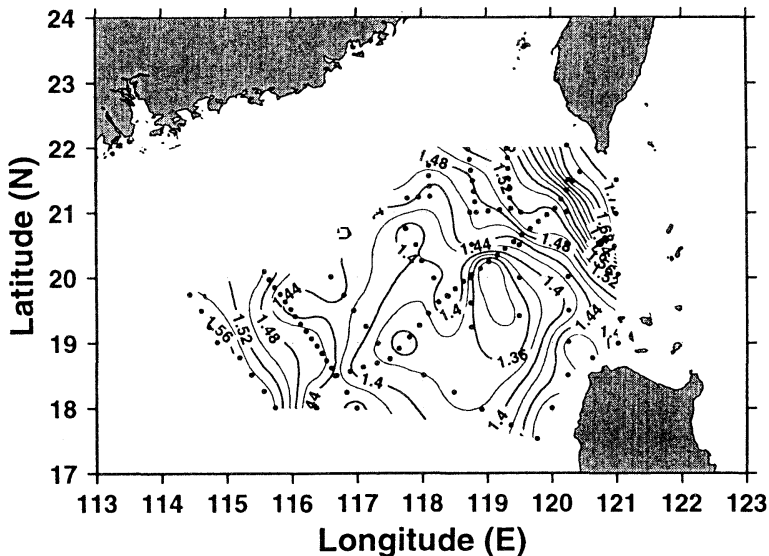


Fig. 4. The distribution of ΔD (in dyn.m) of 20 db with relative to 800 db, during ORI 311, from March 8 to 27, 1992.

In addition to the features in the SCS, the flows east of the Luzon Strait are worth special noticing too. The summer survey shows streamlines converging along the 121°E meridian (Fig. 5). The convergence zone, whose position well matches with that of the salinity front (Fig. 3), thus marks the main stream of the Kuroshio in the Luzon Strait. Obviously, this is a branch of the northward currents flowing

along the east coast of Luzon, i.e. the Kuroshio in its beginning region (NITANI, 1970). After passing the Balintang Channel north of Luzon the branch enters into the Luzon Strait, in which it interacts with the SCS flows. Are cyclonic eddies west of the Kuroshio branch (Fig. 5) the products of the interaction process, or of whatever, deserve for our studies. Additionally, another important feature has been

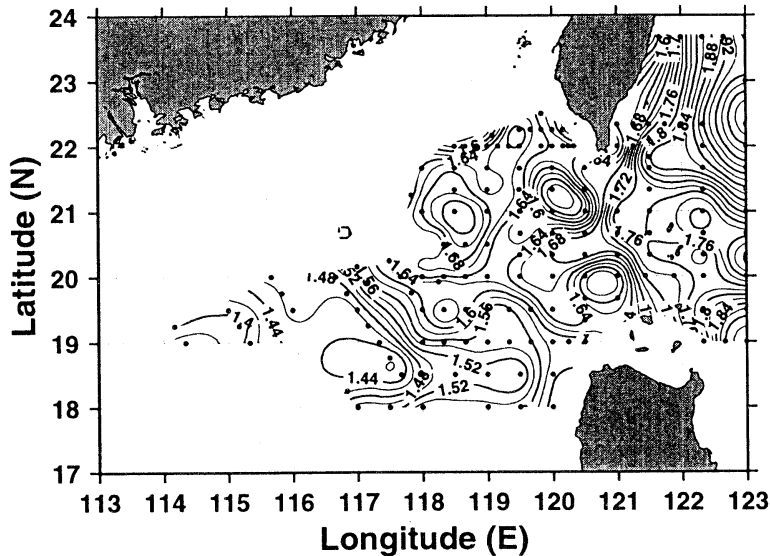


Fig. 5. The distribution of ΔD (in dyn.m) of 20 db with relative to 800 db, during ORI 399, from August 28 to September 10, 1994.

revealed by the summer survey too, i.e., the region east of 122°E and north of 21°N in which appears the second convergence zone of streamlines (Fig. 5). Vertical sections of geostrophic currents along several latitudinal transects east of Taiwan show that the current field frequently possesses a multiple core structure. This particular feature, had been noticed by CHU (1970), is likely caused by the confluence of different branches of the Kuroshio and outflows from the SCS, as suggested in Fig. 5.

The way how the flow pattern shown in Fig. 4 evolves into that in Fig. 5 is an interesting topic for the SCS regional oceanography. Hydrographic data collected from ORI cruises 283, 391 and 415 (Table 1) may illuminate some of ambiguities on the inter-seasonal transition process. Figs. 6 to 8 present the spatial distributions of ΔD on 20 db⁶ as well as S_{\max} in the northeastern SCS in April, May and June, respectively; from which an acute reader may notice the retrocession sequence of the high salinity Kuroshio intrusion waters from the SCS to the Pacific since March (*cf.* Figs. 2, 6, 7a, 8a and 3). The evolution of the pattern of ΔD

shows that the Kuroshio intrusion waters, which are associated with the northwestwards flows on the upper-right portion of Fig. 4, may be disintegrated into two parts. The eastern one is a loop-like current pattern which recedes and returns to the Pacific side of the Luzon Strait since spring (Figs. 6 and 7), the other may stay at the region east of Tung-Sha Tao and south of the Formosa Banks (Fig. 5). Meanwhile, cyclonic eddies penetrate into the middle area from the south (Figs. 5 and 7).

5. Implications of sea surface slope

The differences of MMSLs between two opposite stations across a stream, $\Delta\zeta$, had long been used for the inference of volume transports of currents in between (e. g., CHU 1976, among others). There are two tide stations in or near the Luzon Strait, i.e. Kao-Hsiung and Port Irene, their data are appropriate for our discussions. Additionally, the MMSLs at San Jose, likely representing the variation of the sea-level along the eastern coast of the central SCS, are cited too. Fig. 9 shows the time series of $\Delta\zeta$ between Kao-Hsiung and San Jose ($\Delta\zeta_{KS}$), and that between Kao-Hsiung and Port Irene ($\Delta\zeta_{KP}$). However, for unknown reasons, the MMSLs of 1991 summer are unusually higher at Kao-

⁶ The depth of reference level used in Figs. 6 to 8 is dependent on the maximum depth of CTD casts, which was not unified during these cruises.

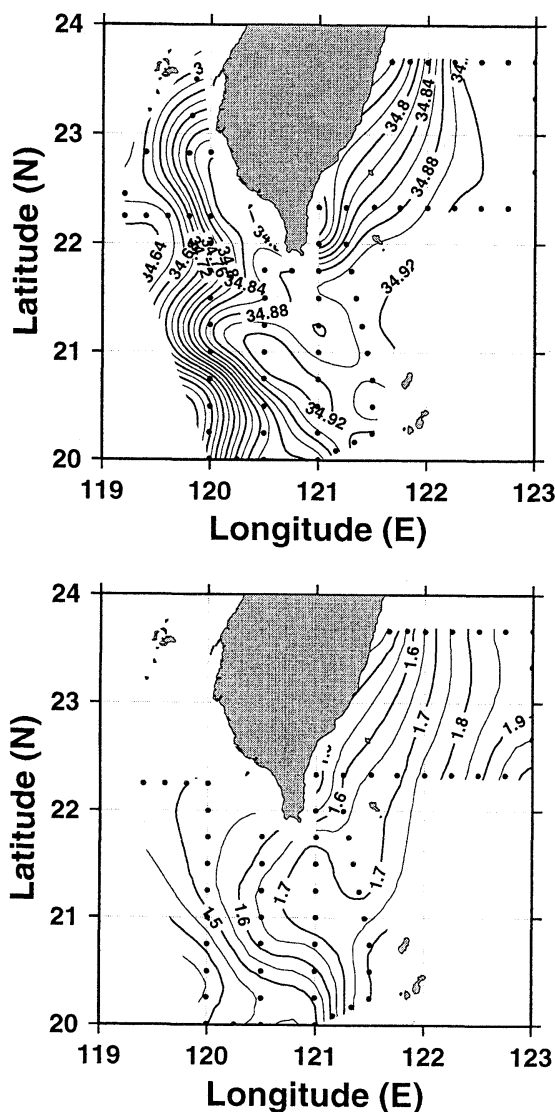


Fig. 6. The distribution of (a) S_{max} (in psu, upper panel), (b) ΔD (in dyn.m, lower panel) of 20 db with relative to 600 db, during ORI 415, from April 4 to 13, 1995.

Hsiung and lower at San Jose than other years, also there were many missing data in Port Irene during 1991, so discussions are restricted on the 1992 and 1993 time series only.

Several factors, e. g. the variation of atmospheric pressure, the bench mark of tide stations, longshore wind stress and the large scale currents, etc., are influential to the magnitude of MMSL (CHU, 1976). In the Luzon Strait area, however, the barometric effect may provide a

minor contribution to $\Delta\zeta$. On the other hand, the uncertainty of the bench mark of tide stations can induce only a constant offset which is irrelevant to the annual variation of $\Delta\zeta$. Therefore, what we present in Fig. 9 are caused mainly by the joint effects of geostrophy and wind stress. The time series of $\Delta\zeta_{KP}$ reveals a regular annual cycle; it is high from October to February and low from May to September and the annual range is about 25~30cm⁷ (Fig. 9). However, $\Delta\zeta_{KS}$ possesses an entirely different structure; it is biannual with both peaks occur in March to May and in August to September and with contiguous troughs in June to July and in October to November, respectively. The annual range of $\Delta\zeta_{KS}$ is relatively small and its magnitude merely about 15 cm (Fig. 9). The annual variation of $\Delta\zeta_{KP}$ is consistent with our previous knowledges, i.e., water flows are outward from the SCS to the Pacific during summer and reverse in winter (WYRTKI, 1961; CHU, 1972; Fan, 1982), but $\Delta\zeta_{KS}$ is rather curious because of its biannual behavior really beyond our intuition.

To conceive the causation of the biannual cycle, we have to inspect the original time series carefully. The MMSLs of San Jose in 1992 and 1993 are, on the average, lower than those of the other two stations in August and/or September, but higher in October and/or November, respectively. However, the highest MMSL shifts to Kao-Hsiung in March to May, and to Port Irene in June and July. What effects cause this variation? Beforehand any speculations, perhaps we could use the method of empirical orthogonal decomposition for exploring modal structures embedded in the time series; for details one should refer to KUNDU, ALLEN and SMITH (1975). Table 2 gives the eigenvalue λ_n , the explained variance $\lambda_n / \sum \lambda_n$ (in percentage of total variance) and the three components of the eigenfunction $\phi_n(x_n)$ resolved, where the subscript n denotes mode number, $n=1, 3$, $\phi_n(x_i)$ the normalized eigenfunction of mode n and x_i three different tide stations, i.e., x_1 represents Kao-Hsiung, x_2 San Jose and x_3 Port Irene, respectively. The time series of amplitudes of three empirical modes, $E_n(t)$, acquired from the decomposition is shown in Fig. 10. By definition,

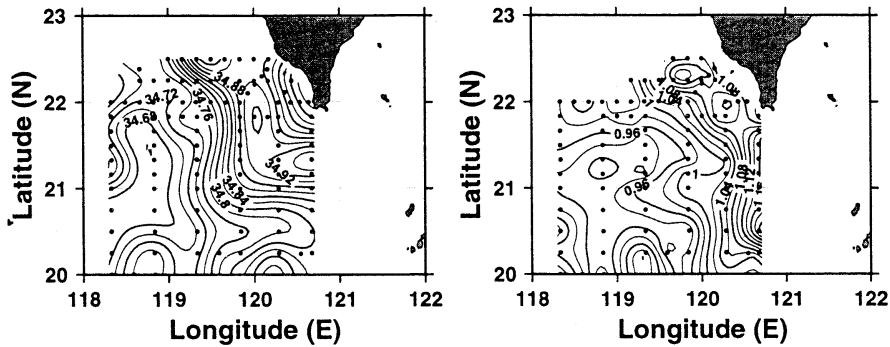


Fig. 7. The distribution of (a) S_{\max} (in psu, left panel), (b) ΔD (in dyn.m, right panel) of 20 db with relative to 400 db, during ORI 283, from May 23 to 28, 1991.

we have

$$\zeta_{xi}(t) = \sum_{n=1}^3 E_n(t) \phi_n(x_i) \text{ and} \\ E_n(t) = \sum_{i=1}^3 \zeta_{xi}(t) \phi_n(x_i),$$

where $\zeta_{xi}(t)$ denotes the MMSLs of the tide station x_i (KUNDU *et al.*, 1975).

Obviously, both of modes 1 and 2 are dominated by the annual cycle, only mode 3 is principally biannual (Fig. 10). By simple manipulation on the above equations, we have

$$\Delta \zeta_{KS} = \sum_{n=1}^3 E_n(t) (\phi_n(x_1) - \phi_n(x_2));$$

from Table 2, $(\phi_n(x_1) - \phi_n(x_2))$ is 0.13, -0.12 and 1.40 for modes 1, 2 and 3, respectively. Though the energy density of mode 1, i.e. λ_1 , is about 9 and 37 times to that of mode 2 (λ_2) and mode 3 (λ_3), after taking square root this proportion (of E_n) becomes 1 : 0.33 : 0.16. So their contribution to $\Delta \zeta_{KS}$ is 1 : -0.31 : 1.57 for modes 1, 2 and 3, respectively, which confirms that $\Delta \lambda_{KS}$ is mainly induced by modes 3 and 1 fluctuations. Similarly, $\Delta \lambda_{KS}$ is caused principally by modes 2 and 1. Comparing the flow patterns presented in the last section with the time series plot of E_3 in Fig. 10, we may suggest that the hump of E_3 in March, 1992 is due to the fact that Kao-Hsiung was located on the right-hand side of the northwestward Kuroshio intrusion currents, thereby surface elevation of Kao-Hsiung is relatively higher (Fig. 4). The other hump, occurred in August or September, however, was likely due to the geostrophy of

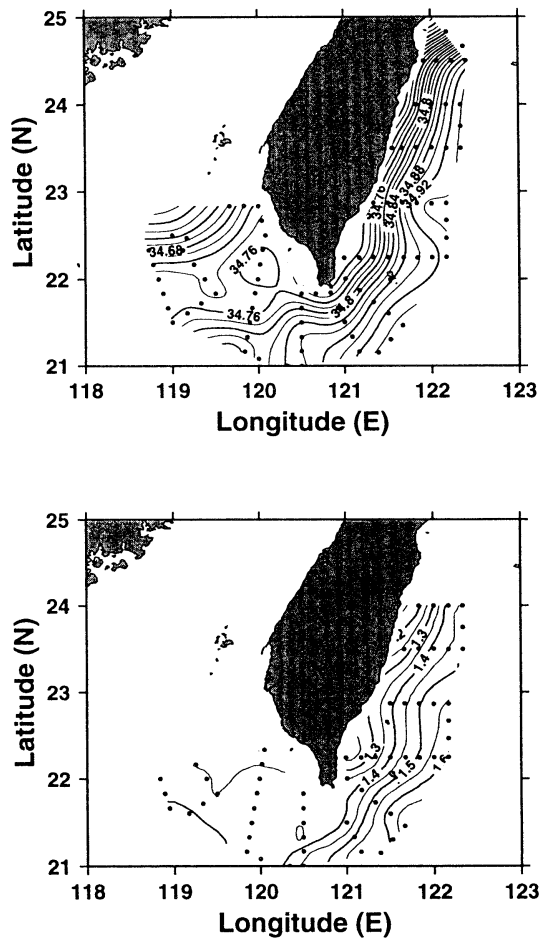


Fig. 8. The distribution of (a) S_{\max} (in psu, upper panel) (b) ΔD (in dyn. m, lower panel) of 20 db with relative to 600 db, during ORI 391, from June 14 to 20, 1994.

⁷ The magnitude exceeds WYRTKI'S (1961) result a lot.

Difference of MMSL (cm) between

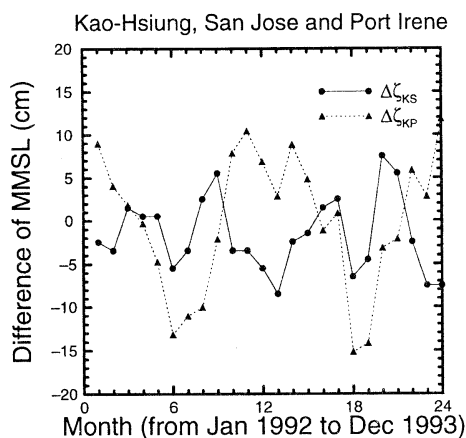


Fig. 9. The time series plot of $\Delta\zeta_{KS}(t)$ and $\Delta\zeta_{KP}(t)$, from January 1992 to December 1993.

the northward currents along the southwest coast of Taiwan as well as the southeastward flows from the central SCS into the Sulu Sea (WYRTKI, 1961); both may induce a similar effect on $\Delta\zeta_{KS}$ (Fig. 5).

In addition to the peaks of $E_s(t)$, the troughs, appeared in June and in October, November or January respectively, are worth noticing too. The prior one is likely associated with the entirely eastward movement of waters from the SCS to the Pacific, either by the retrocession of the Kuroshio intrusion waters in the northern Luzon Strait⁸ or by the northward extension of the above-mentioned cyclonic-flow system from the central SCS to the southern Luzon Strait (Figs. 6 to 8), the latter is likely associated with the cessation of winter monsoon and the later inception and augmentation of summer monsoon. The posterior one may correspond to the net outward flows from the SCS to the Pacific through the northern reach of the Luzon Strait, which is in compensation with the intrusion of Kuroshio waters on its south. Recent observations of CHUANG (personal communication) from a moored current meter⁹ may partially support the latter speculation. Another interesting point is that the timing of the occurrence of these troughs matches quite well with the onset of southwesterly or northeasterly monsoon respectively. This can not attribute simply to coincidences but might imply

Amplitude of eigen modes of MMSL

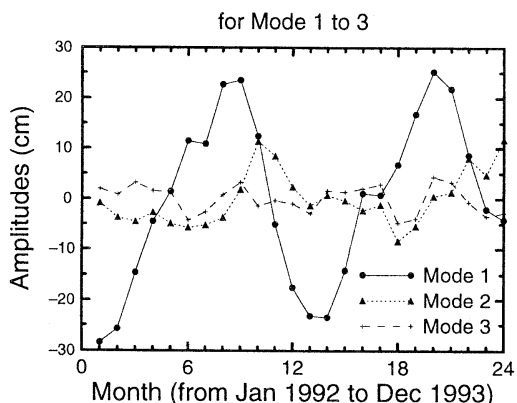


Fig. 10. The time series plot of $E_n(t)$ for all three eigen modes resolved, from January 1992 to December 1993.

Table 2. Empirical eigenfunctions for MMSLs of Kao-Hsiung, San Jose and Port Irene.

Items	Mode 1	Mode 2	Mode 3
$\lambda_n(\text{cm}^2)$	263.3	28.4	7.1
$\lambda_n / \sum \lambda_n$	88.1%	9.5%	2.4%
$\phi_n(x_1)$	0.50	0.50	0.71
$\phi_n(x_2)$	0.37	0.62	-0.69
$\phi_n(x_3)$	0.79	-0.61	-0.12

the significance of the monsoon driven effects on the SCS circulations.

6. Discussion and summary

Foregoing investigations reveal quite a complicated flow pattern occurred in the northern SCS, which is in general not in accordance with our previous knowledges. Nevertheless, from them we have identified several dynamically-active systems, i.e., firstly, the system with cyclonic flows in the central SCS, which is a common feature for both the spring and summer surveys; secondly, the Luzon Strait branch of Kuroshio and its intrusion motions; and thirdly, the anti-cyclonic gyre south of Formosa Banks as well as its neighbors, the cyclonic eddies west of the Luzon Strait, found during the summer cruise. The synoptic-scale variation of the northern SCS is basically governed by these systems.

The cyclonic-circulation system is likely a permanent feature of the central SCS. The

report of SCSIOAS (1985) had documented the finding of a seemingly persistent structure, i.e., a cold eddy appears at southwest of Tung-Sha Tao almost all the year round. Based on Fig. 5, we may suggest that the foregoing two are actually the same thing. However, not all observations support this view point; e.g., in the central SCS, though a cyclonic gyre does present in WYRTKI'S (1961) current chart of winter but the position deviates a lot, also it is absent in other seasons¹⁰. LIU and SU (1992) had suggested a nonlinear advection mechanism, i.e., the cyclonic system could be induced by the fluxes of positive vorticity from the west flank of the Kuroshio through the Luzon Strait to the central SCS. However, during summer the thermocline in the northeastern SCS is usually much steeper and shallower than that in the Kuroshio (cf. NITANI, 1970). These might imply upwelling motions are more energetic in the SCS basin. Could the cyclonic system be simply a manifestation of the latter activity? This is an interesting topic deserving for further studies.

The behavior of the Luzon Strait branch of Kuroshio (Fig. 5) is of significance to the interaction of the South China and western Philippine Seas. Extended southward from the southern tip of Taiwan is the Heng-Chun Ridge, a steeply-raised submarine topography. Geostrophic currents calculated, along meridional transects across the Luzon Strait¹¹, show the segment in between 20.5 and 21°N is seemingly a major pathway for surface waters flushing into or out of the SCS, where the latter latitude is just near the southernmost sill of the foregoing ridge. This suggests the importance of flow-topography interaction on the dynamics of the SCS. With a favorable flow direction, the Kuroshio branch may interact with the ridge; inevitably, this will induce many interesting features, e.g., branching of inflows in front of the ridge (cf. WHITEHEAD 1985) and

also its influences on the downstream.

The anti-cyclonic eddy south of Formosa Banks and its counterparts, the cyclonic ones west of the Luzon Strait (Fig. 5), are unknown features that have never been well-documented in literatures hitherto. WANG (1986) had reported the lower layer structure of the cold eddy southwest of Taiwan, whose cyclonic motions could extend from the surface down to 1500 db and even below. However, the connections between this eddy and the cyclonic flows in the central SCS were unknown during that time. Now, from Fig. 5, clearly the former is likely an extension of the latter, but how and why the latter evolves into a series of eddies remains to be studied.

The circulation of the SCS is governed principally by the alternative exertion of northeasterly and southwesterly monsoons as well as the influence from the Kuroshio east of the Luzon Strait; the latter is also a major provider of salt, mass, heat and vorticity to the SCS. This nature has been illuminated by a number of numerical experiments (e. g. SHAW and CHAO 1994; CHAO, SHAW and WU 1996, among others). So, intuitively, we may suggest that the evolution of above-mentioned dynamically-active systems is driven by these factors too. However, the flow pattern in the northern SCS, as emerged from our observations, is far more complicated than that had ever been derived from numerical models. This might be attributed to the coarse resolution or the false usage of open boundary conditions, especially across the Luzon Strait, in the numerical calculation. Recently, a scientific plan on the monitoring of currents in the Luzon Strait has been shaped and granted in Taiwan; which anticipates to install several arrays of current-meters and to make repeated CTD surveys, in and across the Luzon Strait, in the following two years. Only through these efforts can details of the foregoing processes be clarified.

In summary, in terms of field hydrographic

⁸ Perhaps in the form of a loop current, as suggested by LI and WU (1989).

⁹ Which shows persistently eastward to southeastward flows occurred from late October of 1994 to February of 1995, where the location of the current matter is in the northern Luzon Strait (CHUANG, 1995).

¹⁰ Neither found in numerical model results derived from climatological data, e.g. SHAW and CHAO (1994).

¹¹ For those cruises shown in Table 1, as well as others not cited.

surveys and the MMSLs of coastal tide stations, we may suggest that the flow pattern of the northeastern SCS is governed basically by aforementioned dynamical systems. The less variant one is likely the cyclonic system located at the northern central SCS basin to the northwest of north Luzon, in which is the center of the monsoon-driven cyclonic gyre in winter, but the stem of a series of cyclonic eddies in summer; the latter then separates the Kuroshio east of the Luzon Strait and the anti-cyclonic eddy south of Formosa Banks. After the onset of winter monsoon, the northern extension of the cyclonic system withdraws southwards, meanwhile the Luzon Strait branch of the Kuroshio penetrates into the northeastern SCS and the intruded waters, as well as circulating waters, may develop anti-cyclonic gyres or eddies in the northern SCS during winter and spring (WANG and CHERN, 1987a). As the cessation of winter monsoon in spring, the intruded Kuroshio waters retreat eastwards and northwards; some of them are flushed out through the Taiwan Strait by the northward currents along the west coast of Taiwan (the Kuroshio branch in the Taiwan Strait, WANG and CHERN, 1988), the remainder may form a loop-like flow pattern in the northeastern SCS. As time goes by, the aforementioned cyclonic system, stimulated further by the inception and augmentation of summer monsoon, extends northwards continuously. So, the anti-cyclonic gyre at the northern SCS breaks; one of it, the loop pattern, migrates to the Pacific side of the Luzon Strait gradually (Figs. 6-8), the rest, still in the form of anti-cyclonic motions but having a much reduced size, resides at the south of Formosa Banks in summer; the space left is then replaced by cyclonic eddies penetrated from the central SCS (Fig. 5). Obviously, the scenario is quite different from that presented by WYRTKI's (1961) flow chart; so far many aspects are preliminary and some of them still obscure, all of these deserve for further studies in the future.

Acknowledgments

This study is sponsored by the National Science Council, the Republic of China, Grants No. NSC83-0209-M-002A-017 and NSC84-2611-M-002

A-0160S. The MMSL data are provided by BODC (for San Jose and Port Irene) and CWB (for Kao-Hsiung), respectively.

References

- CHAN K. -M. (1970): The seasonal variation of hydrological properties in the northern South China Sea. *In* The Kuroshio-A Symposium on the Japan Current, J. C. MARRY, (ed). East-West Center Press, Honolulu, 143-162.
- CHAO S. -Y., P. -T. SHAW and WU S. Y. (1996): El Niño Modulation of the South China Sea. *Deep Sea Res.* (submitted.)
- CHU T. -Y. (1970): Report on the variation of velocity and volume transport of the Kuroshio. *In* The Kuroshio - A Symposium on the Japan Current J. C. Marr, (ed). East-West Center Press, Honolulu, 163-174.
- CHU T. -Y. (1972): A study on the water exchange between Pacific Ocean and the South China Sea. *Acta Oceanogr. Taiwanica*, **2**, 11-24.
- CHU T. -Y. (1976): Study of the Kuroshio current between Taiwan and Ishigaki-jima. *Acta Oceanogr. Taiwanica*, **6**, 1-24.
- FAN K. -L. (1982): A study of water mass in Taiwan Strait. *Acta Oceanogr. Taiwanica*, **13**, 140-153.
- HU T. -K. (1995): On the distribution of water masses in the northern South China Sea during spring-time. Master Thesis, Institute of Oceanography, National Taiwan University (in Chinese).
- KUNDU P. K., J. S. ALLEN and R. L. SMITH (1975): Modal decomposition of the velocity field near the Oregon coast. *J. Phys. Oceanogr.* **5**, 683-704.
- LI L. and B. -Y. WU (1989): A Kuroshio loop in South China Sea? - on circulations of the northeastern South China Sea. *Taiwan Strait* **8**, 1, 89-95 (in Chinese with English abstract).
- LIU X. -B. and SU J. -L. (1992): A reduced gravity model of the circulation in the South China Sea. *Oceanologia et Limnologia Sinica*, **23**, 2, 167-174 (in Chinese with English abstract).
- NITANI H. (1970): Oceanographic conditions in the sea east of the Philippines and Luzon Strait in summers of 1965 and 1966. *In* The Kuroshio - A Symposium on the Japan Current, J. C. MARRY, (ed). East-West Center Press, Honolulu, 213-232.
- QIU D. -Z., T. -H. YANG and Z. -X. GUO (1984): A west-flowing current in the northern part of the South China Sea in summer. *Tropic Oceanology*, **3**, 4, 65-73 (in Chinese with English abstract).
- SCSIOAS (1985): A research report on the general survey of the South China Sea (II). Science Pub., Beijing (in Chinese).
- SHAW P. -T. (1989): The intrusion of water masses into

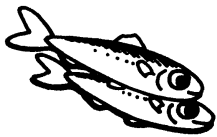
- the sea southwest of Taiwan. *J. Geophys. Res.*, **94**, 18213–18226.
- SHAW P.-T. and S.-Y. CHAO (1994): Surface circulation in the South China Sea. *Deep Sea Res.*, **41**, 1663–1683.
- WANG J. (1986): Observation of abyssal flows in the northern South China Sea. *Acta Oceanogr. Taiwanica*, **16**, 36–45.
- WANG J. and C.-S. CHERN (1987a): The warm-core eddy in the northern south China Sea. I. Preliminary observations on the warm-core eddy. *Acta Oceanogr. Taiwanica*, **18**, 92–103 (in Chinese with English abstract).
- WANG J. and C.-S. CHERN (1987b): The warm-core eddy in the northern south China Sea. II. A simple mechanism for the establishment and development of the warm-core eddy. (*Acta Oceanogr. Taiwanica*, **18**, 104–113 (in Chinese with English abstract).
- WANG J. and C.-S. CHERN (1988): On the Kuroshio branch in the Taiwan Strait during wintertime. *Prog. Oceanogr.*, **21**, 469–491.
- WHITEHEAD J. A. (1985): The deflection of a baroclinic jet by a wall in a rotating fluid. *J. Fluid Mech.*, **157**, 79–93.
- WU B.-Y. (1982): Some problems on circulation study in Taiwan Strait. *Taiwan Strait*, **1**, 1, 1–7 (in Chinese with English abstract).
- WYRTKI K. (1961): Scientific Results of Marine Investigations of the South China Sea and the Gulf of Thailand 1959–1961-Physical Oceanography of the Southeast Asian Waters. *NAGA REPORT*, Vol.2, pp. 195.
- XU J.-P. and J.-L. SU (1993): Water mass analysis on the Kuroshio water intruding into the South China Sea (abstract). Abstracts of the Taiwan Strait and nearby marginal seas oceanography workshop, August 12–16, Amoy, China.

Received January 4, 1996

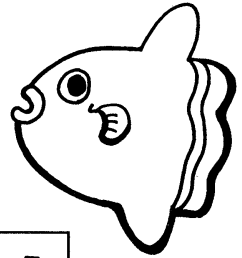
Accepted May 31, 1996

賛 助 会 員

阿 部 嘉 方	東京都練馬区春日町 2-15-6
株式会社 内田老鶴園 内田 悟	東京都文京区大塚 3-34-3
有限会社 英和出版印刷社	東京都北区中里 2-7-7
株式会社 カ イ ジ ョ ウ	東京都西多摩郡羽村町栄町 3-1-5
㈱ 海洋生物環境研究所	東京都千代田区内神田 1-18-12 北原ビル内
株式会社 川合海苔店	東京都大田区大森本町 2-31-8
株式会社 自然・情報環境研究所	横浜市栄区桂町 1-1, 3-401
新日本気象海洋株式会社	東京都世田谷区玉川 3-14-5
全日本爬虫類皮革産業連合会	東京都足立区梅田 4-3-18
株式会社 高 岡 屋	東京都台東区上野 6-7-22
株式会社東京久栄技術センター	埼玉県川口市芝鶴ヶ丸 6906-10
株式会社西日本流体技研	長崎県佐世保市棚方町 283
日本アクアラング株式会社	神奈川県厚木市温水 2229-4
㈱ 三 菱 総 合 研 究 所 (社会情報システム部)	東京都千代田区大手町 2-3-6
㈱ 本 地 郷	東京都千代田区神田須田町 2-2-4 須田町藤和ビル7F
株式会社 読売広告社	東京都中央区銀座 1-8-14
渡辺機開工業株式会社	愛知県渥美郡田原町神戸大坪 230
株式会社 渡部計器製作所	東京都文京区向丘 1-7-17



海洋生物資源を大切に利用する企業でありたい
 —— 青魚(イワシ・サバ・サンマ)から宝を深し出す ——



母なる海・海には愛を!

La mer la mère, l'amour pour la mer!



SHIDA

信田 缶詰 株式会社

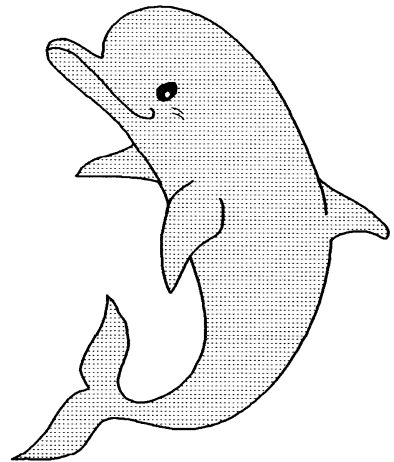
〒288 千葉県銚子市三軒町2-1 TEL 0479(22)7555 FAX 0479(22)3538


● 製造品・水産缶詰・各種レトルトパウチ・ビン詰・抽出スープ・他

街をきれいにしてイルカ?

事業内容

- 産業廃棄物、一般廃棄物の収集運搬処理
- 各種槽、道路、側溝の清掃
- 上下水道、排水処理施設運転管理
- 下水道管内TVカメラ調査
- 総合ビル管理
- その他上記に付随する一切の業務



 株式会社 春海 丸工営

本社 〒312 茨城県ひたちなか市長砂872-4 ☎029-285-0786 FAX285-7519
 銚子支社 〒288 千葉県銚子市長塚町6-4490-1 ☎0479-22-4733 FAX22-4746
 水戸支社 〒310 茨城県水戸市中央 2-2-6 ☎029-226-9639 FAX226-9855

日仏海洋学会入会申込書

(正会員・学生会員)

	年度より入会	年 月 日 申込
氏 名		
ローマ字		年 月 日 生
住 所 〒		
勤務先 機関名		
電 話		
自 宅 住 所 〒		
電 話		
紹介会員氏名		
送付金額	円	送金方法
会誌の送り先 (希望する方に○をつける)	勤務先	自 宅

(以下は学会事務局用)

受付	名簿 原簿	会費 原簿	あて名 カード	学会 記事
----	----------	----------	------------	----------

入会申込書送付先： 〒150 東京都 渋谷区 恵比寿 3-9-25

(財)日仏会館内

日 仏 海 洋 学 会

郵便振替番号： 00150-7-96503

日 仏 海 洋 学 会 編 集 委 員 会 (1996-1997)

委員 長: 山口征矢

委 員: 青木三郎, 半沢正男, 堀越増興, 前田 勝, 落合正宏, 松山優治, 柳 哲雄, 渡辺精一

海外委員: H. J. CECCALDI (フランス), E. D. GOLDBERG (アメリカ), T. ICHIYE (アメリカ), T. R. PARSONS (カナダ)

幹 事: 落合正宏, 佐藤博雄

投 稿 の 手 引

1. 「うみ」(日仏海洋学会機関誌; 欧文誌名 *La mer*) は, 日仏海洋学会正会員およびそれに準ずる非会員からの投稿(依頼稿を含む)を, 委員会の審査により掲載する。
2. 原稿は海洋学および水産学両分野の原著論文, 原著短報, 総説, 書評, 資料などとする。すべての投稿は, 本文, 原図とも正副2通とする。副本は複写でよい。本文原稿用紙はすべてA4判とし, 400字詰原稿用紙(和文)に, または厚手白紙にダブル・スペース(和文ワープロでは相当間隔)で記入する。表原稿および図説明原稿は, それぞれ本文原稿とは別紙とする。
3. 用語は日, 仏, 英3カ国語の何れかとする。ただし, 表および図説明の用語は仏文または英文に限る。原著論文(前項)には約200語の英文または仏文の要旨を, 別紙として必ず添える。なお, 欧文論文には, 上記要旨の外に, 約500字の和文要旨をも添える。ただし, 日本語圏外からの投稿の和文要旨については編集委員会の責任とする。
4. 投稿原稿の体裁形式は最近号掲載記事のそれに従う。著者名は略記しない。記号略号の表記は委員会の基準に従う。引用文献の提示形式は, 雑誌論文, 単行本分載論文(単行本の一部引用を含む), 単行本などの別による基準に従う。
5. 原図は版下用として鮮明で, 縮尺(版幅または1/2版幅)に耐えられるものとする。
6. 初校に限り著者の校正を受ける。
7. 正会員に対しては7印刷ページまでの掲載を無料とする。ただし, この範囲内であっても色彩印刷を含む場合などには, 別に所定の費用を著者負担とすることがある。正会員の投稿で上記限度を超える分および非会員投稿の印刷実費はすべて著者負担(10,000円/頁)とする。
8. すべての投稿記事について, 1篇あたり別刷50部を無料で請求できる。50部を超える分は請求により, 50部単位で作製される。別刷請求用紙は初校と同時に配布される。
9. 原稿の送り先は下記の通り。

〒108 東京都港区港南4-5-7 東京水産大学 山口征矢 気付
日仏海洋学会編集委員会

1996年8月25日 印刷
1996年8月28日 発行

う み 第34巻
第3号

定 価 1,600 円

編 集 者 山 口 征 矢

発 行 所 日 仏 海 洋 学 会

財団法人 日仏会館内

東京都渋谷区恵比寿3-9-25

郵便番号: 150

電話: 03(5421)7641

振替番号: 00150-7-96503

印 刷 者 佐 藤 一 二

印 刷 所 (有)英和出版印刷社

東京都北区中里2-7-7

郵便番号: 114

電話: 03(5394)4856

SOMMAIRE

Proceedings of the Eighth JECSS & PAMS Workshop,
26-28 September 1995, Matsuyama, Japan

Preface	T. YANAGI	93
Embedding an oceanic mixed layer model into an ocean general circulation model of the East Sea (Japan Sea)	Y. NOH, C. I. JANG, C. H. KIM and J. H. YOON	95
A hindcast experiment in the East Sea (Sea of Japan)	I. BANG, J. K. CHOI, L. KANTHA, C. HORTON, M. CLIFFORD, M. S. SUK, K. I. CHANG, S. Y. NAM and H. J. LIE	108
Comparison of sea water carbonate parameters in the East China Sea and the Sea of Japan	S. L. WANG and C. T. A. CHEN	131
Mode of mud deposition on shelf to basin area off Akita, north east Japan Sea	K. IKEHARA, H. KATAYAMA and T. NAKAJIMA	137
Separation of the Tsushima Current from the Kuroshio : A numerical study with an idealized geometry	S. Y. NAM, M. S. SUK, I. BANG, K. I. CHANG and Y. H. SEUMG	152
Time variation of the current northwest of Tsushima	T. SHINOZAKI, A. TASHIRO, T. NAGAHAMA, H. ISHII, K. OMURA, Y. OUCHI, Y. HASHIMOTO and K. KAWATATE	163
Seasonal variation of the East Korea Warm Current and its relation with the cold water	Y. K. CHO and K. KIM	172
The stratification variations during spring and neap tidal periods in Deukryang Bay, Korea	B. G. LEE, T. YANAGI, H. TAKEOKA and K. D. CHO	183
Tidal energy in Suyoung Bay, Korea	D. S. KIM and T. YANAGI	192
Numerical modelling on atmospheric circulations over the eastern mountainous coastal seas of Korea	H. CHOI	199
ERS-1 SAR observations of dynamic features in the southern East China Sea	L. M. MITNIK, M. K. HSU and C. T. LIU	215
Variability of suspended particle concentration due to tidal influences in the shelf sea north of Taiwan	C. H. TSAI and I. J. CHENG	226
A paleoenvironmental record during 7-21 Ka BP in the sediments off northeastern Taiwan	J. Y. LOU and C. T. A. CHEN	237
Some aspects on the circulation in the northern South China Sea	J. WANG and C. S. CHEN	246